Characterising Three Dimensional Deformations and Strains of Orthodontic Archwires under Torsion

by

Bill Thien Tam Tran

A thesis submitted in partial fulfillment of the requirements for the degree of

Master of Science

Department of Mechanical Engineering

University of Alberta

ABSTRACT

In orthodontics, braces are commonly used to correct dental misalignments. Third-order torque refers to the application of torsion to correct angular inclinations of teeth. Its application involves the use of a twisted archwire inside of an orthodontic bracket to generate the required forces and moments to achieve tooth movement. Third-order torque is continually researched in hopes of gaining fundamental knowledge with regards to its biomechanics. Understanding the interactions between an archwire and bracket are important in the application of torque. The Orthodontic Torque Simulator (OTS) is an in vitro simulator of third-order torque mechanics. Studying archwire and bracket mechanics using the OTS can be aided with the use of three-dimensional (3D) digital image correlation (DIC). The implementation of 3D DIC enables surface deformations and strains to be measured throughout an applied third-order rotation, where the response of the archwire can be quantified. The 3D DIC system was rigorously verified to ensure measurements were representative of actual third-order mechanics. In applying third-order torque, comparisons were made between 0.019”x0.025” stainless steel and titanium molybdenum alloy archwires. Surface shear strains were used to characterise the archwire behaviour during third-order torque, using both orthodontic brackets as well as a custom rigid dowel. It was found that surface shear strains vary due to differing contact conditions. Further, archwires may undergo permanent deformation as determined by the presence of residual shear strains. The application of 3D DIC with third-order torque experiments aids in the assessment of archwire and bracket interactions under applied loads, which can be used to better understand the biomechanics of third-order torque.

ACKNOWLEDGEMENTS

This thesis is the culmination of my academic journey. Its completion includes the efforts of many along the way. First and foremost, I'd like to thank my supervisors, Drs. Jason Carey and Dan Romanyk, whose unwavering support and encouragement has been fundamental in my growth and accomplishments, both as a graduate student and as a person. They challenged me to be my best self and do my best work, gave me every opportunity to improve and succeed, and most importantly stood beside me through all my trials and tribulations. I will be forever indebted to them for being cornerstones in my endeavours.

I would also like to express my gratitude for Drs. David Nobes and Samer Adeeb, whose expertise and critical guidance were paramount in the progression of my research. They helped me problem solve and continually move forward, overcoming whatever technical challenges that came up. Both were always available for technical advice and guidance that was truly invaluable for my research.

Further, I'd like to thank the brilliant members of the Carey Lab and Romanyk Lab. Everyone looked out for each other with an overwhelming sense of community and collaboration. It's an honour to call these exceptional people my friends.

And finally, this thesis would not have been possible without the endless support of my family and friends. Consistent in their reassurance and encouragement, they were my foundation from day one and I'm so proud to share my triumphs with the people who care most about me.

TABLE OF CONTENTS

LIST OF TABLES

LIST OF FIGURES

LIST OF ABBREVIATIONS

2D	Two-Dimensional
3D	Three-Dimensional
ANOVA	Analysis of Variance
DIC	Digital Image Correlation
FE	Finite Element
IBD	Inter-Bracket Distance
LSM	Least Squares Matching
OTS	Orthodontic Torque Simulator
PDL	Periodontal Ligament
RD	Rigid Dowel
SS	Stainless Steel
TMA	Titanium Molybdenum Alloy

LIST OF SYMBOLS

x	Direction in the long axis of the archwire (axis of third-order rotation) and the horizontal dimension of images
y	Direction describing the vertical dimension of images
z	Direction describing depth and out-of-plane motion
u	Horizontal cross-sectional displacement from rotation
v	Vertical cross-sectional displacement from rotation
θ	Angle of rotation
w	Cross-sectional warp
ψ	Warp function
δ_x	Displacement in the x-direction
δ_y	Displacement in the y-direction
δ_z	Displacement in the z-direction
$\varepsilon_x = \varepsilon_{xx}$	Principal strain in x-direction
$\varepsilon_y = \varepsilon_{yy}$	Principal strain in y-direction
ε_z	Principal strain in z-direction
$\gamma_{xy} = \varepsilon_{xy}$	Shear strain on xy-plane
γ_{xz}	Shear strain on xz-plane
γ_{yz}	Shear strain on yz-plane
p	Probability value
η^2	Effect size
α	Probability of Type I error
β	Probability of Type II error

CHAPTER 1 INTRODUCTION

1.1 Motivation

Dental care and associated costs contribute to a large proportion of health spending in Canada. A total of $11.7 billion was spent in 2012, making dental care the second largest expenditure in private-sector health spending behind pharmaceuticals [1]. Orthodontics, a subset of dental care, is the practise of moving and aligning teeth to improve occlusion (i.e. how teeth contact one another) and aesthetics. In Canada, an estimated 799 orthodontists were practising in 2016 [2].

Malocclusions (inter- and intra-arch tooth misalignments) can degrade dental health, and are caused when the dental arches in the maxilla (upper jaw) and mandible (lower jaw) do not interact in an optimal manner [3]. Different factors can contribute to malocclusions, such as missing, crowded, misshaped, or misaligned teeth, among others [3]. There are various ways to treat malocclusions, including traditional fixed appliances (braces) and clear aligners. Additionally, digital technologies aiding in the treatment process are becoming increasingly common [4]–[6]. Fixed appliances refer to orthodontic materials that are attached to a patient's teeth over the span of their treatment [7]. One such utilisation of fixed appliances is the edgewise system, commonly referred to as braces. Braces include orthodontic brackets that are bonded to teeth and orthodontic archwires that are shaped to induce tooth movement when engaged inside brackets. A schematic showing the conventional edgewise fixed appliance is shown in Figure 1.1.

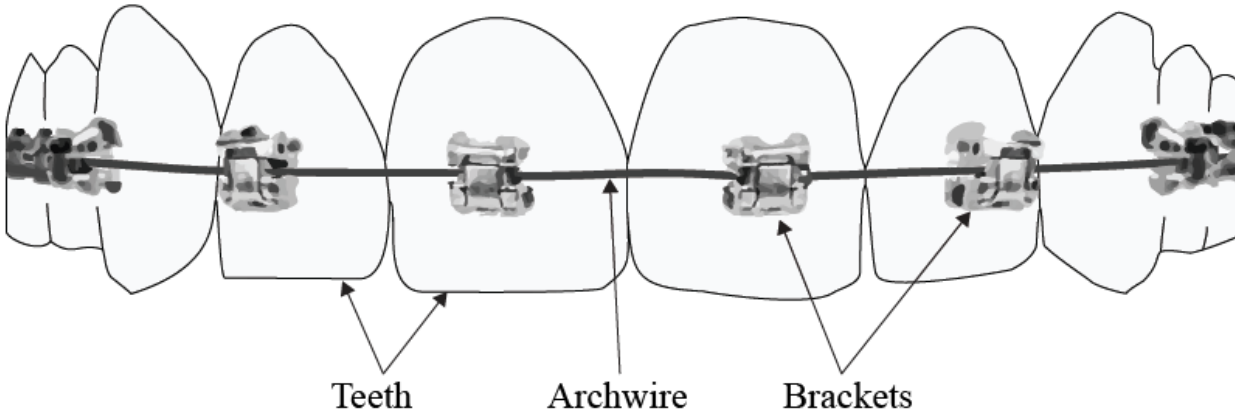

Figure 1.1. Schematic of an example fixed orthodontic appliance. Brackets are shown individually bonded to maxillary teeth and an archwire is engaged inside brackets.

Tooth movements arise as a result of the forces and moments applied to them. Forces and moments result from archwire interactions within each bracket, whereby the deformed and consequently strained archwire will impose forces onto brackets. These loads are transmitted to the tooth on which the bracket is bonded. This leads to further force and moment transfer onto the periodontal ligament (PDL), which is a unique tissue able to facilitate remodelling of the alveolar bone surrounding the tooth. It is this mechanism that results in permanent change in tooth position in the dentition [8]–[10]. Some concerns that may arise during orthodontic treatment may be inflammatory root resorption, where applied forces from an orthodontic appliance may cause inflammation of the PDL, resulting in the resorption of root tissue; or hyalinization, in which tissue necrosis may occur [8], [11]. There is a necessity to study the nature of the forces and moments generated throughout orthodontic treatment as it is crucial for long-term dental and periodontal health [9].

Misalignments in the angular inclination of teeth in the labiolingual (towards the lips/tongue) or buccolingual (towards the cheeks/tongue) directions for anterior and posterior teeth, respectively, can contribute to malocclusions. A schematic showing the dental directions is shown in Figure 1.2,

which labels the anterior and posterior teeth, as well as the relation between the mesial versus distal and labial/buccal versus lingual directions.

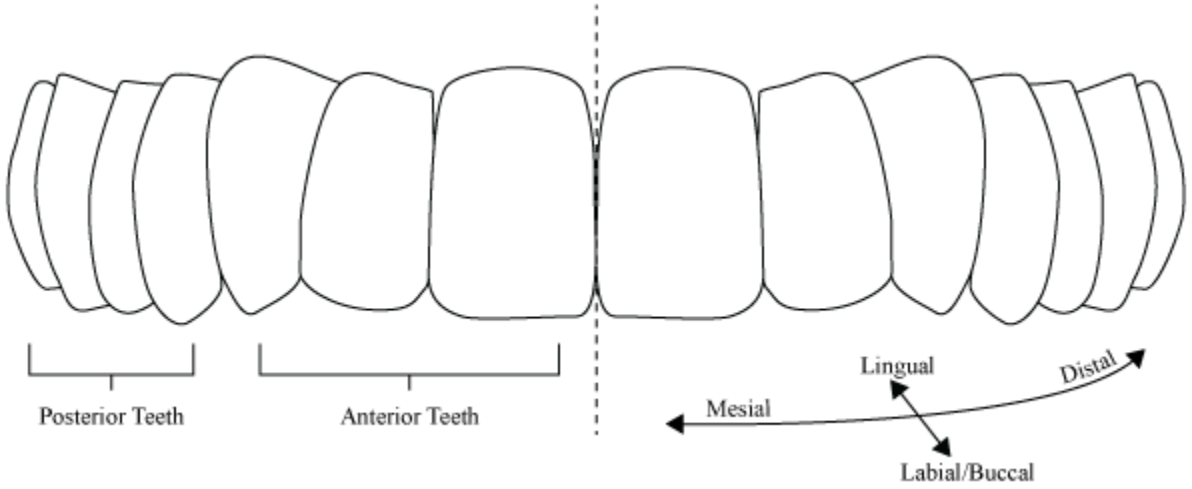

Figure 1.2. Schematic of teeth positions, indicating the anterior versus posterior teeth on the left side of the figure and the mesial versus distal and buccal/labial versus lingual directions on the right side.

To address this, the application of third-order torque resolves tooth angular inclination in said labiolingual or buccolingual directions [12]. In orthodontics, third-order torque refers to the rotation of a tooth about the axis along the mesiodistal direction (towards the middle of the jaw/temporomandibular joint).

At the University of Alberta, an apparatus called the Orthodontic Torque Simulator (OTS) was designed and built by Badawi *et al.* [13]. The OTS is an in-vitro third-order torque apparatus made to measure the reaction forces and moments exerted onto a bracket as an archwire is rotated along its long axis. Modifications to system components have allowed for various studies associated with third-order torque, including exploring the effects of a periodontal ligament simulant and bracket misalignments, as well as measuring bracket deformation during torsion [14]–[16].

In studying bracket deformation during third-order torque, imaging techniques, specifically digital image correlation (DIC) provides a viable option to track movements throughout applied loads. DIC is an optical method used to measure the surface response of a test specimen developed during a mechanical test [17]. Cameras are used to track changes in surface position over an applied load. By applying a stochastic speckle pattern onto the surface of a specimen, regions can be uniquely identified and individually tracked. Tracked regions can then be used to calculate full-field surface displacements and strains over the entire correlated surface of the test specimen [17], and these measurements can be taken in both two- and three-dimensional (3D) settings. The advantages of using DIC include its non-contact measurement capabilities, as well as the ability to resolve small-scale deformations and strains, both of which allow for mechanical testing and evaluation of orthodontic materials in a full-field context. The implementation of a 3D DIC system to measure surface deformations and strains of archwires during third-order torque is desirable and should be pursued to better understand archwire and bracket mechanics during orthodontic treatment. In doing so, system verification is a crucial step to ensure that measurements taken with DIC are true to the physical behaviour of the orthodontic materials under torsional load. Access to this additional information can aid in both qualitative and quantitative analyses and evaluations of fixed appliance orthodontics. Qualitatively, the development of 3D deformation and strain can be realised by comparing consecutive images over the applied torsion. Quantitively, the magnitudes of deformations and strains on both archwires and brackets can be studied to reveal how different materials may affect elastic and plastic deformation of orthodontic appliances during torsion.

1.2 Thesis Scope

This thesis involves two major components. First, the modification of the OTS to enable 3D DIC to be performed during in-vitro third-order torque simulations, as well as the verification of the 3D DIC system. Second, a study is performed on the OTS using 3D DIC to measure archwire deformations and strains with clinically representative orthodontic archwires and brackets. 3D deformations can be compared between groups to determine how torsion regimes are affected within orthodontic contexts, such as localised twisting versus rigid body rotation of an archwire, as well as comparing isolated deformations in x-, y-, and z- directions. The development of surface strains, specifically shear strains, can be used to indicate whether archwire deformations remain elastic or if there is a transition into plastic deformation. Previously, testing with the OTS consisted of applying third-order rotation using a rectangular archwire inside commercial orthodontic brackets and measuring the resultant torque. However, in characterising the independent response of archwires to torsion with respect to deformation and strain development, an additional custom rigid dowel was machined and used as an attempt to isolate the archwire response from bracket effects. When applying third-order torque with the archwire engaged in the rigid dowel, the archwire is expected to undergo a larger twist than with orthodontic brackets, where typical bracket materials and geometries can lead to higher bracket compliance and reduced torque [18]. Studying the archwire behaviour without the influence of orthodontic brackets and the consequent change in torsion mechanics may better reveal how deformation and strain develops on the archwire over a prescribed range of rotation.

In setting up a DIC system for use with the OTS, the methodology in performing DIC and the verification of the system must be thoroughly investigated, including the preparation of the

orthodontic materials for successful image correlation, camera calibration, and image processing to obtain displacement and strain results. Once the system is functional and verified, a study with clinical implications may be performed to characterise archwire and bracket behaviour during third-order torque.

1.3 Thesis Outline

This thesis consists of five chapters. In Chapter 2, background information pertaining to third-order torque and DIC techniques were reviewed and discussed, as well as relevant definitions and identification of areas of research where 3D DIC can improve current understandings of third-order torque mechanics. In Chapter 3, the process in setting up and verifying the DIC system are detailed. In verifying the displacement and strain parameters as measured by the DIC system, an idealised finite element analysis was performed by modelling the rigid dowel and a stainless steel archwire with a bilateral torsional load, as per OTS procedures. In Chapter 4, a two-by-two factorial study was designed and performed to compare differences in torque, deformation, and strain when using the custom rigid dowel versus commercial maxillary central incisor orthodontic brackets, as well as between stainless steel and titanium molybdenum alloy archwires. The inclusion of commercial orthodontic brackets enabled the exploration of clinical implications that may arise when performing 3D DIC, and also allowed for comparisons between the rigid dowel with commercial brackets. Finally, in Chapter 5, conclusions are made with the results of the studies summarised. Further, the limitations of the studies and recommendations on future work are also highlighted. Additional materials complementary to this work are included in the appendices. Appendix A includes data showing the reusability of the rigid dowel, Appendix B shows data used in the backlash calculation of the OTS gear train, Appendix C covers the archwire

speckling procedure for DIC preparation, Appendix D details the preliminary setup of the finite element model of third-order torque with the rigid dowel and stainless steel archwire, Appendix E includes all R code used throughout the thesis, similarly Appendix F includes all MATLAB code, and finally Appendix G details the pilot study conducted for sample size calculation prior to performing the full two-by-two factorial study.

CHAPTER 2 LITERATURE REVIEW

In orthodontics, tooth movements can be achieved through various treatment methods. One such method is using edgewise appliances, conventionally known as braces, which have been commonly implemented to generate tooth movements since their development in the 1920s [19]. Edgewise appliances function based on forces and moments generated by archwires ligated inside brackets which are individually bonded to teeth. When undergoing orthodontic treatment, movements must be carefully planned by the clinician to preserve the dental and periodontal health of patients throughout treatment [9]. A common orthodontic correction involves the rotation of a tooth in the buccolingual directions, which adjusts a tooth's angular inclination in the dental arch. To accomplish this movement, a third-order rotation is imposed on the archwire and ligated in the bracket to rotate a tooth about the mesiodistal axis. However, in applying third-order torque, careful considerations must be made to distinguish between controlled and uncontrolled tipping, where the former is desirable in clinical contexts and the latter is not [20]. As discussed in the introduction chapter, controlled tipping refers to rotation about a root apex, and uncontrolled tipping refers to rotation about the centre of resistance, a theoretical point in the tooth root where applied forces passing through the centre of resistance produce translations and forces about the centre of resistance produce moments that consequently induce rotation [20]. The static analysis of applied forces and moments determines the resultant tooth movement.

Characterising archwire behaviour during third-order torque elucidates how different factors associated with orthodontic treatment can interact with each other during treatment. Some factors that affect torque are archwire material and size, bracket manufacturer, bracket placement, and ligation method, among others [18], [21], [22]. By being able to compare factors at various levels,

more information can be gained towards a fuller understanding of the relationship between these factors and resultant torque. This chapter details current methods in measuring third-order torque in in vivo, finite element models, and in vitro, and details the digital image correlation (DIC) process and its application in in vitro orthodontics research.

2.1 Definition of Third-Order Torque

With edgewise systems, third-order torque is applied using archwires with rectangular cross-sections. When twisted and engaged inside brackets, the resultant interaction between the rectangular archwire and the bracket slot induces third-order torque by generating a moment couple. By applying third-order torque, rotational tooth movement may occur. The rotation of the tooth moves about the root apex with controlled tipping, as opposed to uncontrolled tipping where the rotation is about a tooth's centre of resistance [20]. A schematic of the generation of third-order torque using an edgewise appliance is shown in Figure 2.1.

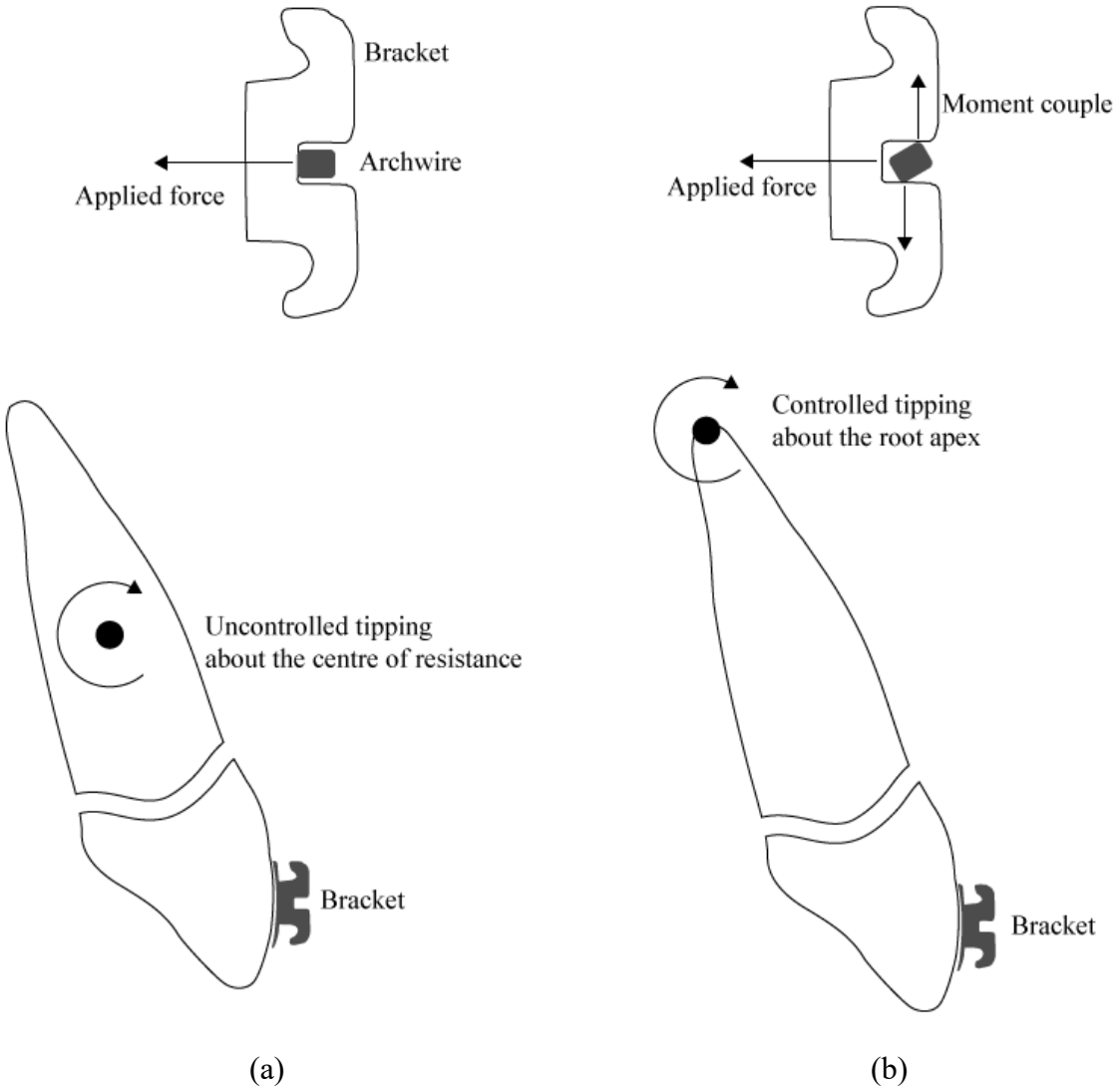

Figure 2.1. Tooth movement schematic using fixed appliances indicating (a) uncontrolled tipping and (b) controlled tipping when applying third-order torque with a rectangular archwire inside a fixed bracket.

Many investigations seeking to better characterise third-order torque have been performed in in vitro settings, where controllable factors such as archwire size and material or bracket design are isolated compared to explore their effects on resultant torque [21]. The pursuit of a comprehensive understanding and characterisation of third-order torque mechanics will continue as orthodontic technologies improve. With respect to fixed appliances, one aspect of third-order torque that has not been explored in depth is the isolated mechanical response of archwires under torsion in an

orthodontic context. In past studies, third-order torque is often measured as an output parameter [21]; however, the development of deformations and surface strains on an archwire under torsion is not fully understood. In particular, the small size of archwires and their unique geometries, in addition to compliance in orthodontic brackets while under load, all introduce complexities in the torsion regimes of archwires. By isolating the behaviour of an archwire during torsion application, a better appreciation of the roles different factors play in the generation of third-order torque application using fixed appliances can be formed, such as the differences between archwire materials, or how bracket deformations affect archwire deformations and resultant third-order torque magnitudes.

2.2 Assessment of Third-Order Torque

When an archwire is ligated within an orthodontic bracket, the previously mentioned factors can all affect the resulting interactions between the two components. Therefore, it is paramount that the effects of the factors on third-order torque are well-understood and can be utilised during treatment. The moment couple generated when a twisted archwire is inserted into a bracket has a large role in determining the nature of tipping, whether controlled or uncontrolled. Studies regarding third-order torque often consider the torque capabilities of archwire and bracket combinations under various experimental settings. Having a comprehensive knowledge base of the mechanical responses of archwires and brackets can aid in clinical practise as treatments can be applied with more efficiency and confidence in the procedure. Third-order torque studies have utilised different experimental methods to attempt to better characterise third-order torque mechanics. Due to the clinical implications of performing studies, both in vitro and in vivo experiments are common in evaluating third-order torque efficacies and quantifying the effects

that the orthodontic materials, dimensions, and usage has on third-order torque generation and application. In addition, in silico methods such as finite element analyses have become more common in simulating third-order torque experiments. Details regarding the current state of research in third-order torque experiments are highlighted for each of the experimental methods.

2.2.1 Clinical Assessments of Third-Order Torque and Angular Inclination

In clinical settings, it is difficult to mechanically isolate third-order torque as there are many factors that confound with torque expression. In practise, a majority of orthodontic treatments involves more than just buccolingual/labiolingual tooth rotation/translation [19], [23]. With orthodontic movements, considerations towards the forces and moments induced by the entire orthodontic system is necessary to prevent the creation of new misalignments when fixing present misalignments [24], [25]. Clinically, an orthodontist can apply third-order torque to fix a tooth's angular inclination and stop the torque application when they subjectively deem that the position is either adequately or optimally rotated [22]. Each patient presents a unique dental anatomy and must be independently monitored throughout treatment; however, patients with similar skeletal and dental presentations can be grouped to better discriminate these anatomical differences [26]. Clinicians can have varying assessments of final tooth inclinations that can agree with or contradict another clinician's assessment [22]. The subjectivity associated with third-order torque prescriptions makes it evident that clinician-selected treatment paths may ultimately result in different outcomes. However, measuring contributions from the orthodontic materials used in treatment such as archwire properties and bracket types can provide objective measures of clinical efficacy.

Measuring forces and moments generated by an orthodontic system directly during treatment is difficult. Direct measurements during treatment requires a method that can implemented in vivo. Friedrich *et al.* [27] developed an in vivo measurement system that utilised a custom modular bracket attached to a load cell that could be detached from a tooth while still engaged with an archwire; however, detaching a bracket from its bond to a tooth changes the loading conditions. With third-order torque, the change in position of a bracket with respect to the dental root can alter the axis in which the third-order torque is applied and shift the force vectors from the archwire. The resulting differences and unbalancing of the forces and moments can cause the rotation about the dental root to be about another point in the dentition, thus deviating from controlled tipping. Instead of directly affecting the orthodontic system to make measurements, retrospective studies are commonly employed to evaluate clinical results, including angular inclinations.

Retrospective evaluations involve assessing completed orthodontic treatments with respect to initial tooth positions/alignments. Different methods to measure angular inclination post-treatment have been employed. Moesi *et al.* [22] used dental casts to create physical models for clinical assessment purposes, where models were given to independent clinicians for their personal assessments and then compared across clinicians, which highlighted subjective differences. With appropriate instrumentation, dental casts may provide an objective measure of angular inclination [28]. However, such measurements are not always practical in clinical settings when determining teeth positions during treatment due to their time involvement and generation of excessive casts requiring storage/disposal. Sfondrini *et al.* [26] used radiographs to mark key points for measuring tooth positions and angles for comparative analysis between different brackets. Comparing conventional brackets to self-ligating bracket and aligners, it was found that conventional brackets

led to higher variance in final incisal positions, though the systems tested all demonstrated clinical reliability in upper incisor torque control [26]. Additional imaging techniques include three-dimensional (3D) laser scanning of dental casts, and more recently cone-beam computed tomography enable in vivo spatial measurements pre- and post-treatment for digital analysis [29], [30].

The commonalities between these measurement techniques is that clinically assessed angular inclinations may have varying degrees of final positions based on the clinician [22]. In particular, incisor and canine inclinations in similar positions may have different assessments due to a clinician's perception of dental aesthetics [22]. Better quantification of archwire and bracket mechanics during third-order torque may aid in allowing for more objective third-order torque applications. Characterising third-order torque mechanics can be explored with in vitro experiments to attempt direct and objective quantifications of differences between orthodontic materials by measuring their responses.

2.2.2 Finite Element Modelling of Third-Order Torque

The onset of numerical methods such as finite element (FE) analyses into orthodontic contexts has enabled studies on third-order torque to be simulated in silico using computer models. The models can vary in complexity in terms of geometries and the application of boundary conditions. Testing different model inputs and boundary conditions can give insight on the mechanical response of archwires in third-order torque contexts.

The advantage of FE models is that they can be used to modify single factors and hold all other factors in a model constant. Single-tooth FE models have been used to study factors such as bracket

and archwire material properties and geometries, ligatures, and adhesives [31]. Models of higher complexity have simulated periodontal ligament (PDL) and alveolar bone to better quantify reaction forces and strains that arise from applied prescriptions [31]. Models can introduce small differences in bracket positioning with respect to tooth morphology to explore the impact of bracket position on third-order torque [32]–[34]. Further, models can consist of multiple teeth along a dentition to better characterise the effect that third-order torque may exhibit on adjacent teeth [35], [36]. Models with multiple teeth can enable explorations on additional variables such as inter-bracket distance and how bracket geometries and placements on adjacent teeth can impact the third-order torque application [36]. In broader applications of orthodontic treatment, models have simulated the full fourteen tooth maxillary dentition that included PDL and alveolar bone, and an archwire/bracket system with skeletally-anchored power arms [37], [38]. While the model explored anterior teeth movement using a power arm orthodontic system, third-order archwire rotation induced by the power arms was seen, where using archwires with minimal torsional play in brackets can lead to controlled lingual root tipping of anterior teeth [37], [38]. FE models can be effective for orthodontic simulations. Depending on the context of a study and the complexity of a model, clinical variables can be simulated to compute their effects on the mechanical response of the orthodontic materials used.

There are limitations in FE models as the applicability of each model is largely dependent on model assumptions and the resulting errors. Especially with biomechanical studies, the transition to clinical relevance may not be confirmed until additional in vivo studies are performed; however, baseline models and comparisons may aid prescriptions and variable selection in future studies. Utilising FE models can be beneficial in isolating the effects of independent factors. In the context

of third-order torque, it can be useful to understand how the archwire and bracket interaction affects torque magnitudes, as well as the mechanical response of an archwire when twisted with complex boundary conditions.

2.2.3 In Vitro Third-Order Torque Measurements

In vitro experimental designs can isolate or systematically combine factors to better understand the mechanical interactions between orthodontic materials during third-order torque and consequently ascertain their independent or codependent contributions to torque expression.

At the University of Alberta, the Orthodontic Torque Simulator (OTS) has been used extensively to conduct third-order torque experiments. Past studies include comparisons between archwire material and bracket type [13], [39], torsional loading versus unloading [40], second-order bracket position [15], and PDL simulant effects [14]. More recently, Romanyk *et al.* [41]investigated the effects of buccolingual slot dimension on third-order torque by comparing three different orthodontic brackets with two archwire sizes.*et al.* They also found that reducing bracket dimensions resulted in earlier engagement between the archwire and bracket during the loading phase; however, during unloading, it was seen that brackets with reduced slot dimensions resulted in lower torque values than those with larger slot dimensions. It was proposed here, though not directly measured, that these results were due to excessive deformation of the bracket door leading to a reduced stiffness of the bracket [41]. In these studies, third-order torque was measured as a function of the angular rotation of an archwire. The mechanical operation of the OTS evidences the ability to isolate and compare different experimental factors. Further details of OTS operation will be discussed in Chapter 3. In addition to third-order torque measurements, bracket

deformations were measured by implementing optical imaging methods which will be detailed later in this chapter [18], [42]–[47].

Other researchers have also used in vitro apparatuses to characterise third-order torque mechanics [48]. Studies have been designed to compare differences in third-order torque based on slot sizes [49], archwire materials [50], and square versus rectangular archwire cross-section torque capabilities [51]. These studies allow for direct comparisons of third-order torque; however, an important aspect of torque application is the dimensional differences between an archwire and a bracket slot. An archwire must be smaller than a bracket slot for the practical purpose of fitting within the bracket slot, and commonly there are dimensional differences between the two (i.e. they are not perfectly matched). The differences result in torsional play, a physical phenomenon where there exists a region inside a bracket slot such that inserting a twisted archwire does not result in enough interaction and contact between an archwire and bracket to generate clinical torque thresholds [21]. Studies commonly explore the effects of different factors on torsional play and consequently on third-order torque [21]. Combinations and archwires materials, cross-sectional areas, and bracket types have been tested to compare their effects on torsional play [52]–[54]. Further, archwire cross-sections are studied as the rectangular or square cross-sections include rounded corners or bevels. Various studies measuring third-order torque attempt to directly address the corner geometry by measuring the corner radii [55]–[58]. Sebanc *et al.* [55] found that deviations between an applied torque to actual measured third-order torques may arise due to the corner radii presenting different interactions with the bracket slot. The greater the amount of rounding at the corners, the greater the deviation between ideal rotation angle versus measured rotation angle. It was also found that larger angles of rotation magnified the amount of deviation

which was again attributed to the amount of rounding at the archwire corners when manufactured [55]. Meling and Ødegaard [57] found that bevel variations can differ based on archwire cross-sectional areas, which could be attributed to allowable manufacturer tolerances; however, manufacturers did not state their tolerances. Lombardo *et al.* [58] directly imaged archwire cross-sections as a means to determine the amount of rounding that occurs at the corners. It was found that a single archwire could have four corners with varying radii, and the radii were not always representative of circular arcs. In applying third-order torque, the archwire corners have large contributions to the resultant torque. It is evident that archwire manufacturing and the consequent variation in cross-section profiles can affect applied third-order torque despite being an archwire of the same size and material.

The application of third-order torque inherently has many sources of variation. When manufacturing orthodontic materials, tolerances can result in different geometries and consequently present different archwire/bracket interactions when applying third-order torque [58]–[60]. The attempts to understand the extent to which different factors contribute to the variation may lead to better implementations of third-order torque in clinical contexts. As evidenced by the studies performed in literature, third-order torque measurements often address torsional play and torque magnitudes. In addition, mechanical properties of orthodontic materials such as archwire torsional stiffnesses [57], [61]–[63], sliding friction during third-order torque [64], [65], and archwire characteristics after clinical use [66]. Efforts to directly characterise the archwire and bracket interaction during third-order torque can produce more insight with regards to the mechanical response of the materials. However, the fundamental characterisation of archwire mechanics using archwire deformations and strains during third-order torque is not

readily available in the literature. Since the behaviour of an archwire dictates the third-order torque application, understanding the changes in archwire behaviour over the duration of an applied tipping correction may be beneficial in advance third-order torque techniques.

2.2.4 Advanced DIC Measurement Techniques in Orthodontic Measurements

Directly measuring third-order torque provides information on the efficacy of treatments; however, enabling optical methods such as DIC to be included during experimentation can provide additional information regarding the interactions between orthodontic materials during load application. This can improve orthodontic treatment by allowing a more comprehensive understanding of material interactions and thus allowing for improved designs and applications in the future.

Using DIC techniques in tandem with third-order torque has been previously explored with the OTS. Mainly, bracket deformations from third-order torque were measured using various DIC systems. Lacoursiere *et al.* [45] initialised optical measurements using the OTS and measured bracket tie-wing separation throughout and after third-order torque applications using a single camera system by tracking relative differences between tie-wing positions. Image subsets were individually placed on each bracket tie-wing and displacement vectors were calculated throughout the applied archwire rotation, and permanent deformation of the brackets was found from a single load application, where the final distance between the top and bottom tie-wings were not the same as the initial distance [45]. Major *et al.* [43], [46] also utilised 2D DIC to measure tie-wing separation of self-ligating brackets using cross-correlation algorithms and also found evidence of permanent deformation. The subsets were similarly placed on bracket tie-wings, and depending on

the geometry of the brackets, the shapes of the subsets varied to best conform to the surface area [43], [46]. Melenka *et al.* [18], [47] expanded the use of DIC with the OTS by initialising a 3D DIC camera system. Using a stereo microscope as the imaging device, a stereo camera system was implemented to perform cross-correlation image matching to obtain 3D displacements. Full-field 3D measurements of the bracket under third-order torque loading confirmed that bracket tie-wings were subject to movement and permanent deformation of the brackets occurred after loading. In addition, the movement of the archwire retentive component for self-ligating brackets were also measured and were seen to undergo motion when under third-order torque loading [18], [47]. The DIC studies previously performed using the OTS demonstrated bracket measurement capabilities and showed agreement in their results, indicating that sufficiently large third-order torque prescriptions can lead to permanent bracket tie-wing deformations.

These measurements were primarily focused on bracket deformations; however, archwire deformations were omitted. The inclusion of measuring archwire deformations during third-order torque is novel. Studying the mechanical response of the archwire may reveal additional insights regarding its interactions with the brackets and consequently its effect on third-order torque.

2.3 Digital Image Correlation Background

DIC is a non-contact, full-field measurement technique that captures surface deformations and strains on a specimen using optical cameras [67]. Images of a test specimen under a mechanical load are captured in succession and are then analysed. Fundamentally, the DIC process is a subset of computer vision; utilising image matching algorithms, images are matched and compared to calculate full-field positional differences between successive images and compute the differences

as deformations and strains [67]. DIC experiments generally consist of the setup of a camera system to fit within the constraints of an experiment, camera system calibration to obtain the intrinsic and extrinsic parameters, sample preparation for compatibility with DIC, performing the experiment coupled with image acquisition, and finally image processing and analysis [67].

2.3.1 Two-Dimensional Versus Three-Dimensional Measurement Systems

DIC can be adapted to different experimental conditions, such as two-dimensional (2D) versus 3D imaging based on the use of one camera or two cameras in a stereo camera setup [17], [67]. In practise, using a single camera system to capture 2D measurements is only representative of specimen displacements and strains when the specimen response to an applied load demonstrates in-plane motion. To obtain measurements in 3D, a stereo camera system must be used. In a stereo camera system, two cameras are placed such that they share one plane called the stereo plane. On the stereo plane, a stereo angle is created between the sensor of one camera to the test specimen to the sensor of the other camera. A schematic of the stereo plane and angle is shown in Figure 2.2. Conventionally, stereo angles range between 15° to 35°, but can be larger if carefully considered for the given region of interest and desired measurements [17], [68].

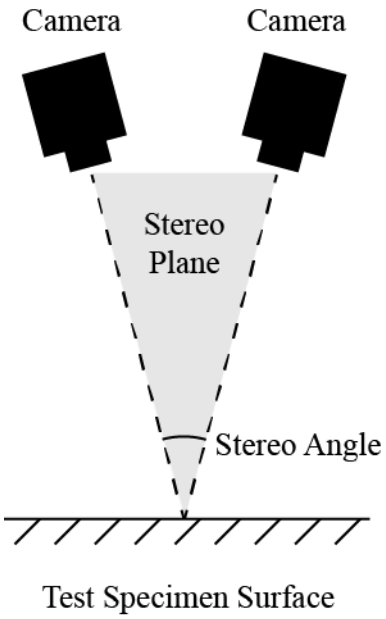

Figure 2.2. Schematic depicting stereo angle created between two cameras and the test specimen.

Regardless of the number of cameras, the images obtained by any camera follows the pinhole camera model, whereby objects in 3D space are projected onto a 2D image plane. Information regarding the third dimension (out-of-plane) is lost and non-recoverable [67]. By using a stereo camera system, information lost from one camera's point of view is kept intact with the second camera. An example of how using two cameras enables 3D information to be resolved is shown in Figure 2.3. When using one camera, two different points of a 3D object can project onto the same point on an image, whereas when using two cameras, the same two points no longer collapse into one point, thus recovering the 3D information.

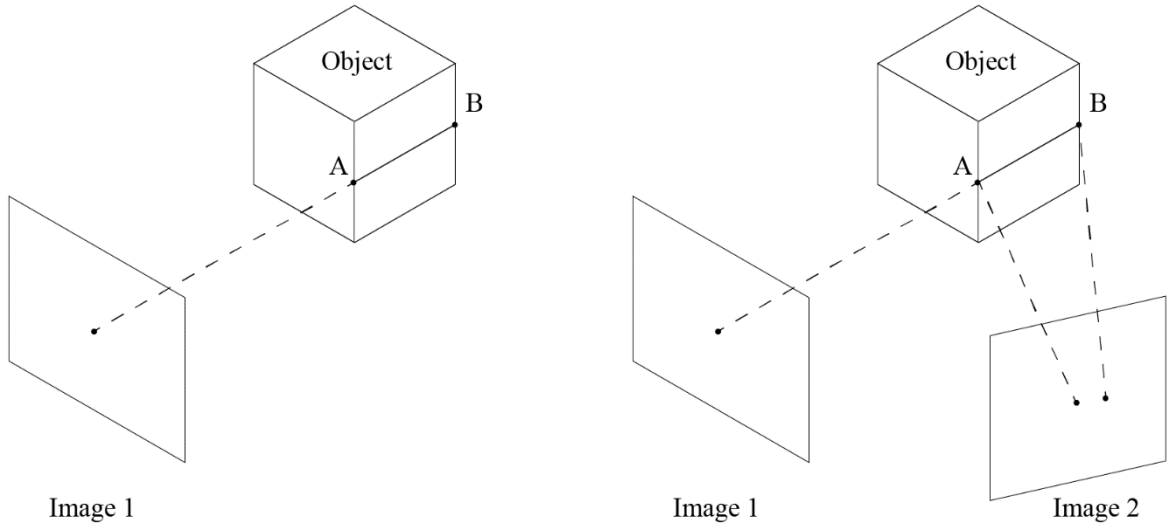

Figure 2.3. Schematic depicting how spatial information between two points A and B is lost when using a single camera system and recovered when using a stereo camera system.

When performing 2D DIC, the camera can be strategically positioned such that its image plane is parallel to the surface of interest on the specimen. This aids in keeping the projection of the surface onto the image free of distortions due to perspective. However, in a stereo camera system, the camera perspectives between the two cameras are guaranteed to be different, as seen in Figure 2.3(b). This introduces a complexity where image matching must account for these differences in perspective. Camera calibration allows for the perspectives to be accounted for such that image matching can be achieved by applying transformations between two views [69], [70]. The advantage of 3D DIC is that stereo camera systems can measure out-of-plane motion, which would in fact be sources of error in 2D DIC systems. Stereo camera systems can resolve out-of-plane motion and, in effect, eliminate projection errors that would arise when out-of-plane motion is captured with a single camera. When using a stereo camera system, the stereo angle (the angle created between the two cameras and the image origin) plays into the relationship between in-plane displacement accuracy and out-of-plane uncertainty [17]. In practise, a smaller angle will

lead to more accurate in-plane measurements at the expense of increased out-of-plane uncertainty [17]. It is necessary to find the optimal stereo angle based on the camera setup, the geometry of the test specimen, and the overall field of view available to capture the region of interest [17]. The optimal stereo angle should enable the field of view to fully contain the region of interest before and during loading, and should be checked to ensure image correlation is achievable [17]. Using stereo camera systems can be useful in measuring surface deformations and strains that display non-planar responses. In utilising any camera system for measurement purposes, calibration is a procedural step that enables the projection between physical space and captured image space.

2.3.2 Camera Calibration

The camera system consists of several components that should be optimised for imaging the test specimen. To region of interest on the test specimen should fit within the field of view of the camera setup, which can be dictated by the camera sensor size and type and the lens assembly [17], [71], [72]. Selecting the right system components can lead to successful imaging during experimentation, and each camera system needs to be fully defined to achieve image correspondence. In performing both 2D and 3D DIC, camera calibration is a crucial step that resolves intrinsic and extrinsic camera parameters.

Intrinsic parameters refer to the individual properties of a camera such as focal length, image centre, and lens distortions, and extrinsic parameters refer to a camera's orientation in space and distance relative to the imaged object [17]. Calibration is often performed by capturing images of a calibration target. Typically, a target will consist of a repeated pattern of known size and spacing. Calibration targets can be either 2D or 3D [73], [74]. Using a 2D target may require multiple views

to be imaged at various orientations and positions to manually introduce the out-of-plane component [17], [73]. In contrast, 3D targets often include alternating ridges where the pattern can be present at the top or bottom of the ridge. Therefore, across the calibration target, the pattern includes different surface heights, resulting in less images required for the calibration image set [17], [74]. The ridges automatically allow for the inclusion of the out-of-plane component that can be used to resolve the camera parameters. A schematic of the two types of calibration targets are shown in Figure 2.4, where the flatness of a 2D target is compared to the additional depth component of the 3D target.

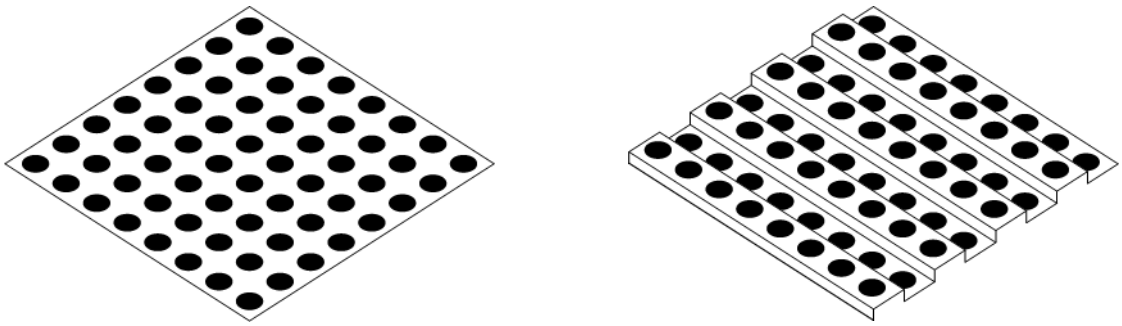

(a) (b)

Figure 2.4. Schematic showing the differences between the pattern layout of a standard circular pattern on (a) a 2D calibration target with all points being planar versus (b) a 3D calibration target with two planes with individual points exhibiting planarity in either plane.

In either case, the purpose of the calibration target is to obtain images where the imaged pattern is fully defined. Since the pattern is known, calculations can be made to directly solve for the intrinsic and extrinsic parameters of a camera system [67]. In a stereo camera system, there exists the additional requirement that the region of the calibration target imaged between the two cameras consists of the same pattern such that they can be matched between the two camera views. This can be controlled by having the calibration target being smaller than the field of view such that all pattern features of the target are visible, or by including an identifying mark on the target such that

both cameras capture the mark and thus capture the same region of the target. When capturing images of the targets, the size, spacing, perspective, and distortions of the pattern features are all used to solve for the camera parameters by following the pinhole model [67]. Solving a system such that all pertinent camera properties are known is paramount for image correspondence [17]. With a calibrated camera system, test specimen preparation and image acquisition can then be addressed.

2.3.3 Specimen Preparation

To make measurements on test specimens, the surfaces of interest must be prepared to allow for image matching. In general, most test specimens are not immediately suitable for DIC purposes; surface reflectivity, textures, and geometry can all factor into poor conditions for DIC. A surface that is too reflective can have an adverse effect on the intensity of an image making it difficult to process; surface textures, or the lack thereof, may result in too many repeated features or too little features to obtain unique correspondence; and the geometry of a specimen make result in complex deformations that make it difficult to measure using DIC [67], [75].

One technique commonly used to achieve correspondence consists of applying a stochastic speckle pattern to the surface, which allows for unique regions of a surface to be tracked throughout an applied load or movement [17], [67], [75]. The prepared surface should have a high contrast pattern, which refers to the difference in intensity between dark versus bright speckles [17], [67], [76], [77]. Speckles can be grouped together into subsets, which are regions that contain a unique pattern of speckles. Consequently, subsets are also unique and the motion of a subset between images can be computed into vectors for deformations and strains [17]. Tracking the motion of all

subsets over an entire surface therefore results in the full-field deformations and strains that DIC is capable of measuring. Various speckling techniques are utilised in DIC applications, with common ones being the use of airbrushing and spraying, lithography, scratching and abrading, among others [75]. Applying an appropriate speckle technique based on the specimen type and scale without altering local material properties/behavior is an important step in obtaining valid results in DIC measurements, as different techniques may alter the DIC process in terms of sample preparation and image analysis [17]. Further, the relationship between the speckle size and subset size should be carefully considered during image processing to increase the probability of achieving correspondence. A subset should contain enough speckles within it such that the resultant pixel intensities of the subset is unique [67]. The size of speckling features may be controlled by changing the medium and application method or by changing the magnification of the surface using the cameras to change the field of view within captured images [67], [75]. Ensuring that the surface of interest is compatible with DIC is a crucial step that can involve experimenting to find the optimal combination of surface pattern application and image processing.

2.3.4 Image Acquisition

When performing DIC experiments, image acquisition requires careful attention as high versus low quality images can significantly alter image correspondence and consequently measurement accuracy [17], [67], [77]. The process of capturing images of a test specimen through the duration of an applied load can vary due to differences in experimental conditions. However, there are necessary steps required to obtain an optimal DIC setup [17]. Preparations such as having adequate lighting, a clean camera assembly from the lens to the sensor, ensuring the cameras are stationary,

and aiming at the region of interest are all paramount for successful image acquisition [17]. With respect to 3D DIC systems, it is also necessary to have camera synchronicity such that matched images are temporally identical [17].

In assessing a captured image, the region of interest should be fully contained in the fields of view of all cameras, with the speckling pattern visible under the experimental lighting conditions. Image quality should be maximised by changing the physical parameters of the camera system and lighting to achieve high contrast between the speckles and the background of the surface. While it is possible to digitally alter the camera settings to obtain more contrast such as increasing the gain, it is not ideal as doing so can introduce more noise into an image [17]. The image acquisition process dictates whether an image set is of high or low quality with respect to DIC and should be tested with to obtain optimal settings prior to actual experimentation.

2.3.5 Image Matching and Correlation

Many image matching algorithms have been utilised for DIC applications. In general, the different image processing software packages can implement various algorithms that utilise different matching criterion based on the application [17]. In principle, as the images are divided into subsets, the speckles within a subset present a unique pattern that can be used to match with other images both spatially and temporally. For all image matching, the desired outcome is image correspondence. Matching criteria (or correlation criteria) are used to determine the local surface response by matching subsets across images. Matching criterion can include sum of square differences, cross-correlation, and least squares matching (LSM), among others [17], [69].

The criteria have different mathematic methods applied to perform image matching. Algorithm development may revolve around reducing computation time in image processing, increasing correspondence probability, or other factors that can improve the DIC process [67]. As different software packages utilise different criteria, considerations should be made towards the software package, experimental setup, computing power available, and desired measurement accuracy in performing DIC. Some algorithms may be more computationally efficient at the expense of having less accuracy [78]. In practise, the algorithm selected for DIC can be contingent on any factor, and the software package is often a common determinant [17]. The two more commonly used methods are cross-correlation and the LSM method. Differences exist between the two methods such that selecting the right method can lead to more accurate results based on the loading conditions during testing [77]. Cross-correlation attempts to match subsets by translating subsets between two images, whereas the LSM method minimises the squared differences between subsets based on pixel grey values or intensity [77]. Cross-correlation is the most commonly used algorithm due to its simplicity and consequent computational requirements; however, it can result in lower accuracy. It is well-suited for simpler loading scenarios, especially when deformations remain plane. The LSM method can provide more accurate local surface deformations since subsets can be transformed in lieu of minimising squared differences rather than just translated [77]. The LSM method will be further detailed in Chapter 3 as it pertains to the DIC process performed.

2.4 Conclusion

The application of third-order torque is a common process in orthodontic treatment. Many studies are performed with efforts to better characterise third-order torque mechanics. There are clinical considerations when applying third-order torque, such as archwire material, size, and geometry;

bracket type and torque prescription; and overall third-order torque application with respect to a treatment timeline. All of these factors affect the mechanical interactions between the archwire, bracket, and a patient's dentition. It is necessary to inquire and obtain more information about the mechanical response of the materials associated with third-order torque. Third-order torque is readily applied during treatment; however, archwire characterisation during third-order torque may be a viable consideration that can reveal additional insights with respect to the overall third-order torque response. A twisted archwire inside a bracket may show behaviour that is consistent with torsion of prismatic bars, or the geometric complexities of an orthodontic environment may ultimately affect archwire behaviour.

Studying third-order torque in any form has a common goal of better characterising the underlying mechanics of prescribing torque to a tooth. Using different techniques to quantify aspects of third-order torque, whether in vivo, in vitro, or in silico, all contribute to the advancement of orthodontic treatments. The study of archwire mechanics is currently lacking in that information about archwires during third-order torque mainly consists of known material properties and measurable responses; the direct mechanical response and behaviour of the archwire itself is not well documented. In particular, archwire deformations and strains during third-order torque have not been measured. The research will attempt to use 3D DIC techniques to image the mechanical response of archwires during third-order torque to enable direct measurements of the mechanical responses. The setup and verification of the 3D DIC system for use with the OTS will be documented, upon which successful verification is followed with experimentation using orthodontic materials. Archwire deformations and strains during third-order torque will be

investigated using the 3D DIC system to better characterise and understand the interactions between archwires and orthodontic brackets during third-order torque.

CHAPTER 3 DEVELOPMENT AND VERIFICATION OF THREE-DIMENSIONAL DIGITAL IMAGE CORRELATION METHOD TO STUDY ARCHWIRE STRAINS DURING IN VITRO TORSIONAL LOADING

3.1 Introduction

Research exploring third-order torque is a prevalent topic in the literature as it is a major component of orthodontic treatment. The clinical aim of moving teeth is governed by the magnitude and direction of forces and moments that an archwire will generate through its interaction with the orthodontic bracket. Applying too little forces will not result in movement, and too much can cause root resorption and damage to teeth and the periodontium [9]. Studying third-order torque generated by orthodontic appliances gives a direct measure of the magnitude of forces and moments generated. Using insights from third-order torque studies can lead to improvements in the delivery of orthodontic treatment if the roles of different factors associated with third-order torque can be isolated and measured.

In this chapter, work completed to develop and verify a three-dimensional (3D) digital image correlation (DIC) system to measure surface displacements and strains during third-order torque application is detailed. The 3D DIC system is designed and adapted for a current third-order torque experimental unit called the Orthodontic Torque Simulator (OTS). Implementing DIC when measuring third-order torque with the OTS may expand the understanding of third-order torque mechanics by directly imaging the mechanical response of orthodontic materials. The DIC system,

image processing process, and measurement verification using a finite element (FE) model and torsion theory are explained. The inclusion of DIC during third-order torque measurement may lead to a more complete understanding of the torsion mechanics associated with orthodontic treatment. Third-order torque measurements, among others, can provide insight on how to plan orthodontic treatment. Fundamentally, a rectangular archwire is twisted to a prescribed angle and engaged inside an orthodontic bracket. The resultant interaction between the archwire and the bracket slot induces a moment couple that results in tooth movement. In vitro systems can be used to directly measure the resultant moments that arise from the interaction of a twisted archwire inside a bracket.

3.2 Experimental Methods

The experiment consists of the implementation and verification of the 3D DIC camera system in tandem with current OTS experimentation. The 3D DIC system provides a non-contact measurement technique that allows OTS operations to be independent of image acquisition. The intent of the 3D DIC system is to capture full-field images to measure surface deformations and strains associated with third-order torque. The overarching purpose of experiments described and performed in this chapter is to verify the use of the 3D DIC system used to measure mechanical strains of orthodontic archwires developed during simulated third-order torque procedures.

As the measurement system presents a novel case of measuring the response of orthodontic archwires under torsional loading, the system does not have traditional validation methods such as comparisons to an established “gold standard”. Rather, the system was setup following best DIC practises and archwire measurements would be rigorously verified [17], [67]. For the 3D DIC

system setup for use with the OTS, the verification involved the utilisation of an FE model as well as comparisons to theory of prismatic bars in torsion to ensure that measurements agreed across the methods. Successful verification of the system enables confidence in using the 3D DIC system to directly quantify the mechanical response of archwires.

3.2.1 Orthodontic Torque Simulator

The OTS is an in vitro testing apparatus designed and built by Badawi *et al.* [13] at the University of Alberta to perform third-order torque experiments. The experiments performed in this thesis will be similar to testing protocols previously utilised on the OTS [16]. Compared to previous experimentation, the third-order torque mechanism of the OTS is unmodified and only experimental parameters are varied for compatibility with 3D DIC measurements, mainly the angular range and increments. For completeness, a short description of the OTS and its operation is included. In using the OTS, a segment of straight rectangular archwire is bilaterally twisted about a fixed orthodontic bracket. Reaction forces and moments are measured with a six-axis load cell (Nano17 SI-25-0.25, ATI Industrial Automation, North Carolina, USA) and collected with a data acquisition system (DAQ 16-Bit E series NI PCI-6033E, National Instruments, Texas, USA). Knowing the relative distance between the bracket and the load cell, the appropriate linear transformations may be performed to convert the forces and moments measured by the load cell to the location of the bracket [16].

The OTS is shown in Figure 3.1, which includes all relevant components pertaining to its operation including the rotation mechanism (Figure 3.1(a)), the utilisation of a rigid dowel (RD) in place of

conventional orthodontic brackets (Figure 3.1(b)), and the overlaid coordinate system (Figure 3.1(c)). The use of the RD is further detailed in a later section.

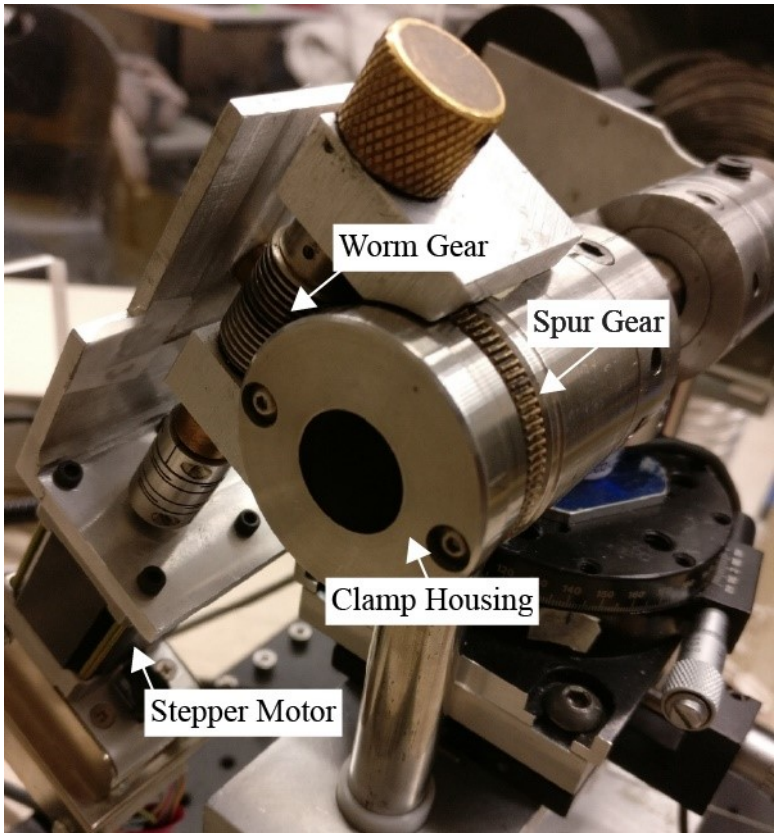

(a)

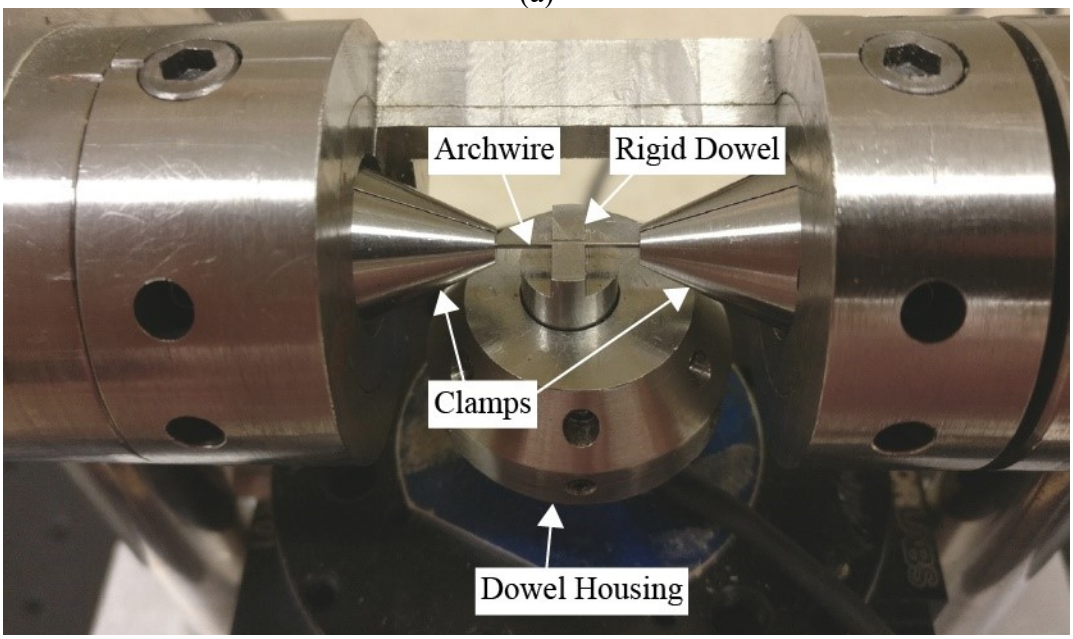

(b)

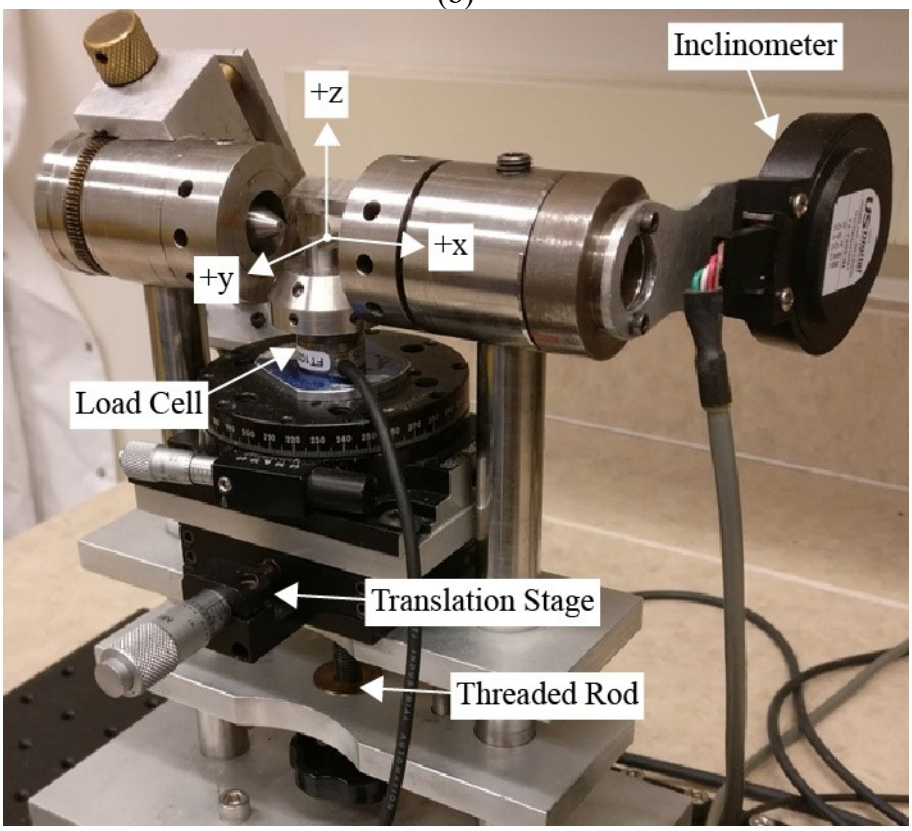

(c)

Figure 3.1. System components of the Orthodontic Torque Simulator, showing (a) the archwire rotation mechanism, (b) the bracket and archwire torsion interface using a rigid dowel, and (c) the overall assembly with coordinate system.

3.2.1.1 Archwire Rotation Mechanism

In the system setup and verification experiments, 0.019”x0.025” stainless steel rectangular archwires (Ormco Corporation, California, USA) were used. The rotation of the archwire consists of several components. Figure 3.1(a) shows the OTS’s mechanism for rotation. The stepper motor (Cool Muscle CM1-C-11L30, Myostat Motion Control Inc., Ontario, Canada) drives a gear train consisting of a worm and spur gear which rotates the clamp housing. The rotation angle is determined by the number of stepper motor rotations and the resultant reduction through the gear train, whereby 1,000 motor steps equates to 3.75° of rotation. The clamp housing is shown in

Figure 3.1(b), where archwire clamps are used to firmly hold the archwire in place, thus coupling the rotation of the archwire to be equal to the rotation of the housing. The only degree of freedom in motion that the archwire has once clamped is the motor-driven rotation about the x-axis as labelled in Figure 3.1(c).

3.2.1.2 Bracket Positioning

As the OTS rotates an archwire, contact is established between the archwire and bracket and resultant forces and moments are generated. To position the brackets to allow for force and moment measurements, orthodontic brackets are attached to stainless steel dowels using adhesive, and the dowels are placed into a housing designed to directly attach onto the load cell. The dowel is inserted into the housing with a clearance fit, which allows for minor adjustments in the angle of the dowel about the z-axis to align with the archwire. Once the position of the dowel is finalised, it is fixed in place by set screws in the dowel housing. This fixes the relative position between the bracket and load cell. When fixed, the bracket can be translated with the load cell, as both are mounted on a translation stage (LT01 Translation Stage, Thorlabs Inc., New Jersey, USA). The stage allows for fine control of the bracket's y-position. The stage is also coupled with a threaded rod that allows for z-translation, and a rotational stage (PR01 Rotation Stage, Thorlabs Inc., New Jersey, USA) for z-axis rotation. In applying these translations, the rigid body motion of the load cell and bracket are coupled and their position relative to one another remain constant.

3.2.1.3 Archwire-Bracket Interaction

The degrees of freedom of the archwire and the bracket enables the positioning of the archwire to fit inside the bracket slot prior to third-order torque application. The translation stage is used to place the bracket directly underneath the archwire before vertically translating the bracket upwards

to enclose the archwire. Once the archwire is inside the bracket slot, the archwire is ligated and the positions of the clamps are adjusted such that the distance between the tip of the clamp and the edge of the bracket is 5 mm. This value represents the inter-bracket distance (IBD), where the clamp tip is placed to the same position the edge of an adjacent bracket would be in a multi-tooth system. Minute adjustments in bracket position in the y- and z-directions and rotation about the z-axis are made to ensure that the forces and moments are minimised as per the zeroing protocol of the OTS. The last step prior to third-order torque is to adjust the angle of the archwire about the x-axis (third-order rotation). The goal of the angular adjustment is to ensure archwires are at the same starting angular positions relative to the bracket slot walls where the archwire is passive in the slot and does not impart reaction forces or moments onto the bracket. This is achieved by rotating the archwire in the loading direction until a torque threshold of 4.00 N·mm is reached, then rotating the archwire in the unloading direction until the same torque threshold of 4.00 N·mm reached in magnitude, but in opposite direction. Then the archwire is rotated to the midpoint of the two values based on motor steps. An archwire is considered passive inside a bracket if all reaction forces are below 0.050 N and all reaction moments are below 0.200 N·mm. With the archwire being in its passive position with respect to the bracket slot, third-order torque experiments can be performed with various archwires and brackets from different manufacturers.

3.2.1.4 Rigid Dowel

Conventionally, commercial orthodontic brackets are used when measuring third-order torque. However, to remove the effects of bracket manufacturing tolerances and bracket deformations during third-order torque, a stainless steel RD was designed and machined, which can be seen used with the OTS in Figure 3.1(b). The RD is designed to have minimal torsional play when used with

0.019”x0.025” archwires and is also designed to not deform under third-order torque loading. This isolates the third-order torque response as a result of archwire behaviour and removes the effects from the response of orthodontic brackets. The dimensions of the RD were selected such that the torsional play between the RD and a 0.019”x0.025” archwire would be minimised. The slot depth (z-direction) was dimensioned to be between 0.030” and 0.040”. Evidently, the slot depth in the RD is larger than the dimensions of the archwire. This was intentional to allow for vertical adjustment of the RD to obtain a passive position prior to applying torque. The slot width (y-direction), however, was limited between 0.0190” and 0.0195”. By having a tight tolerance on the bracket width, it ensures that the archwire is aligned parallel to the RD walls prior to experiments.

In addition to the slot dimensions, the effective RD width in contact with the archwire was also dimensioned to 2.8 mm, based on representative measurements of Damon Q (Ormco Corporation, California, USA) brackets for a central incisor as measured using a digital caliper (Mitutoyo America Corp., Illinois, USA). Lastly, the height of the RD in the z-direction was determined by utilising OTS dimensions such that the location of the RD slot would be in the same position as an orthodontic bracket slot when testing with orthodontic brackets. The dimensions of the RD as designed can be seen in Figure 3.2. All solid modelling was completed using SolidWorks (SolidWorks, Dassault Systèmes SE, Île-de-France, France).

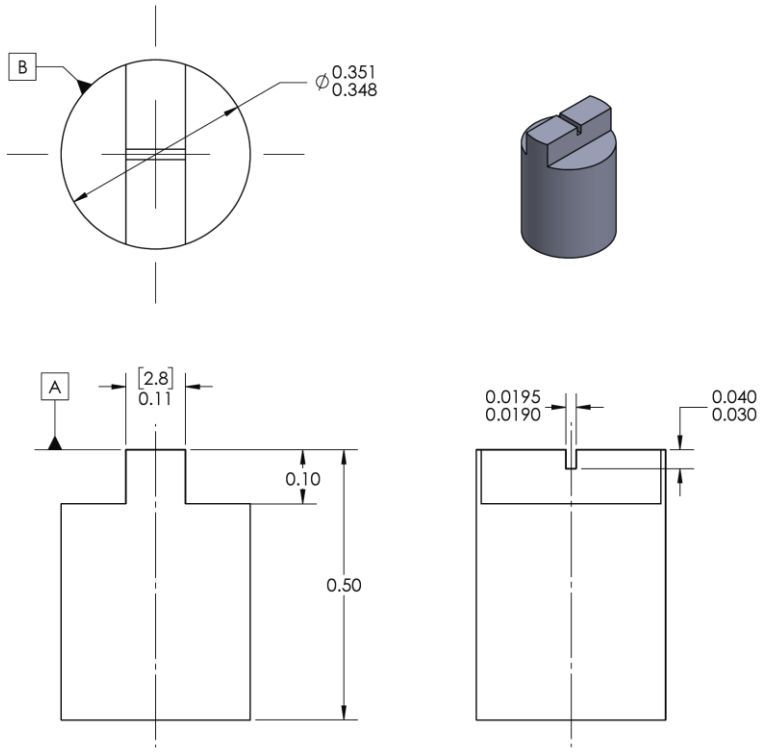

Figure 3.2. Dimensions of rigid dowel shown in inches, bracketed values are in millimetres.

Typically, when performing third-order torque experiments with an orthodontic bracket, a single bracket is used per trial and would not be used again for data collection. This is to remove any additional effects that may arise from applying a load to the bracket, such as permanent deformation and consequent changes in bracket functionality. However, with the RD that was used for testing, there were no indications that archwire behaviour significantly altered between consecutive trials using the same RD. Preliminary testing was performed with the RD to confirm that archwire behaviour did not change over time. Had there been an effect, resultant torque values would lessen over time due to a widening slot. The preliminary testing included plotting the maximum torque values achieved with the RD using various archwires of different materials and rotation angles, and it was confirmed that the phenomenon of lessened torque over time was not

seen during preliminary testing. This justified the use of the same RD for all trials. All data associated with measuring maximum torque over time with a single RD is shown in Appendix A.

In using the RD with the OTS, the applied rotation of the archwire was expected to cause the archwire to deform and twist as the angle of rotation increases. A schematic of the archwire from one clamp tip to the other is shown in Figure 3.3. At the centre of the archwire, the interaction with the RD was expected to behave close to a fixed support, which spans 2.8 mm. With 5 mm IBDs on either side of the RD, the rotation of the archwire is symmetrically applied at both clamp tips, where the rotation is in the same direction. Assuming ideal conditions such as fit between the archwire and the RD slot, the archwire would undergo a pure torsional response with no rigid body rotation.

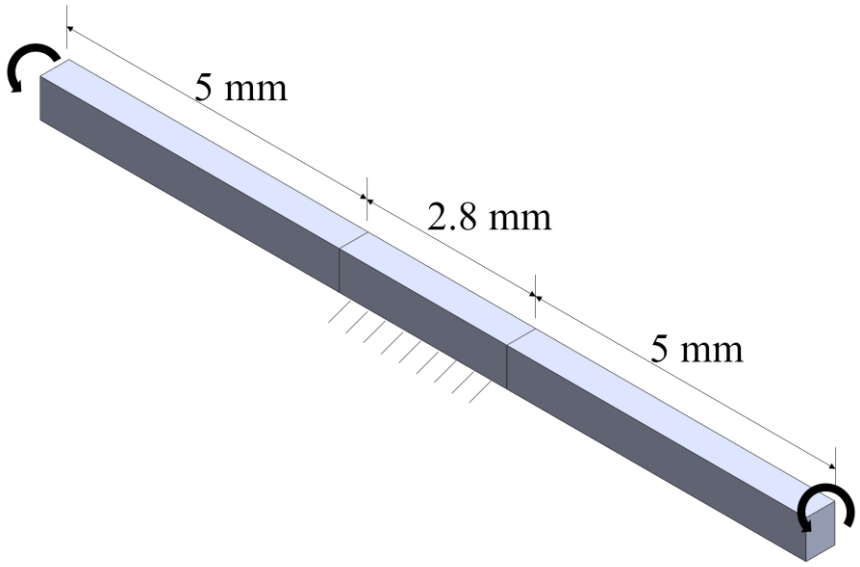

(a)

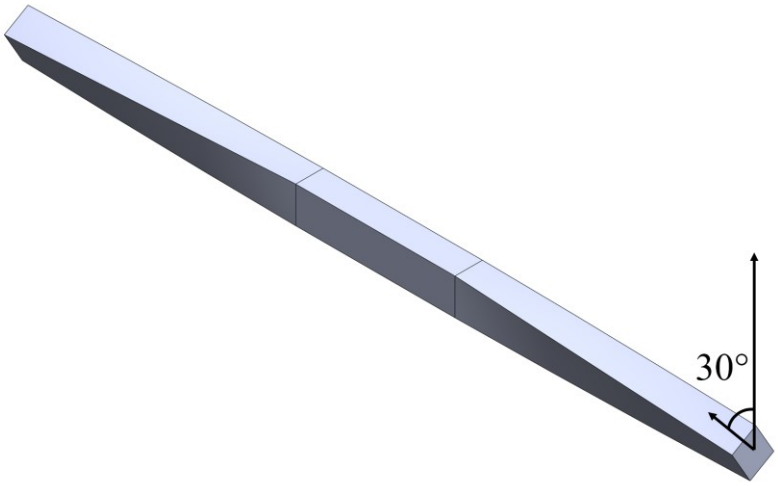

(b)

Figure 3.3. Schematic of expected deformation of an archwire during third-order torque experiments with the Orthdontic Torque Simulator, showing the (a) initial straight archwire segment and (b) twisted archwire segment when using the rigid dowel rotated up to 30°.

3.2.1.5 Third-Order Torque Data Acquisition

In performing the third-order torque experiments, the range of archwire rotation and rotation increments are program-controlled. In efforts to characterise archwire behaviour under torsion, a large range of rotation combined with a small rotation increment was deemed most suitable in the application of third-order torque. Smaller rotations allow for more data to be collected rather than interpolated between increments. As such, the range of rotation and rotation increments were prescribed as 30° and 1°, respectively. When applying third-order torque, the stepper motor controls the angular position of the archwire. The rotation is not continuous and instead is broken into increments with pauses in between. Measurements are only recorded during the pauses so that resultant torque values are measured when the system is in a static state which is representative of orthodontic treatment which proceeds in a quasi-static manner. Further, the gear train driving the

rotation mechanism of the OTS will inherently have backlash as a result of the fit between gear teeth. Since the gear train only consists of one worm gear and one spur gear, backlash in minimal as it is only dependent on a single coupling between gears. As the worm gear drives the rotation of the OTS, backlash will occur when the worm gear changes its direction of rotation. This backlash was previously measured in internal tests and was determined to be 1.03°. Further detail regarding the backlash testing can be found in Appendix B. Due to the rotation increment being 1°, it is important to account for the backlash to accurately portray third-order torque as a function of rotation angle. The backlash is applied as a linear data transformation after data collection.

With both torsional loading and unloading of the archwire considered, an individual experiment will consist of 62 third-order torque readings using the load cell: 31 readings each for loading from 0° to 30° and unloading from 30° to 0°. For system verification, 10 trials were performed to both ensure repeatability as well as to acquire sufficient data for analysis. A new archwire was used for every trial to ensure the tests were independent.

3.2.2 Digital Image Correlation

Determining the fundamental mechanical behaviour of an archwire being loaded with third-order torque can be aided with DIC techniques. DIC is an optical method used to measure full-field surface strain and displacements of test specimens under load [17]. Using a single camera system to image a test specimen over the duration of a load application enables DIC to be performed to measure two-dimensional (2D) surface strains and displacements. To obtain measurements in 3D, a stereo camera system must be used. The images obtained by any camera follows the pinhole camera model, whereby objects in 3D space are projected onto a 2D image plane. Information

regarding the third dimension (out-of-plane) is lost and non-recoverable [67]. By using a stereo camera system, information lost from one camera's point of view is kept intact with the second camera. Relevant preliminary DIC background was presented in Chapter 2. Further details regarding DIC as it pertains the OTS is detailed in this chapter.

3.2.2.1 DIC of Archwires in Torsion

To measure the response of the archwire during third-order torque, the deformation will include out-of-plane motion relative to the image plane (xy-plane). This is due to the rotation causing portions of the archwire to rotate upwards in the positive z-direction, and other portions to rotate downwards in the negative z-direction. In application, a torsional load is only plane if the image plane is perpendicular to the axis of rotation. In the case of the third-order torque, it would be equivalent to capturing the rotation of a cross-section of the archwire.

To capture the 3D deformations of an archwire under torsional load, it is necessary to use a stereo camera system to enable 3D measurements, as it is not possible to use a single camera system that can resolve the rotational displacements and deformations of the archwire. In setting up the stereo camera system, the orientation of the cameras with respect to the OTS affects which archwire surfaces can be imaged. Due to the geometry of the OTS apparatus, it was most appropriate to install the cameras overhead of the OTS to prevent any physical interference from the cameras when applying third-order torque while still providing a robust and repeatable setup. The overall OTS apparatus with a stereo camera system installed is shown in Figure 3.4. This orientation of the cameras results in the top-down imaging of the archwire surface; a schematic of this is shown in Figure 3.5. Relative to both the OTS and DIC camera system's coordinate system, the imaged surface of the archwire is parallel to the xy-plane.

During third-order torque application, the two ends of the archwire at the clamp tips are bilaterally twisted by the OTS. Using DIC, the development of strains and deformations on the top surface over the range of rotation of the archwire can be measured. Using strain and deformation of the archwire in tandem with the torque measured by the load cell, the mechanical response of the archwire under torsion can be characterised.

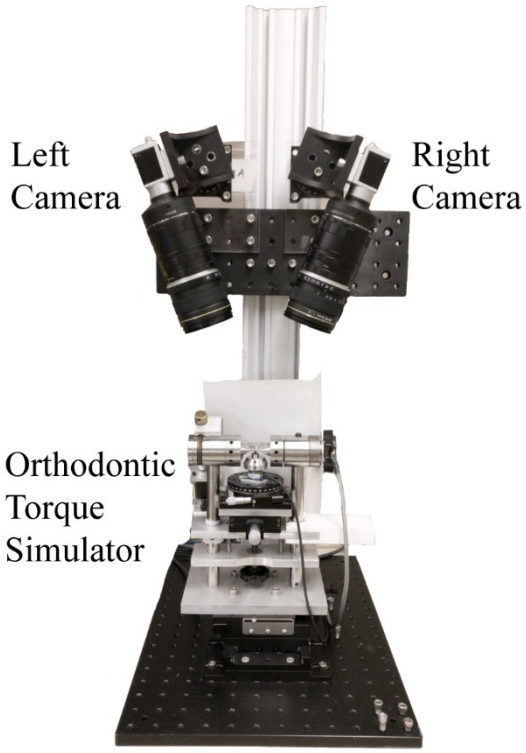

Figure 3.4. Orthodontic Torque Simulator with stereo camera system mounted overhead.

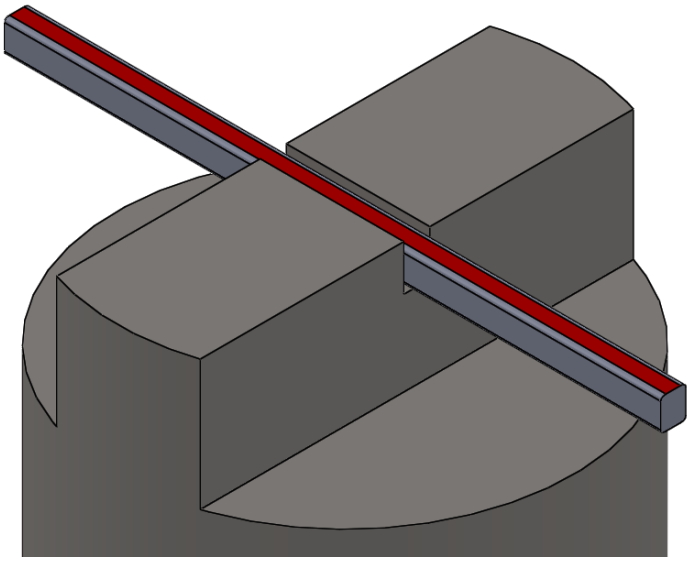

Figure 3.5. Isometric schematic indicating the surface (red) of a 0.019”x0.025” archwire imaged with DIC during third-order torque application inside a rigid dowel.

3.2.2.2 Stereo DIC System Parameters

The stereo DIC system was mounted overhead the OTS with no interference or interactions with the existing third-order torque application. Two area scan cameras (acA3800-10gm, Basler AG, Ahrensburg, Germany) were used to capture images of the archwire during third-order torque application. The resolutions of the cameras are 2748 px x 3840 px (width x height), and images were taken at full resolution during experiments. On each camera, a set of extension tubes (Polaroid, Minnesota, USA) were attached to increase the distance between the camera sensor and lens by a total of 49 mm to increase the overall magnification. The camera lenses used were 85 mm telephoto lens (Opteka, New York, USA). The focuses of the lenses are adjustable and were independently adjusted to maximise the intersection of the focal plane of each camera and the plane of the archwire. The apertures of the lens were set to an f/stop value of f/10 to maximise the depth of field while maintaining adequate light exposure. A diffuse light-emitting diode light

source (T100, Neewer, New Jersey, USA) was placed adjacent to the OTS to saturate the region of interest with white light.

3.2.2.3 Speckling

Preparation of the archwires for DIC includes speckling of the surfaces, which is the process of applying a unique pattern onto the deformed surfaces such that image correlation between images can occur [67]. Due to the size and geometry of archwires, the surface area of the top surface is highly limited. Therefore, the speckling technique was carefully considered. The archwires needed to exhibit a high contrast stochastic speckle pattern on the top surface as shown in Figure 3.6.

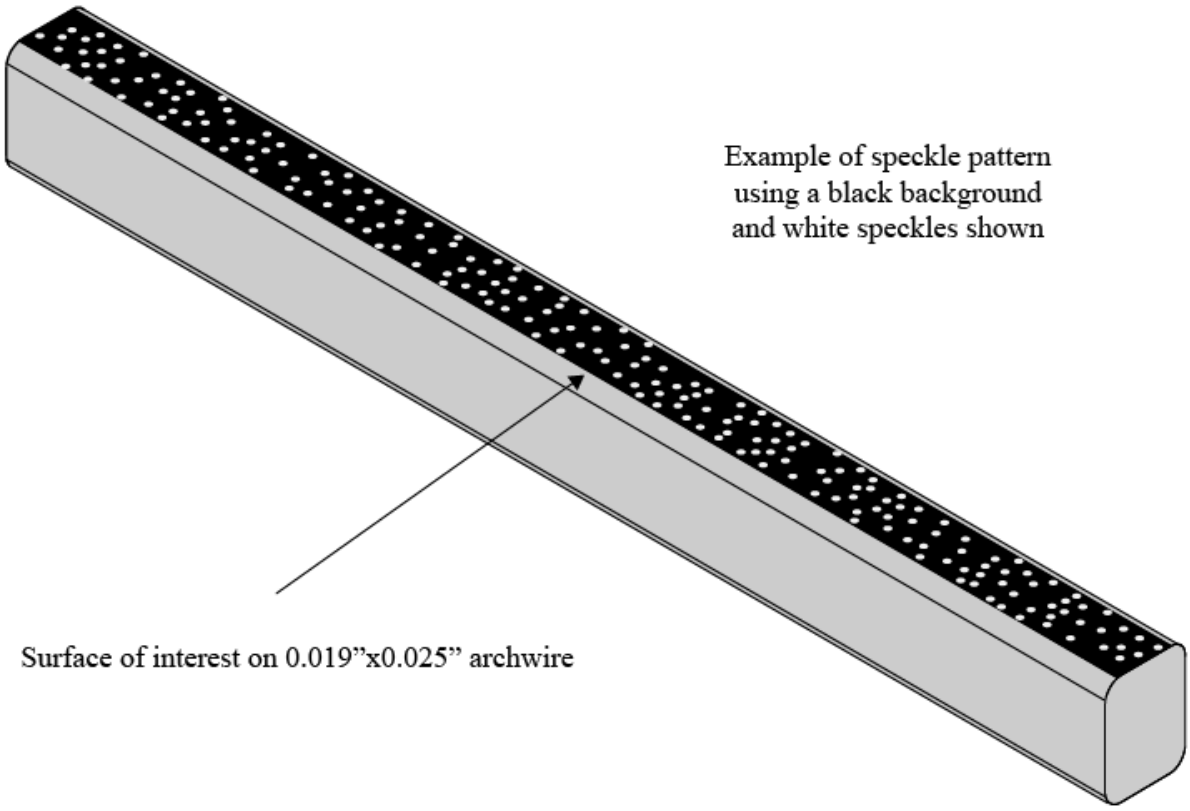

Figure 3.6. Schematic of a speckled top surface of a 0.019”x0.025” archwire segment with the intent of performing digital image correlation during third-order torque application.

Further, archwire widths are nominally 0.019”, but archwire cross-sections are rectangular with rounded corners. As a part of the manufacturing process of rectangular archwires, the corners are rounded [55], [57], [58], [79]. This further limited the surface area available to apply the speckle pattern. In Figure 3.6, the corner radii are shown without speckling, but in practise, it is difficult to speckle the top surface without speckling the corners. However, data recorded at the rounded corners should not be considered for the intents and purposes of obtaining deformation and strain values, as the change in geometry will have an affect on the local deformation behaviour. To determine an appropriate speckling procedure for the archwire given the available surface area, a test to determine speckle quality was performed by spraying pre-cut corrugated fibreboard samples with surface areas large enough to cover the entire field of view of the cameras. The enlarged surface area can be optically evaluated using the stereo camera setup with better fidelity.

The speckling procedure for the archwires was experimentally determined using various airbrush media to obtain speckle patterns that were appropriate for the archwire surface. The experimental procedure in archwire speckling is fully detailed in Appendix C. Ultimately, the speckles were applied using silver-coated solid glass microspheres (Cospheric LLC, California, USA) and were adhered onto the surface by airbrushing the microspheres onto the archwires. This was accomplished by mixing the microspheres with a water and polyvinyl acetate glue solution and agitating the solution to ensure the microspheres were suspended in solution rather than settled at the bottom of the container. The outcome of the speckling is highlighted in Figure 3.7.

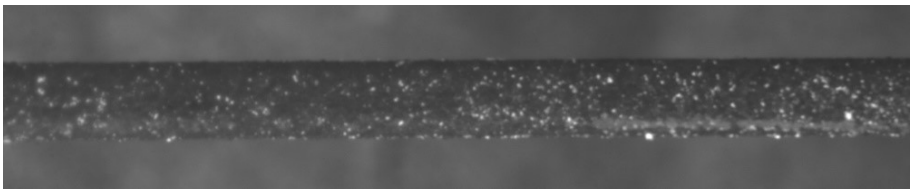

Figure 3.7. Archwire speckling using silver-coated solid glass microspheres on top of a matte black spray painted base layer.

3.2.2.4 DIC Camera System Calibration

To obtain image correlation, the camera system must be calibrated to solve its intrinsic and extrinsic parameters. The intrinsic parameters include properties that are specific to an individual camera, such as focal length, principal point (the image centre), lens distortions, and the conversion of pixel to spatial dimensions. The extrinsic parameters include positional information of objects in the system, such as the translations and rotations required to define where the cameras are with respect to the origin defined from system calibration.

In calibrating the DIC system to obtain the intrinsic and extrinsic camera parameters, the RD and archwire were first mounted to the OTS to locate the region of interest. The cameras were adjusted to align the horizontal image centres to the archwire. The position and focal length of each camera were then adjusted to ensure maximum overlap between the two field of views. With the positions of the cameras finalised, a 2D calibration target (R2L2S3P3, Thorlabs Inc., New Jersey, USA) was placed in the field of view, and the calibration procedure was performed. Lighting and camera exposures were adjusted to obtain high contrast between the dots on the calibration target and the background. Given that the calibration target is 2D, multiple views of the target must be captured. The OTS allowed for vertical translation of the calibration target, which moved the target towards the cameras. A dial gauge (TFT Tools Inc., California, USA) was used to measure the vertical

translations. A total of five views spaced 0.010” apart were used in the calibration image set. In positioning the calibration target, it is critical that the calibration volume contains the region of interest of the archwire. With the calibration target mounted onto the OTS, the axis of rotation (x-axis) was located by translating the target in the z-direction until it was aligned with the tip of the clamp. Using the axis of rotation as a landmark, as the calibration target was translated vertically upwards towards the camera, where the first view was taken slightly below the axis of rotation, and the final view was captured slightly above. In other words, the resultant calibration volume fully contained the surface of the archwire as well as the bounded the possible maximum deformations an archwire could exhibit under torsion. An example of a calibration image pair taken by both cameras is shown in Figure 3.8.

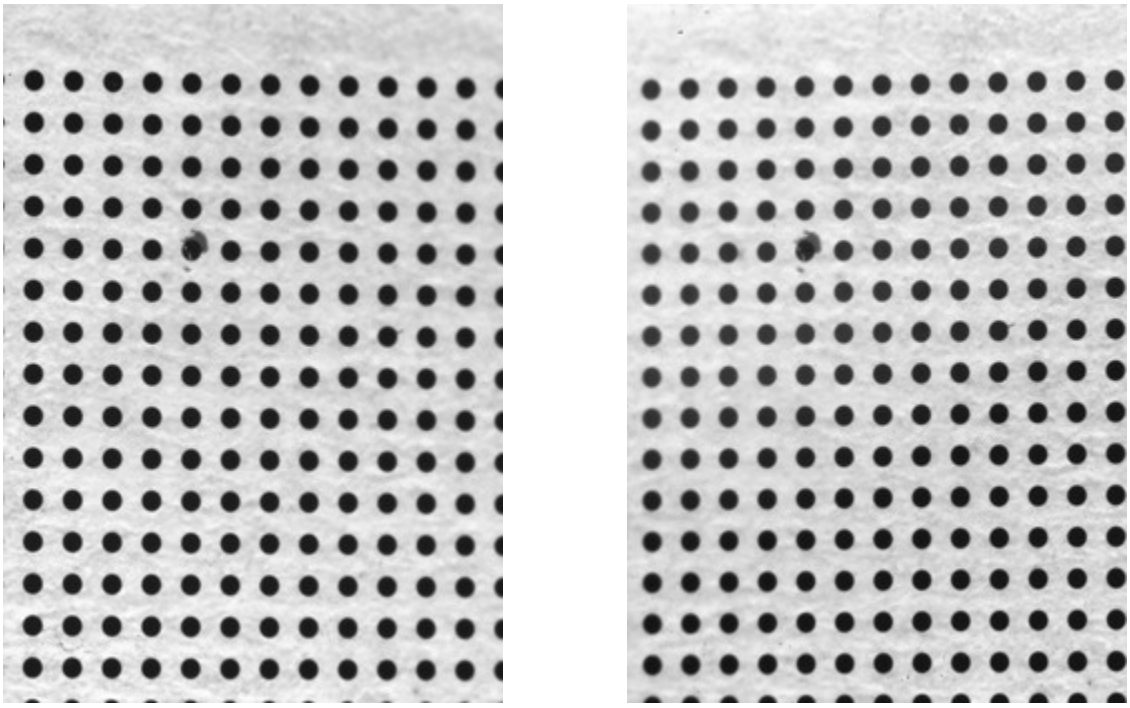

(a) (b)

Figure 3.8. Calibration image pair as captured by the (a) left and (b) right cameras.

The calibration image set was imported into a commercial DIC software package (DaVis 8.4, LaVision GmbH, Göttingen, Germany) to calibrate the DIC setup. The calibration images were preprocessed using a non-linear intensity normalisation filter to optimise the contrast between the dots and the background, which maximises the number of identifiable dots in each calibration image. The calibration follows a pinhole calibration as opposed to a generic polynomial third-order function. The advantage of using the pinhole calibration is that if there was uncontrolled tilting of the calibration target during its vertical translation, the tilt can aid in the minimisation of mapping error [80]. Conversely, using the generic polynomial third-order function mandates that all calibration views are equidistant and coplanar. In prescribing vertical translations of the calibration target with the OTS, it is entirely possible that there are minute deviations from equidistance and coplanarity between views. Therefore, the pinhole calibration is the most suitable.

The corrected and dewarped image of the calibration target is shown in Figure 3.9. The overall dimensions of the corrected image are 3027 px x 3938 px. For corrected images, the calibration determined that the scale factor was 461.817 px/mm, and the origin of the coordinate system relative to the corrected image was at (1104.97, 1858.37). All relevant intrinsic and extrinsic parameters relative to this origin point are shown in Table 3.1.

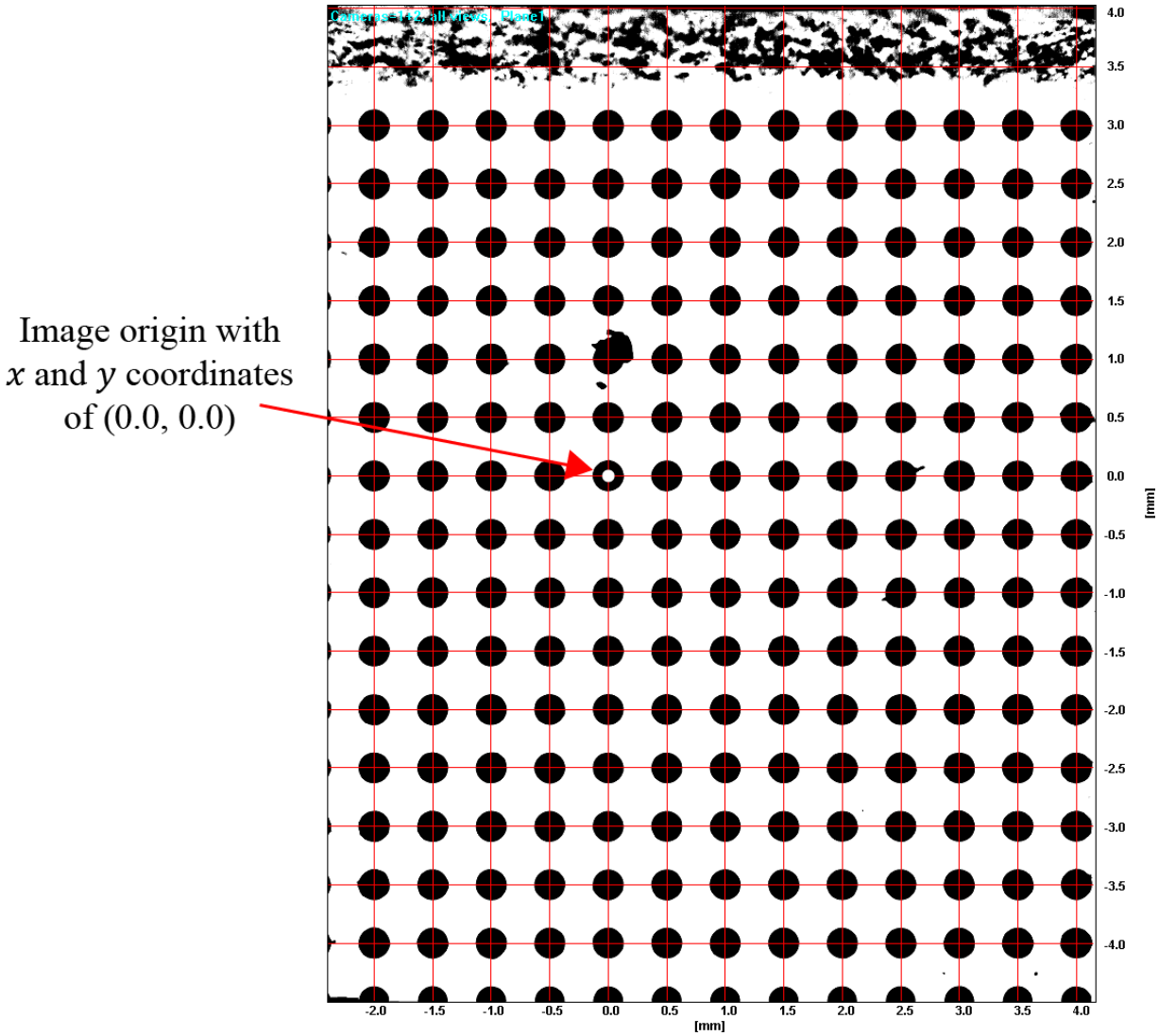

Figure 3.9. Corrected image of calibration target with dimensions rescaled to spatial values. The origin of the image coordinate system is marked with a white circle at (0.0, 0.0) mm.

Table 3.1. Reported intrinsic and extrinsic digital image correlation system parameters for imaging the third-order torque of 0.019"x0.025" stainless steel archwires in a rigid dowel.

Parameter	Left Camera	Right Camera
	Intrinsic	
Focal length [mm]	173.108	170.828
Principal point (x, y) [px]	(1374, 1920)	(1374, 1920)
First-order radial distortion	-0.0160975	-0.0163834
	Extrinsic (Relative to origin)	
Translation (x, y, z) [mm]	(-0.738576, 0.234537, 225.579)	(-0.871918, 0.239472, 225.645)
Rotation (x, y, z) [°]	(1.80951, -19.8467, -0.739881)	(2.00260, 20.6696, 0.868717)

The intrinsic and extrinsic parameters are fully described after calibration, and the coordinate system of the cameras of the DIC setup is shown in Figure 3.10. In this coordinate system, captured images are parallel to the xy-plane with the positive z-direction being upwards and vertical towards the cameras. Coincidentally, this coordinate system matches the OTS's physical coordinate system as well.

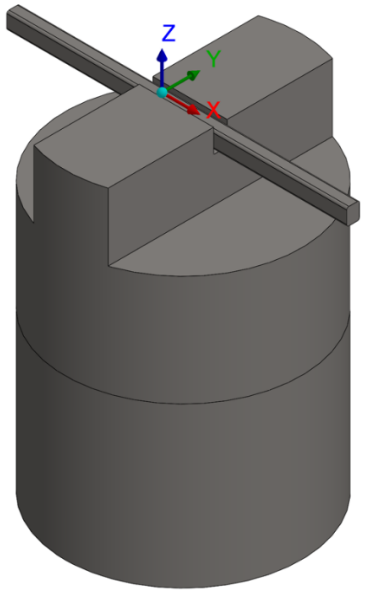

Figure 3.10. Schematic of the coordinate system of all DIC images and results as captured with the OTS.

3.2.2.5 Image Capture

The testing procedure using the OTS is stepwise static, whereby reaction forces and moments as measured by the load cell are logged after every incremental rotation when the OTS is in a static state and not actively applying any rotation. Once the measurements are logged, the OTS continues to the next angular position. The OTS program controls allow for adjustment of the angular increments and time between rotation, resulting in said stepwise static torque application. The image acquisition rate of the camera system therefore follows the same timing, capturing image pairs after each rotation in the same intervals as the load cell. In addition to image acquisition rate, the exposure times for the cameras were set to be 0.450 seconds, which was experimentally determined as an exposure time that resulted in adequate lighting conditions in the images taken throughout the range of rotation. The exposure duration can be long since the OTS remains static throughout the exposure, meaning images will not be subject to any motion blur or other artefacts of motion since the archwire remains at rest during image capture.

3.2.2.6 Image Preprocessing

The images of the archwire and RD obtained during third-order torque application were imported into DaVis for image correlation. The calibration provided the appropriate image scales, but additional preprocessing steps such as image pairing, masking, and filtering were performed. Image pairing combined the images from the left and right cameras into image pairs, which match temporally. Image masking was applied to reduce the region of interest to contain just the archwire, and various filters were explored with the intent of increasing image quality for correlation. In testing different image filters, it was found that linear filters decreased image quality and led to the inability to achieve image correlation. Instead, non-linear filters were investigated, as their

properties and performances with respect to image processing were appropriate for the nature of the loading. When capturing images during third-order torque, the images taken of the archwire consists of a surface that changes relatively quickly over the image set. Since each consecutive image includes an additional 1° of rotation, the rapid movement can lead to large changes in intensity, particularly as the rounded corners of the archwires become more visible in the field of view. The intensity normalisation filter and the subtract sliding minimum filter were chosen as candidates for appropriate filters for the image set, with the aim of higher quality images for correlation. Both filters require a filter length as an input. The intensity normalisation filter subtracts the local intensity average from a pixel and divides the result by the local intensity standard deviation [80]. The subtract sliding minimum filter is a high-pass filter that computes local intensity minimums and subtracts these values, effectively filtering out the average background high intensity fluctuations and passing small intensity fluctuations, making the background of an image more constant in intensity without affecting the resultant image correlation [69], [81].

Between these two filters, a properly tuned subtract sliding minimum filter gave the best performance. Given the size of the speckles on the archwire surface, a filter length of 11 pixels was found the most suitable, balancing between the removal of high intensity fluctuations with minimal confounding between adjacent speckles, as well as comparing image correlation quality. A summary of the archwire image preprocessing steps are shown in Table 3.2 and a comparison between a masked archwire image prior to and after non-linear filtering is shown in Figure 3.11.

Table 3.2. Summary of preprocessing steps performed on speckled archwire images

Image preprocessing step	Result
Pairing	Combine images from the left and right cameras
Masking	Region of interest reduced to remove non-critical pixels
Filtering	Subtract sliding minimum with a filter length of 11 px.

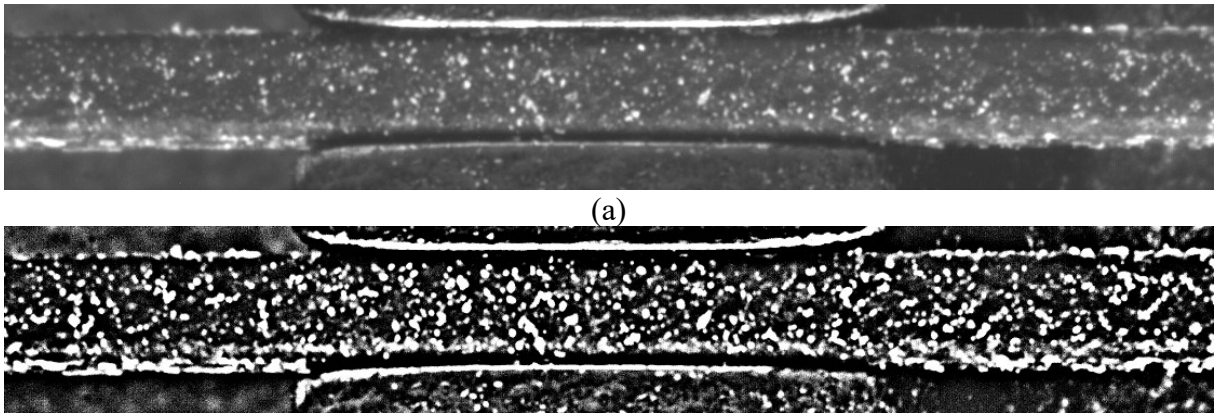

(a)

(b)

Figure 3.11. Comparison between raw archwire image with a filtered preprocessed image using a subtract sliding minimum non-linear filter.

3.2.2.7 Image Correlation

Once all images within a given set were preprocessed, image correlation was performed for all trials. The size of the interrogation window was selected with the width of the archwire in mind. In the context of the field of view of the DIC setup, the width of an archwire would span approximately 250 pixels. An interrogation window should be large enough to contain sufficient information to make each subset unique from all other subsets [17]. For the archwire, the size of the interrogation window was selected at 63 x 63 pixels in order to have sufficient information within each subset. Seeding points were placed along the length of the archwire, with careful attention to the contents within the windows being uniquely identifiable, as well as containing at least three speckles/features to aid with image correlation [17]. An example of an archwire with seeding points placed along its length is shown in Figure 3.12.

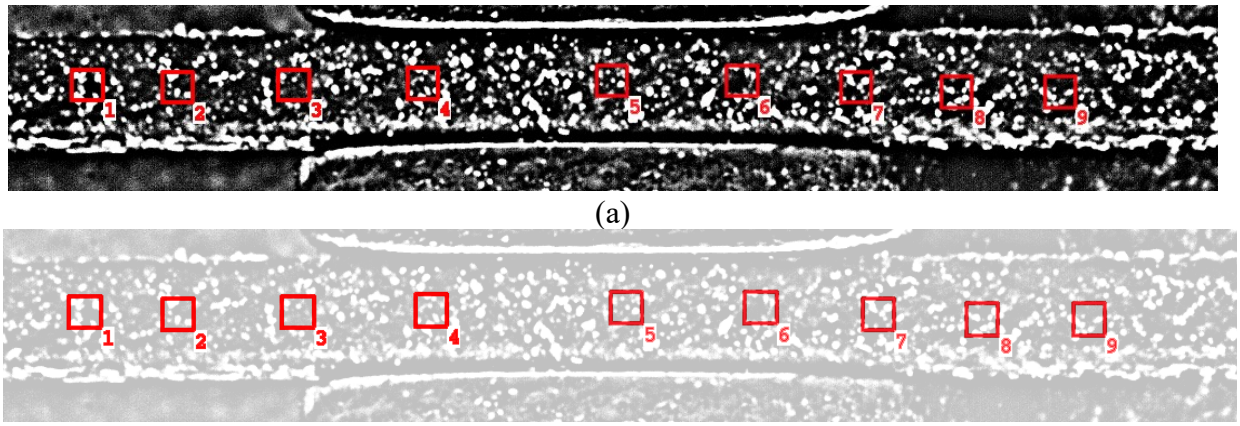

(a)

(b)

Figure 3.12. Example of archwire with nine seeding points of 64 x 64 pixels (a) shown in red boxes and (b) with reduced archwire opacity for seeding point clarity.

In determining the step size, it was important to consider the trade-off between vector density and error in strain calculation. A lower vector density would lead to larger gaps in data but allow for smaller strain errors as the vectors are further apart. It was decided that minimising strain error was more desirable than a large vector density for purposes of system verification, therefore a step size of approximately half the interrogation window size was selected at 31 pixels. When using interrogation windows of 63 x 63 pixels, the accuracy of a calculated vector is between 0.02 – 0.05 pixels [81]. In calculating strain error, it is described as the error between two vectors divided by the distance between the two vectors. Using the lowest accuracy value of 0.05 pixels for a vector position, strain error is calculated as:

$$\frac{0.05 \text{ px} \times 2 \text{ vectors}}{31 \text{ px}} = 0.003 = 0.3\%$$

A strain error of 0.3% was deemed acceptable and would be adequate for further system verification. 3D displacement and surface strain values obtained from DIC could be used for further analysis.

The twisting nature of the archwire results in the speckles moving at different rates over the span of the archwire in the IBD. Speckles that are closer to the clamp tip will undergo the most movement, as that region of the archwire will rotate closer to the maximum 30°, whereas speckles closer to the RD will see less overall rotation. This mandated that deformations and strains were calculated with the summation of differentials. Every consecutive image is correlated with respect to the previous image, rather than with respect to the initial image. This differs from the technique of correlating deformations and strains relative to the first image in an image set. By using the sum of differentials, large deformations, as exhibited when applying torsion to an archwire, are determinable over the entire range of rotation.

In performing image correlation, the least squares matching (LSM) method was utilised. The main premise of LSM consists of computing optical flow by minimising the squared differences between subsets while having the ability to account for translations, rotations, other geometries, and radiometric transformations [69], [70], [77], [82]. To address these differences between subsets, mathematical transformations such as affine, projective, or polynomial transformations can be applied to subsets to obtain better correspondence [69], [70]. Whether two images differ spatially or temporally, one image is assigned as the reference, where subsets are fixed while transformations are applied to the complementing image, which is considered to have deformed subsets [69], [70]. Subsets between images achieve correspondence when their grey values (or intensities) of the subsets are in agreement, which is measured using a correlation coefficient [77], [78], [82]. LSM is iterative as the subset transformations can be continuously applied until the correlation coefficient is maximised and the match can be improved no further [69]. Once correspondence is achieved, deformations, strains, and surface reconstructions can be performed

[69]. One favourable aspect of LSM is that it can enable sub-pixel accuracy in measurements requiring complex transformations [70], [77], [78]. However, it is necessary that images are of higher quality with regards to surface illumination and contrast between speckles when compared to other matching algorithms. Careful attention during image acquisition and preprocessing can aid in obtaining correspondence more representative of the actual specimen responses [17], [69], [77]. Therefore, optimisation of an experimental setup should be considered with a priority of obtaining high quality images with respect to LSM requirements. Overall, the practicality of LSM makes it a commonly used method for image matching purposes [70], [77]. In the context of performing third-order torque experiments with the OTS, the loading and geometric responses of the archwire is relatively complex compared to other mechanical loading scenarios, making the LSM method a suitable option to achieve successful image correlation.

3.2.2.8 DIC Output Parameters

DIC can yield valuable insight on the strain and deformation behaviour of any test specimen, but the geometry and orientation of a test specimen as well as the camera positioning dictate what outputs are valid. In the case of the archwire, only the top surface is imaged, which results in the inability to resolve strains involving z-components. This is because nowhere along the imaged surface will adjacent vectors have an initial difference in the z-direction. Consequently, in resolving the strain fields, all strains involving a z-component cannot be determined due to definition of strain, where a change in length is divided by the initial length. In the case of strain involving z-components, dividing by zero would not be computable. Computed vectors will only have initial distances in the x- and y-directions. Therefore, the outputs that can be measured from

DIC are surface displacements in the x-, y-, and z-directions, principal surface strains in the x- and y-directions, and surface shear strain in the xy-plane.

3.2.3 Verification of DIC Measurements with Analytical and Numerical Solutions

The use of 3D DIC to measure archwire characteristics during application of third-order torque is novel in the literature. As such, scientific rigor should be exercised to investigate the accuracy of this method. In its implementation, outputs from the DIC would have to be carefully considered given the scale of the experiment as well as the out-of-plane motion of the archwire during rotation. Due to the physical archwire deformations that arise during third-order torque, surface strains would be computed over a surface that is not flat and instead indicates a twisted surface. Therefore, performing an FE analysis may provide a numerical verification of the DIC measurements. An FE model was set up to replicate the third-order torque loading conditions as prescribed by the OTS. Only the archwire and RD were considered in the model, as model simplifications using appropriate boundary conditions replicates the physical boundaries of the OTS without complications introduced when using an orthodontic bracket. The analysis was performed using academic finite element analysis software (ANSYS Academic Research Mechanical, Release 19.2, ANSYS Inc., Philadelphia, USA). In performing the FE analysis, a preliminary model was used to contextualise the model parameters and get a better sense of the model geometry, boundary conditions, and contact behaviour between the archwire and RD. The development and analysis of the preliminary model is detailed in Appendix D.

3.2.3.1 Finite Element Model

Using the results of the initial model, several aspects of the model were updated to increase model accuracy and efficiency. First, as the stresses on the RD were localised around the slot, modelling the entire RD was unnecessary. For simplicity, the model was updated to remove the cylindrical portion of the RD while keeping the rest of the RD geometry, and the bottom face was set as fixed. A schematic of the final model as used in the FE analysis with all geometric simplifications is shown in Figure 3.13.

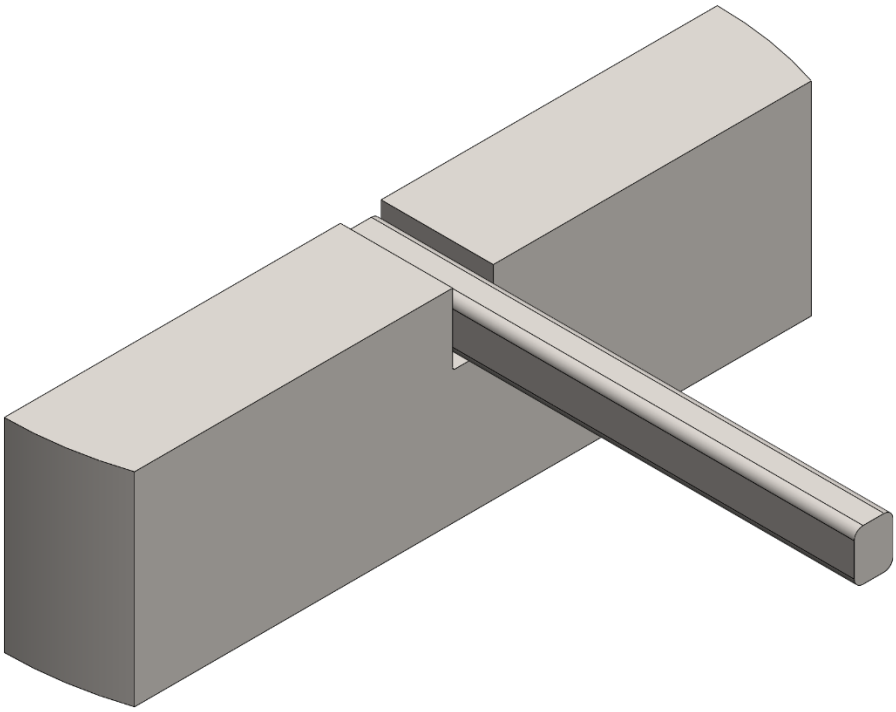

Figure 3.13. Isometric view of final model used in finite element analysis of third-order torque between a rigid dowel and 0.019”x0.025” archwire.

The stainless steel on the RD was updated to become non-linear stainless steel, whereas the stainless steel of the archwire was updated to match high-strength stainless steel as per manufacturer specifications [83]. However, due to incompleteness in manufacturer-reported properties, the only known property was that the stainless steel used to manufacture archwires

were 300-series stainless steel with ultimate tensile strengths greater than 300,000 psi. Using this information, material properties were sourced from an online database to match the ultimate tensile strength [84]. Making conservative assumptions, a 304V high strength stainless steel was found, which stated an ultimate tensile strength of 306,000 psi [84]. This stainless steel was then used to fill out non-linear stainless steel properties for the archwire. Material properties for the archwire and RD as used in the FE model are stated in Table 3.3. Bilinear isotropic hardening was applied to both non-linear stainless steels using a tangent modulus value of 1.80 GPa once the yield strength was reached, making the materials elastic-near-perfectly plastic [85]. Finally, the analysis settings of the non-linear model are listed in Table 3.4.

Table 3.3. Non-linear stainless steel material properties used in the final finite element analysis of third-order torque of a 0.019"x0.025" archwire in a rigid dowel [84], [85]**.**

Body/Material	Property	Value [Unit]
Rigid Dowel/	Density	7,750 kg/m^3
Non-linear stainless steel	Young's Modulus	193 GPa
	Poisson's Ratio	0.31
	Yield Strength	210 MPa
	Tangent Modulus	1.80 GPa
Archwire/	Density	7,916.5 kg/m^3
304V high strength	Young's Modulus	196.5 GPa
non-linear stainless steel	Poisson's Ratio	0.29
	Yield Strength	1,689.2 MPa
	Tangent Modulus	1.80 GPa

Table 3.4. Analysis settings used in the finite element analysis of third-order torque of a 0.019"x0.025" archwire in a rigid dowel.

Setting	Value
Solver type	Direct
Weak springs	On
Spring stiffness	Program-controlled
Solver pivot checking	Program-controlled
Large deflection	On
Inertia relief	Off

3.2.3.2 Analytical Solution to Torsion of Prismatic Bars

In evaluating the results of the FE model, torsion theory of prismatic bars can be utilised. The results that arise from an analytical solution can complement the findings with DIC and the FE model. The purpose of performing the FE analysis was to obtain an understanding of how the archwire deforms under torsion and to have the ability to directly compare DIC measurements with FE results. By including an analytical solution, the FE solution can be cross-verified and checked to ensure that the behaviour of the archwire is logical and matches what the analytical solution presents. The archwire should show behaviour that matches that of prismatic bars in torsion. Mainly, the maximum shear stress of a rectangular prismatic bar during torsion occurs at the midpoint of the longer side of the rectangular cross-section [86]. This result can be confirmed with the FE model, and the value of the maximum shear strain at the midpoint along the 0.025" side of the archwire can be used as the parameter of interest in testing for convergence. A solution to torsion of rectangular prisms was given by Saint Venant [87] using the semi-inverse method. The solution assumes that cross-sections perpendicular to the long axis of a rectangular beam in torsion will warp relative of the section plane, but the warping is equal for all cross-sections. A brief description of Saint Venant's solution is shown for a prismatic bar in torsion as defined in Figure 3.14.

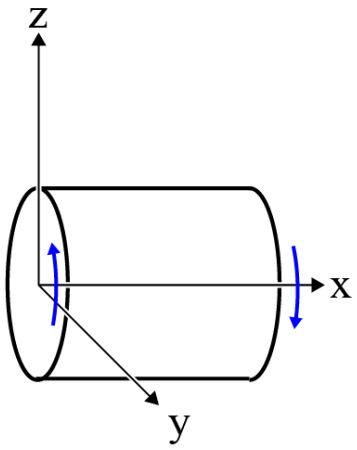

Figure 3.14. Schematic of torsion (blue) applied to a prismatic bar with a coordinate system defined with the *z*-axis as the axis of rotation.

The displacements from the torsion of the cross-sections are:

$$u = -\theta xy, v = \theta xz$$

θx represents the angle of rotation at a distance x from the origin. Under torsion, the warping of cross-sections is defined by:

$$w = \theta\psi(y, z)$$

The displacements and warps are used to define the strain components as:

$$\varepsilon_x = \varepsilon_y = \varepsilon_z = \gamma_{yz} = 0,$$

$$\gamma_{xz} = \frac{\partial w}{\partial z} + \frac{\partial u}{\partial x} = \theta\left(\frac{\partial \psi}{\partial z} - y\right),$$

$$\gamma_{xy} = \frac{\partial w}{\partial y} + \frac{\partial v}{\partial x} = \theta\left(\frac{\partial \psi}{\partial y} + z\right)$$

As surfaces are free to warp, it is seen that principal surface strains are zero, but surface shear strains in contrast, are present [87]. This result is true for all prismatic bars, including rectangular prism like archwires. However, this is only true in the case of the ends of the bar being free with no additional forces. With the OTS, the archwire is bilaterally twisted, clamped on both ends, and contacts the RD in a unique loading condition, thus deviating from the theory developed for prismatic bars in torsion. For archwires twisted based on the OTS coordinate system, surface strains in the x- and y-directions may be present in addition to expected shear strains on the xy-plane due to the applied torsion. Given the torsion theory, the results from the FE model can be verified. The response of the archwire and the characterisation of surface stresses and strains on the archwire can show that the model conforms to the theory, and consequently the development of surface strains on the archwire as measured by DIC could also be verified to ensure that strains values are in agreement with the model.

3.3 Results

In applying the bilateral rotation to the archwire placed inside the RD, the outputs measured with the OTS were third-order torque, and the outputs measured with DIC were surface deformations in principal directions as well as principal and shear strains on the surface. Third-order torque as measured by the load cell is described as the torque present at the base of the orthodontic bracket where the adhesive would be applied. With the RD, the measured forces and moments are transformed to the same theoretical position. The outputs measured using DIC are compared to the FE model and torsion theory for verification.

3.3.1 Third-Order Torque

The third-order torque data collected between the 10 trials performed with the RD is averaged and plotted with standard deviations, shown in Figure 3.15. The direction of torque is presented as negative to match the coordinate system of the OTS. All plot generation comparing two variables was completed using R, and in particular using the R package "ggplot2" as a part of the "tidyverse" package collection [88]–[90]. The associated R code can be found in Appendix E.

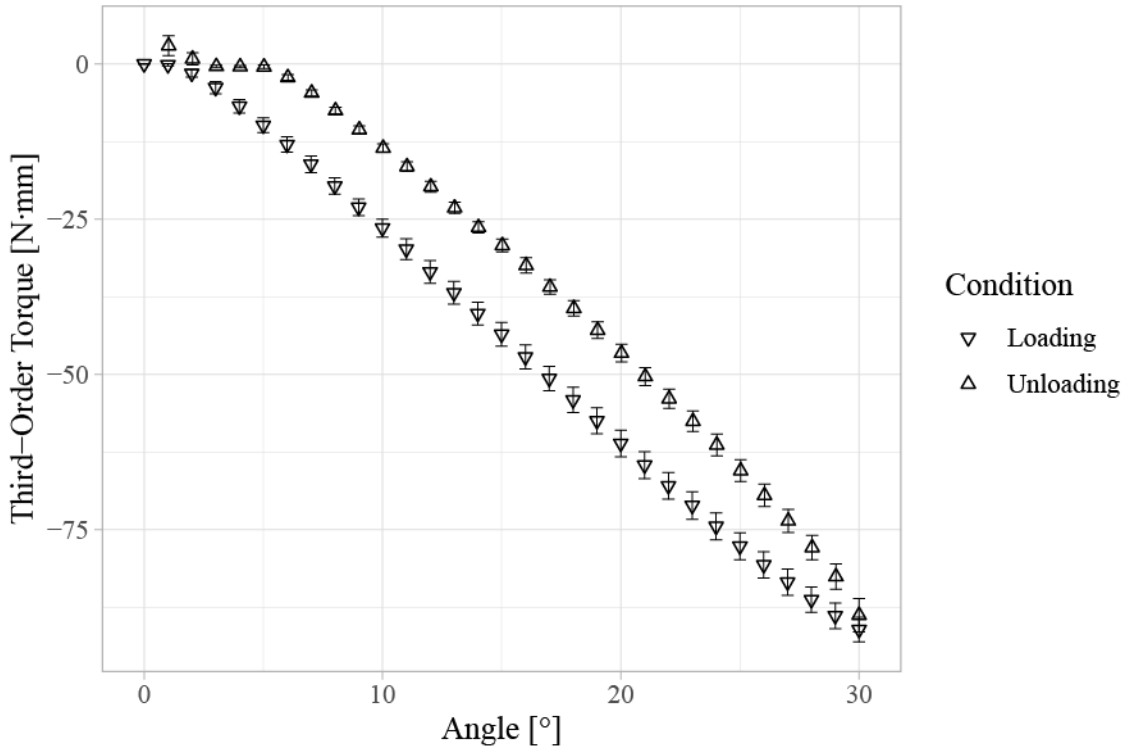

Figure 3.15. Third-order torque for a 0.019"x0.025" stainless steel archwire in a rigid stainless steel dowel over a rotation of 30°. Error bars indicate one standard deviation.

The torsional play when using the RD is comparatively smaller than when using orthodontic brackets [40]. It is seen that third-order torque rapidly arises, surpassing 10 N·mm of torque by 6° of rotation, whereas previous testing of stainless steel archwires in Damon Q brackets displayed torsional play in angles upwards of 10° and did not surpass 10 N·mm of torque until the archwire

was rotated between 15°-18° [40]. A direct result of this is also more overall torque at 30° loading. Further, variance between trials was found to be smaller, as evidenced by the small standard deviations. With the same RD being used for all trials, it was paramount that the application of third-order torque did not exhibit varying behaviour as trials progressed. Deformation in the RD could result to a decrease in torque between consecutive trials. To ensure the validity of reusing a single RD throughout third-order torque experimentation, maximum torque values were referenced from previous experimentation and current experimentation to check that maximum torque values did not decrease over time. As previously mentioned, the validation is detailed in Appendix A. Given the outcome of the validation, it was justifiable to continue using the RD for further third-order torque testing.

3.3.2 Archwire Deformations and Strain from DIC

Outputs from DaVis are exported as vector fields and were analysed using a post-processing toolbox (PIVMat 4.10, F. Moisy, Île-de-France, France) created for use with MATLAB (MATLAB 2019a, The MathWorks, Inc., Massachusetts, USA) [91]. The colour maps used in the plots were imported from a MATLAB package [92]. The associated MATLAB code for DIC plot generation can be found in Appendix F. Full-field outputs are available for all angles of rotation, but for brevity, only results at 30° archwire rotation are shown in the full-field format. An example correlated vector map of archwire y-displacements at 30° is approximately superimposed onto an as-captured image of the archwire at 0° rotation, shown in Figure 3.16. The difference in angles was intentional since DaVis similarly projects measurements at all angles onto the initial image, which is the undeformed archwire. Displacements δ_x, δ_y, and δ_z and strains ε_{xx}, ε_{yy}, and ε_{xy} are

shown in Figure 3.17 and Figure 3.18, respectively. Note that in all images, the x- and y-axes represent spatial coordinates and the colour maps show the magnitude of the specified parameter.

The colour scales showing displacements in millimetres are at the same limits for the three displacements; however, for strains, the colour scales showing strain in millimetres per millimetre is only the same for principal strain the x-direction and surface shears strain on the xy-plane. For principal strain in the y-direction, the rounded corners of the archwire cause the strain development in the y-direction to have comparatively higher values due to the optical effect of rapidly changing perspective of the speckles on the corner compared to the flat surface. In reality, these large strains do not exist and are a consequence of the camera orientation and the initial interpretation of the speckles on the corners. From the perspective of a camera, consecutive images may show speckles on the rounded corners significantly deforming when in actuality there is little deformation compared to rigid movement of the corner surface. In evaluating archwire behaviour, results on the rounded corners were omitted both due to the perspective challenges as well as being close to boundaries of the speckle pattern. For all images, colour map limits were determined by first finding the maximum and minimum values for each parameter and fitting the limits to bound all measured values for fair comparisons across the x-, y-, and z-directions. All parameters are projected onto the un-deformed archwire.

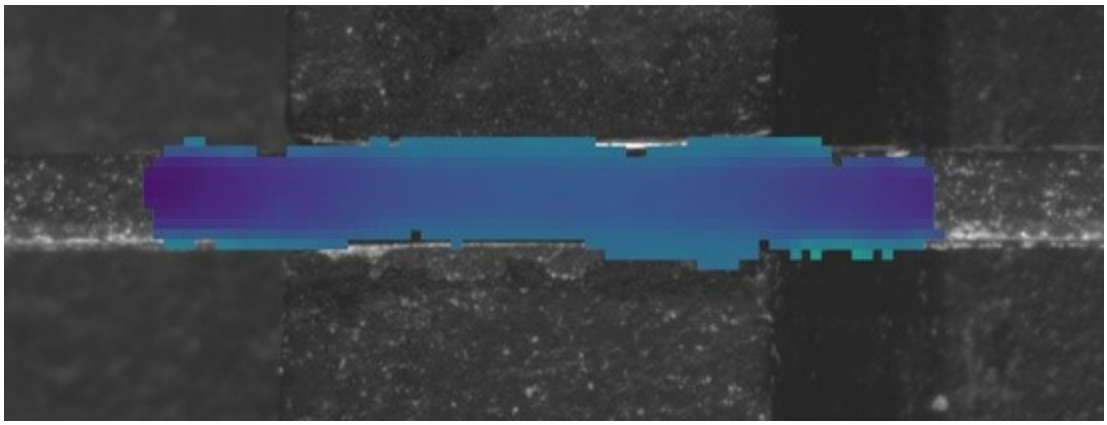

Figure 3.16. Superimposition of correlated archwire surface showing *y*-displacements at 30° onto raw captured image of undeformed archwire.

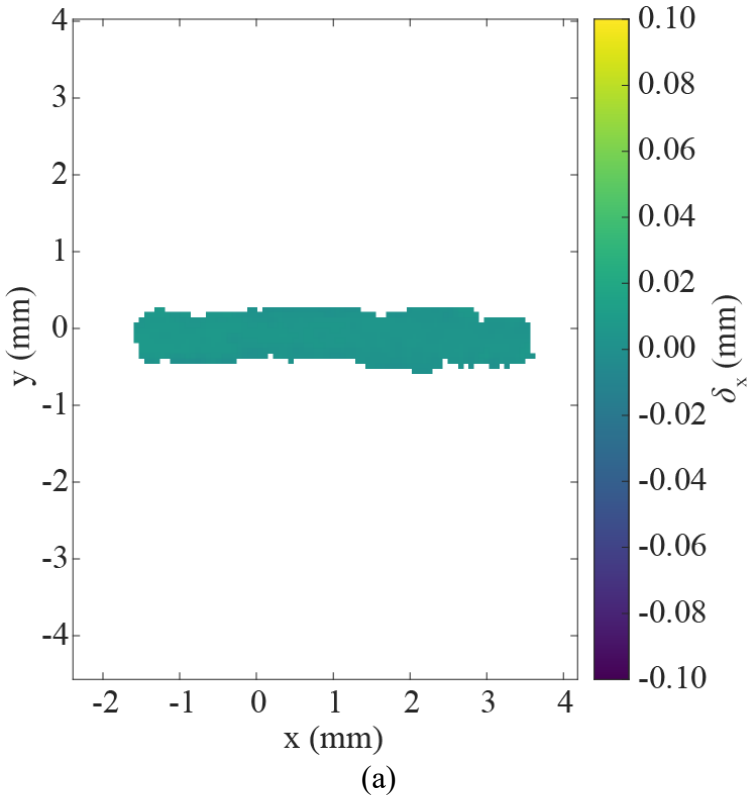

(a)

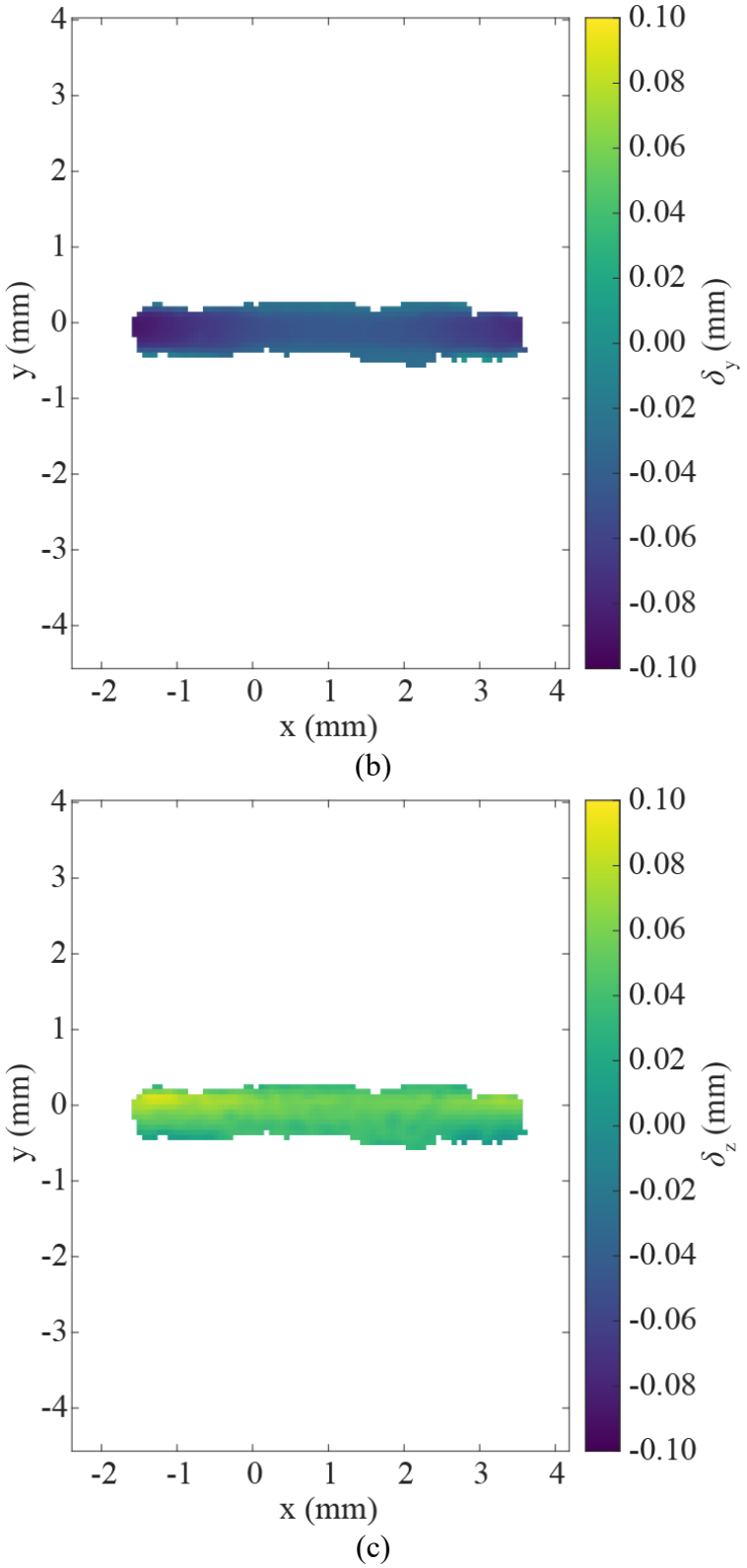

Figure 3.17. Digital image correlation output showing surface deformations of the archwire in the (a) *x*-, (b) *y*-, and (c) *z*-directions at 30° archwire rotation.

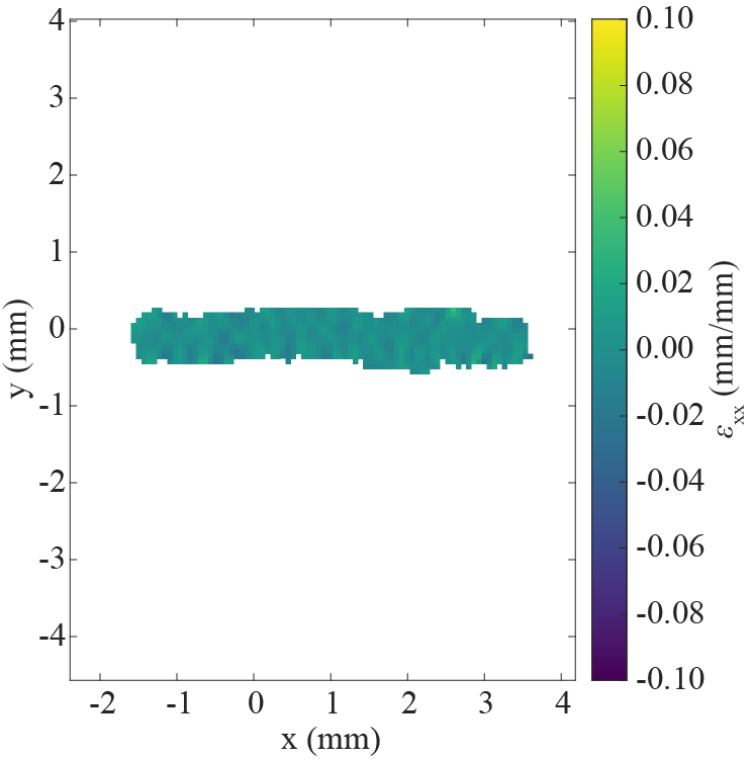
y (mm)
x (mm)
ε_{xx} (mm/mm)
0.10
0.08
0.06
0.04
0.02
0.00
-0.02
-0.04
-0.06
-0.08
-0.10

(a)

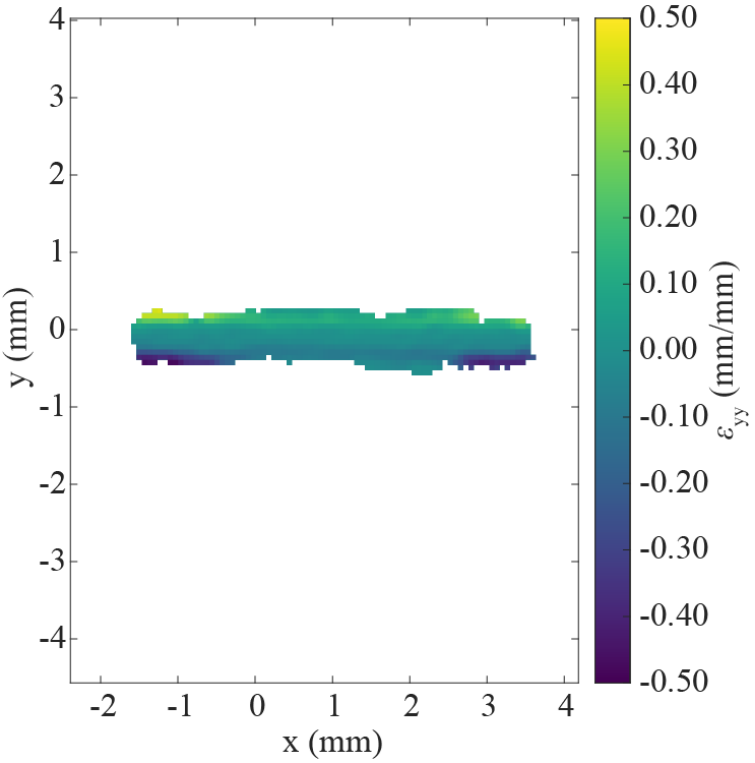
y (mm)
x (mm)
ε_{yy} (mm/mm)
0.50
0.40
0.30
0.20
0.10
0.00
-0.10
-0.20
-0.30
-0.40
-0.50

(b)

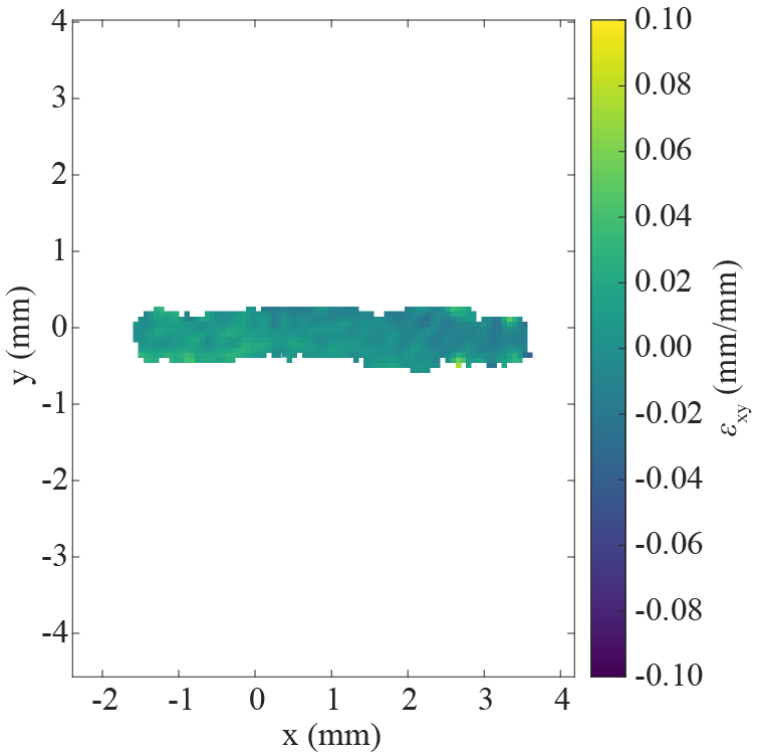

(c)

Figure 3.18. Digital image correlation output showing surface strains of the archwire with principal strains in the (a) x- and (b) y-directions, and (c) shear strain on the xy-plane at 30° archwire rotation.

At the 30° rotation point, the archwire should exhibit appreciable deformations on either side of the RD while being limited within the RD slot. This is evidenced by all three directional displacements. Due to being clamped on both sides, x-displacements were near zero, whereas the y- and z-direction displacements exhibited the behaviour of a bilaterally twisted bar. The left and right extremities of the correlated region both move negatively in the y-direction and positively in the z-direction in the areas outside of the RD.

Strains on the top surface of the archwire were also near zero away from the rounded corners for both principal strains in the x- and y-directions. When looking at surface shear strain on the xy-plane, there is evidence that the left side tends towards a positive shear strain value whereas the right side tends towards a negative value. To confirm this effect, the shear strains are replotted

with a smaller range on the colour map shown in Figure 3.19. Note that there is a small region of shear strain values greater than the maximum limit of the colour map, which is indicated by a bright yellow spot; however, the new limits better indicate the positive and negative shear strain development on the left and right sides of the archwire, respectively.

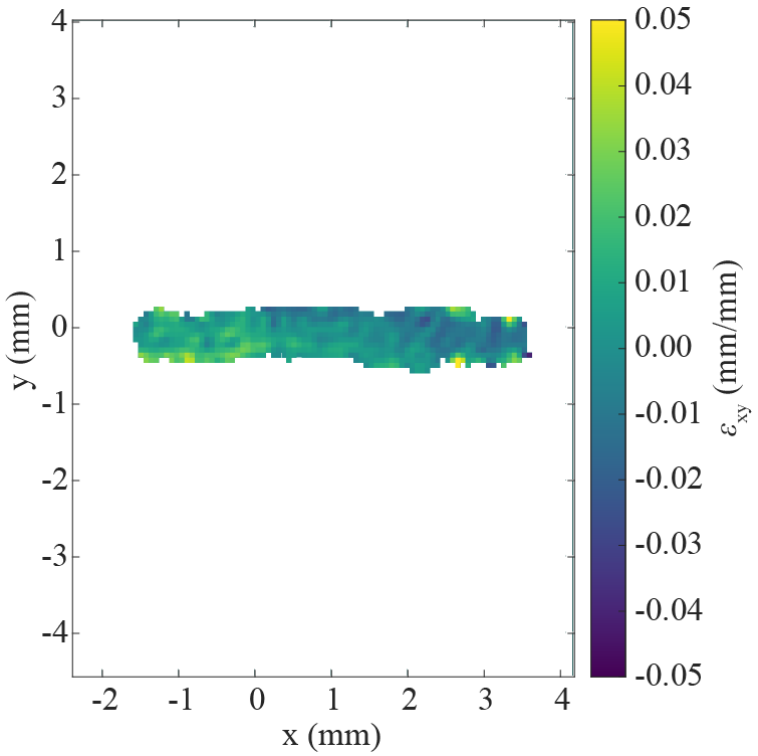

Figure 3.19. Digital image correlation output showing surface shear strain on the xy-plane at 30° archwire rotation.

In addition to the full-field strain plots, average strain values from the 10 trials for every angular position during loading were obtained by creating a local vector map of the archwire on either side of the RD. Due to the limited available surface area, vector regions were defined as being 1 mm long in the x-direction, and two vectors long in the y-direction, (two vectors is the minimum when extracting vector maps using PIVMat). The placements of the vector maps were determined by locating the centre of the archwire using the plot of principal strain in the y-direction. The colour map scale was adjusted to a smaller range, resulting in the centre of the archwire becoming more

visually discernible as the influence from the rounded corners were more apparent. In the x-direction, the regions were placed close to the edge as to avoid effects from the RD. An example of the vector regions can be seen in Figure 3.20. All vectors in the region are averaged and the same regions are used for both principal strains and shear strains. Probed regions changed in location on a per trial basis, but the method of obtaining the regions by referencing the y-direction principal strains first were consistent.

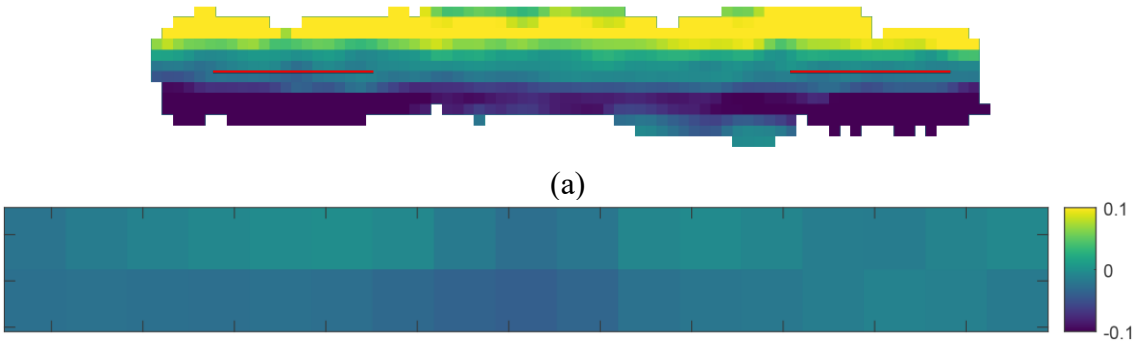

(a)

(b)

Figure 3.20. Example vector regions used to extract average strain values on the archwire (a) shown as red lines on either side of the rigid dowel and (b) the resultant colour map of the left region.

The resultant strain plots indicate the average principal strains and shear strains measured on either side of the archwire using the probed vector maps and are shown in Figure 3.21. It is seen that principal strains in the x-direction are consistently zero throughout the rotation. In contrast, the principal strains in the y-direction have significantly more variance. This is due to the influence of the archwire corners and the subset size used during image correlation. Since the archwire geometry is limited in the y-direction being 0.019" and even lesser taking the rounded corners into account, principal strains measured in this direction should be omitted for analysis and verification. Lastly, the shear strains on the surface show clear indication that shear strains increase with the angle and differ in directionality when comparing the left and right sides.

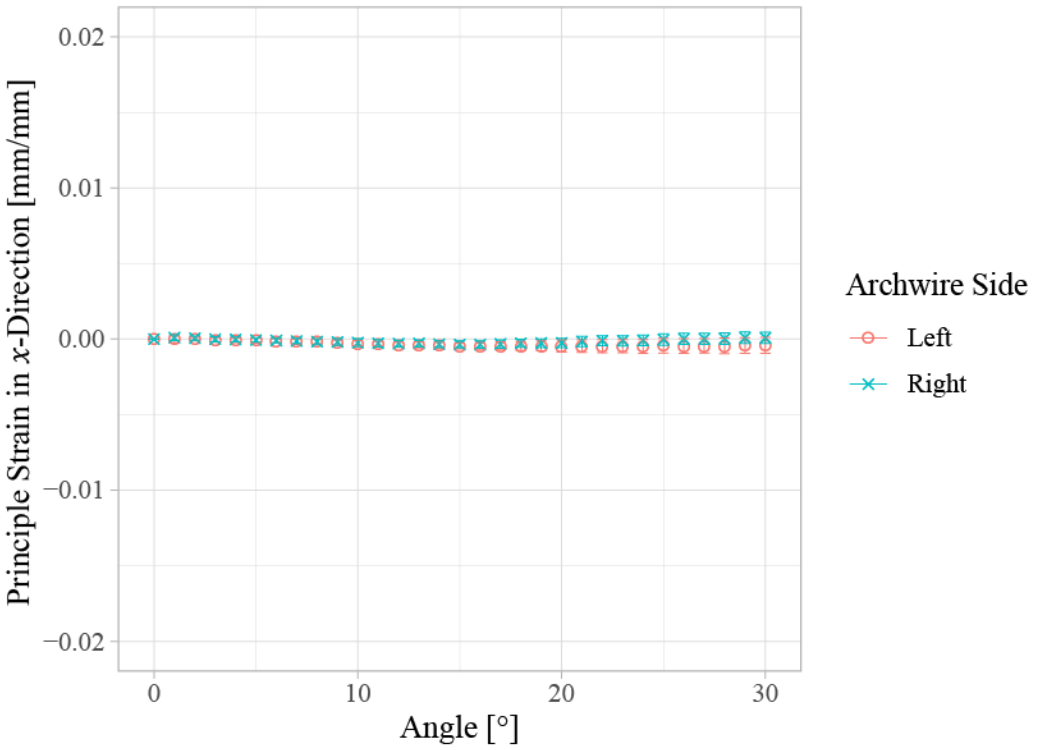
Principle Strain in x-Direction [mm/mm]
0.02
0.01
0.00
−0.01
−0.02
0
10
20
30
Angle [°]
Archwire Side
Left
Right

(a)

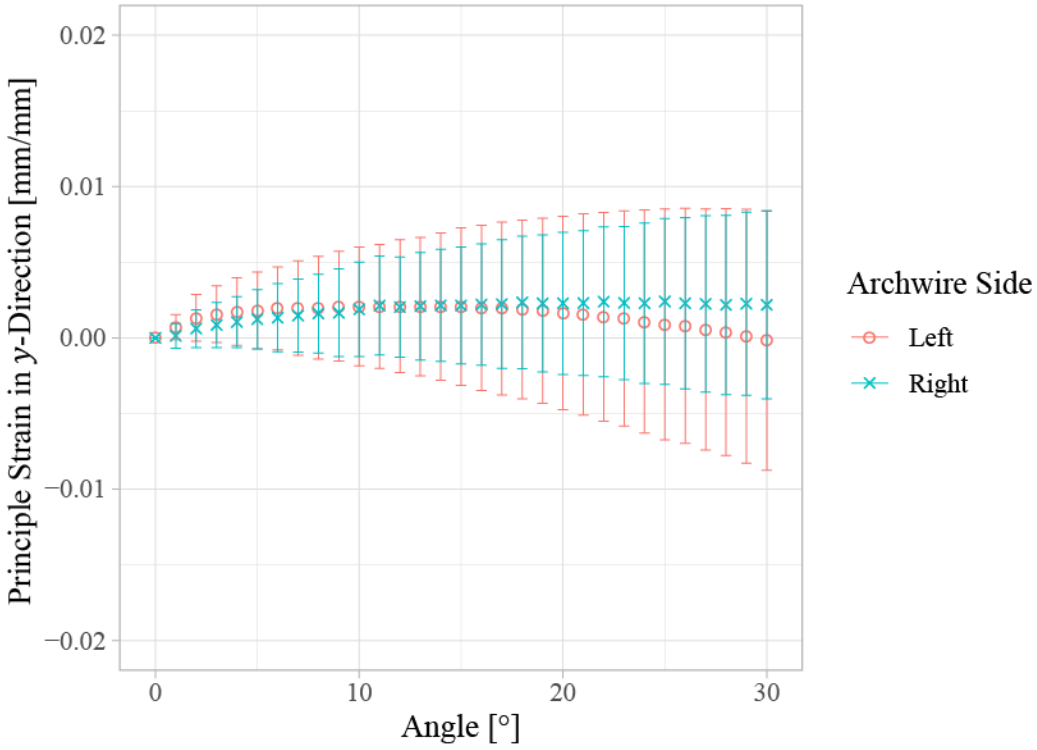
Principle Strain in y-Direction [mm/mm]
0.02
0.01
0.00
−0.01
−0.02
0
10
20
30
Angle [°]
Archwire Side
Left
Right

(b)

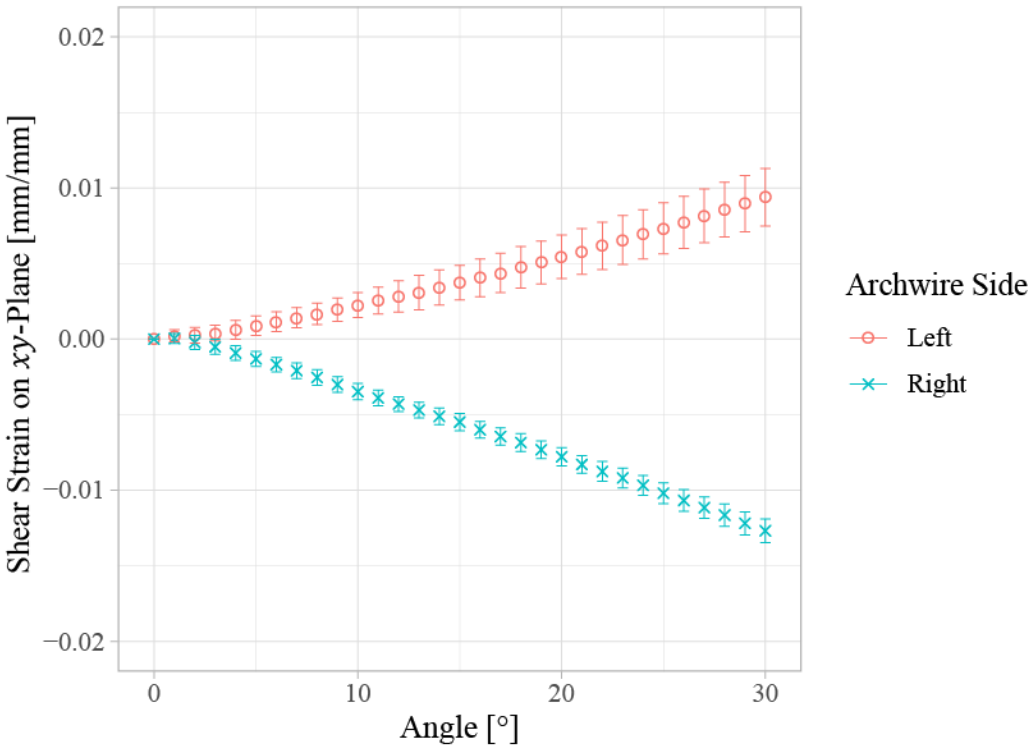

(c)

Figure 3.21. Average surface strains on a 0.019"x0.025" stainless steel archwire from 0° to 30° loading using probed vector maps to the left and right of the rigid dowel, with principal strains in the (a) x- and (b) y-directions, and (c) shear strain on the xy-plane. Error bars indicate one standard deviation.

Overall, the strains measured using DIC indicate that the behaviour of the archwire matches the torsion theory described in Section 3.2.3.5, but additional comparison with FE results can further verify the magnitudes and behaviour of the parameters obtained using DIC.

3.3.3 Finite Element Model

The FE analysis of the RD and the section of archwire led to several confirmations. First, results from the FE model were compared to the theory of rectangular bars in torsion. Second, the FE model was compared to the DIC results to confirm that the deformations and calculable strains

from the images were in the right magnitude. Before any comparisons were made, the FE model itself was checked to ensure that the solution converged.

3.3.3.1 Mesh Convergence

A mesh convergence test was performed using the final FE model. The von Mises stresses of the final model did not exhibit the same discontinuities as seen in the preliminary model. To choose a parameter for mesh convergence, it was noted that the torsional load was expected to result in an area of infinitely increasing von Mises stresses around the contact surfaces. As the element size decreases, the local von Mises stresses would tend to infinity given the same load. Instead, maximum surface shear stress on the archwire was a viable parameter for convergence. This was contingent on the maximum shear stresses occurring where they were expected to on the archwire: at the midpoint of the 0.025” side of the archwire. To confirm this, a subsection of the archwire 2.5 mm in length was selected, where it contained all the nodes within the subsection volume. The segment was placed such that it was sufficiently far from both boundaries of the contact surfaces and the rotated face at the end of the archwire. The maximum shear stresses were plotted. The subsection of the archwire and the resultant shear stresses in the subsection volume are shown in Figure 3.22. It was found that the maximum shear stresses of the whole volume were internal in the body, but probing surface shear stresses, it was confirmed that the maximum stresses were at the midpoint. It was also seen that the shear stress profiles were consistent when probing any arbitrary cross-section, which matched the theory.

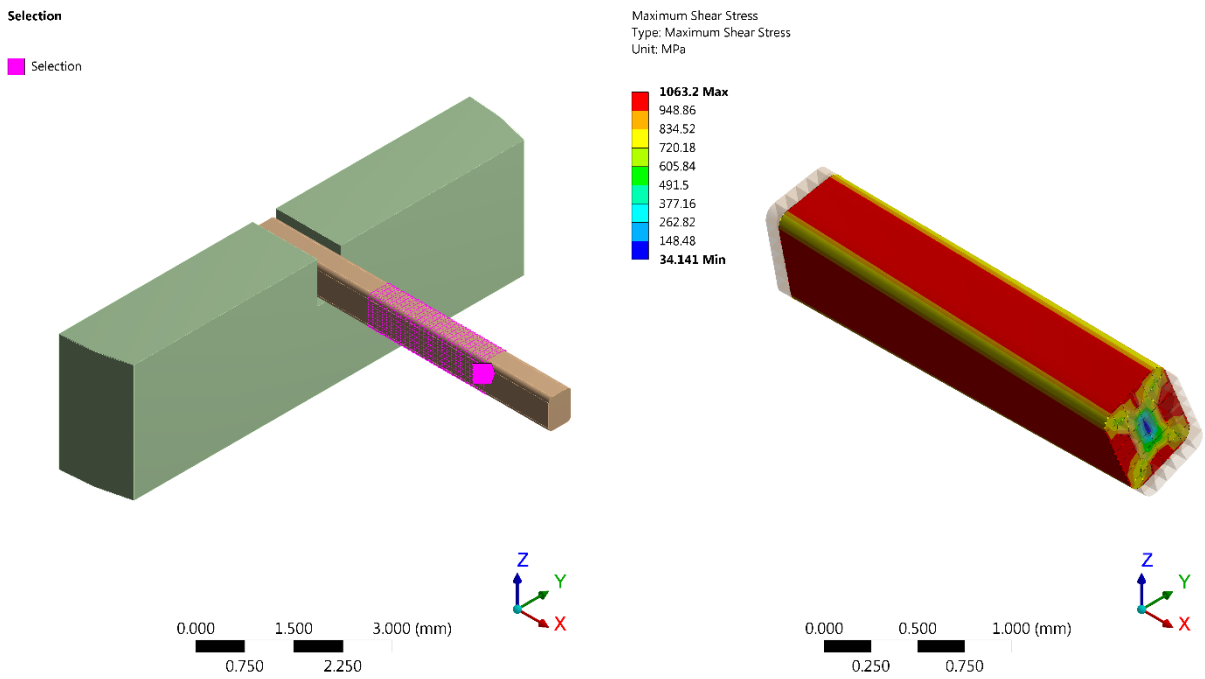

Figure 3.22. Subsection of 0.019”x0.025 archwire used in the determination of shear stresses in MPa during torsion with (a) the nodes selected highlighted and (b) the shear stress distribution.

The shear stress along the midpoint was then probed by using a 2.5 mm line that extended along the midpoint in the x-direction in the same location as the archwire subsection. The line and shear stresses along the line are shown in Figure 3.23. The maximum shear stresses along the line ranged from 987.11 to 987.74 MPa, which is a 0.063% difference. For all intents and purposes, the shear stress along the line was considered constant, and the absolute maximum value would be used in the mesh convergence test.

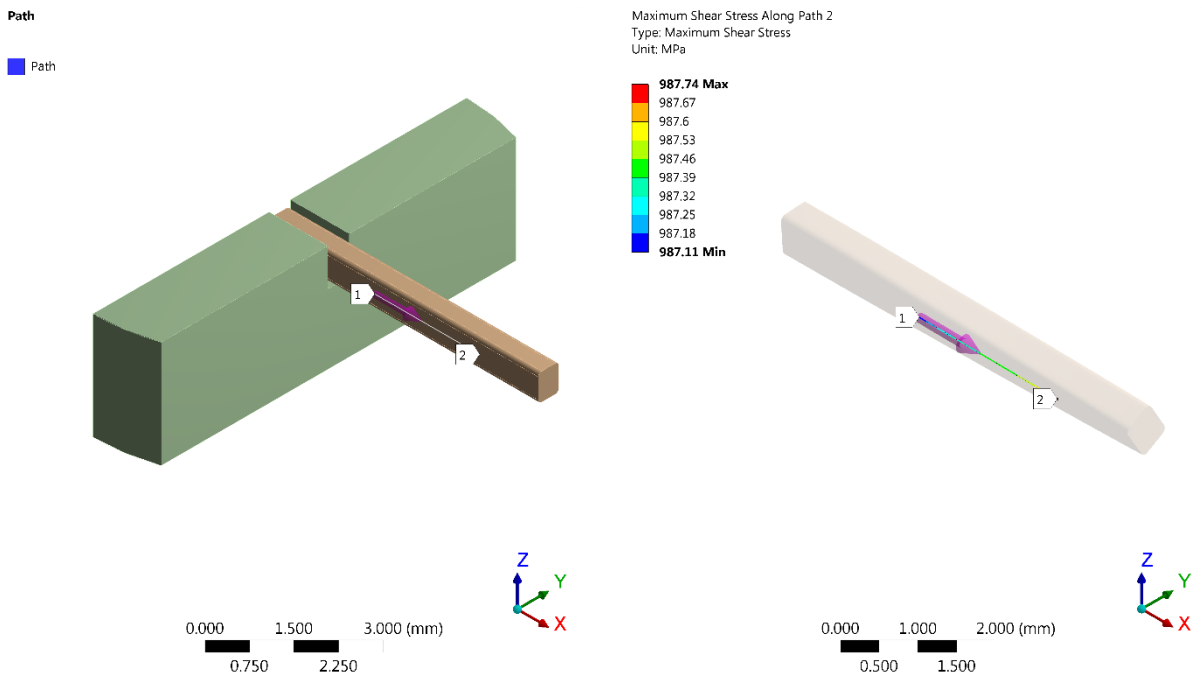

Figure 3.23. Line selection along the midpoint of the 0.025" length of the archwire during torsion with (a) the selection highlighted and (b) the shear stresses in MPa along the line.

The mesh refinement consisted of changing the element size on the archwire, and also using contact refinements for the contact surfaces in the RD slot. For every increase in mesh refinement, the size of the archwire elements both near and far from the contact were kept in close relation to each other to ensure there were no sudden changes in body stiffness. In other words, the element size of the archwire was kept consistent throughout its body, and the elements in the RD slot were refined to match. Element sizes were decreased from 0.10 mm to 0.075 mm and finally to 0.06 mm. The maximum shear stress compared to the total number of nodes in the model can be seen in Figure 3.24, and the actual values and percent changes between iterations can be seen in Table 3.5. From the mesh convergence test, there was confidence that the solution to the model was properly converged.

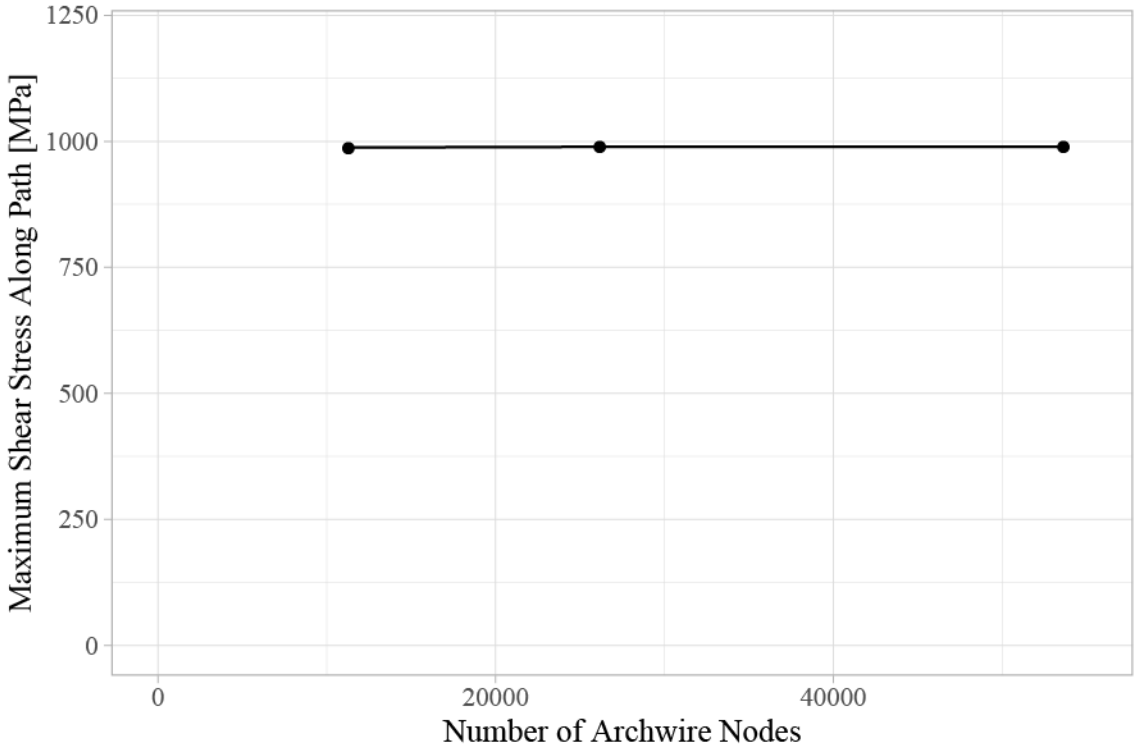

Figure 3.24. Mesh convergence of finite element model comparing maximum shear stresses in MPa with the number of nodes on the 0.019"x0.025" archwire.

Table 3.5. Maximum shear stress along probed line with percent changes between rigid dowel mesh refinements

Archwire Nodes	Maximum Shear Stress [MPa]	Percent Change in Shear Stress [%]
11263	987.74	N/A
26194	989.12	-0.140
53654	989.43	-0.031

3.3.3.2 Surface Deformations and Strains

All following results from the FE model will utilise the model with the finest archwire mesh with 0.06 mm elements. The main parameters of interest are the deformations and strains on the top surface of the archwire. These results can directly verify the archwire DIC measurements from Section 3.3.3. Similar to the DIC measurements, the results shown are also at 30° archwire rotation and include the top surface as well as the two rounded corners of the archwire. First, deformations in x-, y-, and z-directions are compared. The results are shown in Figure 3.25 and are shown from

a top-down view with the archwire in a non-deformed state to match the configuration of the DIC images. In Figure 3.32, the colour maps are adjusted to match the DIC outputs for better comparability, but it is noted the DIC surfaces and FE surfaces do not project on top of each other. While the DIC images have the RD centred, the leftmost side of the FE archwire is at the very centre of the RD and the rightmost side is at the clamp tip (not imaged with the DIC measurements). With projection differences accounted for, it is seen that x- and y-displacements match, as x-displacements are near-zero throughout the entire surface and y-displacements are all negative and become more negative going from the RD towards the clamp tips.

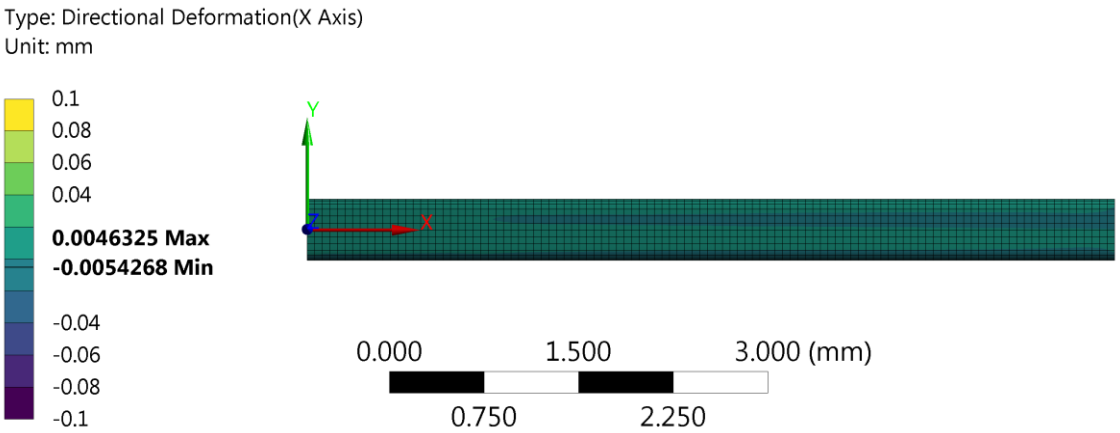

(a)

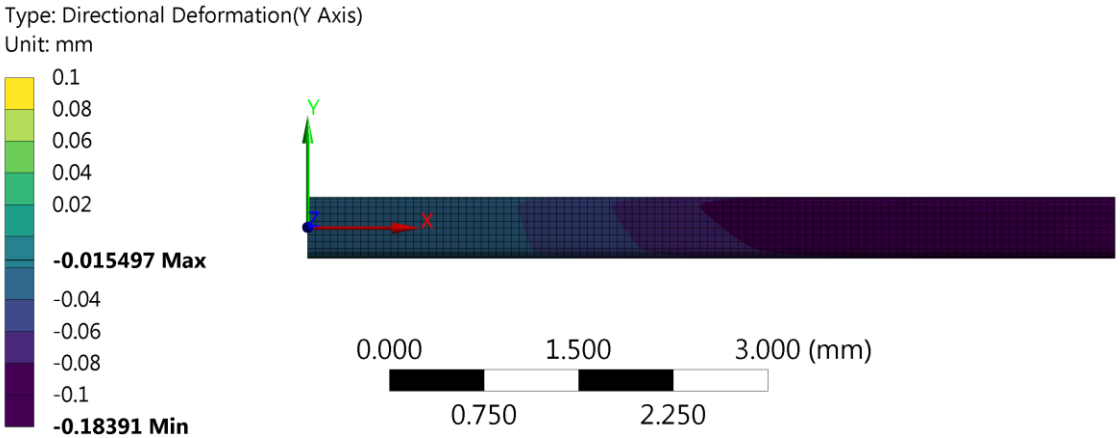

(b)

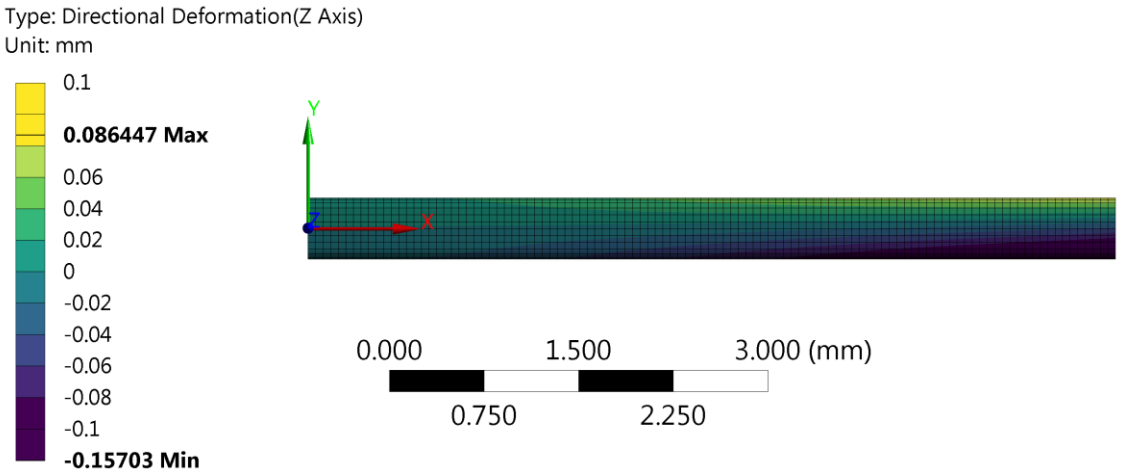

(c)

Figure 3.25. Finite element output showing surface deformations in millimetres of the archwire in the (a) x-, (b) y-, and (c) z-directions at 30° archwire rotation.

Surface strains from the FE model are similarly compared to the DIC measurements and are shown in Figure 3.26. For both the principal strains in the x- and y-directions, the colourmaps are set to match the x-direction in Figure 3.18, while the colourmap for the surface shear strain is set to match that of Figure 3.19. Principal strains are confirmed to be near-zero, with maximum and minimum strains being near boundary conditions and the rest of the surface area being bounded by these values. Further, the y-direction principal strains on the rounded corners are shown to be near-zero as well, confirming that the strains on the corners imaged using DIC were influenced by the speckle/corner geometry interaction with the camera perspective.

Type: Normal Elastic Strain(X Axis)
Unit: mm/mm

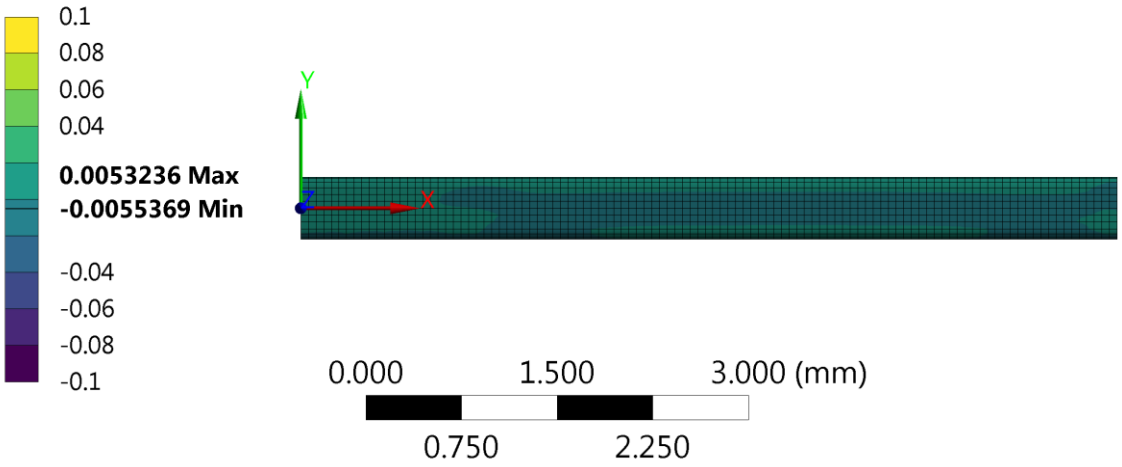

(a)

Type: Normal Elastic Strain(Y Axis)
Unit: mm/mm

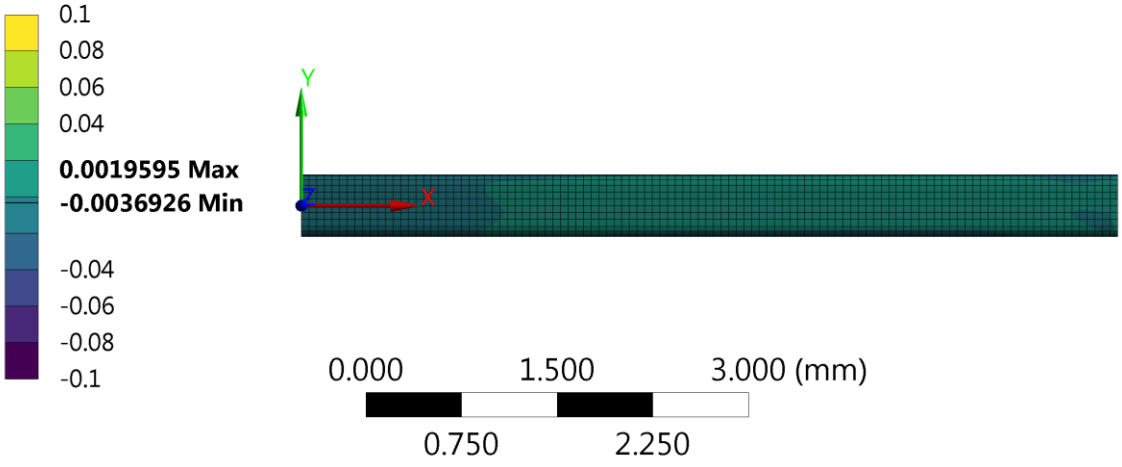

(b)

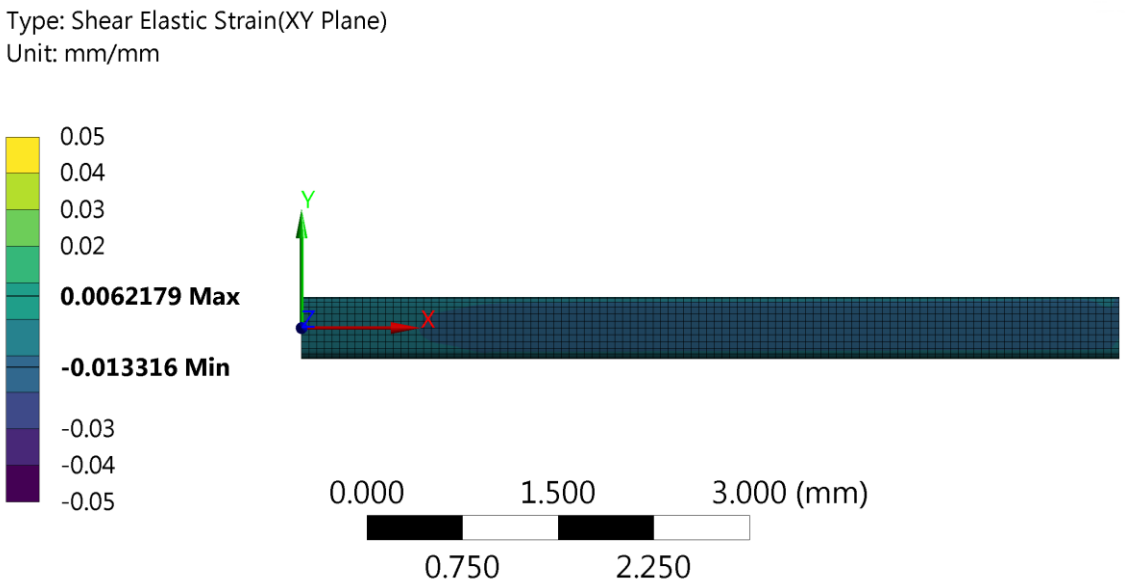

(c)

Figure 3.26. Finite element output showing surface strains of the archwire with principal strains in the (a) x- and (b) y-directions, and (c) shear strain on the xy-plane at 30° archwire rotation.

Using the shear strains measured from the vector map regions in Figure 3.21, a similar probing method was utilised for the FE model for a direct comparison. The top surface nodes of the model were probed to fit an area of the same as the vector map and is shown in Figure 3.27. The length of the probed area was kept at 1 mm and was placed in a similar location on the archwire as shown in Figure 3.20. The average shear strain among the nodes were plotted against the shear strains measured on the right side of the archwire and is shown in Figure 3.28.

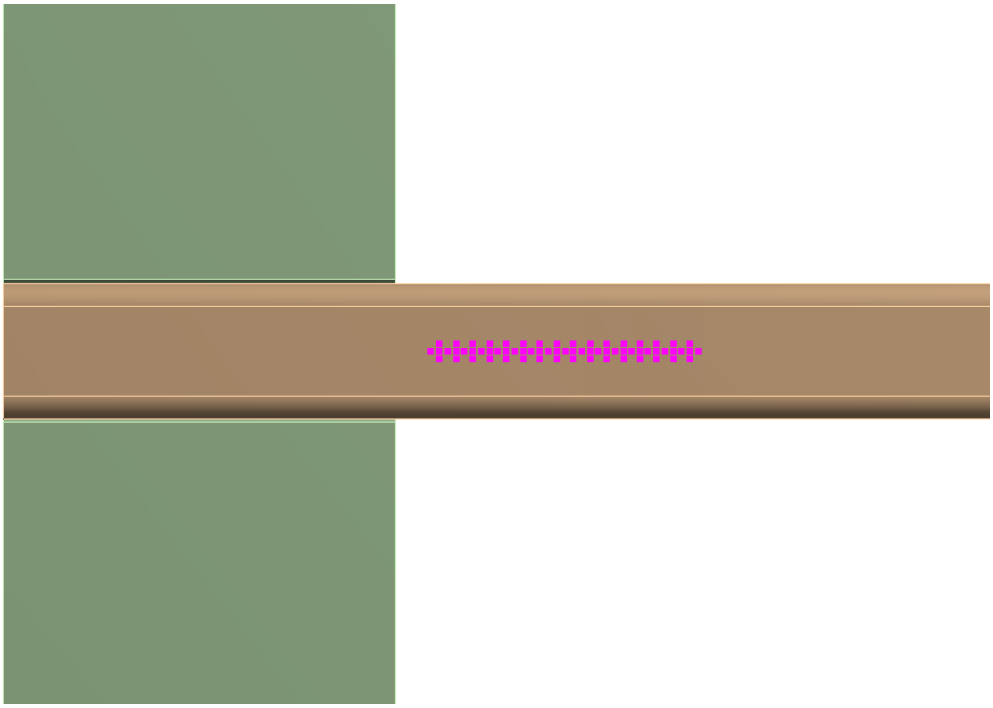

Figure 3.27. Finite element surface probe for average shear strain measurement.

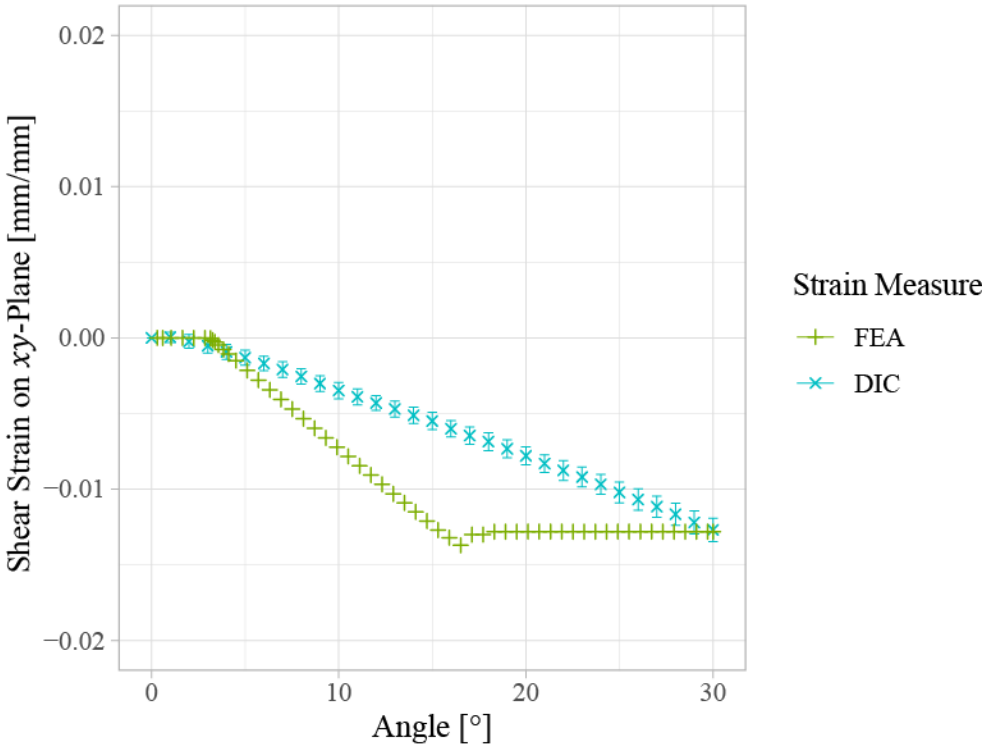

Figure 3.28. Surface shear strains in probed region on the right side of the archwire as measured by the finite element model and digital image correlation.

The difference in shear strain as measured by DIC differed from that as simulated with the FE model. This warranted an investigation into which model parameters in the FE model attributed to the steeper slope. It was found that the geometry of the RD slot could affect the contact development between the archwire and the RD slot as the archwire rotates. When using parallel slot walls, the archwire rotation caused the archwire to go from a state of no contact to an immediate full line contact along the entire slot wall. The physical RD had a slot width that was narrower at the centre and widened further away from the slot. This geometric deviation from parallel walls changes the contact with the archwire, as the contact is first made at the narrower centre and propagates outwards along the slot as more rotation is applied.

The solid model of the RD was modified to change the RD slot geometry. Using an image of the RD as captured during experimentation, geometric features of the RD were digitally edited to produce a clear outline of the slot curvature. A centreline was drawn, and the image was then superimposed within the solid model to remodel the slot geometry. Simplifications in the FE model were applied as only the top surface of the RD was imaged; all internal slot geometry would have to be assumed. The internal slot was modelled to have the same curvature as the top, essentially creating a slot with consistent curvature from the top to the bottom of the slot. The process of remodelling the RD is shown in Figure 3.29, and a comparison between the two versions of the RD slot walls is shown in

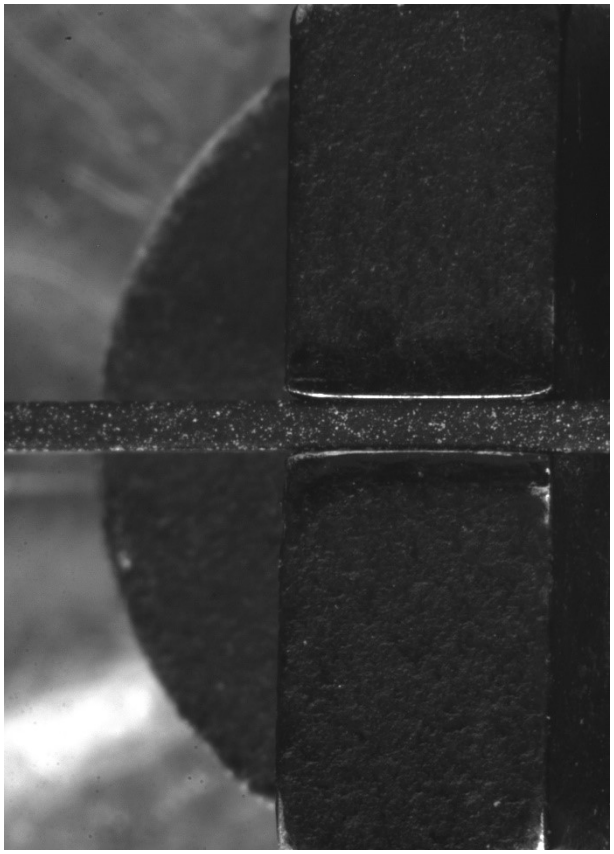

(a)

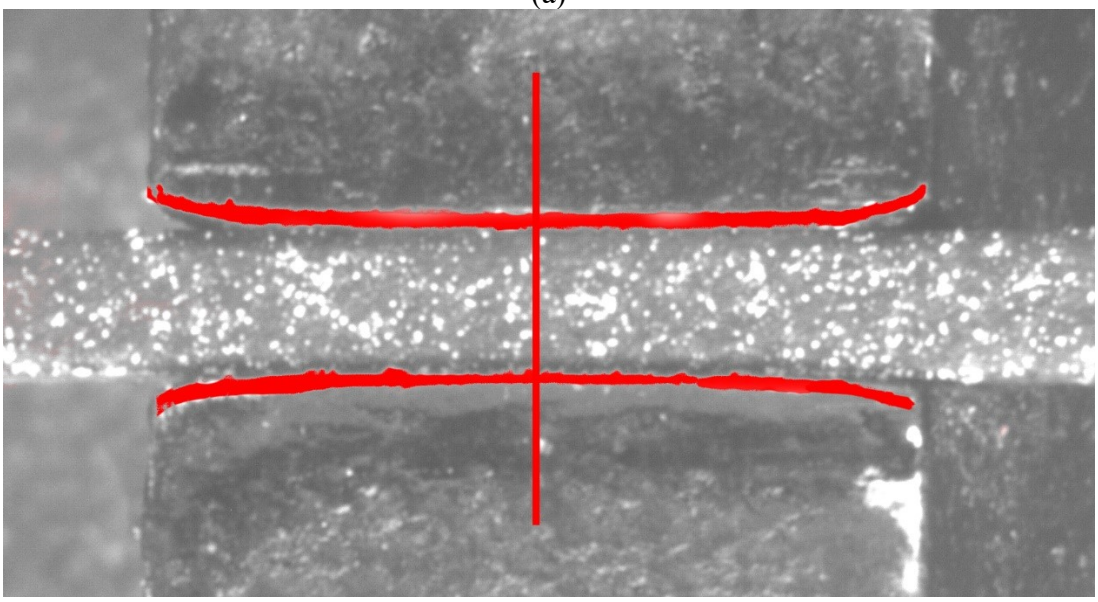

(b)

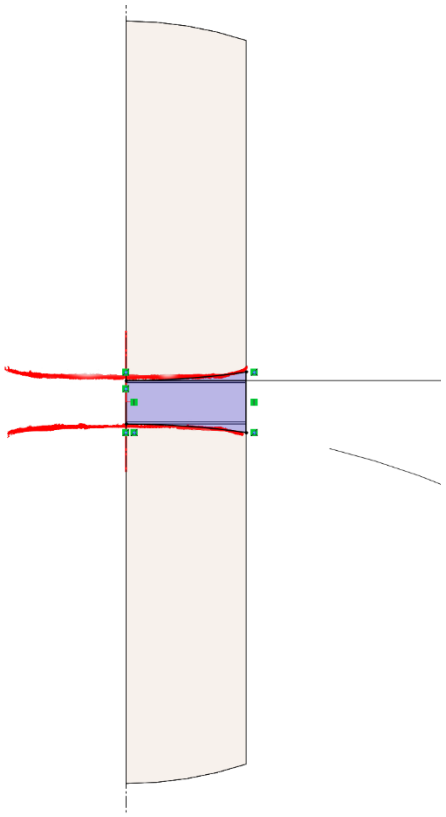

(c)

Figure 3.29. Rigid dowel slot geometry remodelling process using (a) a reference image, (b) editing the image to get slot edge contours and (c) superimposing the edge contours into the solid model.

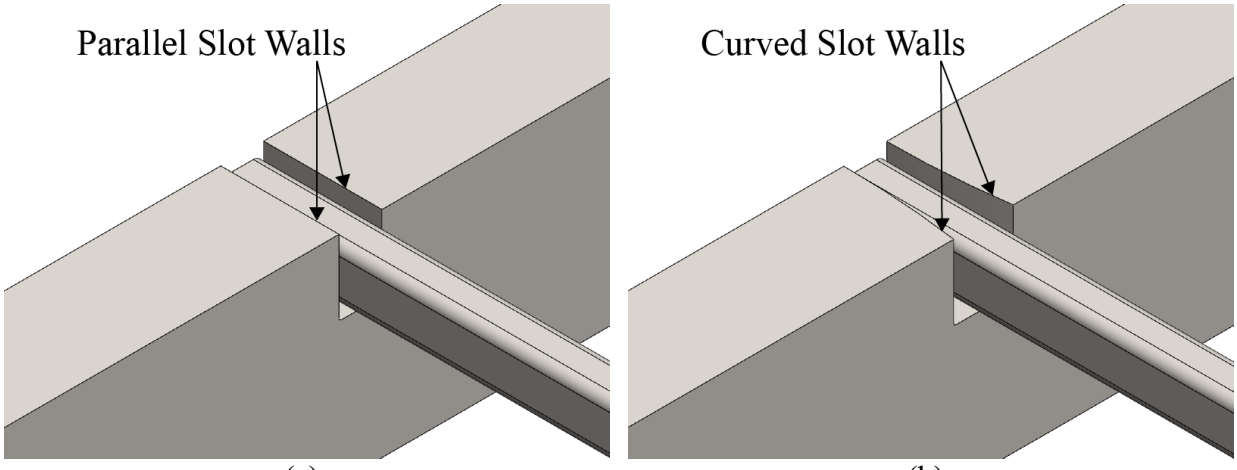

(a) (b)

Figure 3.30. Isometric comparison between (a) parallel and (b) curved rigid dowel slot wall models.

The FE model was simulated again and the shear strain development on the archwire surface demonstrated a slower rate of increase, shown in Figure 3.31. The outcome of the additional test showed evidence that the slot geometry had a demonstrable effect on the slope of the shear strain of the archwire and presents a possible explanation regarding the differences between the DIC and FE results.

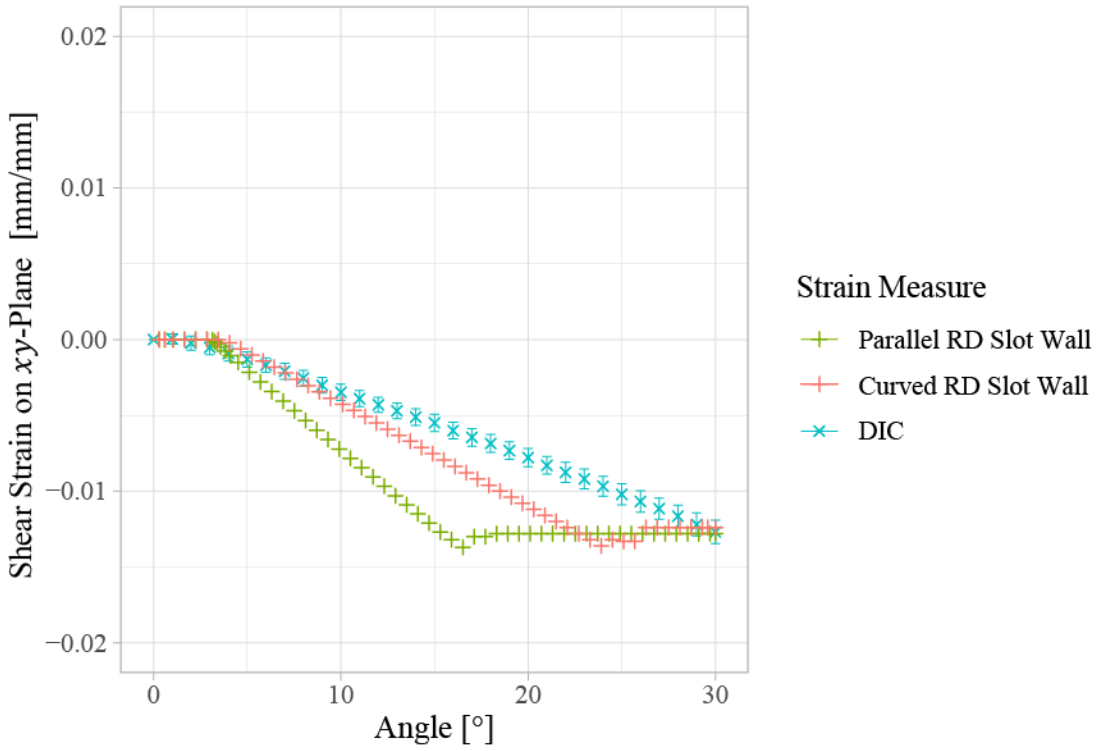

Figure 3.31. Surface shear strains in probed region on the right side of the archwire as measured by the finite element models with parallel and curved rigid dowel slot walls compared to digital image correlation measurements.

3.4 Discussion

The addition of a 3D DIC system to the OTS with capabilities of measuring archwire deformations and strains during third-order torque experiments provides an entirely novel dataset with respect

to third-order torque mechanics. In previous studies performed with the OTS, third-order torque was measured as the resultant torque from the interaction of an archwire inside an orthodontic bracket [40], [41]. Orthodontic brackets introduce additional factors to third-order torque mechanics such as bracket compliance and different contact areas between brackets and archwires. Additional experiments measured bracket deformations during third-order torque using imaging techniques [47], [93]. However, by removing the effects of bracket deformations as seen with using the RD, the study of archwire deformation during third-order torque can be used to elucidate archwire contributions to resultant torque in an idealised scenario. Further explorations of archwire strains, particularly in residual strains after unloading may be used to analyse whether an archwire reached its yield stress and underwent plastic deformation or if it remained in an elastic deformation regime. Understanding the development of strain along an archwire under torsion in tandem with third-order torque curves can lead to better appreciations of how varying components associated with third-order torque (such as archwire material and size, or bracket types) can lead to different clinical third-order torque applications. While the use of the RD significantly changes the third-order torque response, particularly in the reduction of torsional play and the increased maximum torque, measurements of surface strains on the archwire can be used to further expand clinical options when forming archwires to generate third-order torque.

With respect to the bilateral torsion applied using with the OTS, the rotation mechanism is highly isolated. With clamps on either end of the IBD, the boundary conditions are simplified to a pure torsion of the archwire. Studying archwire mechanics in this configuration closely resembles torsion of a prismatic bar aside from the contact made between the archwire and bracket. In reality, this is not the case. Similar studies have been performed measuring torsion as applied in a bilateral

manner, but instead of clamps holding the archwire additional orthodontic brackets were used [94]. This introduces more complexities in third-order torque mechanics, and the archwire may exhibit different behaviours depending on the setup. The inclusion of adjacent brackets changes the boundary conditions present on the archwire compared to clamps when analysing third-order torque as a response due to bracket deformations, as well as manufacturing tolerances that can introduce additional variability between trials. This is one example of why having the ability to measure surface deformations, allowing for determination of strains, of an archwire under torsion may lead to more comprehensive understandings of how archwire behaviour changes in various third-order torque loading scenarios. The effects of different boundary conditions on an archwire can be compared for valuable insight on archwire torsion mechanics. The full-field imaging of surface responses to applied loads allows for the isolation of archwire and bracket effects with respect to third-order torque.

3.4.1 Comparisons Between DIC Measurements and the FE Model Results

The FE model was used to verify the that the measurements obtained from DIC were sensical and indicative of the physical behaviour of the archwire during third-order torque. There were assumptions made with the FE model to simplify the boundary conditions that results in minor deviations from the physical operation of the OTS.

With respect to z-displacements, there is a notable difference whereby the FE model indicates positive and negative surface movements, whereas the DIC indicated the surface of the archwire almost entirely moved in the positive z-direction. The archwire in the FE model perfectly rotates about its central axis, which ensure that portions of the top surface will rotate upwards and other

portions will rotate downwards. Third-order torque applied using the OTS is assumed to follow the same behaviour; however, there may by mechanical deviations and the archwire may not rotate perfectly about its central axis in practise. Factors such as clamp geometry and tolerances, archwire and rigid dowel manufacturing tolerances, and OTS assembly tolerances may all contribute to the archwire having a different centre of rotation. However, the bulk movement of the archwire is still a bilateral rotation, and as the archwire contacts the RD, a third-order torsional response is still exhibited. This is confirmed as the z-displacements measured using DIC still indicate that the archwire undergoes bilateral twisting.

There were similarities and differences in shear strain measurements between DIC outputs and the FE model. In particular, the directionality and magnitude of the shear strains measured agreed, whereas the slope of the strains measured in Figure 3.31 differed. The differences may be attributed to the assumptions applied to the model as well as assumptions associated with using the OTS. The stainless steel properties in the FE model, particularly that of the archwire, was assumed based on high-strength 300-series steel. While representative of stainless steels used for archwires, it may not be a direct match to manufacturer specifications of the archwires used during DIC.

The FE model results indicated that the surface of the archwire had two separate behaviours with regards to shear strain, where shear strain initially increased with the rotation angle then plateaued (Figure 3.31). This behaviour indicated that the archwire possibly reached its proportional limit with respect to torsion over the region probed in the FE analysis, which would then lead to strains developing in other regions of the archwire away from the region probed here. The archwire material used in the FE model utilised a bilinear stress-strain curve with near-perfectly plastic behaviour after the yield point (i.e. minimal strain hardening occurs once the material yields). This

assumption may change the behaviour of the archwire once it reached its proportionality limit and thus cause the plateau regions in the strain curves seen in Figure 3.31. It may be deemed that further exploration of the FE model with refined parameters can be used to obtain better agreement with DIC measurements, but this necessitates the use of a stress-strain curve that better matches manufacturer specifications of the archwire to remove the assumption of a bilinear stress-strain curve.

In comparing the two FE models with varying RD slot geometry, it was seen that the RD slot geometry had an effect on shear strain. The slope of the strain was found to be lower when the RD slot had curvature, and this was a possible explanation for the differences in slopes between the DIC measurements and the FE analyses results. The inclusion of the curved RD slot walls changed the onset of twist in the archwire compared to parallel slot walls. When using parallel slot walls, the archwire was more constrained, with the onset of twist occurring sooner and over a larger region of the archwire. Conversely, the curved slot walls changed the contact behaviour between the archwire and the RD, where the contact initiated from the centre of the RD slot and propagated outwards to the edge of the slot as the rotation was applied. As a result, at lower angles of twist, less of the archwire was constrained leading to a decrease in developed strain (i.e. for a given rotation of the archwire, having less material constrained at the boundary resulted in lower strain values developed in the archwire). Though the inclusion of RD slot wall curvature led to closer agreement with between the FE results and the DIC measurements, there was still a discrepancy. With the knowledge that the slot wall geometry influenced strain development, it is important to note that while the curvature modelled was based on physical imaging of the RD, it was assumed that the same curvature propagated through the entire slot depth (i.e. the slot walls had the same

curvature with no variation along the z-direction). The curve was modelled to represent the actual curvature of the RD slot as seen from the top; however, there may be additional deviations from the curvature within the slot wall that could further affect shear strain development.

Lastly, the boundary conditions in the FE model were applied to represent ideal conditions when using the OTS; however, real-world deviations may also occur. Overall, the confirmation that the measured displacements and strains from DIC match the FE outputs in magnitude and directionality gives confidence that using the DIC system is functional and verified and the FE model is representative of the third-order torque mechanics as applied with the OTS. Further, the DIC and FE parameters both followed torsional theory of prismatic bars independently of one another. This further strengthens and justifies the use of DIC to obtain surface measurements during third-order torque application.

3.4.2 Further Uses of DIC with Orthodontics

The implementation of 3D DIC with orthodontics can lead to future explorations to characterise archwire and bracket behaviour under various conditions and loading scenarios with full-field measurements of surface responses. Previous tests utilising DIC with the OTS focused on tie-wing separation and archwire retentive component movement throughout third-order torque loading [18], [43], [45], [46]. Having the capability to image both the archwire and the bracket can lead to a more comprehensive understanding between the interactions of an archwire and bracket as more torque is generated. This can be useful as it may lead to the ability to directly capture the material responses and interactions, thereby filling the gaps in current understandings and knowledge with respect to third-order torque. Further, it may be feasible to incorporate various factors that have

not been tested before. For example, temperature effects on rectangular nickel titanium archwires were previously researched, but only measured resultant torque [61], [63]. However, the inclusion of 3D DIC to measure nickel titanium archwire responses in various temperatures may reveal if archwires strains develop due to thermal expansion of an archwire compared to applied torsions.

There are many other factors associated with third-order torque that may benefit from archwire deformation and strain data, such as the aforementioned multiple bracket systems, temperature effects on various archwire materials, and initial archwire geometries such as straight lengths compared to lengths with loops or bent to fit dentitions. With all inquiries, the use of 3D DIC can provide additional information on different variables when applying third-order torque and their effects on orthodontic treatment that were not readily apparent without archwire deformation and strain data. The power of 3D DIC when measuring archwire mechanics is evident and can be utilised beyond the scope of third-order torque. The study of in-vitro third-order torque mechanics using 3D DIC explores only one type of tooth movement during orthodontic treatment; however, the technology can potentially be further expanded to investigate other aspects of orthodontics. The rigorous verification of the current 3D DIC setup with the OTS enables confidence in the data produced. Further testing of additional in vitro orthodontic experiments should mandate similar verifications if explored. Archwire mechanics of other orthodontic movements can all be studied in depth with deformation and strain data available for analysis. The setup of a 3D DIC system to measure archwire behaviour under torsion is an initial step that can lead to the comprehensive expansion of the knowledge base of archwire mechanics during orthodontic treatment.

3.5 Conclusions

The initialisation of a 3D DIC setup to measure surface deformations and strains of rectangular archwires under third-order torsion was explored. A speckling technique was developed to match the scale of orthodontic materials and DIC images were collected during third-order torque experiments. A verification of the system was performed by creating and FE model to simulate the same torsional loading conditions as the OTS. Both results from DIC and the FE model were verified using theory and solutions for prismatic bars in torsion and were found to behave consistent to the theory when considering differences in loading conditions. In addition, the FE model provided verification for the DIC system by revealing the magnitudes of surface deformations and strains. With the DIC measurements in agreement with the FE outputs, it was recommended that additional experimentation can move forward with an application-based study.

CHAPTER 4 ASSESSMENT OF MECHANICAL RESPONSES OF ORTHODONTIC APPLIANCES TO TORSIONAL LOADING USING THREE-DIMENSIONAL DIGITAL IMAGE CORRELATION

4.1 Introduction

The experimental protocol of using three-dimensional (3D) digital image correlation (DIC) to measure surface deformations and strains of an archwire surface during third-order torque has been established, as discussed in Chapter 3. Testing third-order torque with the rigid dowel (RD) provided a way to verify the 3D DIC measurement system as well as to study the archwire response to torsion where the archwire undergoes twisting over the inter-bracket distance (IBD). The lack of torsional play and consequent mechanical response of the archwire with the RD was not representative of clinically relevant situations. In past studies of third-order torque using the Orthodontic Torque Simulator (OTS), it was seen that orthodontic brackets may be subject to plastic deformation after applied third-order torque through an archwire [18], [43], [45]–[47]. The permanent bracket deformations indicate that clinical edgewise applications of third-order torque may have lower efficacies than expected due to mechanical losses in the system. The quantification of the mechanical interactions between an archwire and bracket during third-order torque can lead to better understandings of edgewise treatment, particularly with respect to material responses to applied loads. Using 3D DIC with intents of measuring the archwire strain can produce more information on the archwire and bracket interaction during third-order torque. The desire to use

the 3D DIC system for more clinically applicable studies included third-order torque using archwires of different materials as well as using clinically representative orthodontic brackets. An attempt to simultaneously measure archwire and bracket deformations and strains was also made. By directly measuring the surface response of orthodontic materials during third-order torque, a more complete understanding of how different factors associated with archwire properties and bracket behaviour can be revealed by analysing the full-field 3D DIC outputs.

4.2 Experimental Methods

To further investigate archwire surface deformations and strains using 3D DIC, a two-by-two factorial design was created to include new factors: archwire material and bracket type, both with two groups each. Stainless steel (SS) and titanium molybdenum alloy (TMA) archwires (G&H Orthodontics, Indiana, USA) were compared, and self-ligating Damon Q brackets (Ormco Corporation, California, USA) were used to compare with the RD. Archwires of different materials produce different torque magnitudes. By choosing two contrasting materials, any correlation derived from material properties on third-order torque can be determined based on the surface response. The use of Damon Q brackets in comparison with the RD can reveal how the mechanical responses of archwires differ when third-order torque application is representative of a clinical setting with torsional play and bracket deformation versus an idealised contact regime using the RD with minimal torsional play and no bracket deformation.

The third-order torque experiment parameters were kept consistent to that of the procedure in Chapter 3, where archwires are rotated within the RD or bracket slot to a passive position, and 30° of total rotation was applied in 1° increments in the loading and unloading directions. In

performing the 3D DIC experiments, the camera system was setup in the same manner as Chapter 3, in which neither the intrinsic nor extrinsic parameters of the cameras were modified. By maintaining the same camera system setup as previously used, it was known that image correlation would be obtained along the archwire surface. With the physical system parameters remaining intact, improvements to overall image correlation could be considered with respect to sample preparation and image processing, which are detailed in following sections. To move forward with the study, the experimental design of the two-by-two factorial was considered given that the material factors and RD versus Damon Q brackets led to four distinct groups. Their effects could be determined by performing a pilot study. The purpose of the pilot two-by-two factorial was to determine the appropriate sample size necessary for the full study.

4.2.1 Pilot Study

Due to the large difference in archwire material properties and the resultant interaction with the RD versus orthodontic brackets, third-order torque responses were expected to differ, and a two-way analysis of variance (ANOVA) could be performed on the pilot study torque data to determine sample size. With third-order torque being the only parameter of interest for sample size calculation, DIC was omitted for the pilot study and was only utilised for the full study.

The pilot study consisted of five trials per group for a total of 20 trials, making it a balanced design. Instead of a full randomisation between all 20 trials, archwire material was randomised, while all testing with the rigid dowel was completed prior to testing with the Damon Q brackets. Statistical analysis including randomisation sequencing and ANOVA was conducted with R (R Core Team, 2017) [88]. Figure generation through R was completed using the R package “ggplot2” as a part

of the “tidyverse” package collection [89], [90]. All R code used throughout the chapter can be found in Appendix E. The statistical analysis and sample size calculation resulted in a two-by-two factorial design with 23 trials per group for a total of 92 trials. The analysis of the pilot study can be found in Appendix G.

4.2.2 DIC Experimental Setup and Adjustments

The full study was a repetition of the pilot study with the inclusion of 3D DIC with 23 trials per group. To ensure that data collected was independent, no third-order torque data from the pilot study was used for analysis in the full study.

In preparation for the full study, considerations about modifying the DIC system parameters were made to enable additional DIC data collection as compared to Chapter 3. First, a desire to also capture the deformations of the Damon Q brackets necessitated that the brackets be prepared with the same speckling procedure as the archwires using silver-coated silver microspheres. Second, since the field of view of the cameras did not fully capture the IBD of the archwire in the previous trials, the field of view was shifted such that the RD and brackets would be situated as rightward as possible in the field of view, which increased the length of archwire visible in the left IBD. An example of the increased surface area of the left IBD prior to and after shifting the dowel placement with respect to the camera field of view is shown in Figure 4.1.

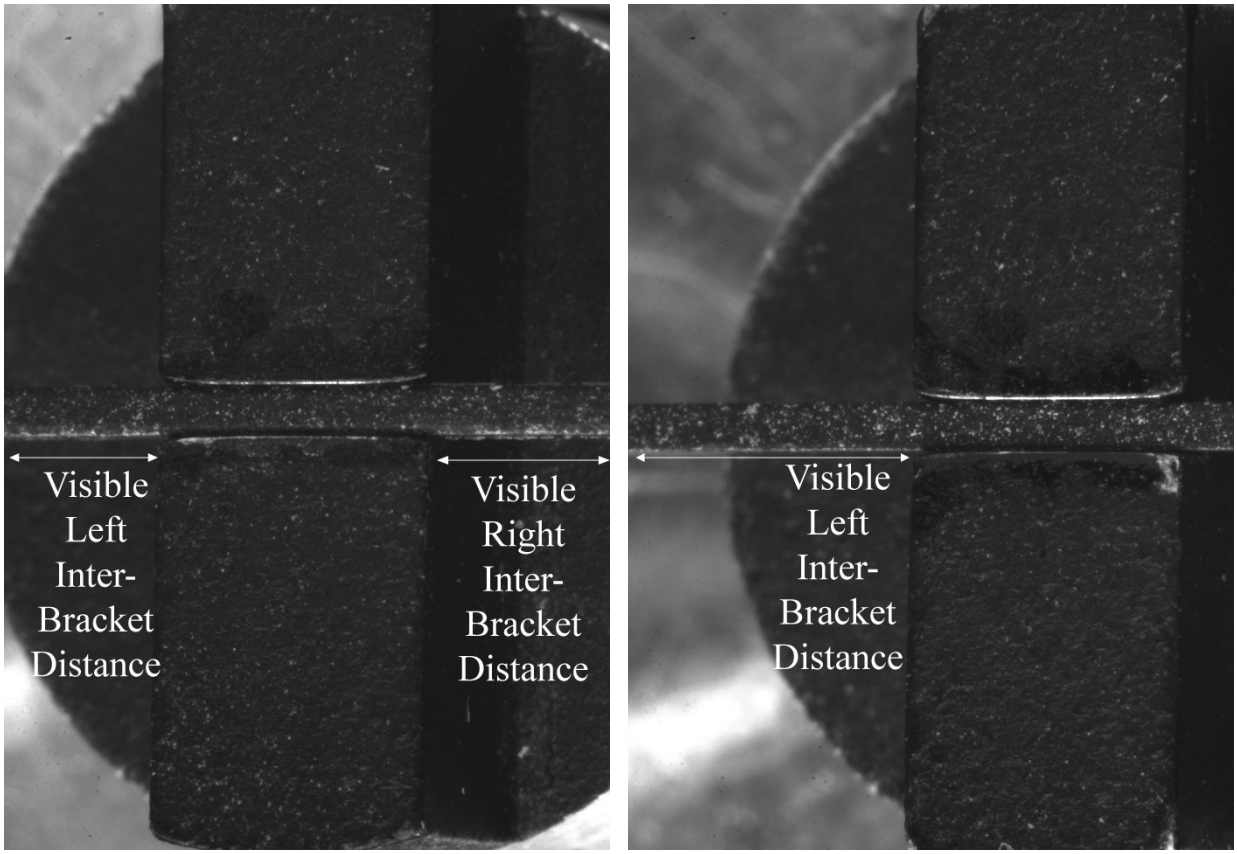

(a) (b)

Figure 4.1. Rigid dowel positions shown (a) centred and (b) shifted towards the right side of the field of view and the resultant increase in imaged surface area of the archwire in the left inter-bracket distance.

The consequence was the entire right side of the archwire was no longer visible; however, the assumption of the bilateral torsion being equal on both ends justified this change. In effect, a larger region of the archwire could be captured. The deformations and strains were assumed to be similar in magnitude (but not necessarily in direction as seen with surface shear strain) on the non-imaged right IBD. Lastly, changes to image processing settings were considered to optimise the data analysis. In particular, image correlation settings were explored to increase overlap between subsets as a means to gain more data along the flat surface of the archwire, as well as experimentally determining the optimal surface area for shear strain calculation.

4.2.2.1 Sample Preparation

For tests performed with the RD, only the archwires had to be speckled, which matched the procedure in Chapter 3. However, since the Damon Q brackets had to also be speckled, the speckling procedure was modified for these trials. Prior to speckling, individual Damon Q brackets were attached to stainless steel dowels using a two-part epoxy (LOCTITE EA E-60HP, Henkel Corporation, Connecticut, USA).

The order of spray painting and speckling the Damon Q brackets were tested to determine the best technique and order of operations. First, brackets were spray painted and speckled with the door closed with and without an archwire ligated. It was found that without an archwire, spray paint would be present inside the bracket slot, which was unacceptable as spray paint inside the slot would alter contact mechanics between the archwire and bracket in subsequent tests. A comparison of the bracket slot as spray painted with and without a ligated archwire is shown in Figure 4.2. Evidently, having an archwire occupy most of the bracket slot was effective in preventing spray paint from reaching the slot walls; however, using archwires prompted another consideration in the preparation of individual brackets. An archwire used during bracket speckling could be sacrificial and only serve to keep the bracket slots clean, or archwire segments could be spray painted and speckled simultaneously with the intention of performing DIC and third-order torque experimentation. The latter option was chosen to ensure the speckle quality and density achieved between the brackets and archwires would be relatively consistent, thus enabling similar image processing techniques on both components. However, this added a new complication of having to hold the archwire such that it would not slide inside the slot during spray painting and speckling. A viable solution was using elastic ligatures to hold the archwire in place and also act as a mask

to prevent spray paint from coating undesired surfaces. This method proved successful in ensuring that spray paint only coated external surfaces.

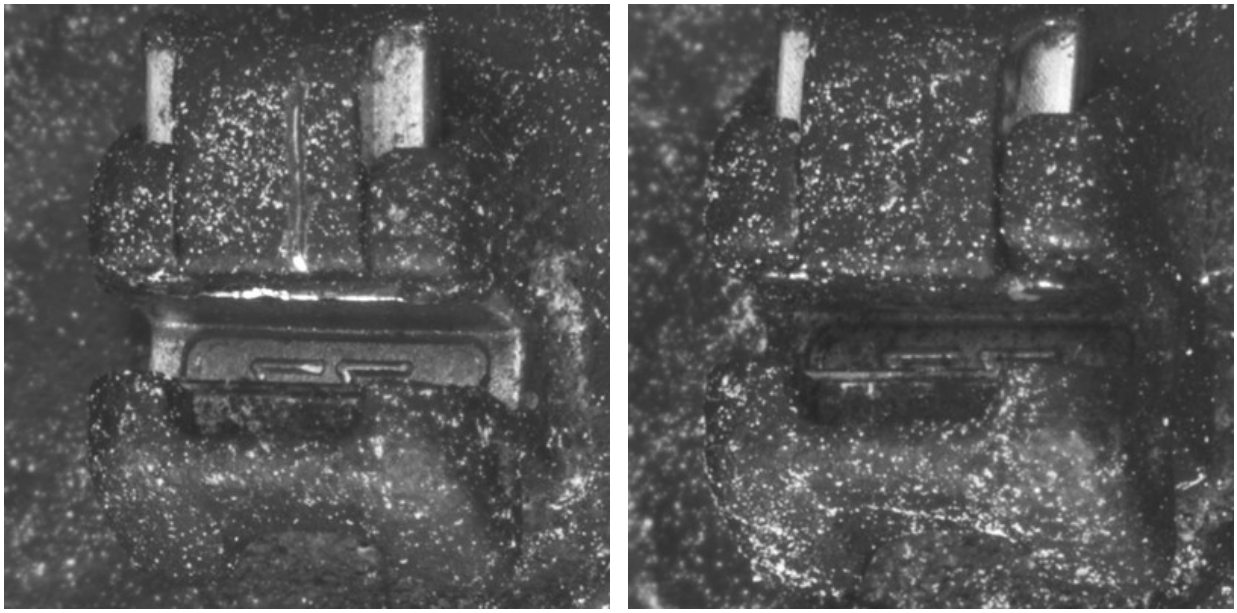

(a) (b)

Figure 4.2. Damon Q bracket slot after spray painting, (a) with an archwire inside the slot and (b) without and archwire in the slot during painting.

4.2.2.2 Shifting Region of Interest

In the previous chapter, the field of view of the images had the RD as centred as possible as a means to capture data on both sides of the twisted archwire. Shifting the field of view to contain more of the left IBD of the archwire simply involved adjusting the position of the OTS relative to the overhead cameras. Since capturing bracket deformations were also desired, the amount to shift the field of view was tested by checking the camera images to ensure that brackets were always fully visible in the field of view while being as close to the right border of the image as possible. A comparison between the field of views are shown in Figure 4.3, which includes the field of view with a Damon Q bracket. Between the RD images, it is evident that more archwire surface area is available for image correlation. When viewing the Damon Q image, the bright white spot is the

reflective unpainted archwire surface that was previously covered with the elastic ligature. When using the elastic ligatures, a larger length of the archwire is unpainted relative to the length required inside the bracket slot. Prior to clamping the archwire into position, the archwire is physically shifted towards the right to ensure that the region of archwire enclosed inside the bracket slot is unpainted, and that the extra length of unpainted archwire is only visible on the right IBD as to not affect image correlation quality on the left IBD.

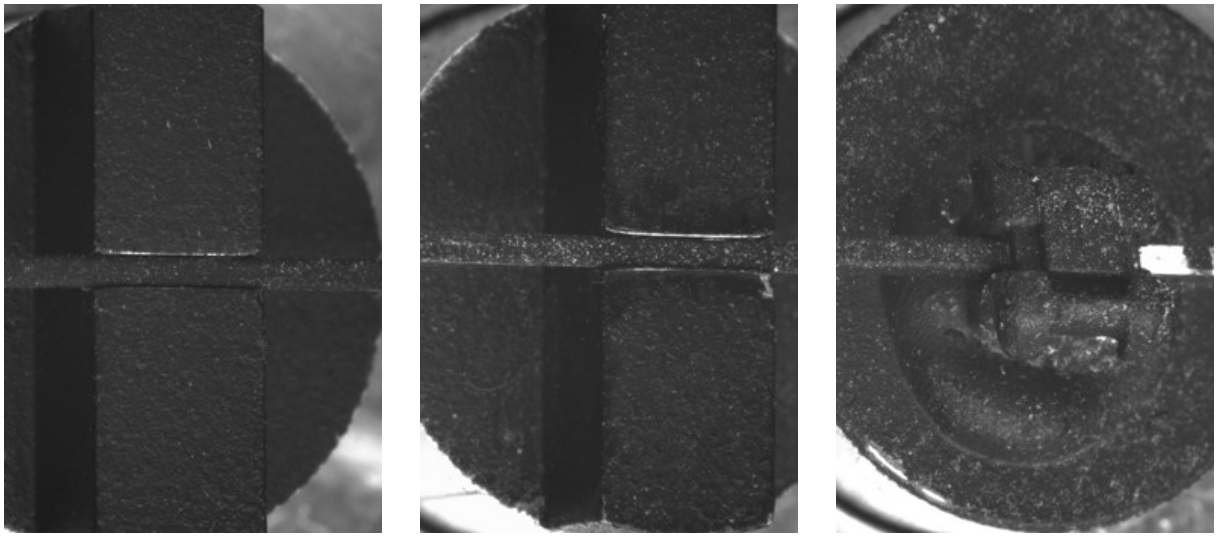

(a) (b) (c)

Figure 4.3. Field of views of 0.019”x0.025” archwire inside the rigid dowel with (a) the dowel centred versus (b) the dowel set towards the right, and (c) the archwire inside a Damon Q bracket.

Initial test images not a part of the full two-by-two factorial study were processed to ensure that image correlation was not negatively affected by the relatively high intensity reflection and confirm that this setup procedure was viable for achieving image correlation for both bracket and the left IBD of the archwire.

4.2.2.3 Increased Subset Overlap During Image Correlation

Beyond the physical adjustments made to the 3D DIC system, the image processing workflow using DaVis (DaVis 8.4, LaVision GmbH, Göttingen, Germany) was also adjusted. In Chapter 3, results were computed using subset sizes of 63 x 63 pixels with an overlap of 31 pixels between adjacent subsets, which led to relatively large distances between resultant vectors. The geometry of the archwires presented a relatively small surface area for vector computation. With rectangular archwires, the rounded corners were found to impact vector calculations and parameter outputs, particularly those that involved a y-component. By increasing the subset overlap between adjacent subsets, more vectors can be calculated without the influence of the archwire corners and instead be fully contained on the flat surface of the archwire. The imaged size of the archwire mandated that the subset size should be no smaller than 63 x 63 pixels to contain sufficient information to ensure subset uniqueness; however, the overlap could be readily changed to increase the vector density [17].

Using images taken during experimentation, the appropriate overlap values would be determined by comparing image correlation quality using different overlaps. It is noted that a consequence of increased overlap is increased vector computation, which in turns requires more processing power and time. Ultimately, these factors would be considered when doing final image processing. The overlaps used were 31 pixels, 15 pixels, and 8 pixels, which translate to approximately 50%, 75%, and 88% overlap, respectively. Comparisons between these subset overlaps can be determined before processing all the collected data. Further, overlapping subsets by greater amounts will increase the vector density with the trade-off of larger error in strain calculations. The error increases due to the distance between adjacent vectors decreasing when more overlap is present.

Since the position of each computed vector inherently has its own error, decreasing the distance between two vectors will increase the error of the computed distance, which directly affects the strain calculation [69]. The strain error varies as follows:

$$31 \text{ px overlap: } \frac{0.05 \text{ px} \times 2 \text{ vectors}}{31 \text{ px}} = 0.003 = 0.3\%$$

$$15 \text{ px overlap: } \frac{0.05 \text{ px} \times 2 \text{ vectors}}{15 \text{ px}} = 0.007 = 0.7\%$$

$$8 \text{ px overlap: } \frac{0.05 \text{ px} \times 2 \text{ vectors}}{8 \text{ px}} = 0.013 = 1.3\%$$

The change in strain error with increased overlap is not significant in comparison to the strain errors when there is less overlap. Therefore, given the geometry of the archwires, any of the subset overlaps can be justified, and will be selected based on the image correlation quality and consequent vector computation on the archwire surface.

4.2.2.4 Optimising Shear Strain Surface Area

In calculating the shear strain, the surface area can be manually adjusted. The vector field outputs from DIC were exported and analysed with MATLAB (MATLAB 2019a, The MathWorks, Inc., Massachusetts, USA) using a post-processing toolbox (PIVMat, 4.10, F. Moisy, Île-de-France, France) [91]. The MATLAB code for DIC plot generation can be found in Appendix F. Since surface shear strain involves using vectors with x- and y-components, the influence of the archwire corners can affect the resultant strain values when taking an average strain value over a rectangular surface area. As such, it is necessary to determine what the optimal area for strain averaging would

be, particularly in the y-dimension of the rectangle. The y-dimension can be as small as two vectors in length or include the entire 0.019" dimension of the archwire with corners included.

Determining an optimal area prioritised removing the influence of the vectors on the archwire corners in the strain averaging, but also sought to maximise surface strain values among the various areas that could be averaged for strain values. A single trial using an SS archwire with the RD was selected, and a range of rectangular areas on the left IBD were compared. First, a horizontal centreline was determined by placing a 2 mm line on the top surface of the archwire as centred as possible. Note that the centreline may have different positions across different trials as archwire and bracket positions relative to the field of view would have minute differences. The length of 2 mm was determined by going through all trials and ensuring the length of correlated archwire for every instance spanned at least 2 mm was with no discontinuities (i.e. missing vectors that were unable to be computed). This was found to hold true, but a maximum length of 2 mm also ensured that its placement would be adequately far away from the contact region between the archwire and the RD/Damon Q brackets, but also fit the archwire surface without surpassing the left boundary for all trials. The 2 mm line thus represented the length of the rectangles in the x-direction and was kept consistent for all rectangular areas. In the y-direction, the height started from 0.0 mm (effectively a line) and was increased incremental in both the positive and negative y-directions relative to the centreline. The increments were determined based on the subset overlap. Surface strains were measured for every increment, and the rectangle was increased in size until the number of vectors in the area did not increase between increments. In effect, this ensured that the largest rectangle included all surface strain vectors over a 2 mm span, which contained vectors on the top surface as well as all vectors from both corners. Plotting shear strain versus the number of vectors

was expected to reveal an optimal area could be determined and used for all shear strain outputs. An example schematic showing average shear strain as a function of archwire surface area is shown in Figure 4.4 (the plot uses artificial data for illustrative purposes only). From Saint Venant's solution to prismatic bars in torsion, the shear strain should remain constant as long as the surface area being averaged remains on the flat portion of the archwire [87]. When the rounded corners are included, the average shear strain would deviate from the established average due to different strain values being included in the average.

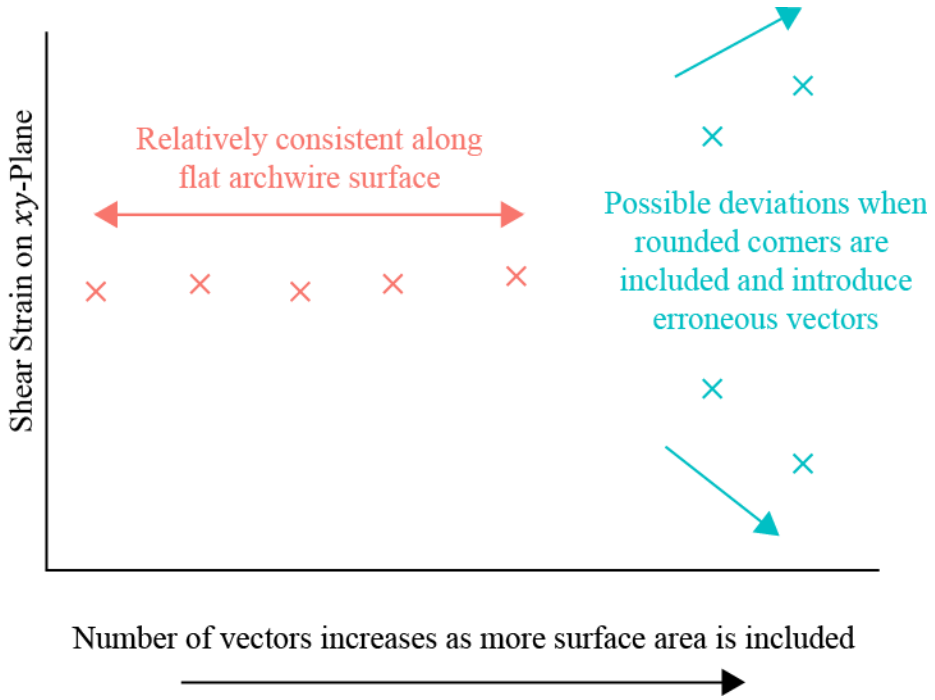

Figure 4.4. Possible behaviour of surface shear strain when averaging vectors on the flat archwire surface versus when vectors on the rounded corners are included. The points shown are artificially placed for illustrative purposes only.

Selecting a surface area to take shear strain averages should include a large vector count to better represent the flat portion of the archwire, and careful attention to only average vectors along the flat portion is necessary to properly measure the surface shear strain without introducing erroneous values.

4.2.3 Full Study

The full study was carried out in a similar fashion to the pilot study with the addition of 3D DIC. Archwire material order was randomised using R, in which trials with the RD were completed prior to the trials with Damon Q brackets. Due to the large number of trials, multiple camera calibrations were performed throughout testing to reduce the chances of random perturbations to the system that may affect image correlation.

A new calibration was performed at the start of each day of testing, as testing could not be completed in one consecutive testing period. Calibrations were also performed whenever there was a break in testing to ensure the cameras were stationary for all images taken within a calibration period. This effectively grouped sequences of trials into separate camera calibrations in a random manner. While the number of trials per calibration varied, it was paramount that extrinsic camera parameters remained constant within a sequence for each calibration. Slight changes in extrinsic parameters between calibrations would not pose a problem as each calibration was unique to the sequence of trials it contained. Overall, eight separate camera calibrations were performed throughout testing. The scale factors were averaged across the eight calibrations and was found as 464.457 ± 1.850 px/mm, and all extrinsic parameters of the cameras were found to be consistent with negligible differences.

For the intents and purposes of performing 3D DIC during third-order torque experiments, the camera positions and resultant camera calibrations were in close agreement based on the consistency of the scale factors. Given that multiple unique images of the calibration target were captured for every calibration, the resultant scale factors indicate that the calibration volume and

camera positions remained consistent. Captured images were matched with the appropriate calibration, ensuring that the DIC performed would produce outputs that were true to each individual test. Since captured images of individual trials correspond directly with a camera calibration, there was confidence that extrinsic camera parameters would not be a source of variance between trials. This is due to the DIC process mandating that an experimental image set must align with the camera calibration, as the projections from physical space to pixel space would be incorrect in the event that extrinsic camera parameters change between calibration and experimentation.

4.2.3.1 Statistical Methods

The two-by-two factorial design presents two factors at two distinct levels. The null hypotheses of this design are that the main effects from archwire materials (SS and TMA) and bracket types (RD and Damon Q brackets) will show no statistical differences on third-order torque. The third-order torque measured at maximum rotation, as measured at 30° loading, will be used to perform a two-way ANOVA to compare means for each group and test if there is a statistical difference between the levels in each group.

4.3 Results

The results of the study include the third-order torque measurements and the ANOVA of maximum third-order torque, the analysis of the optimisation of the 3D DIC image processing process with respect to imaging archwires and brackets with the OTS, and finally the analysis of the 3D DIC surface measurements of the archwires and brackets.

4.3.1 Third-Order Torque

The absolute values of third-order torque at 30° loading are individually shown in Figure 4.5, with archwire material separated between columns and bracket type separated by colour. The points are randomly dispersed horizontally using a jitter effect and each point represents an individual trial. Third-order torque values over the range of rotation were averaged and plotted in Figure 4.6. Each group had different torque curves for loading and unloading, which confirmed the differences between archwire materials and the RD versus Damon Q brackets.

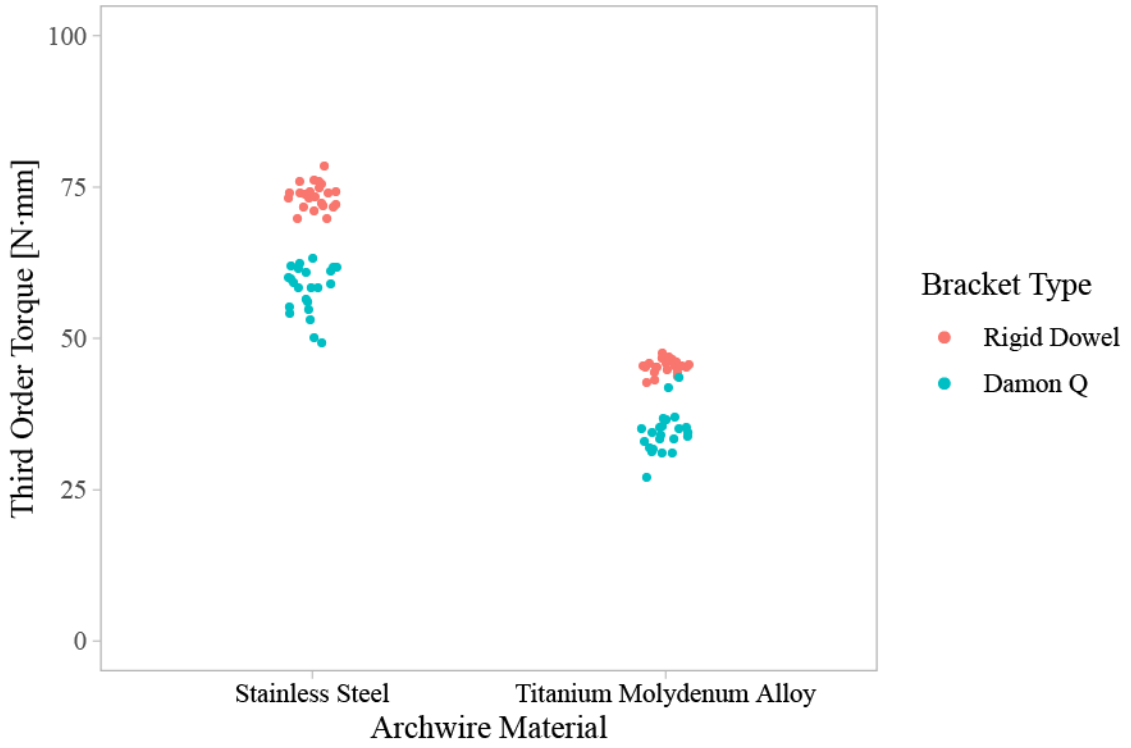

Figure 4.5. Individual maximum torques of 0.019”x0.025 archwires at 30° loading among all trials in the full study.

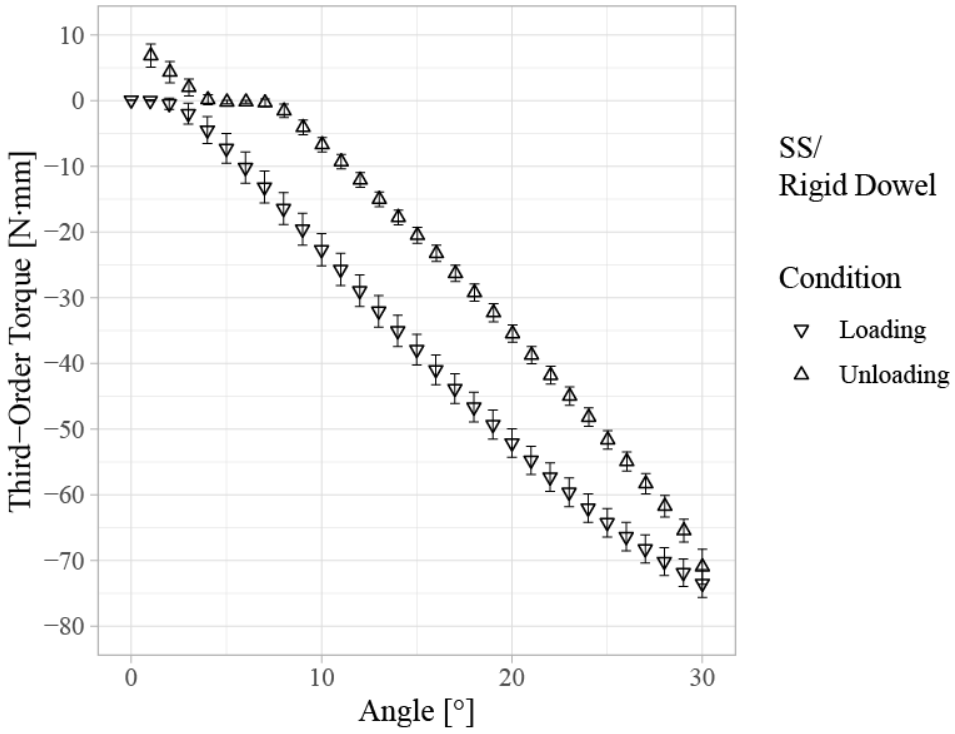
Third−Order Torque [N·mm]
10
0
−10
−20
−30
−40
−50
−60
−70
−80
0
10
20
30
Angle [°]
SS/
Rigid Dowel
Condition
Loading
Unloading

(a)

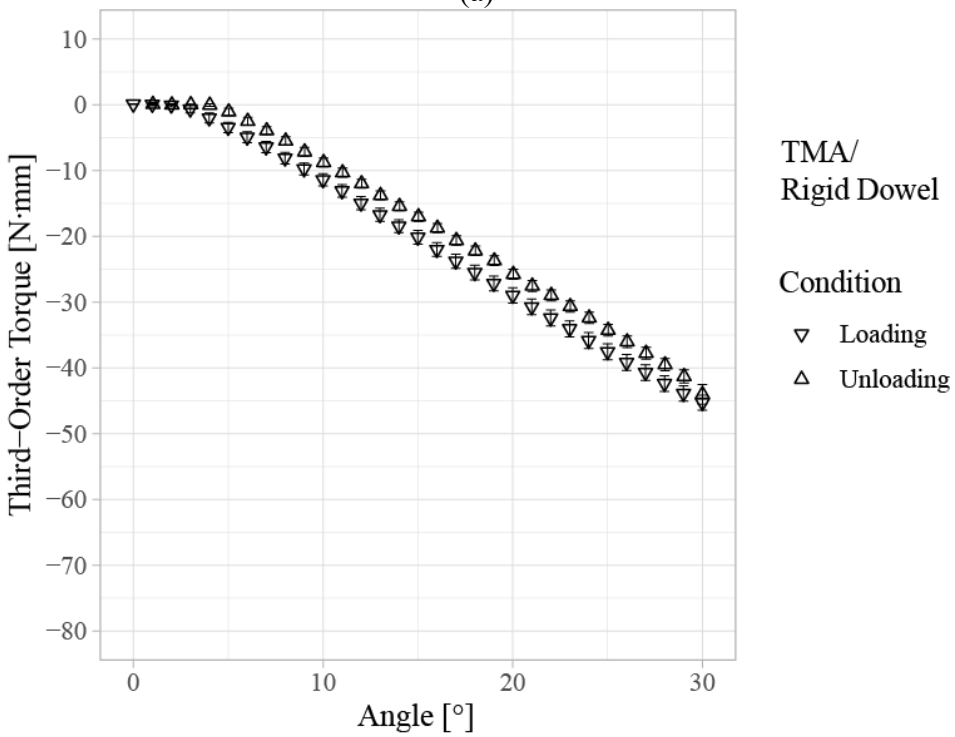
Third−Order Torque [N·mm]
10
0
−10
−20
−30
−40
−50
−60
−70
−80
0
10
20
30
Angle [°]
TMA/
Rigid Dowel
Condition
Loading
Unloading

(b)

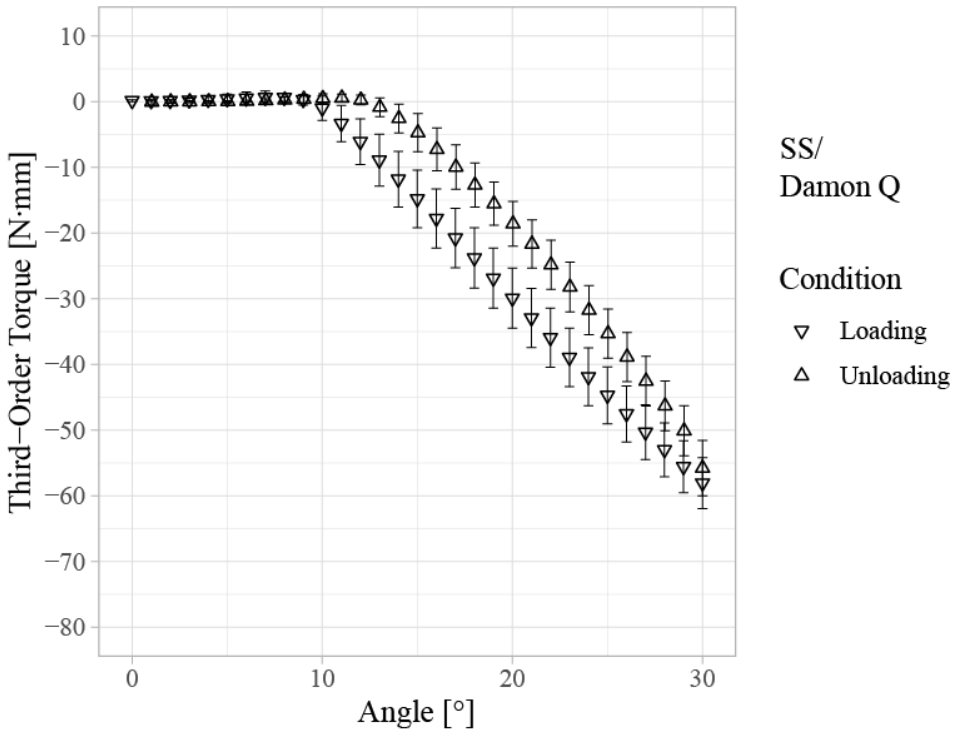

(c)

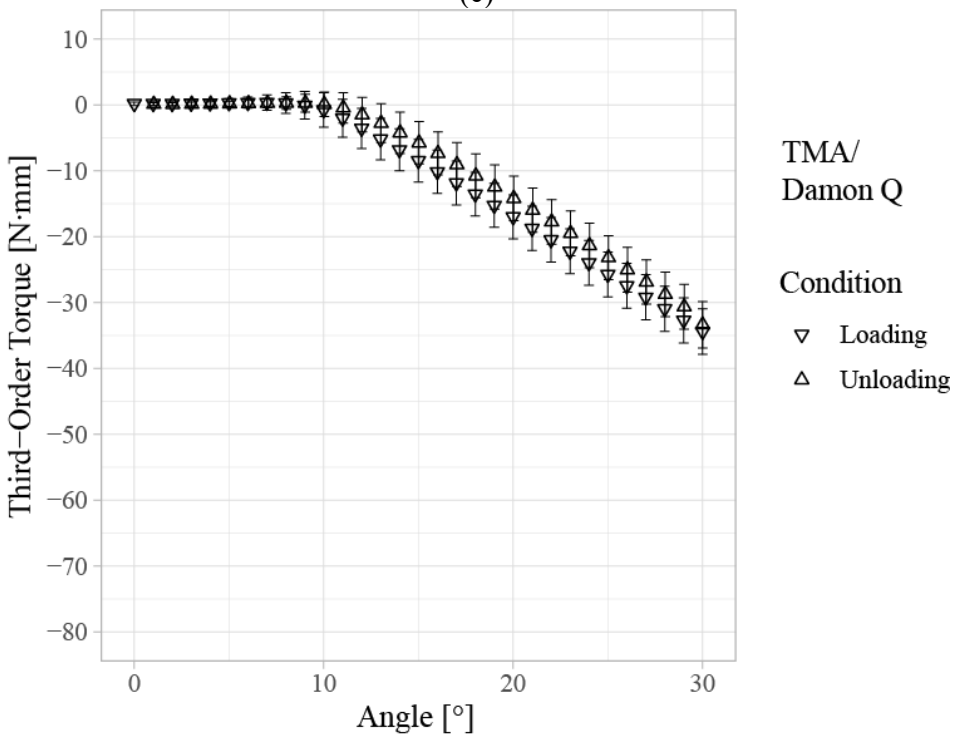

(d)

Figure 4.6. Third-order torque responses of 0.019”x0.025” archwires rotated to 30° with the configurations of (a) stainless steel archwire with rigid dowel, (b) titanium molybdenum alloy archwire with rigid dowel, (c) stainless steel archwire with Damon Q bracket, and (d) titanium molybdenum alloy archwire with Damon Q bracket, n = 23.

4.3.1.1 Two-Way ANOVA of Maximum Torque

Using R, a two-way ANOVA was performed on the maximum loading torque at 30° and is shown in Table 4.1. All p-values were less than 0.1, indicating strong evidence against the null hypothesis and confirming there exists a strong statistical difference in third-order torque between both factors: the SS and TMA archwire materials and the RD and Damon Q bracket types. DIC measurements were omitted from post-hoc statistical analysis; however, large differences in third-order torque were observed, and thus the relationship between torque response and surface response can be considered between the factors in the study.

Table 4.1. Two-way ANOVA table of the two-by-two factorial design used in the full study

	Df	Sum Sq	Mean Sq	F-value	p-value	
Material	1	3978	3978	158.1	**<0.001**	***
Bracket	1	14058	14058	558.8	**<0.001**	***
Residuals	89	2239	25			

Signif. codes: 0 '***' 0.001 '**' 0.01 '*' 0.05 '.' 0.1 ' ' 1						

4.3.2 Image Subset Overlap

In testing for the optimal amount of subset overlap, a trial using an SS archwire with the RD was selected. All subsets were 63 x 63 pixels, and all other image correlation settings kept constant, the overlap increased from 31 to 15 and finally 8 pixel shifts, where smaller shifts result in larger overlaps between adjacent subsets. Comparisons of directional displacements and shear strains measured at 30° loading are shown in Figure 4.7. The colour map scales were kept the same for all measures for comparison purposes. It was seen that increasing the overlap did not change the values obtained for any of the parameters. Rather, a result of increasing the amount of overlap was

a change in the correlation smoothness at the edges of the archwire. Since the main parameter of interest for comparing groups was surface strain, selecting an overlap of eight pixels was justified as it would enable more vectors to be computed that laid on the top surface of the archwire, which were free of influences from the rounded corners of the archwire.

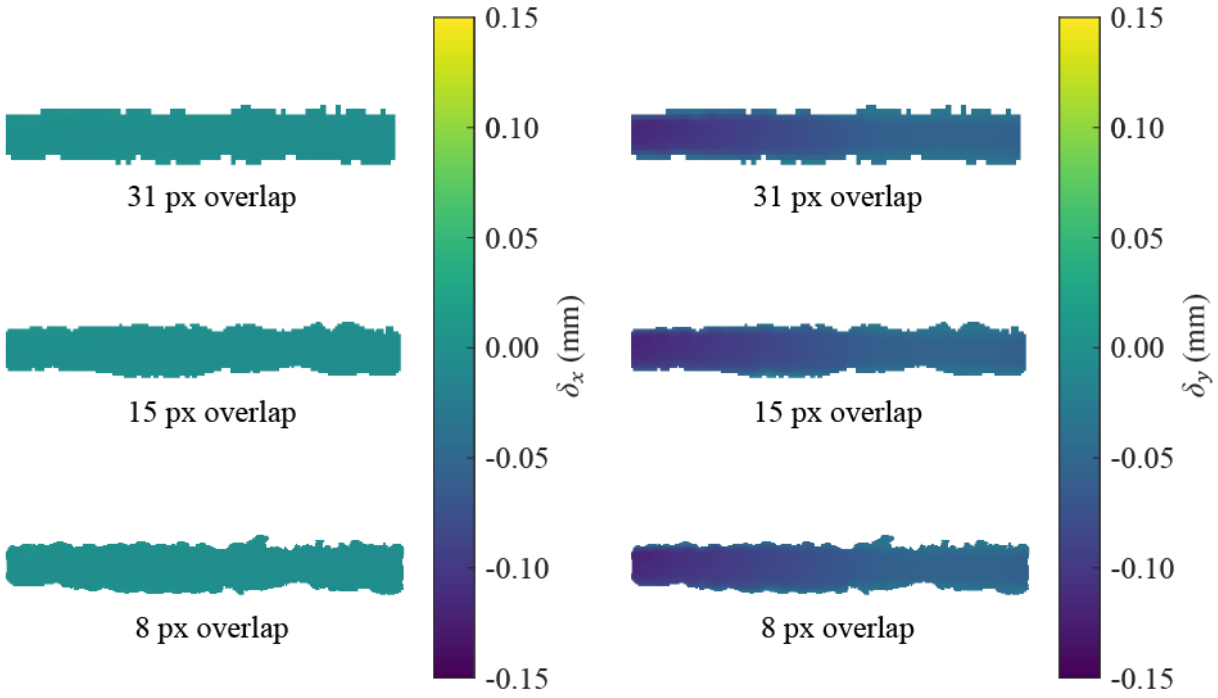

(a) (b)

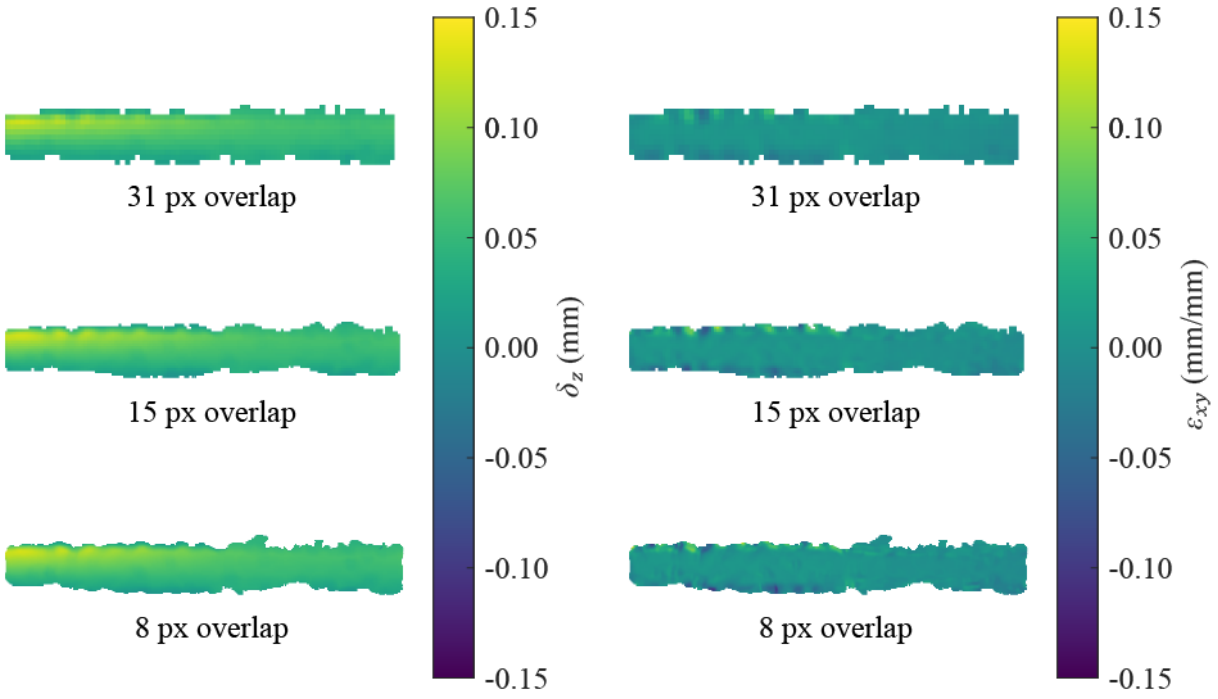

(c) (d)

Figure 4.7. Comparisons of full-field outputs at 30° loading of a stainless steel archwire torqued with the rigid dowel. Varying subset overlaps for (a) x-, (b), y-, and (c) z-displacements and (d) surface shear strain on the xy-plane are shown.

4.3.3 Shear Strain Surface Area

The optimal surface strain area was found by exploring the effects of averaging different rectangular areas on the same archwire from a SS trial using the RD. Given the overlap of 8 pixels, the height of the rectangle could be incrementally increased by 0.01 mm in both the positive and negative y-direction relative to the centre of the rectangle. In effect, surface shear strain values were averaged using rectangular areas that ranged from being a rectangle 2 mm long with zero height through to rectangle that was 2 mm x 0.60 mm, which represented an area that contained all vectors in the y-direction across the 2 mm span. Surface shear strain was plotted versus the number of vectors contained inside each rectangular area. This is analogous to a mesh convergence

test when performing finite element analyses; however, rather than seeking a converging parameter, the desired outcome is instead the optimisation of a parameter, which in this case was shear strain. The plots of surface shear strain versus the number of vectors is shown in Figure 4.8, which shows strain for both loading and unloading. In the plot, each line represents the surface shear strain measured at a single angle of rotation. Essentially, following a line from left to right shows the effect of increasing the rectangular area used to calculate the average shear strain for any given angle. It was seen that using rectangles that were smaller resulted in larger maximum shear strains, and as the rectangular area increased, once vectors located on the rounded corners were included, the resultant shear strains rapidly decreased, and eventually increased. Both the decrease and increase could be attributed to erroneous vectors along the rounded corners that were not indicative of surface shear strain on top surface of the archwire.

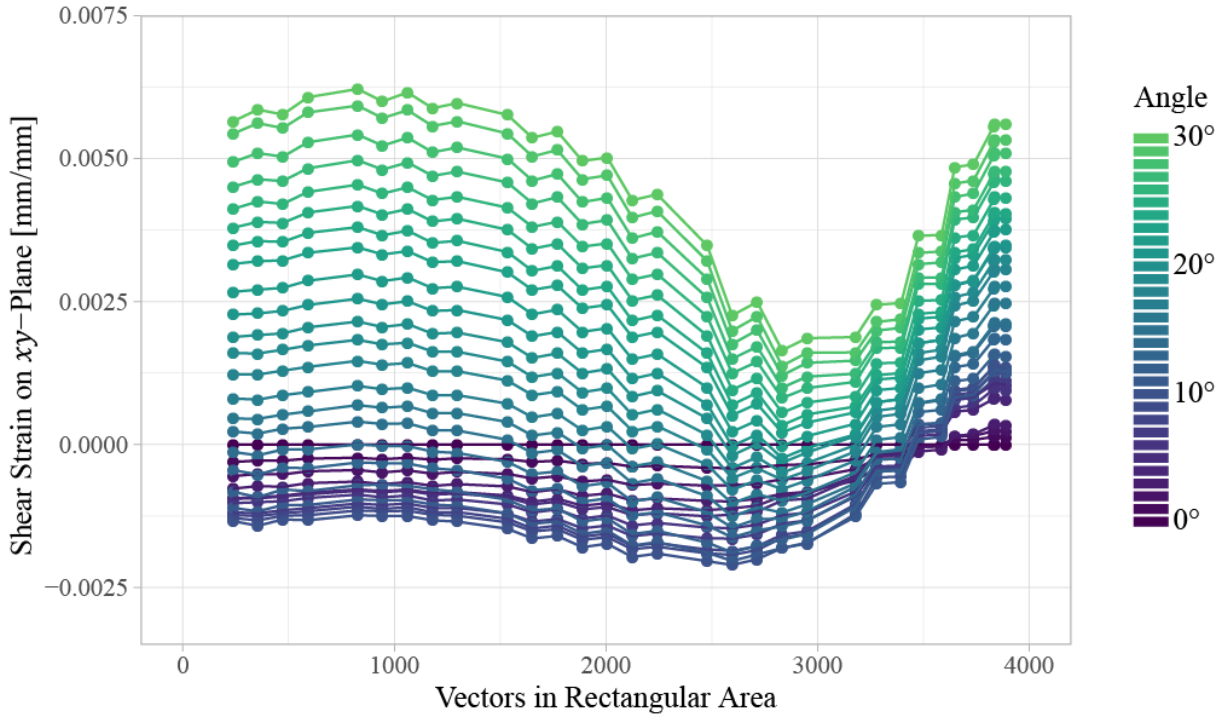

(a)

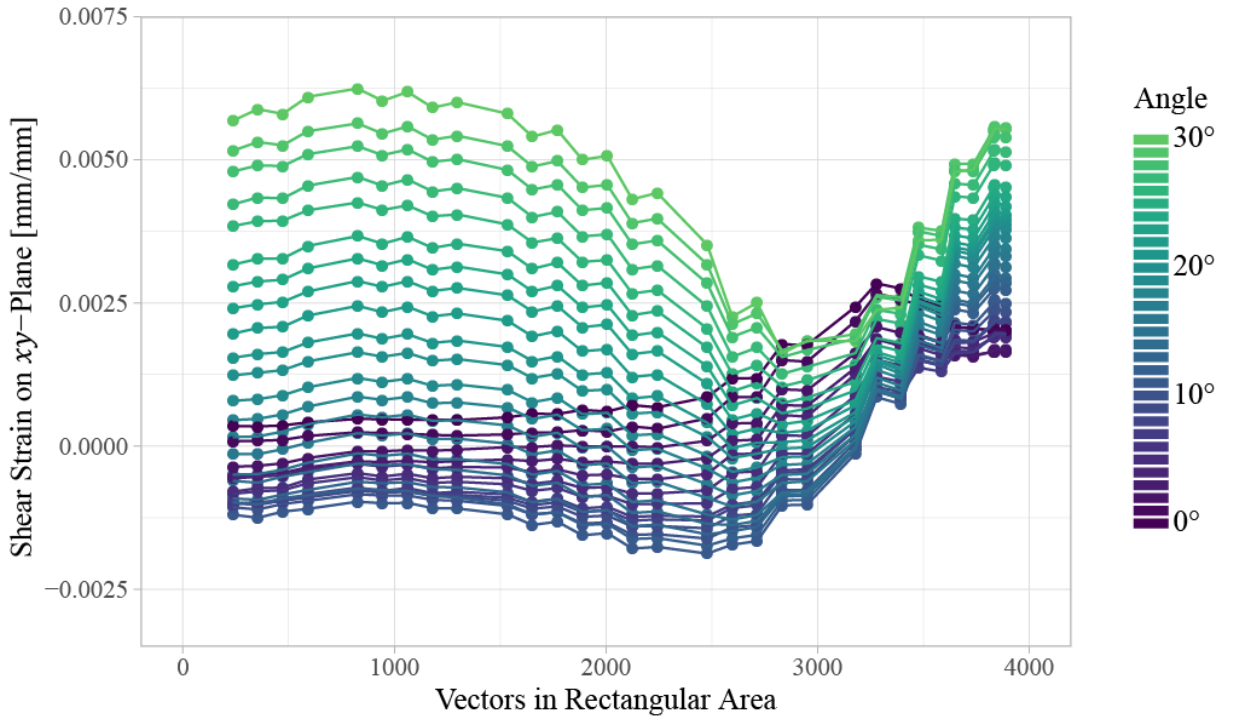

(b)

Figure 4.8. Surface shear strain comparisons from a stainless steel archwire rotated 30° with the rigid dowel using (a) loading and (b) unloading values. Average shear strains are plotted on a per angle basis against the total number of shear strain vectors within a rectangular area.

From the plots, there was clear indication that selecting an appropriate size for shear strain averaging was paramount as measured values could greatly fluctuate. The process of measuring surface strains using varying rectangular areas was repeated for all trials to select the final rectangular area used. However, it was known that using areas that included the corners would not be beneficial in obtaining shear strain, and the results from Figure 4.8 confirmed this. As a consequence, the rectangular size was capped at an upper area of 2 mm by 0.30 mm, which was certain to include some influence of the rounded corners. Instead of using results from every angle, only surface shear strains at 30° loading were used. Each group contained the 23 trials and the averages and standard deviations showing the effects of changing the rectangular area are plotted in Figure 4.9, and the values of shear strain measured for each rectangular area are presented in

Table 4.2. In all cases, the shear strains were largest when using smaller areas. As area increased, the shear strain values decreased, which was attributed to vectors located on the archwire corners. To ensure that reported strain values were not influenced by vectors on the corners, an area of 2 mm by 0.10 mm was selected for all shear strain measurements. The area of the rectangle was large enough to be representative of surface shear strain over an area of the archwire rather than just over a line. In addition, selected percentage differences in measured strains relative to the strains measured with the line are shown in Table 4.3. When using a 2 mm by 0.10 mm area, the percent difference in strain measurement relative to the values as obtained with a 2 mm line were ranged between 0.24% to 3.99%. In comparison, the percent differences were significantly larger when increasing the rectangular area height to 0.20 mm or 0.30 mm, where maximum percent differences were 10.92% and 24.03%, respectively.

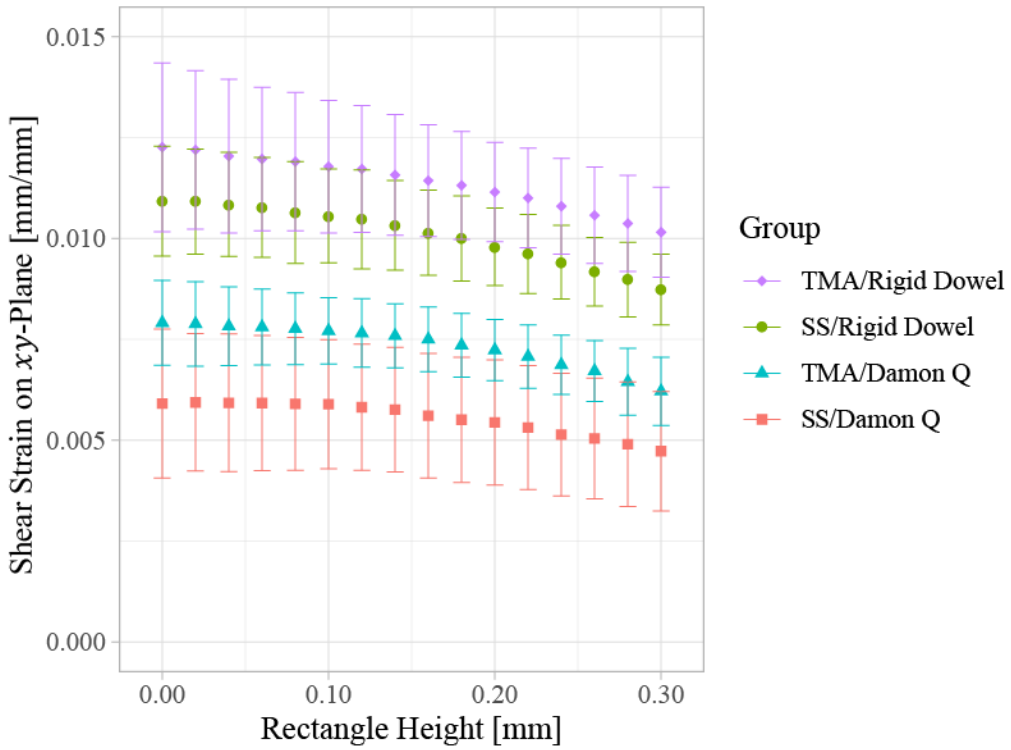

Figure 4.9. Average surface shear strain of all groups measured at 30° loading versus the height of the rectangle used to obtain the averages.

Table 4.2. Comparisons of average surface shear strain values computed over rectangular areas when changing the y-dimension of 2 mm by y mm rectangular areas

Bracket	Archwire Material	Y-Dimension [mm]	Mean Shear Strain [mm/mm]	Standard Deviation [mm/mm]
Rigid Dowel	Stainless Steel	0.00	0.0109	0.0014
		0.02	0.0109	0.0013
		0.04	0.0108	0.0013
		0.06	0.0108	0.0012
		0.08	0.0106	0.0013
		0.10	0.0106	0.0012
		0.12	0.0105	0.0012
		0.14	0.0103	0.0011
		0.16	0.0101	0.0011
		0.18	0.0100	0.0011
		0.20	0.0098	0.0010
		0.22	0.0096	0.0010
		0.24	0.0094	0.0009
		0.26	0.0092	0.0008
		0.28	0.0090	0.0009
		0.30	0.0087	0.0009
	Titanium Molybdenum Alloy	0.00	0.0123	0.0021
		0.02	0.0122	0.0020
		0.04	0.0120	0.0019
		0.06	0.0120	0.0018
		0.08	0.0119	0.0017
		0.10	0.0118	0.0016
		0.12	0.0117	0.0016
		0.14	0.0116	0.0015
		0.16	0.0114	0.0014
		0.18	0.0113	0.0013
		0.20	0.0112	0.0012
		0.22	0.0110	0.0012
		0.24	0.0108	0.0012
		0.26	0.0106	0.0012
		0.28	0.0104	0.0012
		0.30	0.0102	0.0011

Bracket	Archwire Material	Y-Dimension [mm]	Mean Shear Strain [mm/mm]	Standard Deviation [mm/mm]
Damon Q	Stainless Steel	0.00	0.0059	0.0018
		0.02	0.0059	0.0017
		0.04	0.0059	0.0017
		0.06	0.0059	0.0017
		0.08	0.0059	0.0016
		0.10	0.0059	0.0016
		0.12	0.0058	0.0016
		0.14	0.0058	0.0015
		0.16	0.0056	0.0015
		0.18	0.0055	0.0016
		0.20	0.0054	0.0016
		0.22	0.0053	0.0015
		0.24	0.0051	0.0015
		0.26	0.0050	0.0015
		0.28	0.0049	0.0015
		0.30	0.0047	0.0015
	Titanium Molybdenum Alloy	0.00	0.0079	0.0011
		0.02	0.0079	0.0010
		0.04	0.0078	0.0010
		0.06	0.0078	0.0009
		0.08	0.0078	0.0009
		0.10	0.0077	0.0008
		0.12	0.0077	0.0009
		0.14	0.0076	0.0008
		0.16	0.0075	0.0008
		0.18	0.0074	0.0008
		0.20	0.0072	0.0008
		0.22	0.0071	0.0008
		0.24	0.0069	0.0007
		0.26	0.0067	0.0008
		0.28	0.0064	0.0008
		0.30	0.0062	0.0008

Table 4.3. Percentage differences of measured average shear strains using different rectangular areas relative to measured average shear strain values using a line.

Group	Percentage differences compared to 2 mm line Area, x by y [mm by mm]		
	2 by 0.10	2 by 0.20	2 by 0.30
SS/Rigid Dowel	3.41%	10.92%	22.28%
TMA/Rigid Dowel	3.99%	9.49%	18.79%
SS/Damon Q	0.24%	8.23%	22.16%
TMA/Damon Q	2.55%	8.91%	24.03%

With the 2 mm by 0.10 mm area selected, there was confidence that the average strain measurements were maximum shear strain values, the probed area would remain on the flat surface of the archwire rather than the rounded corners, and enough vectors would be included in every average to be representative of shear strain over the flat surface of the archwire (away from boundary conditions). An example of a probed 2 mm by 0.10 mm area is shown in Figure 4.10, which includes the resultant vectors used in the shear strain averages.

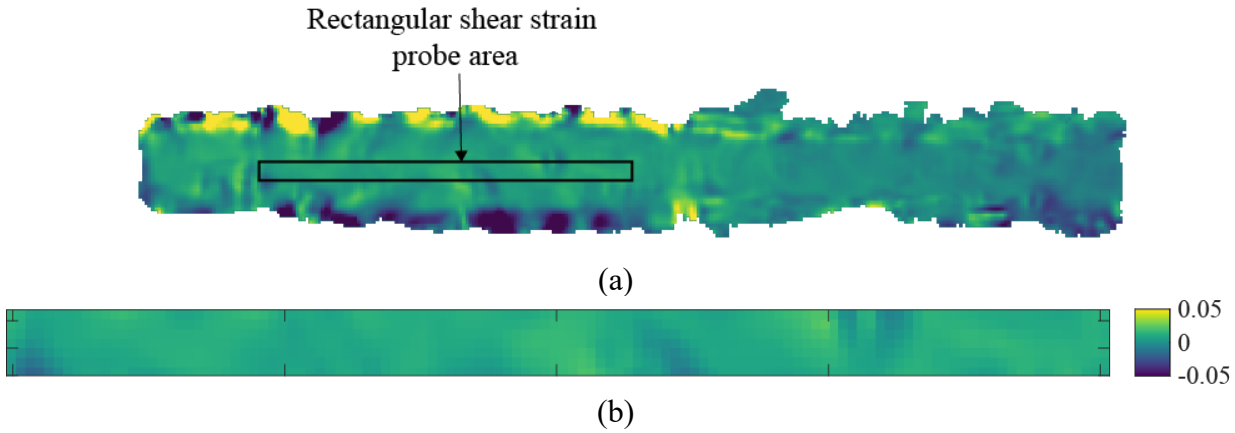

Figure 4.10. Surface shear strain of a 0.019”x0.025” stainless steel archwire rotated at 30°, (a) indicating the probed area for shear strain averaging and (b) the resultant vector map containing all vectors in the probed area.

The goals in the optimisation were to obtain maximum shear strain values, while also ensuring that vectors used in the shear strain calculation were not influenced by the corners. Therefore, the area selected for the average shear strain calculations was justified as the goals were met.

4.3.4 Deformation and Strain

The use of 3D DIC gives full-field information on surface deformations and strains that evolve over the range of rotation. With RD trials, only the top surface of the archwire was imaged for DIC purposes. However, by imaging the top surface of the archwire in tandem with the top surfaces of the Damon Q brackets, more information can be obtained over the rotation, particularly regarding bracket deformations.

4.3.4.1 Archwire Deformations

Archwire deformations during third-order torque can be compared both qualitatively and quantitatively. The DIC outputs present full-field representations of deformations in the x-, y-, and z-directions. As such, it is possible to compare the full-field deformations by qualitatively examining the nature of the deformations en masse. Probing unique values of deformation in specific locations along the archwire may also quantify relevant information with respect to the archwire behaviour; however, doing so was omitted as probing surface strains were the primary parameter of interest.

Insights such as directly quantifying the amount of deformation an archwire undergoes during third-order torque can be gained by probing unique regions. In other loading scenarios, it can also be useful to probe values to directly measure displacements. With respect to third-order torque, the range of motion of an archwire was determined by the OTS and the archwire displacements for all groups would be similar in magnitude and bounded by the rotation. In the case of the experimental design of this two-by-two factorial, it is more valuable to compare the full-field

displacements of the archwires by looking at x-, y-, and z-displacements, which reveals the behaviour of an archwire when rotated inside a bracket.

Comparisons of archwire displacements using single trials from each group are shown in Figure 4.11. It was seen that archwire behaviour varied greatly between the RD and Damon Q brackets. The displacements when using the RD were more indicative of the archwire being twisted from the applied rotation, whereas the displacements when using Damon Q brackets were representative of rigid body rotation. Displacements in the x-direction were found to be negligible for all trials, whereas displacements in the y- and z-directions showed the expected response to an archwire being rotated; y-displacements tended in the negative direction and z-displacements tended in the positive direction. The left side of the archwires were all shown to undergo a negative y-displacement in the direction of rotation. However, the visual gradients seen with the RD trials show that the magnitude of the y-displacements decreases towards the RD, suggesting a twist in the archwire. Conversely, the magnitude is more consistent throughout the length of the archwires for the Damon Q trials, which suggests rigid body rotation. The same effect is seen with displacements in the z-direction, as the RD trials exhibits the same decrease in displacement magnitude going from the left towards the RD, and the Damon Q trials show relatively more consistent displacements throughout the span of the archwire. However, unlike the RD trials, the entire region of the archwire in contact with the Damon Q bracket is occluded; therefore, only the archwire behaviour within the IBD can be compared.

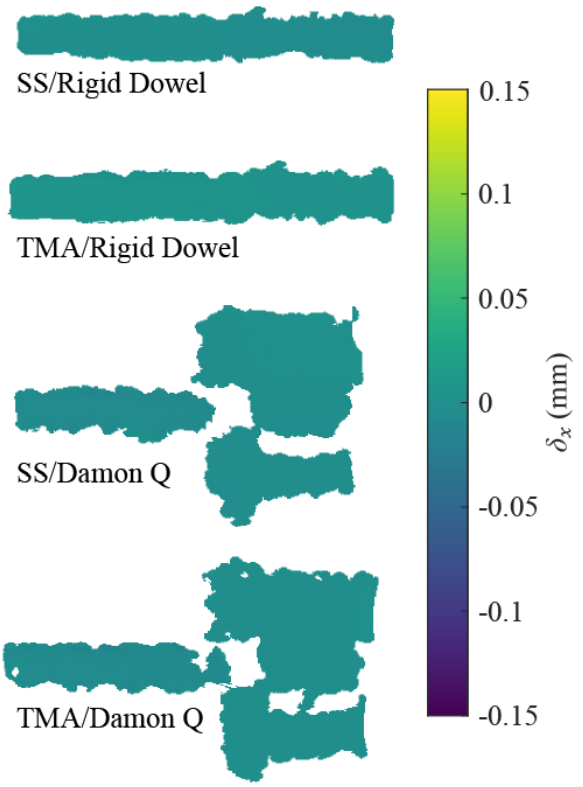
SS/Rigid Dowel
TMA/Rigid Dowel
SS/Damon Q
TMA/Damon Q
0.15
0.1
0.05
0
-0.05
-0.1
-0.15
δ_x (mm)

(a)

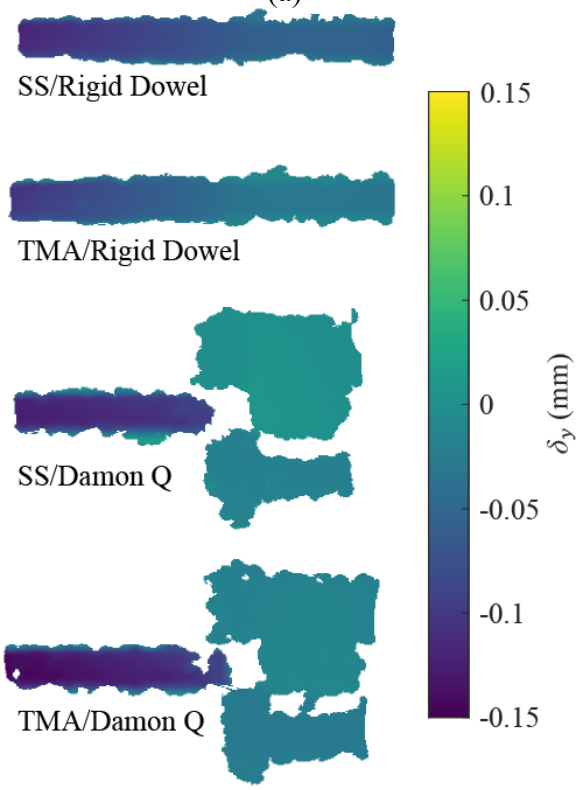
SS/Rigid Dowel
TMA/Rigid Dowel
SS/Damon Q
TMA/Damon Q
0.15
0.1
0.05
0
-0.05
-0.1
-0.15
δ_y (mm)

(b)

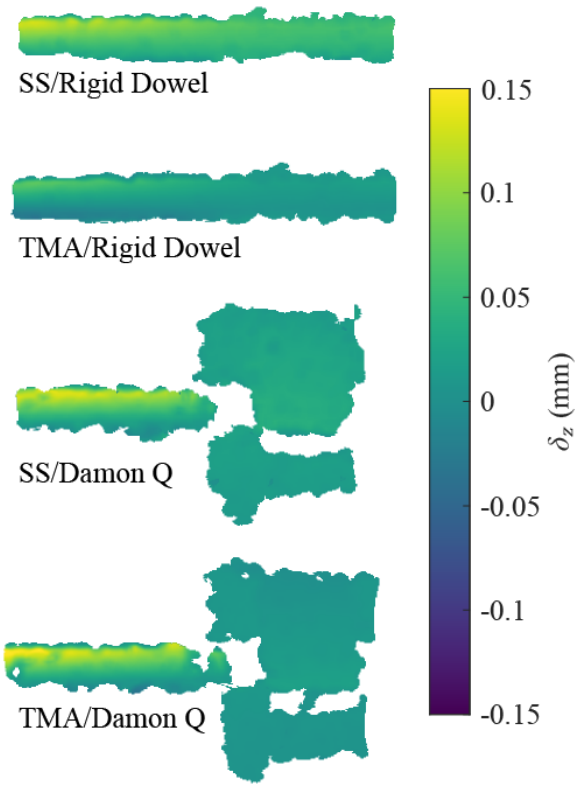

(c)

Figure 4.11. Comparisons of full-field displacements at 30° loading for all groups in the (a) x-, (b) y-, and (c) z-directions using a single trial per group. Damon Q bracket surfaces are shown with features such as tie-wings and the archwire retentive component.

4.3.4.2 Archwire Strains

In terms of surface strains on the archwire, only shear strains were of interest, as was confirmed in Chapter 3 showing the principal strains were negligible, which agreed with the analytical solution for torsion of prismatic bars [87]. As the qualitative results from surface deformations of the archwire suggested different torsion regimes when using the RD versus Damon Q brackets, measuring archwire surface shear strains can further elucidate the differences.

Measured surface shear strains are shown in Figure 4.12. It was found that shear strain development between the RD groups versus the Damon Q groups were not the same. Specifically,

shear strains arose with the RD groups after 4° of rotation and continued to increase as the angle increased. However, shear strains with the Damon Q brackets were seen to initially start in the negative direction before reaching a minimum at approximately 9° of rotation before changing direction and increasing with the angle. This phenomenon was explored and was found to be due to the initial angular position of the archwire in the passive position. When comparing the initial angle of an archwire at 0° rotation, it was seen that the imaged surface of the archwires in the RD were parallel to the xy-plane, whereas archwires in the Damon Q brackets were not. This was due to the bracket slot geometry altering the passive position of the archwire, where minimising third-order torque resulted in the archwire being at an angle relative to the xy-plane.

When comparing the groups in Figure 4.12 against on another, it was seen that the RD resulted in higher shear strains than Damon Q brackets, and TMA archwires exhibited more shear strains compared to SS archwires. SS archwires have higher shear moduli compared to TMA archwires, and there is an inverse relationship between shear modulus and shear strains. The shear strains measured are therefore expected with respect to comparing shear strain magnitudes across the two materials. When looking at unloading, it was seen that the SS/RD group exhibited residual shear strain at the end of the unloading phase, suggesting that plastic deformation of the archwire was present when using SS archwires. However, for the other three groups, residual strains are not apparent, and the unloading strains closely match the loading strains.

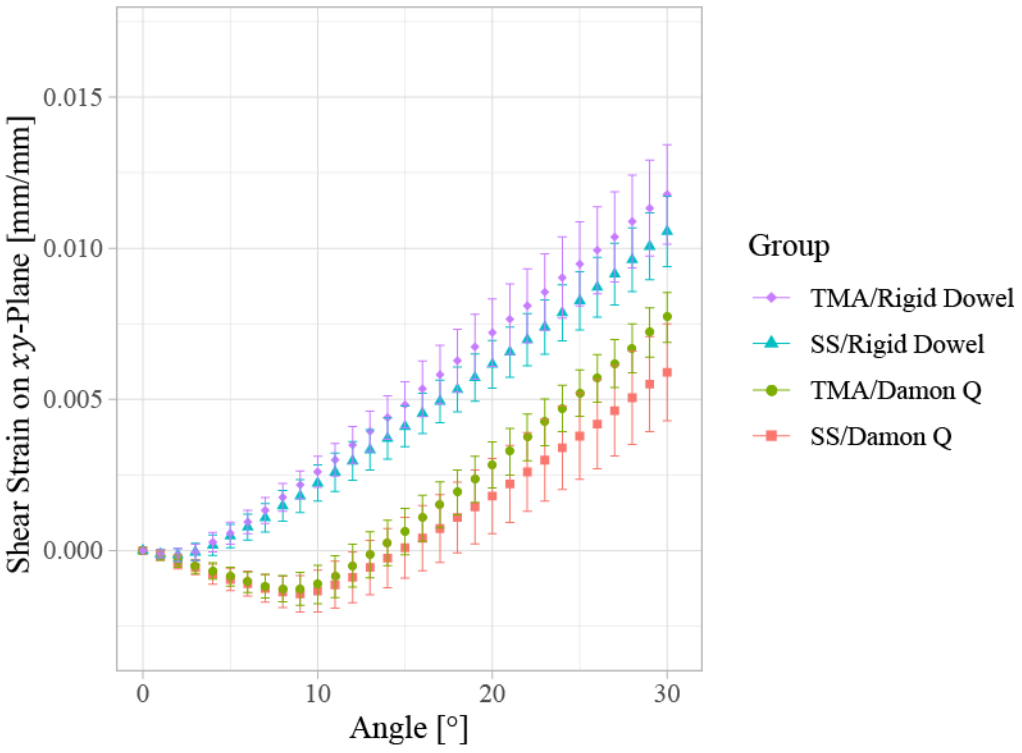

(a)

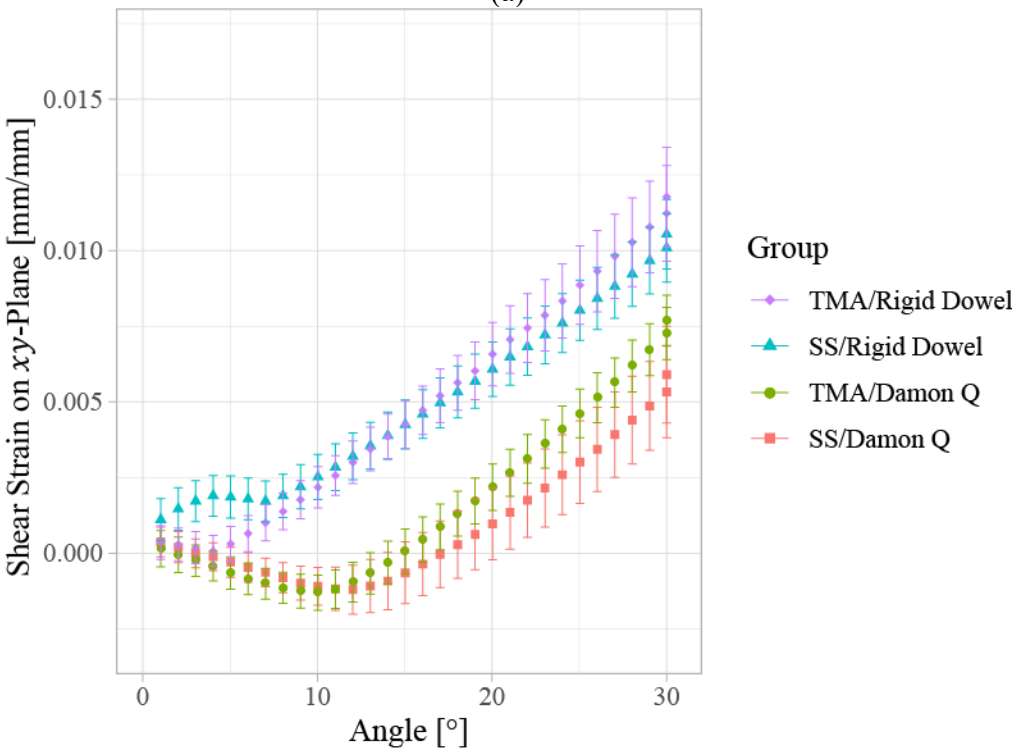

(b)

Figure 4.12. Surface shear strains measured using 3D DIC from third-order torque of 0.019”x0.025” archwires during (a) loading and (b) unloading.

4.3.4.3 Bracket Deformations

With respect to the Damon Q brackets, strains were not a parameter of interest as strain development on the external bracket surfaces were assumed to be negligible. In contrast, deformations can show how the tie-wings of the bracket move over the applied rotation of the archwire. In previous studies, it was seen that deformations in the x-direction were minimal and thus were not of interest for this study [18], [47]. However, deformations in the y- and z-directions are of interest as they show how the bracket deforms over the applied rotation as well as if there is a presence of permanent bracket deformation after unloading.

Since the Damon Q brackets were not centred in the field of view of the cameras, image correlation of all four tie-wings was not always possible as the bracket position could result in occlusions of the right tie-wings, which led to an inability to correlate. Therefore, bracket deformations in the y- and z-directions were measured using only the left tie-wings (which were always correlated) for all trials to maintain consistency. In probing the displacement vectors, 0.5 mm by 0.7 mm rectangular areas were placed on both the top left and bottom left tie-wings. The size was determined to ensure probed regions would be saturated with vectors, and that no correlation boundaries would be present in the regions. Since the parameter being measured with the brackets were only displacements, it was not critical that the size of the rectangle be optimised. Figure 4.13 shows an example of y- and z-displacements at 30° archwire rotation using trial of a TMA archwire with a Damon Q Bracket, and also shows the rectangular areas used on the brackets for averaging probed displacements.

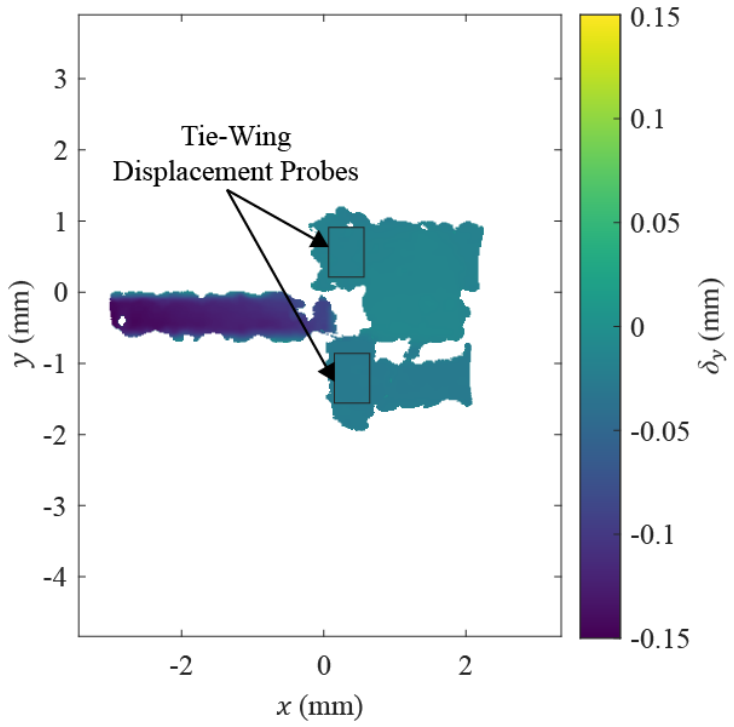

(a)

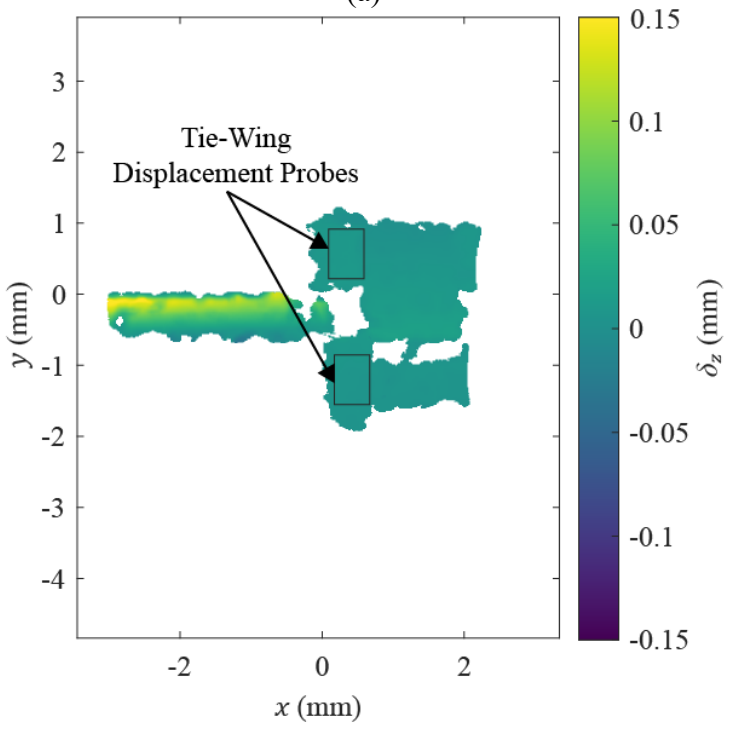

(b)

Figure 4.13. Full-field displacements of a 0.019”x0.025” titanium molybdenum alloy archwire rotated at 30° with a Damon Q bracket in the (a) y- and (z) directions, as well as rectangular areas used to probe displacements of the left tie-wings of the Damon Q bracket.

The y- and z-displacements of the tie-wings were compared by taking the difference between the top and bottom tie-wing displacements, which was similar to the previous method performed by Melenka *et al.* [18], [47]. The measured displacements while loading and unloading are shown in Figure 4.14. Torsional play in the bracket slots are evidenced by the tie-wing displacements, as tie-wing motion was not seen until approximately 9° of archwire rotation. However, it is noted that third-order torque can be generated prior to tie-wing movements, therefore torsional play should not be determined by bracket deformations but rather with measured resultant torques, as seen with Figure 4.6. When loading, it was seen that SS archwires caused more tie-wing movement in the y-direction compared to TMA archwires, and similarly in the z-direction, though displacements in the z-direction are much smaller in magnitude compared to the y-direction. Further, when examining the displacements during unloading, there was evidence that the applied rotation of the SS archwires resulted in permanent deformation of the brackets, as both displacements in the y- and z-directions did not return to zero. In contrast, the tie-wing displacements when using TMA archwires returned to zero after unloading. Measured displacements at 30° loading and 1° unloading are shown in Table 4.4 for comparison.

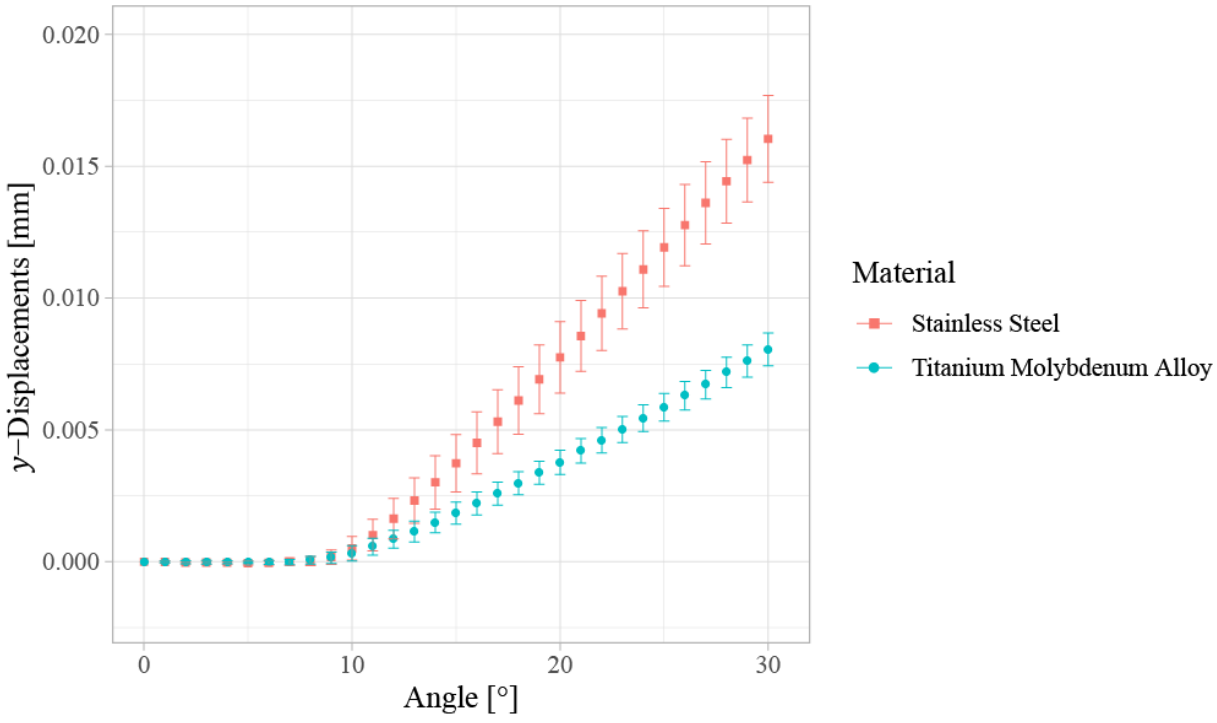
0.020
0.015
0.010
0.005
0.000
y−Displacements [mm]
0
10
20
30
Angle [°]
Material
Stainless Steel
Titanium Molybdenum Alloy

(a)

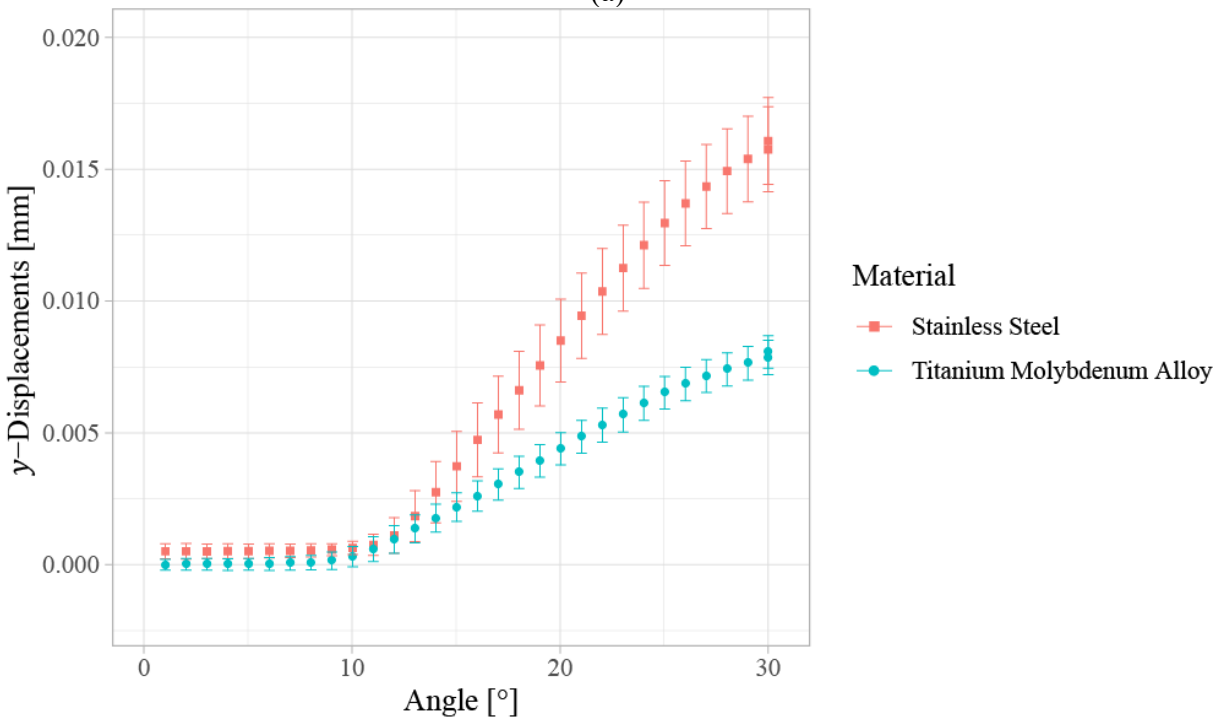
0.020
0.015
0.010
0.005
0.000
y−Displacements [mm]
0
10
20
30
Angle [°]
Material
Stainless Steel
Titanium Molybdenum Alloy

(b)

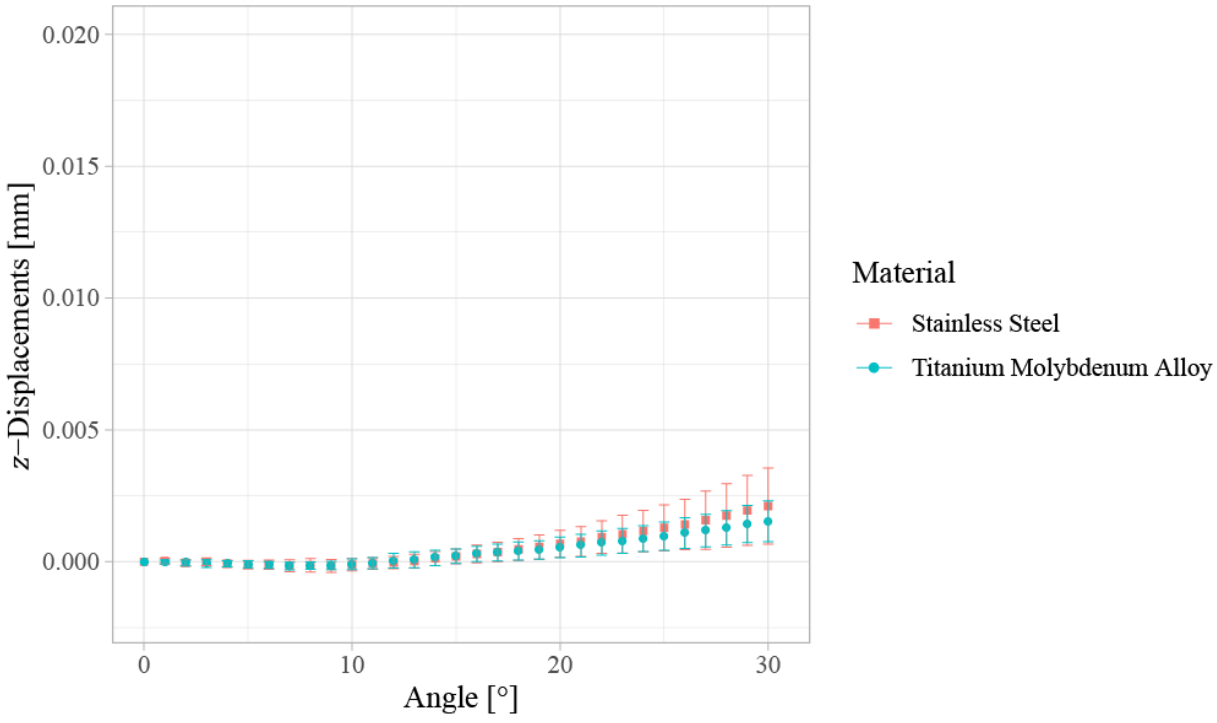

(c)

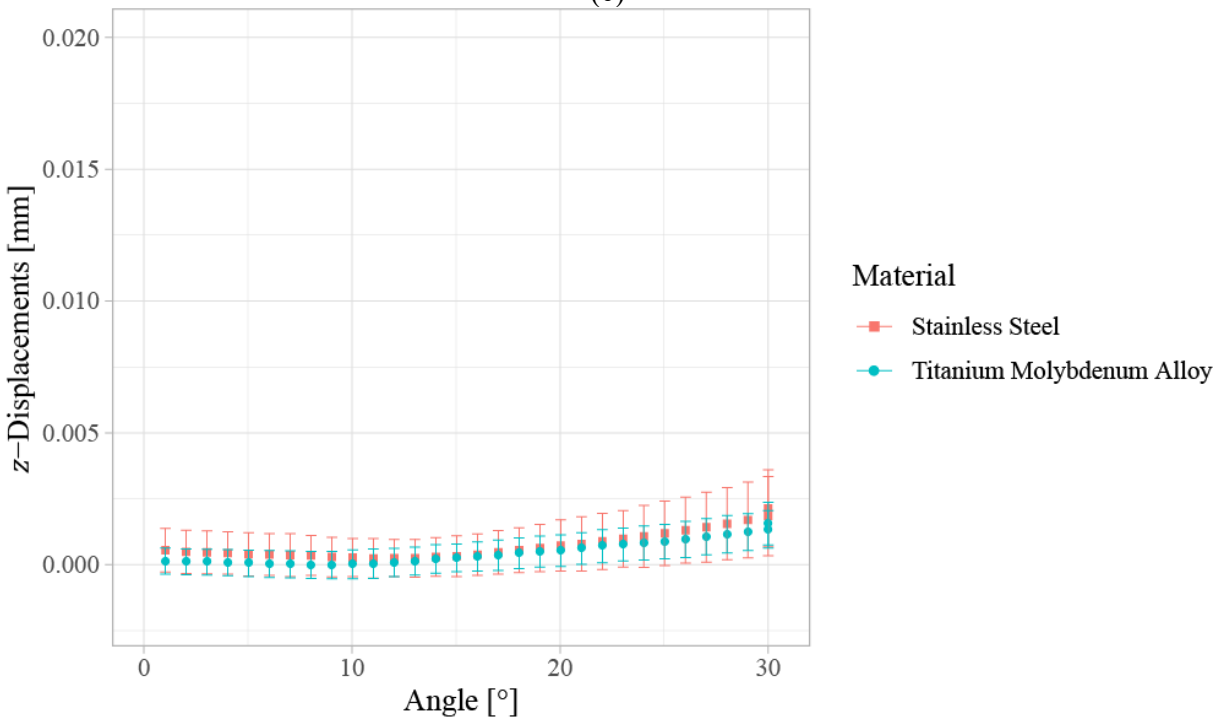

(d)

Figure 4.14. Measured relative displacements of left tie-wings on Damon Q brackets during third-order torque showing the (a) loading and (b) unloading *y*-displacements and the (c) loading and (d) unloading *z*-displacements.

Table 4.4. Average tie-wing displacements in the y- and z-directions at maximum loading and minimum unloading.

Angle	Group	y-Displacement ± Standard Deviation [mm ± mm]	z-Displacement ± Standard Deviation [mm ± mm]
30° Loading	SS/Damon Q	0.0160 ± 0.0017	0.0021 ± 0.0014
	TMA/Damon Q	0.0081 ± 0.0006	0.0015 ± 0.0008
1° Unloading	SS/Damon Q	0.0005 ± 0.0003	0.0005 ± 0.0008
	TMA/Damon Q	0.0000 ± 0.0002	0.0001 ± 0.0005

4.4 Discussion

Performing 3D DIC to capture both archwire and bracket movements simultaneously generated full-field surface deformations and strains over the range of the applied rotation. Deformation characteristics of the orthodontic materials during third-order torque were captured and presented. Further, the measurements of archwire shear strains allows for comparisons of strain development across the groups in the two-by-two factorial design. While the factorial was initially designed to compare third-order torque values due to its known behaviour, additional insight was gathered using 3D DIC. The experimental setup displayed capabilities of measuring surface deformations and strains at the scale of orthodontic appliances and can be used to gain an appreciation into how different factors affect orthodontic prescriptions.

4.4.1 Third-Order Torque

Using SS archwires and the RD led to higher torques compared to TMA archwires and Damon Q brackets, respectively. In terms of clinical application, the results from using the RD would not be relevant as such a component does not exist in orthodontic practise; however, the material comparisons between SS and TMA may still be valuable in evaluating and selecting materials for

third-order torque application. In contrast, the results from using Damon Q brackets are of greater clinical interest. Torsional play with Damon Q brackets were similar between archwire materials, where the onset of third-order torque occurred at approximately 10° (seen in Figure 4.6 (c) and (d)). With respect to third-order torque, the use of 1° rotation increments gave a complete picture of the differences between loading and unloading torque curves. Unloading curves are more useful in clinical contexts and capturing the exact angle that torque vales drop below thresholds can be useful in clinical practise. Both materials fell under 5 N·mm of torque after approximately 15° unloading despite having different maximum torques. Clinically, knowing how various archwire materials behave during unloading at various angles of archwire twist can change treatment options; however, with increased variations under clinical settings, other factors may impact the application of third-order torque. In this study, the torque values for both archwire materials rotated with Damon Q brackets agreed with previous literature that utilised the OTS [15], [40].

In the experiment, the use of the RD enabled archwire comparisons to be made independent of orthodontic bracket behaviour. The RD slot provided a rigid boundary that constrained the archwire significantly more than orthodontic brackets would. The reduction of torsional play as well as the increased stiffness affected the third-order torque generation over the applied rotation. The onset of third-order torque with the RD was more rapid with higher overall torque magnitudes. This result may influence the design and manufacturing of future archwire and brackets, where third-order torque application can be designed considering both archwire material and bracket designs.

From a manufacturer perspective, changes to the geometry around the contact region between the archwire and bracket can alter third-order torque mechanics. Brackets can be made with different

geometries such that the insertion of a twisted archwire can produce higher or lower torque magnitudes, which may include reducing slot areas to reduce torsional play or increasing the stiffness of the bracket to enable larger torque magnitudes. Archwires can be manufactured with different geometries when considering third-order torque. By understanding how the archwire and bracket interact, changes to archwire geometry can allow better torque control, such as having more consistent rounded corners, or altering the corners based on the desired torque.

Clinically, having a better understanding of archwire behaviour during third-order torque with respect to its bracket interactions can allow for more optimised treatments that may be personalised for individual patients. Small changes in the angle of twist can have large effects on the resultant torque generated. A clinician can have more treatment control and consequently make treatment more efficient when these differences are well quantified and highlighted. The quantification of archwire third-order torque capabilities indicated that all orthodontic components contribute to overall third-order torque, and understanding the behaviour of system through various points of third-order torque application can be used clinically to enable more effective treatments.

4.4.2 Deformation and Strain

With respect to the 3D DIC measurements, the study allowed for the investigation of rectangular archwires behaviour during third-order torque. Measured deformations and strains can be used to develop a more comprehensive knowledge of the roles different factors have on third-order torque. Measuring deformations and strains throughout the range of rotation can reveal information not readily apparent prior to using 3D DIC such as plastic deformation, among other things. In performing this study, the explicit factors considered were archwire material and bracket types,

but the utilisation of 3D DIC also mandated that rounded corners of archwires also needed to be considered due to their direct impact on DIC measurements.

4.4.2.1 Archwire Deformations

Using the results from archwire displacements, there was evidence to suggest that third-order torque mechanics varied between using the RD compared to Damon Q brackets. While there may be some degree of twist when rotating an archwire inside the Damon Q bracket, it is not to the same extent as rotating an archwire with the RD. Therefore, third-order torque application with orthodontic brackets using the OTS may not follow conventional torsion of prismatic bars. This finding was made possible using 3D DIC as the surface response of the archwire was directly observed during third-order torque.

Bracket deformations during third-order torque result in the archwire undergoing a combination of less twisting and more rigid body rotation compared to rotation with the RD. Evidently, compliance in the brackets can play a large role in prescribing the degree of twist required during clinical treatment, as third-order torques values can be influenced by the amount of deformation a bracket undergoes in addition to the archwire material. In clinical settings, the interactions presented between an archwire and bracket is not isolated within the dentition and will include additional reactions throughout the dental arch.

Studying the deformations of an archwire with 3D DIC can allow clinicians to better understand the mechanics of third-order torque prescription when preparing archwires. With respect to archwire deformations during third-order torque as performed with the OTS, the 3D DIC measurements highlighted the differences between groups in full-field contexts. Further analysis

with archwire deformations can be performed by using the DIC measurements to compare deformations; however, that was considered out of scope for this study as strains were of higher interest in characterising archwire mechanics.

4.4.2.2 Archwire Strains

When applying third-order torque with the RD, it was seen that the SS archwire has residual strain during unloading. The presence of residual strain suggested that the SS archwires underwent plastic deformation when rotated to 30°. In clinical practise, a clinician twists an archwire prior to ligating it inside brackets. In doing so, plastic deformation should be considered since it can change how third-order torque is applied to a patient's tooth. The ability to quantify the residual strain seen in an archwire after third-order torque can be used to further investigate how varying torque prescriptions can affect the mechanical response of an archwire within clinical settings. This can directly impact the efficacy of orthodontic treatment given different material responses can result in different interactions between the archwire and bracket.

In the study, the shear strain measurements using 3D DIC indicated that the strain development had conflicting behaviour when using Damon Q brackets. The initial strain direction was opposite of what was expected, and it was not until torsional play was removed (by rotating the archwire such that third-order torque was appreciable) that the strain increased in the expected direction. The initial decrease in strain was attributed to the camera perspective of the archwire in the passive position. Since the imaged surface of the archwire was not parallel to the xy-plane of the DIC coordinate system, the initial image captured at 0° rotation showed a skewed surface of the archwire as the reference image. As the archwires began rotating, the change in perspective resulted in artificial strain in the negative direction. Once the archwires reached a vertical position

(where the imaged surface of the archwire was parallel to the xy-plane), strain developed in a positive manner (seen in Figure 4.6). This result suggests that artificial shear strain may be measured when the initial image is skewed. It was seen that the strain rate differed once appreciable third-order torque was reached. In future studies, calibration curves of strains measured using an archwire with no contact with a bracket may be utilised to further explore the effects of strain measurements when dealing with rigid body rotations, or different dowels may be manufactured to account for the bracket slot angle such that when ligated in a passive position, the imaged surface of archwire would be parallel with respect to the xy-plane of the DIC coordinate system.

Characterisation of archwire behaviour during third-order torque can be useful in determining which factors affect resultant torque values. The ability to resolve archwire behaviour during third-order torque using 3D DIC allows for full-field snapshots of the orthodontic materials throughout the applied rotation. The benefit of having full-field deformations and strains is that the measurements can be directly compared to the analytical solution of torsion for prismatic bars, where specific behaviours such as negligible principal strains can be verified. The added complexities of orthodontics make it such that third-order torque of archwires deviates from the analytical solution, but the power of 3D DIC is highlighted by being able to directly image the surface response of the archwire through the entire range of rotation. This gives the opportunity to better characterise the archwire behaviour by being able to systematically compare differences that arose during third-order torque between the groups in the study.

The full-field measurements of shear strain using 3D DIC demonstrated a practical, robust, and repeatable method of extracting strain data over a highly limited surface area. The method of extracting shear strain data was thoroughly tested to determine the most appropriate way to

compare full-field data of twisted archwires. In practise, the full-field nature of DIC outputs can make it difficult to analyse. In using DaVis, virtual strain gauges can be used to compare principal strains [69]; however, the analysis of shear strains was limited to qualitative full-field comparisons and thus warranted the use of MATLAB. The optimisation of the area probed for shear strains was methodical, and ultimately demonstrated the capabilities of 3D DIC, where the extraction of full-field outputs can be used to make scientifically sound comparisons across the groups. In addition, a consequence of using a rectangular area for shear strain measurement with a high number of vectors in the average calculation is that the signal-to-noise ratio is reduced [69]. While this was not an initial goal for the determination of the rectangular area, it was an outcome that complements the method. Given the subset overlap and final size of the rectangular area, there was confidence the signal-to-noise ratio was improved compared to smaller areas.

The DIC measurement capabilities of the archwire surface can be appreciated when evaluating the novelty of the 3D deformation and strain measurements with respect to third-order torque. Previous literature studying third-order torque have sought to isolate the impact of different clinical factors on resultant third-order torque, such as bracket slot sizes[49], archwire materials [50], and archwire cross-sections [51]. These factors all have their own influences on resultant torque and can also be explored for the influence on archwire and bracket interactions. The influence from the geometry of orthodontic materials may be further explored in third-order torque contexts by studying the surface response of the archwire. The direct characterisation of the mechanical response of an archwire during third-order torque can produce information that can aid in the development of future fixed appliances.

4.4.2.3 Bracket Deformations

The measurement of tie-wing displacements during third-order torque highlighted how different archwire materials impact the movements of the tie-wings. The distance between the tie-wings were greater when using SS archwires than with TMA archwires. Further, evidence of permanent deformation in the brackets were only seen with SS archwires. This result indicated that the differences in material stiffness of the archwires led to different tie-wing movements during the range of rotation. Further, the maximum distance between tie-wings were larger with SS archwires at 30° loading, which suggests that the torsion regime of the SS archwire may be different from the TMA archwire. The SS archwire may undergo comparatively more rigid body rotation, thus expanding the bracket slot more than the TMA archwire. Comparisons of bracket deformations shows the same tie-wing behaviour as previous literature; however, permanent deformations differed as maximum rotation angles were not consistent between studies.

Initial and final angular positions of 0.019”x0.025” archwires rotated with Damon Q brackets were previously tested with various combinations of loading, which included rotations from -15° to 63° in 3° increments, 0° to 45° in 3° increments, as well as a series from 0° through varying final angles of 16°, 20°, 24°, 28°, 32°, and 40° in 2° increments [18], [43], [46]. For all studies, the angular position of 0° refers to passive position of the archwire with minimal forces and moments imparted onto the bracket, and all studies ended the experiment returning to the initial angle. The permanent bracket deformations from third-order torque were presented with different rotational prescriptions. As such, the presence of permanent bracket deformation as measured by the current 3D DIC setup is validated with respect to bracket behaviour, and the camera system may be used for further investigations measuring both the mechanical responses of archwires and brackets.

Measured deformations and strains of archwires and brackets using 3D DIC yielded a vast number of outputs that can be readily used for further analysis and comparison. By having an appropriate field of view that includes both the archwire and bracket, multiple parameters from third-order torque were simultaneously measured and analysed.

4.5 Conclusion

From this study, the viability of using 3D DIC concurrently with the OTS during third-order torque experiments was detailed. Using an overhead stereo camera system, the OTS operating procedure can be modified to capture images throughout the duration of the experiment. The use of a two-by-two factorial design introduced additional factors such that 3D DIC measurements can be performed and compared. The inclusion of Damon Q brackets as a group showed similarity with past experiments as third-order torque values and tie-wing displacements were comparable with previous literature [47]. The current 3D DIC setup has an expanded field of view which enabled more full-field measurements to be taken throughout an experiment such that archwire and bracket deformations and strains were simultaneously able to be imaged. The 3D DIC results revealed differences in the material responses of the archwires and the brackets between groups when rotated to 30° with the OTS. SS archwires exhibited evidence of plastic deformation by showing residual surface shear strain after unloading when using the RD. In addition, SS archwires caused Damon Q brackets to permanently deform as the tie-wings did not return to their original positions. In contrast, the TMA archwires showed no residual shear strains, and also did not cause Damon Q brackets to permanently deform.

The capabilities of the 3D DIC system were highlighted, and further studies using it can be recommended to fill additional knowledge gaps. The techniques presented in sample preparation and image processing show a meticulous approach to performing 3D DIC with the OTS. The results from 3D DIC are valuable in obtaining more information regarding the mechanism behind third-order torque by measuring both archwire and bracket responses.

CHAPTER 5 CONCLUSIONS, LIMITATIONS, AND FUTURE WORK

5.1 Conclusions

Using the Orthodontic Torque Simulator (OTS) to perform in vitro studies involving third-order torque has contributed to understanding the biomechanics of edgewise orthodontics. The inclusion of three-dimensional (3D) digital image correlation (DIC) with the OTS enables additional datasets involving archwire and bracket deformations to be obtained during third-order torque experiments. The implementation of the 3D DIC system mandated a verification of the system prior to using it for experimental measurements. By capturing 3D DIC images during third-order torque experimentation with clinically representative orthodontic materials, the characterisation of archwire behaviour throughout an applied rotation was measurable through surface deformations and strains.

5.1.1 3D DIC System Verification

To use 3D DIC with the OTS, a meticulous verification of the camera system and its image correlation capabilities was performed to ensure valid measurements of archwire movements during third-order torque. Due to the size of orthodontic appliances, sample preparation involved the development of a speckling technique to capture surface motions during the applied rotation from the OTS. The DIC apparatus was designed to be capable of tracking archwire deformations and strains by using a sufficiently large field of view, as well as a large stereo-angle between the two cameras, allowing for out-of-plane motion to be measured. DIC measurements were evaluated

by comparing measured parameters with both a finite element (FE) model using representative geometry and an analytical solution for torsion of prismatic bars. The 3D DIC system was used to measure various material responses such as deformations in the x-, y-, and z-directions, as well as principal strains in the x- and y-direction and shear strains on the xy-plane.

5.1.2 Third-Order Torque Experimentation using 3D DIC

The DIC setup was then used to measure 3D surface deformations and strains along the IBD of archwires during third-order torque application using the OTS. The stereo camera setup had a field of view that enabled bracket tie-wing displacements to be measured alongside the surface response of the archwire. Stainless steel (SS) and titanium molybdenum alloy (TMA) archwire materials were compared using both the RD and Damon Q brackets in a two-by-two factorial design. In measuring full-field responses of both the archwire and bracket during third-order torque, the simultaneous quantification of archwire deformations and strains as well as tie-wing displacements were made possible. A robust technique to analyse the full-field data was developed to ensure that unique trials were measured in the same manner. In particular, the measurements of surface shear strains mandated careful attention regarding the archwire geometry and how strain was computed given limited surface area. By outputting full-field data into vector maps, probing results became highly repeatable with a well-defined procedure.

In the experiment, archwires were rotated to 30° and back to 0° with the OTS and archwire and tie-wing deformations and archwire shear strains were plotted. It was found that SS archwires may undergo plastic deformation when rotated in the RD, as indicated by residual shear strains, and SS archwires can cause permanent deformation of tie-wings to occur when using Damon Q brackets.

The work completed highlighted the viability of performing 3D DIC to capture both in-plane and out-of-plane motion with the OTS. The stereo-angle of the current system allowed for both archwire and bracket motions to be captured at the same time, despite having distinct z-heights relative to the cameras.

The 3D DIC system used for experimentation was designed to enable out-of-plane measurements, as third-order torque results in the twisting of an archwire. The twist propagates over the span of the archwire, in effect resulting in no region of the archwire exhibiting planar motion. The 3D DIC procedure presented addresses the complexities of the mechanical movements of third-order torque, including the size and geometries of the orthodontic materials, and the expected loading behaviour. The outcome of performing 3D DIC during third-order torque experimentation showed the capabilities of directly measuring surface deformations and strains to get a more comprehensive understanding of third-order torque biomechanics.

5.2 Limitations and Recommendations

Performing 3D DIC with the OTS during third-order torque included several limitations. Although the camera setup had a large field of view for this application, there was still a limit whereby the entire twisted region of the archwire could not be fully imaged. In order to capture the full inter-bracket distance, the field of view would have to be shifted, meaning bracket deformations may not be measurable to the same extent as shown in this study. It may be of interest to see what occurs to the archwire at the boundary condition of the clamp tip, which can serve as a confirmation of the operational effects of the OTS on third-order torque. Currently, the cameras are mounted such that the archwire spans the smaller width of a captured image as opposed to the longer length.

Adapting the camera mounts to have the cameras rotated 90° such that the image length and width are switched may allow for the archwire to span the length of an image; however, it remains to be determined whether this will adversely affect the depth-of-field of the images. In the event that the depth-of-field becomes less suitable in capturing both the archwire and bracket, it may be necessary to use Scheimpflug adapters in the system setup. However, including Scheimpflug adapters inherently increases the magnification while reducing the field of view, where the latter effect may negate any benefits gained from rotating the cameras. This can be studied and compared to have a definitive result for future system setup.

Further, the microscopic scale of the experiment could result in measurements being influenced by the thickness of the applied spray paint coating and speckling. The effects of paint thickness on 3D DIC measurements were not explored in this study, but it is noted that a thinner layer of paint would be more representative of the surface responses relative to thicker layers. While spray painting the archwires, careful attention was used to apply as little paint as possible that still resulted in full coverage of the highly reflective archwire surfaces; however, it was evident that the paint layer had a non-zero thickness. In the small-scale applications of third-order torque (and other orthodontic contexts), it may be desirable to find alternative sample preparation techniques for better efficiency and representation of the surface response. One such technique may be micro-speckle stamping. Stamping can result in smaller speckles compared to the silver-coated microspheres, but there would have to be considerations regarding the reflective surface of the archwire regardless of the speckling.

It was seen during experimentation with Damon Q brackets that the passive position of the archwires resulted in an initial angle such that the imaged surface of the archwire was not parallel

to the xy-plane of the DIC system. This resulted in artificial strain measurements prior to the onset of third-order torque. The strain was actually indicative of rigid body rotation due to the initial perspective of the archwire relative to the cameras. In performing additional studies, rigid body rotation calibrations should be performed to assess how artificial strain develops as a consequence of non-ideal initial archwire angles.

The verification of the DIC setup using FE analysis involved the development of an FE model that had associated assumptions. While representative of the designed and expected load application of the OTS, there were still physical discrepancies and variability in the OTS operations that resulted in deviations from the boundary conditions as presented in the FE model. Obtaining more accurate geometry of physical materials can reduce the assumptions and simplifications made with the model. In particular, the archwire cross-section and rigid dowel slot geometry were both simplified for the FE model. In actuality, these geometries have more complexity and deviations from nominal dimensions that can affect archwire deformation and strain development over an applied rotation. The FE model was used to verify the DIC measurements regarding magnitudes and directionality; however, additional refinements to the FE model can be explored to obtain a better representation of the physical operations of the OTS. Having a refined model can be used to verify additional parameters that may be investigated in the future.

5.3 Future Work

There are various improvements to the 3D DIC system that can be utilised for future studies. Having expanded 3D DIC measurement capabilities can contribute to more comprehensive understandings of the interactions between the various factors associated with third-order torque.

Additional experiments can be performed with archwires of various materials, cross-sections, IBDs, as well as using other orthodontic brackets designed for third-order torque. The capabilities of 3D DIC measuring archwire deformations and strains can lead to further experimentation where archwire behaviour is suspected to play a significant role in third-order torque mechanics. This can lead to critical comparisons between orthodontic materials and aid with the clinical application of third-order torque. Further, results from 3D DIC can be used in tandem with new FE models that include additional model parameters such as bracket geometries. A valid 3D DIC measurement system can provide additional confidence in the accuracy of the FE analyses.

With respect to the physical DIC apparatus, the stereo setup was capable of measuring deformation and strain fields of a single surface of the archwire. It may be seen in future testing that imaging multiple surfaces or focusing on the rounded corners is desirable. A reconfiguration of the 3D DIC system to include additional cameras or reorientation of the existing cameras with respect to the OTS may be explored to image different regions of interest and consequently additional interactions between an archwire and bracket during third-order torque.

The OTS has been used extensively to study third-order torque mechanics. The inclusion of 3D DIC with the OTS enables more experimentation and data collection regarding third-order torque. In particular, the direct characterisation of orthodontic materials can be used to complement the insights gained from measured forces and moments that arise during loading. The work presented detailed the comprehensive system setup and DIC analysis of third-order torque experiments using the OTS. Further experimentation, including the recommendations and future work avenues listed can improve the performance of 3D DIC with the OTS, allowing for more complex third-order torque mechanics to be investigated.

BIBLIOGRAPHY

[1] Canadian Institute for Health Information, “National Health Expenditure Trends, 1975 to 2014,” 2014.

[2] S. Walker, C. Flores-mir, G. Heo, M. Amin, and L. Keenan, “Work Pattern Differences Between Male and Female Orthodontists in Canada,” *J. Can. Dent. Assoc. (Tor).*, 2016.

[3] Canadian Dental Association, “Orthodontics at Any Age.” [Online]. Available: http://www.cda-adc.ca/en/oral_health/procedures/orthodontics/. [Accessed: 01-Nov-2019].

[4] R. Khosravi, “Biomechanics in lingual orthodontics: What the future holds,” *Semin. Orthod.*, vol. 24, no. 3, pp. 363–371, 2018.

[5] T. Nguyen and T. Jackson, “3D technologies for precision in orthodontics,” *Semin. Orthod.*, vol. 24, no. 4, pp. 386–392, 2018.

[6] N. Al Mortadi, D. Eggbeer, J. Lewis, and R. J. Williams, “CAD/CAM/AM applications in the manufacture of dental appliances,” *Am. J. Orthod. Dentofac. Orthop.*, vol. 142, no. 5, pp. 727–733, 2012.

[7] M. O’Toole, Ed., *Miller-Keane Encyclopedia and Dictionary of Medicine, Nursing, and Allied Health, Seventh Edition*. 2003.

[8] R. S. Masella and M. Meister, “Current concepts in the biology of orthodontic tooth movement,” *Am. J. Orthod. Dentofac. Orthop.*, vol. 129, no. 4, pp. 458–468, 2006.

[9] C. Reichert, M. Hagner, S. Jepsen, and A. Jäger, “Interfaces between orthdontic and

periodontal treatment: Their current status," *J. Orofac. Orthop.*, vol. 72, no. 3, pp. 165–186, 2011.

[10] M. A. Asiry, "Biological aspects of orthodontic tooth movement: A review of literature," *Saudi J. Biol. Sci.*, vol. 25, no. 6, pp. 1027–1032, 2018.

[11] A. Consolaro and L. Z. Furquim, "Extreme root resorption associated with induced tooth movement: A protocol for clinical management," *Dental Press J. Orthod.*, vol. 19, no. 5, pp. 19–26, 2014.

[12] E. D. Rauch, "Torque and its application to orthodontics," *Am. J. Orthod.*, vol. 45, no. 11, pp. 817–830, 1959.

[13] H. M. Badawi, R. W. Toogood, J. P. Carey, G. Heo, and P. W. Major, "Torque expression of self-ligating brackets," *Am. J. Orthod. Dentofac. Orthop.*, vol. 133, no. 5, pp. 721–728, 2008.

[14] M. G. George *et al.*, "Comparison of third-order torque simulation with and without a periodontal ligament simulant," *Am. J. Orthod. Dentofac. Orthop.*, vol. 148, no. 3, pp. 431–439, 2015.

[15] D. L. Romanyk, A. George, Y. Li, G. Heo, J. P. Carey, and P. W. Major, "Influence of second-order bracket-archwire misalignments on loads generated during third-order archwire rotation in orthodontic treatment," *Angle Orthod.*, vol. 86, no. 3, pp. 358–364, 2016.

[16] G. W. Melenka, D. S. Nobes, P. W. Major, and J. P. Carey, "Design of an orthodontic torque

simulator for measurement of bracket deformation," *Sens. Imaging*, vol. 14, no. 3–4, pp. 57–80, 2013.

[17] International Digital Image Correlation Society, *A Good Practices Guide for Digital Image Correlation*. 2018.

[18] G. W. Melenka, D. S. Nobes, J. P. Carey, and P. W. Major, "Three-dimensional deformation comparison of self-ligating brackets," *Am. J. Orthod. Dentofac. Orthop.*, vol. 143, no. 5, pp. 645–657, 2013.

[19] J. Philippe, "How, why, and when was the edgewise appliance born?," *J. Dentofac. Anomalies Orthod.*, vol. 11, no. 1, pp. 68–74, 2010.

[20] G. L. U. Ribeiro and H. B. Jacob, "Understanding the basis of space closure in Orthodontics for a more efficient orthodontic treatment," *Dental Press J. Orthod.*, vol. 21, no. 2, pp. 115–125, 2016.

[21] A. Archambault, R. Lacoursiere, H. Badawi, P. W. Major, J. P. Carey, and C. Flores-Mir, "Torque expression in stainless steel orthodontic brackets," *Angle Orthod.*, vol. 80, no. 1, pp. 201–210, 2010.

[22] B. Moesi, F. Dyer, and P. E. Benson, "Roth versus MBT: Does bracket prescription have an effect on the subjective outcome of pre-adjusted edgewise treatment?," *Eur. J. Orthod.*, vol. 35, no. 2, pp. 236–243, 2013.

[23] I. P. Lin, E. H. H. Lai, J. Z. C. Chang, and C. Y. Wang, "Staged orthodontic treatment in preparation for immediate implant placement: A clinical report with a 5-year follow-up," *J.*

Prosthet. Dent., pp. 1–7, 2019.

[24] R. C. Parkhouse, "Rectangular wire and third-order torque: A new perspective," *Am. J. Orthod. Dentofac. Orthop.*, vol. 113, no. 4, pp. 421–430, 2006.

[25] R. J. Isaacson, S. J. Lindauer, and L. K. Rubenstein, "Moments with the edgewise applicance: Incisor torque control," *Am. J. Orthod. Dentofac. Orthop.*, vol. 103, no. 5, pp. 428–438, 1993.

[26] M. F. Sfondrini *et al.*, "Buccolingual Inclination Control of Upper Central Incisors of Aligners: A Comparison with Conventional and Self-Ligating Brackets," *Biomed Res. Int.*, vol. 2018, pp. 1–7, 2018.

[27] D. Friedrich, N. Rosarius, G. Rau, and P. Diedrich, "Measuring system for in vivo recording of force systems in orthodontic treatment-concept and analysis of accuracy," *J. Biomech.*, vol. 32, no. 1, pp. 81–85, 1999.

[28] M. Knösel, D. Kubein-Meesenburg, and R. Sadat-Khonsaric, "The third-order angle and the maxillary incisor's inclination to the NA line," *Angle Orthod.*, vol. 77, no. 1, pp. 82–87, 2007.

[29] M. Mittal, B. Thiruvenkatachari, P. J. Sandler, and P. E. Benson, "A three-dimensional comparison of torque achieved with a preadjusted edgewise appliance using a Roth or MBT prescription," *Angle Orthod.*, vol. 85, no. 2, pp. 292–297, 2015.

[30] P. M. Cattaneo, R. A. Salih, and B. Melsen, "Labio-lingual root control of lower anterior teeth and canines obtained by active and passive self-ligating brackets," *Angle Orthod.*, vol.

83, no. 4, pp. 691–697, 2013.

[31] S. N. Papageorgiou, L. Keilig, V. Vandevska-Radunovic, T. Eliades, and C. Bourauel, “Torque differences due to the material variation of the orthodontic appliance: a finite element study,” *Prog. Orthod.*, vol. 18, no. 1, pp. 4–11, 2017.

[32] S. N. Papageorgiou *et al.*, “Torque differences according to tooth morphology and bracket placement: a finite element study,” *Eur. J. Orthod.*, vol. 39, no. 4, pp. 411–418, 2017.

[33] V. Jayade, S. Annigeri, C. Jayade, and P. Thawani, “Biomechanics of Torque from Twisted Rectangular Archwires A Finite Element Investigation,” *Angle Orthod.*, vol. 77, no. 2, p. 214, 2007.

[34] A. Sardarian, S. M. danaei, S. Shahidi, S. G. Boushehri, and A. Geramy, “The effect of vertical bracket positioning on torque and the resultant stress in the periodontal ligament—a finite element study,” *Prog. Orthod.*, vol. 15, no. 1, pp. 1–10, 2014.

[35] Y. Huang *et al.*, “Numeric modeling of torque capabilities of self-ligating and conventional brackets,” *Am. J. Orthod. Dentofac. Orthop.*, vol. 136, no. 5, pp. 638–643, 2009.

[36] Y. Huang, L. Keilig, A. Rahimi, S. Reimann, and C. Bourauel, “Torque capabilities of self-ligating and conventional brackets under the effect of bracket width and free wire length,” *Orthod. Craniofacial Res.*, vol. 15, no. 4, pp. 255–262, 2012.

[37] J. Tominaga, M. Tanaka, T. Koga, C. Gonzales, M. Kobayashi, and N. Yoshida, “Optimal Loading Conditions for Controlled Movement of Anterior Teeth in Sliding Mechanics,” *Angle Orthod.*, vol. 79, no. 6, pp. 1102–1107, 2009.

[38] J. Y. Tominaga *et al.*, "Effect of bracket slot and archwire dimensions on anterior tooth movement during space closure in sliding mechanics: A 3-dimensional finite element study," *Am. J. Orthod. Dentofac. Orthop.*, vol. 146, no. 2, pp. 166–174, 2014.

[39] A. Archambault, T. W. Major, J. P. Carey, G. Heo, H. Badawi, and P. W. Major, "A comparison of torque expression between stainless steel, titanium molybdenum alloy, and copper nickel titanium wires in metallic self-ligating brackets," *Angle Orthod.*, vol. 80, no. 5, pp. 884–889, 2010.

[40] T. W. Major, J. P. Carey, D. S. Nobes, G. Heo, and P. W. Major, "Mechanical effects of third-order movement in self-ligated brackets by the measurement of torque expression," *Am. J. Orthod. Dentofac. Orthop.*, vol. 139, no. 1, pp. e31–e44, 2011.

[41] D. L. Romanyk, K. Au, D. Isfeld, G. Heo, M. P. Major, and P. W. Major, "The effect of buccal-lingual slot dimension size on third-order torque response," *Eur. J. Orthod.*, vol. 39, no. 2, pp. 209–214, 2017.

[42] T. W. Major, J. P. Carey, D. S. Nobes, G. Heo, and P. W. Major, "Deformation and warping of the bracket slot in select self-ligating orthodontic brackets due to an applied third order torque," *J. Orthod.*, vol. 39, no. 1, pp. 25–33, 2012.

[43] T. W. Major, J. P. Carey, D. S. Nobes, G. Heo, and P. W. Major, "Measurement of plastic and elastic deformation due to third-order torque in self-ligated orthodontic brackets," *Am. J. Orthod. Dentofac. Orthop.*, vol. 140, no. 3, pp. 326–339, 2011.

[44] H. Al Fakir, J. P. Carey, G. W. Melenka, D. S. Nobes, G. Heo, and P. W. Major,

"Investigation into the effects of stainless steel ligature ties on the mechanical characteristics of conventional and self-ligated brackets subjected to torque," *J. Orthod.*, vol. 41, no. 3, pp. 188–200, 2014.

[45] R. A. Lacoursiere, D. S. Nobes, D. L. N. Homeniuk, J. P. Carey, H. H. Badawi, and P. W. Major, "Measurement of orthodontic bracket tie wing elastic and plastic deformation by arch wire torque expression utilizing an optical image correlation technique," *J. Dent. Biomech.*, vol. 1, no. 1, pp. 1–7, 2010.

[46] T. W. Major, J. P. Carey, D. S. Nobes, G. Heo, G. W. Melenka, and P. W. Major, "An investigation into the mechanical characteristics of select self-ligated brackets at a series of clinically relevant maximum torquing angles: Loading and unloading curves and bracket deformation," *Eur. J. Orthod.*, vol. 35, no. 6, pp. 719–729, 2013.

[47] G. W. Melenka, D. S. Nobes, P. W. Major, and J. P. Carey, "Three-dimensional deformation of orthodontic brackets," *J. Dent. Biomech.*, vol. 4, no. 1, pp. 1–15, 2013.

[48] D. Drescher, C. Bourauel, and M. Thier, "Application of the orthodontic measurement and simulation system (OMSS) in orthodontics," *Eur. J. Orthod.*, vol. 13, no. 3, pp. 169–178, 1991.

[49] I. Sifakakis, N. Pandis, M. Makou, T. Eliades, C. Katsaros, and C. Bourauel, "Torque expression of 0.018 and 0.022 inch conventional brackets," *Eur. J. Orthod.*, vol. 35, no. 5, pp. 610–614, 2013.

[50] I. Sifakakis, N. Pandis, M. Makou, T. Eliades, C. Katsaros, and C. Bourauel, "Torque

efficiency of different archwires in 0.018- and 0.022-inch conventional brackets," *Angle Orthod.*, vol. 84, no. 1, pp. 149–154, 2014.

[51] S. N. Papageorgiou, I. Sifakakis, I. Doulis, T. Eliades, and C. Bourauel, "Torque efficiency of square and rectangular archwires into 0.018 and 0.022 in. conventional brackets," *Prog. Orthod.*, vol. 17, no. 1, pp. 4–9, 2016.

[52] N. Daratsianos, C. Bourauel, R. Fimmers, A. Jäger, and R. Schwestka-Polly, "In vitro biomechanical analysis of torque capabilities of various 0.018" lingual bracket-wire systems: total torque play and slot size," *Eur. J. Orthod.*, vol. 38, no. 5, pp. 459–469, 2016.

[53] A. Arreghini, L. Lombardo, F. Mollica, and G. Siciliani, "Bracket Slots By Changing Archwire Material and Cross Section," pp. 1–18, 2014.

[54] M. M. Huda, E. Siregar, and N. Ismah, "Slot deformation of various stainless steel bracket due to the torque force of the beta-titanium wire," *J. Phys. Conf. Ser.*, vol. 884, no. 1, 2017.

[55] J. Sebanc, W. A. Brantley, J. J. Pincsak, and J. P. Conover, "Variability of effective root torque as a function of edge bevel on orthodontic arch wires," *Am. J. Orthod.*, vol. 86, no. 1, pp. 43–51, 1984.

[56] T. R. Meling and J. Ødegaard, "The effect of cross-sectional dimensional variations of square and rectangular chrome-cobalt archwires on torsion," *Angle Orthod.*, vol. 68, no. 3, pp. 239–248, 1998.

[57] T. R. Meling and J. Ødegaard, "On the variability of cross-sectional dimensions and torsional properties of rectangular nickel-titanium arch wires.," *Am. J. Orthod. Dentofac.*

Orthop., vol. 113, no. 5, pp. 546–557, 1998.

[58] L. Lombardo *et al.*, "Comparative analysis of real and ideal wire-slot play in square and rectangular archwires," *Angle Orthod.*, vol. 85, no. 5, pp. 848–858, 2015.

[59] C. Gioka and T. Eliades, "Materials-induced variation in the torque expression of preadjusted appliances," *Am. J. Orthod. Dentofac. Orthop.*, vol. 125, no. 3, pp. 323–328, 2004.

[60] T. W. Major, J. P. Carey, D. S. Nobes, and P. W. Major, "Orthodontic bracket manufacturing tolerances and dimensional differences between select self-ligating brackets," *J. Dent. Biomech.*, vol. 1, no. 1, pp. 1–6, 2010.

[61] J. De A. Gurgel, S. Kerr, J. M. Powers, and A. Pinzan, "Torsional properties of commercial nickel-titanium wires during activation and deactivation," *Am. J. Orthod. Dentofac. Orthop.*, vol. 120, no. 1, pp. 76–79, 2001.

[62] J. Ødegaard, T. R. Meling, and E. Ø. Meling, "The effects of loops on the torsional stiffness of rectangular wires: An in vitro study," *Am. J. Orthod. Dentofac. Orthop.*, vol. 109, no. 5, pp. 496–505, 1996.

[63] T. R. Meling and J. Ødegaard, "The effect of temperature on the elastic responses to longitudinal torsion of rectangular nickel titanium archwires," *Angle Orthod.*, vol. 68, no. 4, pp. 357–368, 1998.

[64] R. P. Kusy and J. Q. Whitley, "Influence of archwire and bracket dimensions on sliding mechanics: Derivations and determinations of the critical contact angles for binding," *Eur.*

J. Orthod., vol. 21, no. 2, pp. 199–208, 1999.

[65] M. Chung, R. J. Nikolai, K. B. Kim, and D. R. Oliver, "Third-order torque and self-ligating orthodontic bracket-type effects on sliding friction," *Angle Orthod.*, vol. 79, no. 3, pp. 551–557, 2009.

[66] L. C. Articolo, K. Kusy, C. R. Saunders, and R. P. Kusy, "Influence of ceramic and stainless steel brackets on the notching of archwires during clinical treatment," *Eur. J. Orthod.*, vol. 22, no. 4, pp. 409–425, 2000.

[67] M. A. Sutton, J.-J. Orteu, and H. W. Schreier, *Image Correlation for Shape, Motion and Deformation Measurements: Basic Concepts, Theory and Applications*, 1st ed. New York: Springer US, 2009.

[68] P. Reu, "Stereo-rig Design : Stereo-Angle Selection — Part 4," vol. 37, pp. 1–2, 2013.

[69] LaVision GmbH, *DaVis 8.2 StrainMaster Product-Manual, Item-Number: 1003017*. 2014.

[70] F. Bethmann and T. Luhmann, "Least-Squares Matching With Advanced Geometric Transformation Models," *Int. Arch. Photogramm. Remote Sens. Spat. Inf. Sci.*, vol. 38, pp. 86–91, 2010.

[71] P. Reu, "Stereo-rig Design : Camera Selection — Part 2," vol. 36, pp. 3–4, 2012.

[72] P. Reu, "Stereo-rig Design : Lens Selection — Part 3," vol. 37, pp. 1–3, 2013.

[73] P. Reu, "Calibration: 2D Calibration," *Exp. Tech.*, vol. 37, no. 5, pp. 1–2, 2013.

[74] P. Reu, “Calibration: Stereo Calibration,” *Exp. Tech.*, vol. 38, no. 1, pp. 1–2, 2014.

[75] Y. L. Dong and B. Pan, “A Review of Speckle Pattern Fabrication and Assessment for Digital Image Correlation,” *Exp. Mech.*, vol. 57, no. 8, pp. 1161–1181, 2017.

[76] P. Reu, “All about Speckles : Contrast,” vol. 51, no. 4, pp. 1–2, 2015.

[77] R. Roncella, E. Romeo, L. Barazzetti, M. Gianinetto, and M. Scaioni, “Comparative Analysis of Digital Image Correlation Techniques for In-plane Displacement Measurements,” in *5th International Congress on Image and Signal Processing, CISP 2012*, 2012.

[78] B. Pan, A. Asundi, H. Xie, and J. Gao, “Digital image correlation using iterative least squares and pointwise least squares for displacement field and strain field measurements,” *Opt. Lasers Eng.*, vol. 47, no. 7–8, pp. 865–874, 2009.

[79] T. R. Meling, J. Ødegaard, and E. Ø. Meling, “On mechanical properties of square and rectangular stainless steel wires tested in torsion.,” *Am. J. Orthod. Dentofacial Orthop.*, vol. 111, no. 3, pp. 310–320, 1997.

[80] LaVision GmbH, *Davis 8.4 Imaging Tools Product-Manual, Item-Number(s): 1005xxx*. 2017.

[81] LaVision GmbH, *Davis 7.2 StrainMaster Software Product-Manual, Item Number: 1105022*. 2006.

[82] D. J. Fleet and Y. Weiss, “Optical Flow Estimation,” in *Mathematical Models in Computer*

Vision: A Handbook, N. Paragios, Y. Chen, and O. D. Faugeras, Eds. Boston: Springer, 2005, pp. 239–258.

[83] Ormco Corporation, "Ormco Archwires." [Online]. Available: https://ormco.com/products/archwires.php.

[84] Fort Wayne Metals, "304V." [Online]. Available: https://www.fwmetals.com/materials/stainless-steel/304v/.

[85] ANSYS Inc., "ANSYS® Academic Research Mechanical, Release 19.2." .

[86] R. J. Roark, W. C. Young, and R. G. Budynas, *Roark's Formulas for Stress and Strain*, 7th ed. New York: McGraw-Hill, 2002.

[87] S. Timoshenko and J. N. Goodier, *Theory of Elasticity*, 3rd ed. New York: McGraw-Hill, 1970.

[88] R Core Team, "R: A language and environment for statistical computing." R Foundation for Statistical Computing, Vienna, Austria, 2017.

[89] H. Wickham, *ggplot2: Elegant Graphics for Data Analysis*. Springer-Verlag New York, 2016.

[90] H. Wickham, "tidyverse: Easily Install and Load the 'Tidyverse.'" 2017.

[91] F. Moisy, "PIVMat - A PIV post-processing and data analysis toolbox for Matlab." 2017.

[92] A. Biguri, "Perceptually uniform colormaps." 2019.

[93] G. W. Melenka, R. A. Lacoursiere, J. P. Carey, D. S. Nobes, G. Heo, and P. W. Major, "Comparison of deformation and torque expression of the orthos and orthos Ti bracket systems," *Eur. J. Orthod.*, vol. 36, no. 4, pp. 381–388, 2014.

[94] M. Hirai *et al.*, "Measurements of the torque moment in various archwire-bracket-ligation combinations," *Eur. J. Orthod.*, vol. 34, no. 3, pp. 374–380, 2012.

[95] A. S. et mult. al., "DescTools: Tools for Descriptive Statistics." 2019.

[96] Cospheric, "Conductive Silver Metal Coated Soda Lime Solid Glass Microspheres - Classified Grades - Various sizes 1 um to 180 um." [Online]. Available: https://www.cospheric.com/SLGMSAG_silver_coated_solid_glass_spheres_beads.htm.

[97] Matweb LLC, "304 Stainless Steel." [Online]. Available: http://matweb.com/search/DataSheet.aspx?MatGUID=abc4415b0f8b490387e3c922237098da&ckck=1.

[98] ANSYS Inc., *ANSYS® Mechanical Application 19.2, Mechanical User's Guide*. 2018.

[99] P. Lu, J. Liu, and D. Koestler, "pwr2: Power and Sample Size Analysis for One-way and Two-way ANOVA Models." 2017.

APPENDIX A RIGID DOWEL REUSABILITY

The same rigid dowel (RD) was used throughout experimentation with third-order torque. To justify the use of a single RD, it was necessary to confirm that the RD did not exhibit plastic deformation or wear from applied torques that would lead to decreased torque magnitudes as testing progressed.

A.1 Initial RD Usage in Previous Experiments

The RD used during experimentation with digital image correlation (DIC) had previously been used in internal testing with nickel titanium archwires. In the previous third-order torque tests with the RD, 0.019”x0.025” nickel titanium archwires were rotated to a maximum angle of 46° in 2° increments. Eight trials were tested with the archwires, using a new archwire with every test. The torque values at 46° loading are plotted in sequence and shown in Figure A.1. Note the absolute values of torque are shown to better indicate trends of decrease torque if such a trend exists.

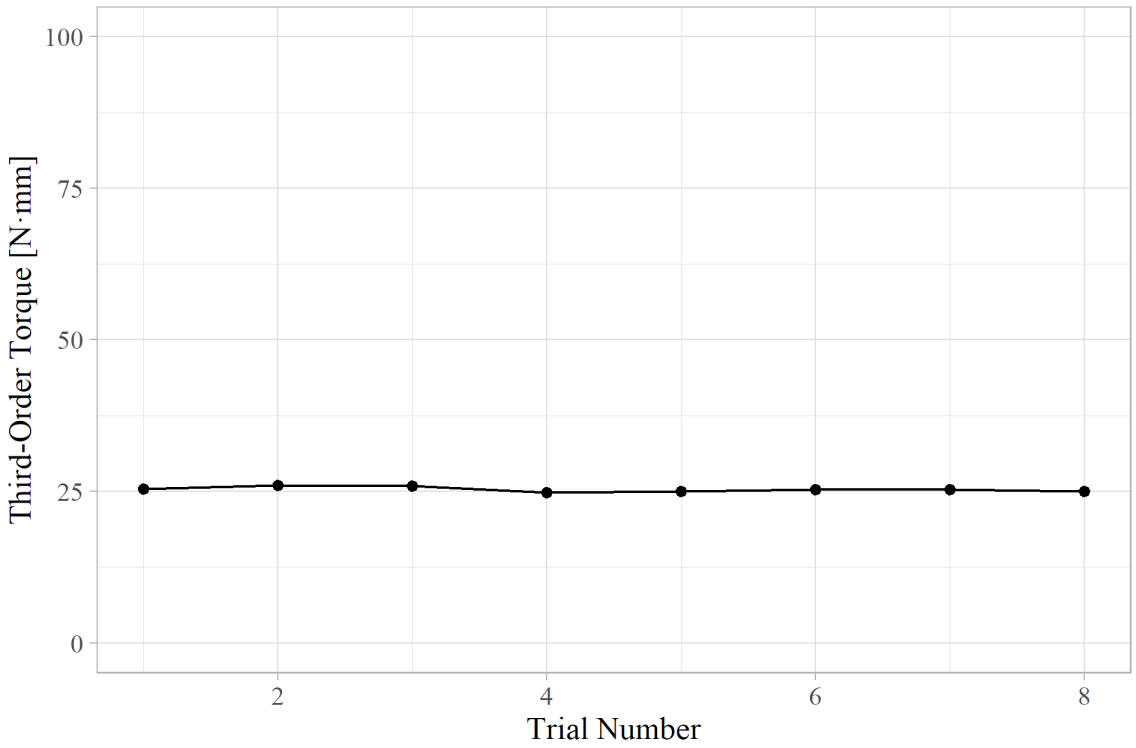

Figure A.1. Maximum torque magnitudes over sequential third-order experiments using 0.019”x0.025” nickel titanium archwires rotated to 46°.

The average torque measured between the eight trials was -25.34 N·mm, with a standard deviation of 0.44 N·mm. It was seen in the testing that the maximum torque magnitudes did not sequentially decrease over the span of testing. This provided confidence that a single RD could be used for testing.

A.2 RD Usage During Experimentation

Since the RD was used throughout DIC experimentation, maximum third-order torque data could be analysed to see if any significant drops in torque was perceived as testing progressed.

A.2.1 Chapter 3 RD Usage

In Chapter 3, 10 trials using stainless steel (SS) archwires (Ormco Corporation, California, USA) with the RD were tested in sequence, rotating to 30° in 1° increments. The torque values at 30° loading are shown in Figure A.2.

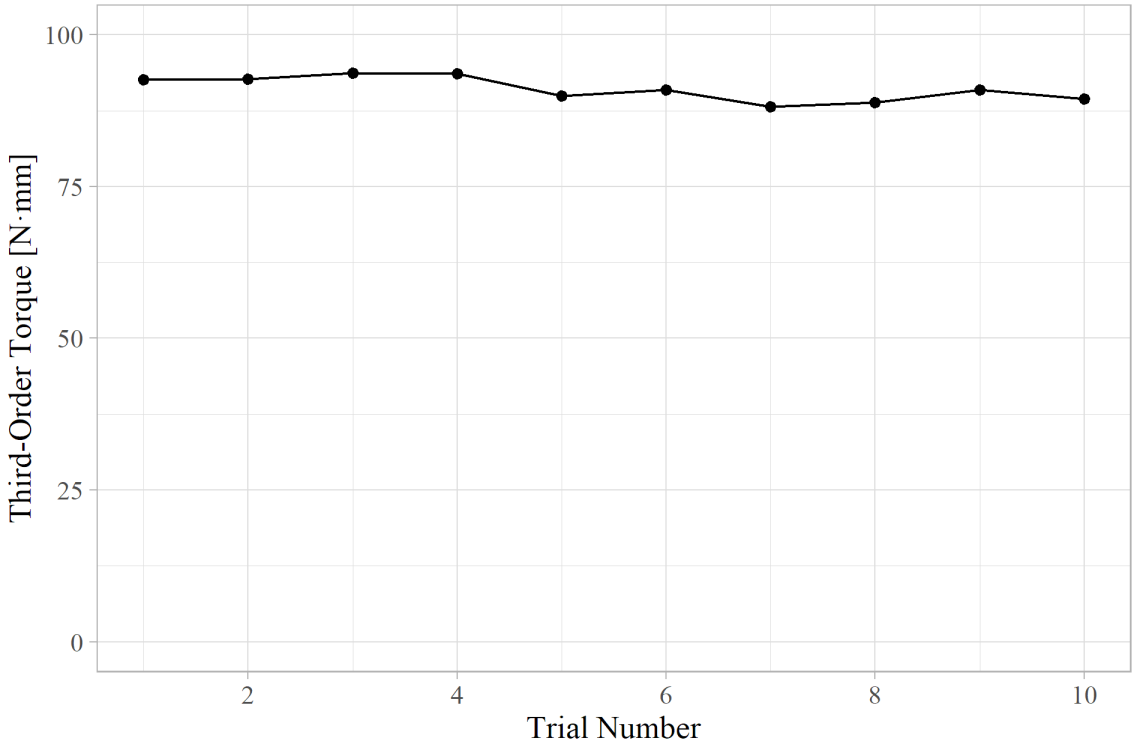

Figure A.2. Maximum torque magnitudes over sequential third-order experiments using 0.019”x0.025” stainless steel archwires rotated to 30°.

Over the 10 trials with SS archwires, the average torque was -91.09 N·mm with a standard deviation of 1.99 N·mm. The torque values did not decrease sequentially even at higher torque magnitudes.

A.2.2 Chapter 4 RD Usage

In Chapter 4, 23 trials were each performed using SS and titanium molybdenum alloy (TMA) archwires (G&H Orthodontics, Indiana, USA), rotating to 30° in 1° increments. During testing, the sequence between SS and TMA archwires was randomised; however, for further confirmation that the RD was reusable, the results were separated by material and maximum torques were plotted in order of testing. The torque values at 30° loading are shown in Figure A.3.

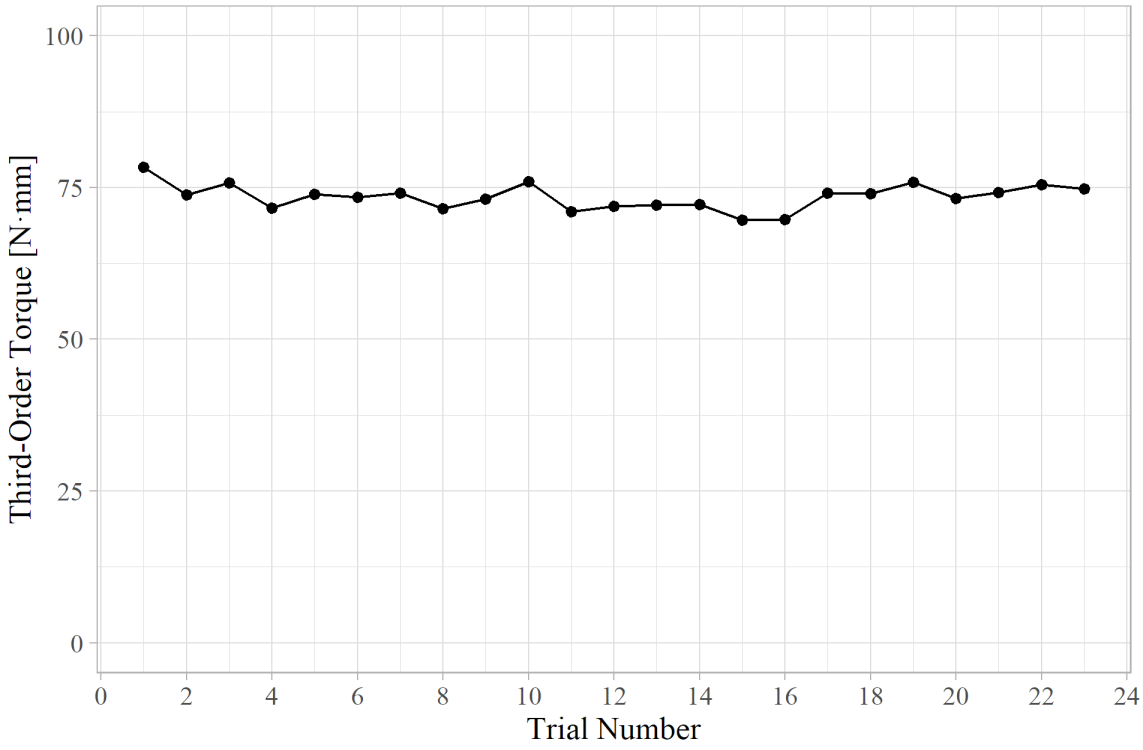

(a)

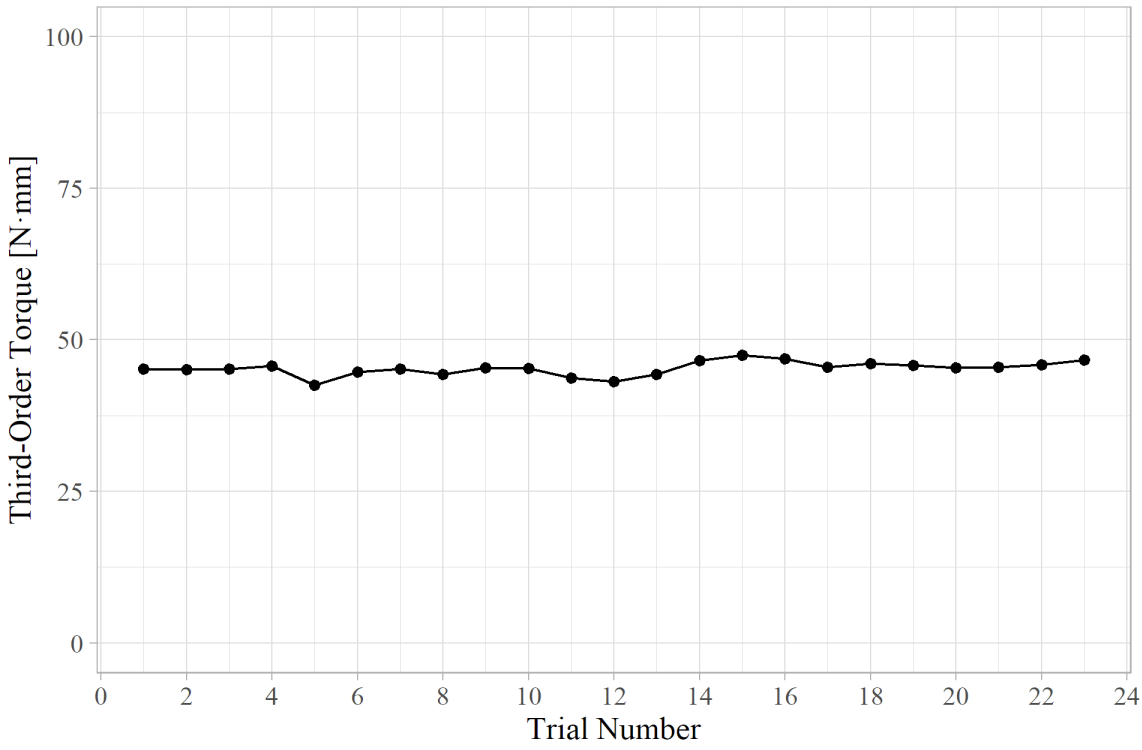

(b)

Figure A.3. Maximum torque magnitudes over third-order experiments using 0.019”x0.025” (a) stainless steel and (b) titanium molybdenum alloy archwires rotated to 30°. Plots are separated by material and resequenced in order of testing.

The average torque and standard deviations for the SS archwires were -73.48 N·mm and 2.10 N·mm, respectively; and were -45.28 N·mm and 1.16 N·mm for the TMA archwires, respectively. Though the testing was not sequential as archwire materials were randomly interchanged, evidence of a decreased torque magnitude over the testing for each material should still be apparent if the RD degrades over time. Ultimately, there was no indication that there was a relationship between maximum torque magnitude and continued testing using a single RD.

A.3 R Code

Figures created using R were done so using the "ggplot2" package as a part of the "tidyverse" package collection [89], [90]. Means and standard deviations were calculated using the "DescTools" package [95].

For all four plots shown, data was tabulated within one data frame, where the columns were organised as:

Material: Indicates the archwire material as "NiTi" or "StSt" for the first two plots, and "SS" and "TMA" for the latter two as character variables

Trial: Indicates trial number as a numeric variable

Torque: Indicates measured maximum third-order torque as a numeric variable

The R code is shown below:

```
# Load libraries
library(tidyverse)
library(DescTools)

# Create variable containing string of where data is saved

filepath <- file.path(
  "[personal filepath redacted]"
)
# Set working directory
setwd(filepath)

# Initiate vector with material labels
mat <- c("NiTi", "StSt", "SS", "TMA")

# Use for loop to create plots for all four material instances
for (i in mat) {
data <- read_csv("RD_MaxTorqueValidation.csv")
data$Torque <- -1*data$Torque
data <- filter(data, Material == i)
```

```
Desc(data)

p1 <- ggplot(data = data, mapping = aes(
  x = data$Trial,
  y = data$Torque
)) +
  geom_point() +
  geom_line() +
  ylim(0, 100) +
  scale_x_continuous(limits = c(0, length(data$Torque)),
                     breaks = seq(0, RoundTo(length(data$Torque), 2,
ceiling), 2))+
  labs(x = "Trial Number", y = "Third-Order Torque [N·mm]") +
  theme_light() +
  theme(
    text = element_text(size = 12, family = "serif")
  )
p1
ggsave(paste0("RDValidation_", i, ".png"), width = 6, height = 4, units =
"in", dpi = 320)
}
```

APPENDIX B ORTHODONTIC TORQUE SIMULATOR GEAR TRAIN BACKLASH

The Orthodontic Torque Simulator (OTS) uses a stepper motor to drive the rotation of the clamp housing. The motor shaft is coupled to a worm gear, and the clamp housing is coupled to a spur gear. When the stepper motor changes direction, there is backlash in the gear train where the clearance between gear teeth elicits a small amount of worm gear rotation prior to re-establishing contact with the spur gear. This backlash results in a small discrepancy of angular position between the program inputs and the physical OTS. The effect of backlash can increase over time as the mechanical components are subject to wearing.

To quantify the backlash in the OTS, an experiment was conducted by a previous lab researcher to measure the differences in angular input versus the actual measured angle. The OTS was rotated from 0° to 15° and back to 0° in 3° increments, in which the angles were measured in the loading and unloading directions. The experimental procedure included rotation with and without and archwire clamped in the housing, and 30 trials were performed for either condition.

In calculating the backlash, angular measurements at 0° and 15° were discarded to isolate the measured values from the change in direction and consequent backlash. If these values were included, it may have been possible that the angular measurements were not actually realised in the physical system due to backlash not being fully removed during the change in direction. The remaining angles between 3°, 6°, 9°, and 12° were used to take the differences in measured angles when loading and unloading, and the differences were averaged for each trial. Finally, all values were averaged for loading and unloading, and averaged once more to compute backlash as 1.0298°.

For all OTS trials, an angular correction of 1.0298° is applied to unloading angular positions to account for the backlash. This is seen graphically when examining charts with measurements as a function of angle. The measured differences from the backlash experiments are reported in Table B.1.

Table B.1. Average differences in angular position when loading and unloading the OTS with and without an archwire in the clamp housing.

Trial	Average Difference with Archwire [°]	Average Difference without Archwire [°]
1	1.00	0.90
2	1.10	1.20
3	1.05	1.10
4	1.10	1.05
5	0.95	0.95
6	1.00	1.10
7	1.25	0.95
8	1.05	0.90
9	1.15	1.05
10	1.35	1.05
11	1.45	1.00
12	1.35	1.00
13	1.10	1.00
14	1.30	1.20
15	1.00	1.05
16	1.00	1.10
17	1.20	0.95
18	1.00	0.95
19	1.05	1.00
20	0.90	1.00
21	1.15	1.05
22	1.05	1.20
23	0.95	1.05
24	1.05	1.10
25	1.05	1.05
26	1.10	1.05
27	0.95	1.00
28	1.00	1.00
29	1.00	1.05
30	1.15	1.00
Average	1.0581	1.0016

It can be recommended that as additional experimentation is performed using the OTS, backlash should be updated to account for further degradation of the gear train tolerance from continued use.

APPENDIX C SPECIMEN SPECKLING PROCEDURE

The initial speckling technique involved using matte black spray paint (Sherwin-Williams, Ohio, USA) applied in thin layers to ensure an even coating on the corrugated fibreboard surface. The speckles were created using diluted white acrylic paint. The paint was applied using a siphon-fed airbrush (Paasche H-Series, Paasche Airbrush Co., Wisconsin, USA). The input air pressure and distance between the airbrush nozzle and test specimen were sequentially varied to determine the nature of the speckle deposition on the spray-painted surface. The air pressure was varied between 20-60 psi in 10 psi increments, and distance between the nozzle tip and specimen was held constant at 10 cm. The speckled corrugated fibreboard samples were compared to evaluate the size and distribution of the speckles. It was found that the samples sprayed at 60 psi had the most uniform speckle size and the least amount of blotchiness. Moving forward using 60 psi as the input air pressure, distance was then varied at 5, 10, and 20 cm by measuring the distance between the samples and airbrush nozzle with a standard ruler prior to spraying. When the nozzle was at 5 cm, speckle density was too high, and when the nozzle was at 20 cm, speckle quality was not as consistent as at 10 cm. Ultimately, speckling with an air pressure of 60 psi and spraying at a distance of 10 cm was the most suitable. The differences in speckles when varying nozzle pressure while keeping nozzle distance constant at 10 cm are shown in Figure C.1; and similarly, differences in speckles when vary nozzle distance while keeping nozzle pressure constant at 60 psi are shown in Figure C.2. When the speckles were applied from the shortest distance of 5 cm, it was found that the speckle density became too high and the contrast between the speckles and the background was poor. When spraying from larger distances of 10 cm or 20 cm, the effect was mitigated, and

the speckle density resulted in better contrast and speckles showed small variation in size over the surface area.

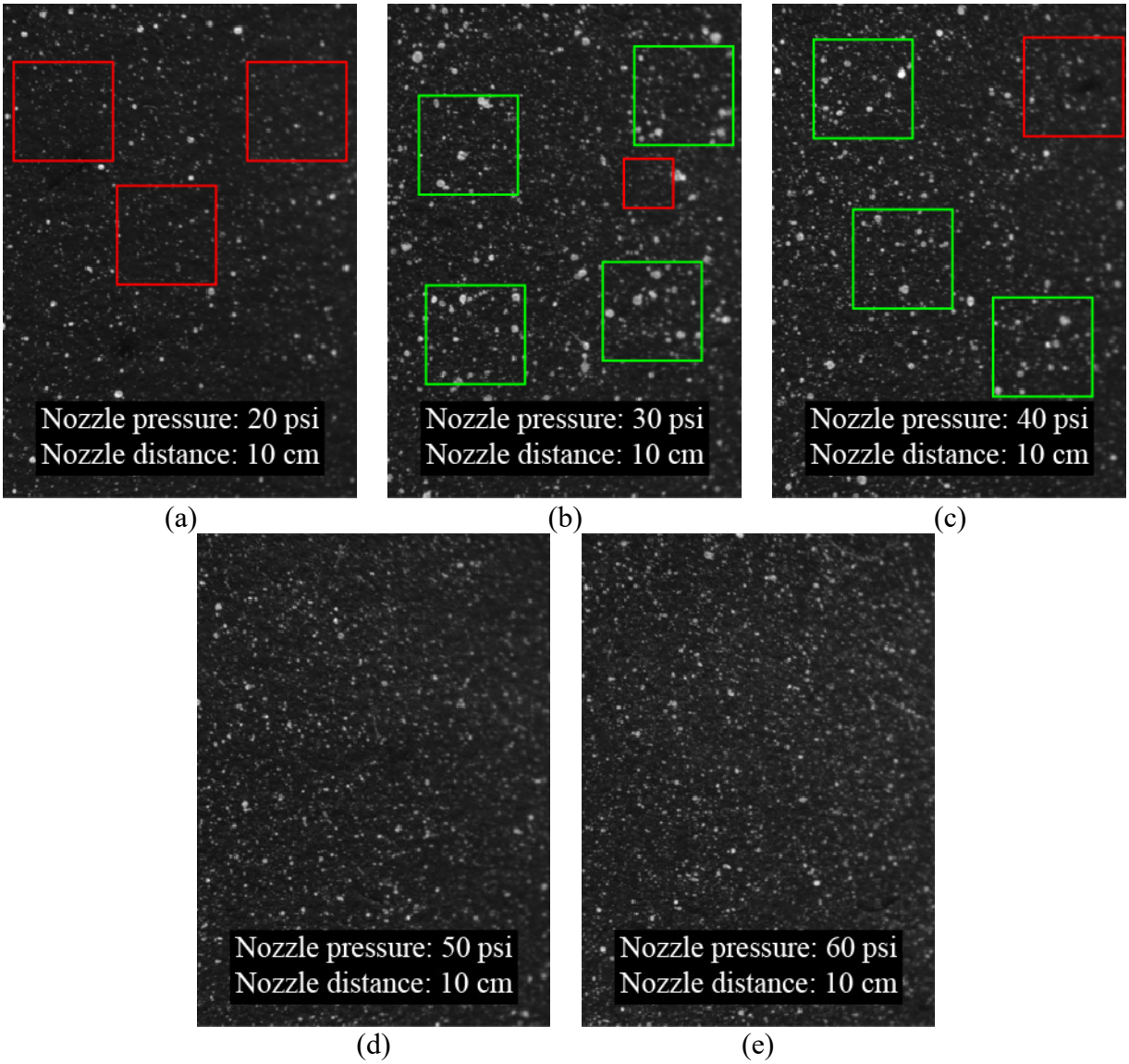

Figure C.1. Differences in speckle patterns on corrugated fibreboard when varying nozzle pressure from (a) 20, (b) 30, (c) 40, (d) 50, and (e) 60 psi while keeping nozzle distance constant at 10 cm. Red boxes indicate example regions of low speckle density, green boxes indicate regions of low consistency in speckle size.

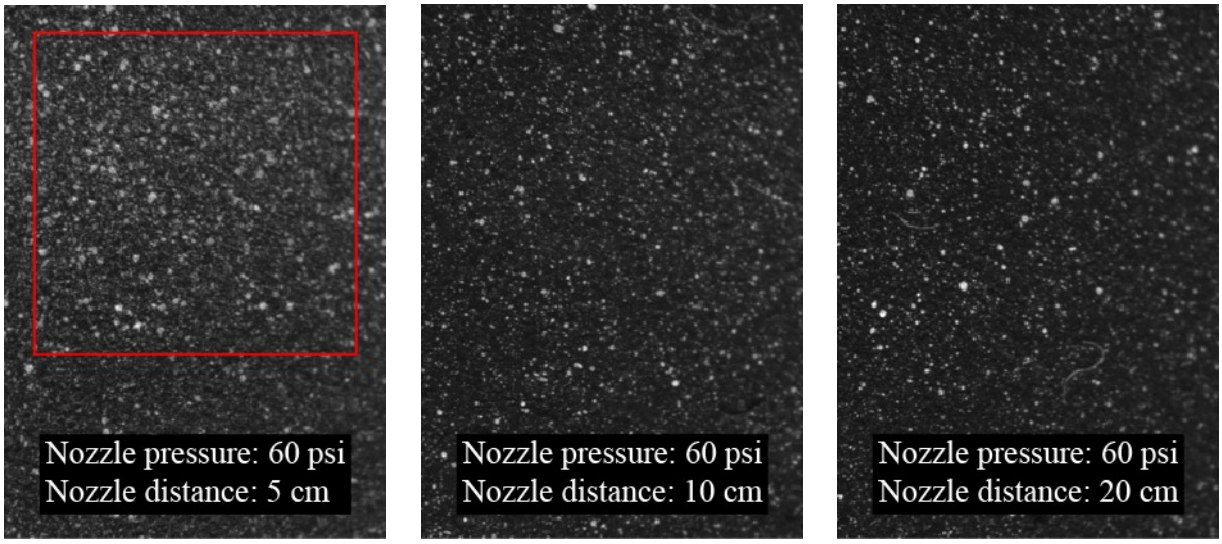

(a) (b) (c)

Figure C.2. Differences in speckle patterns on corrugated fibreboard when varying nozzle distance from (a) 5, (b) 10, and (c) 20 cm while keeping nozzle pressure constant at 60 psi. The red boxes indicate regions of high speckle density and resultant lower contrast.

Given the results from the initial speckling tests, 0.019”x0.025” stainless steel archwires were speckled to determine if the speckling distribution as seen on the corrugated fibreboard was transferrable onto the archwire surfaces. Archwires prepared with a similar base coat of matte black spray paint were then speckled using an air pressure of 60 psi and nozzle distance of 10 cm. However, the resulting speckles were found to be highly irregular with respect to the surface area of the archwire. The inconsistencies seen in the speckle patterns were deemed unsuitable for image correlation. An example of the resulting speckle pattern can be seen in Figure C.3.

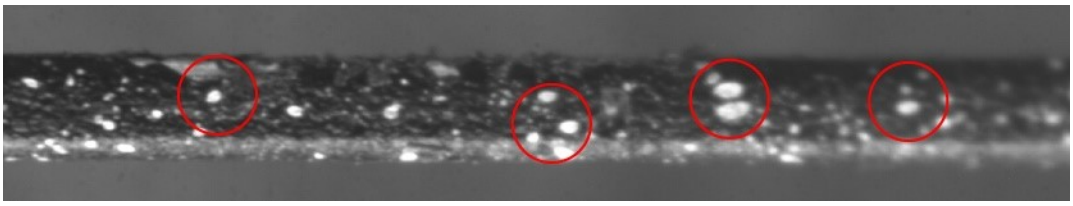

Figure C.3. Archwire speckling with white acrylic paint. Inconsistencies in speckle size are highlighted in circled regions.

The limited available surface area of the archwire necessitated a different speckling technique. The white acrylic paint was replaced with a different medium. Silver-coated solid glass microspheres (Cospheric LLC, California, USA) were explored for their consistent size and high reflectivity. Manufacturer specifications indicated that within a given sample, over 90% of all microspheres would conform to diameters between 1 and 7 microns [96]. When dispersed, these microspheres are invisible to the naked eye; however, with appropriate camera systems and lighting conditions, they appear as white speckles when imaged. The microspheres were deposited onto the archwire using the same siphon-fed airbrush as before. To evaluate the distribution of the microspheres, a similar process using corrugated fibreboard was performed.

Initially, the microspheres were added to water to provide a fluid base to airbrush. It was determined that the microspheres would not adhere to the spray-painted surface when applied in this manner. To ensure adequate microsphere adhesion onto the surface, a solution of water and polyvinyl acetate (PVA) glue was prepared. The ratio between water and PVA was determined by incrementally adding PVA into water until the solution exhibited adhesive properties, which was established at a 10:1 ratio of water to PVA. The microspheres were then added at approximately 1% by mass. Using this mixture, the microspheres showed better adhesion when deposited onto painted surfaces. In this application of speckling with microspheres, it is noted that the air pressure and distance between nozzle tip and archwire have different effects on the speckle pattern

compared to the acrylic paint. Since the size of the microspheres are as manufactured and do not change when speckled, air pressure and distance only affect the density of the microsphere distribution. Therefore, to control the density of microspheres deposited onto the surface, single passes with the airbrush at 10 cm and 60 psi were used, and the samples were checked under cameras after every pass. This was repeated until the speckling density displayed a stochastic pattern with high contrast between the speckles and the background.

Furthermore, it was found that the orientation of a speckled specimen would influence the final speckle pattern. The microspheres would settle over time when suspended in solution. If a specimen is oriented vertically such that the microspheres are deposited onto a sloped surface, then over the duration it takes the solution to dry, the microspheres will sink due to gravity. Conversely, microspheres that were deposited directly above onto a specimen oriented horizontally did not exhibit the same sinking phenomenon. The differences in specking pattern on the corrugated fibreboard samples in the two orientations can be seen in Figure C.4. Note that speckle densities are not consistent between the two orientations, but the undesired settling of microspheres is evident for the vertical specimen and is not apparent for the horizontal specimen.

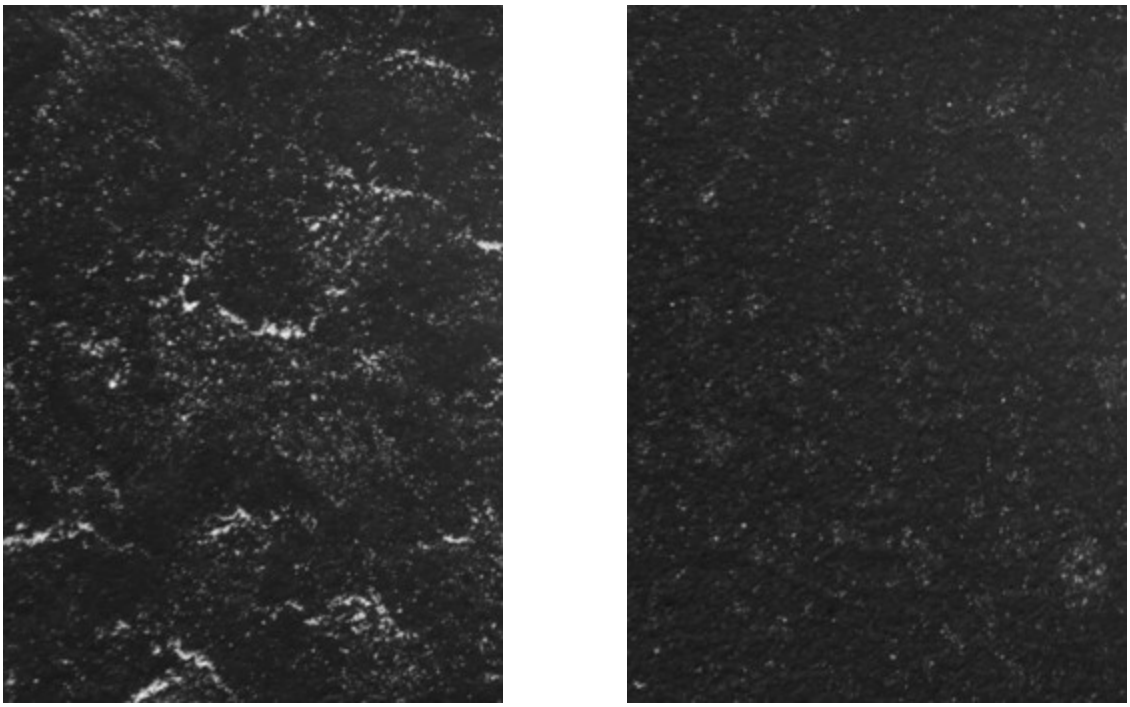

(a) (b)

Figure C.4. Resultant speckle pattern comparisons using silver-coated microspheres for (a) vertically and (b) horizontally oriented test specimens during speckling.

Given the findings from speckling experimentation with the microspheres, the speckling procedure applied to archwires consisted of using the microsphere mixture and spraying on archwires that were laid flat. Straight archwire samples were prepared by arranging several segments of archwires together, such that when spray-painting and speckling, only the top surfaces of the archwire would be exposed. Further, the archwire segments were masked on either end to limit the exposed surface area. The length of the exposed area was 12.8 mm, which matched the span of the rigid dowel (RD) width and the two inter-bracket distances on either side. This length also allowed for fine horizontal adjustment of the archwire position when under the field of views of the cameras. Applying the microspheres was completed over several passes with adequate drying time in between passes. The archwires were checked for speckle quality between consecutive applications of microspheres. The archwire speckling can be seen in Figure C.5. In using the microspheres, the

speckle size and distribution on the archwire surface is more consistent in comparison to acrylic paint speckling; therefore, this speckling technique was used for all consequent tests. In addition, the RD was also spray-painted matte-black to prevent high intensity reflections of light into the camera sensors during testing. A comparison of the RD prior to and post spray-paint application is shown in Figure C.6. The contrast in speckles on the archwire is more evident when the RD is spray-painted, as the exposure is more consistent throughout the field of view of the image.

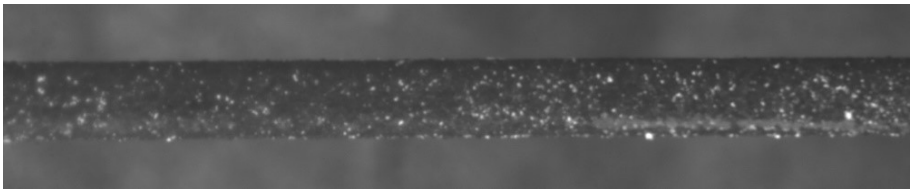

Figure C.5. Archwire speckling with silver-coated solid glass microspheres.

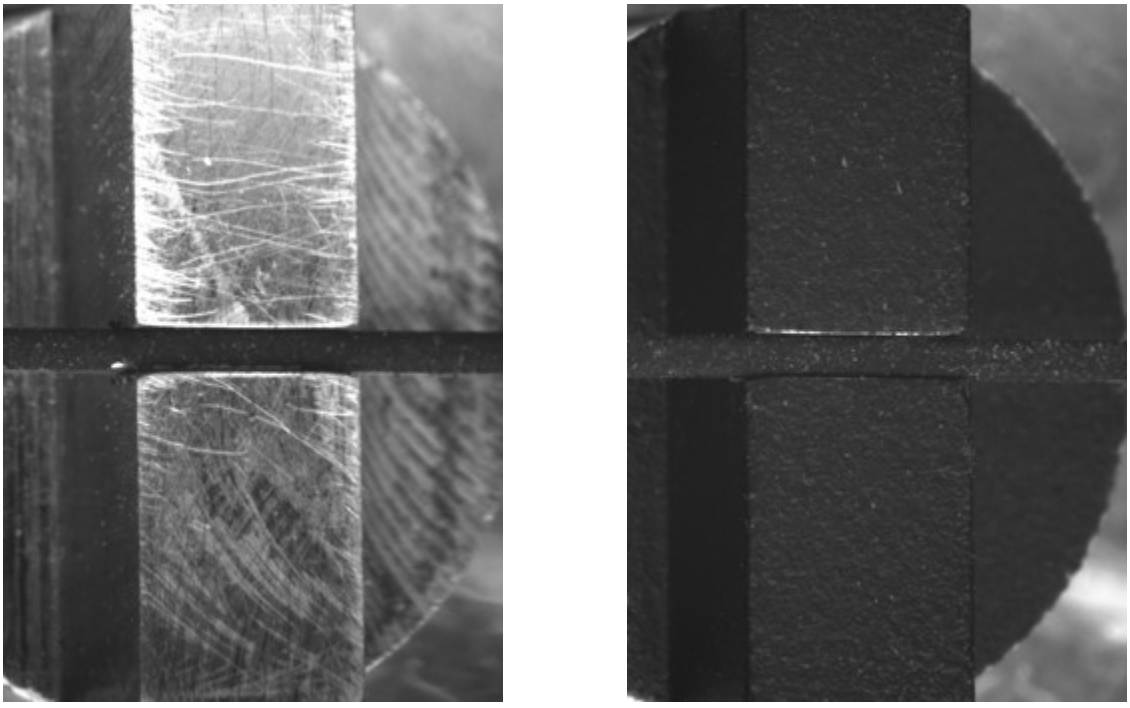

(a) (b)

Figure C.6. Image exposure comparisons of the rigid dowel (a) without and (b) with black spray-paint application. A prepared archwire is included in proper position to compare speckle quality.

APPENDIX D PRELIMINARY FINITE ELEMENT MODEL SETUP

In performing the finite element (FE) analysis for third-order torque mechanics using the rigid dowel (RD), iterations of the model were performed and simulated to better replicate the physical application of the Orthodontic Torque Simulator (OTS). The geometry of the model was simplified to include just an archwire and the RD, removing all other components of the OTS. In doing so, appropriate boundary conditions were considered and applied onto the model, which are detailed in this appendix.

D.1 Initial Model Geometry

D.1.1 Symmetry

The OTS applies third-order torque by rotating an archwire from both ends of the clamp tips. This bilateral torsion enables the utilisation of symmetry in the FE model. Based on the coordinate system shown in Figure D.1, the yz-plane was the plane of symmetry for third-order torque. Therefore, both the archwire and the RD were modelled such that a symmetric boundary condition could be applied onto the surfaces coincident to the yz-plane. The symmetry applied to the model can be seen in Figure D.2(a) and (b).

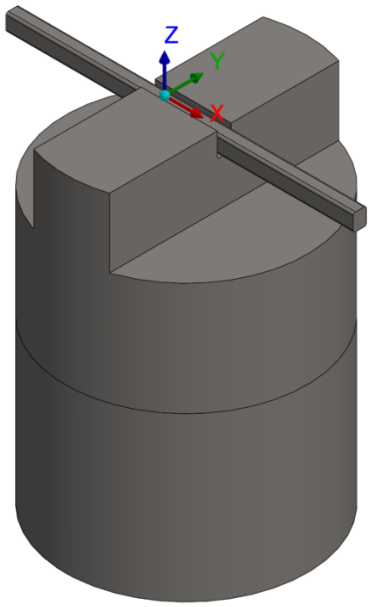

Figure D.1. Schematic of the OTS coordinate system with reference to the archwire and rigid dowel.

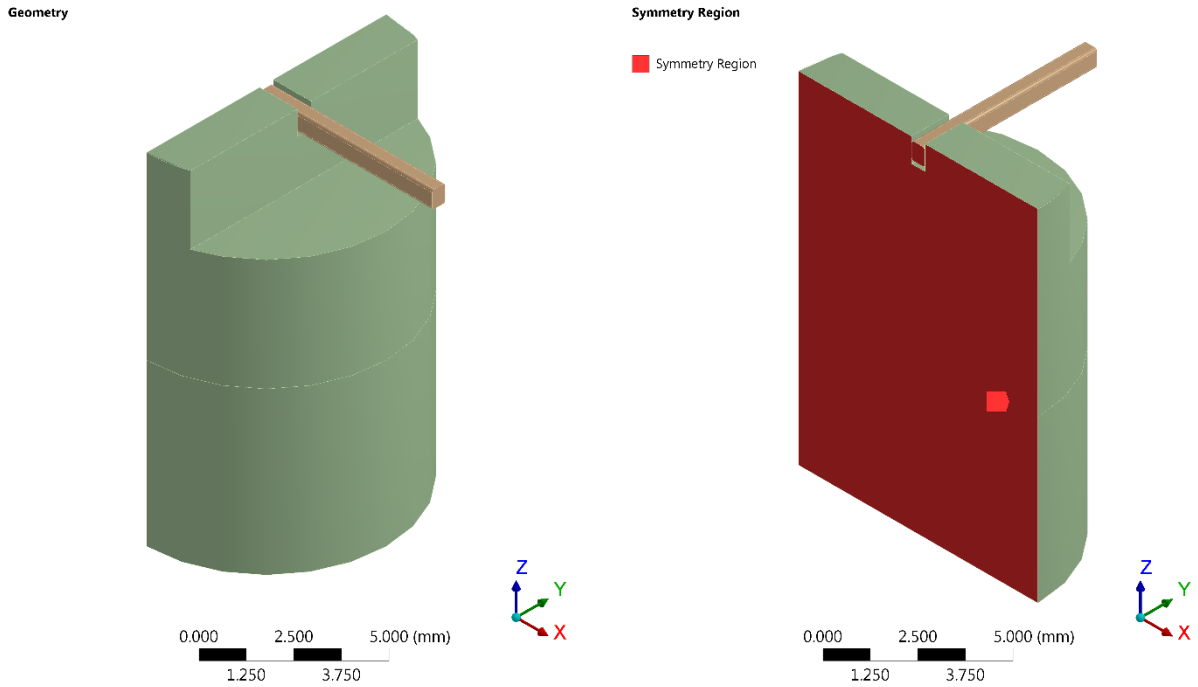

(a) (b)

Figure D.2. Geometry of rigid dowel and archwire showing the (a) isometric view and (b) faces of symmetry.

D.1.2 Rigid Dowel Geometry

The RD was modelled based on the dimensions as prepared for manufacturing as seen in Figure D.3. The variations in geometry between the manufacturer drawing versus the FE model of the RD included the symmetric modelling where only half the RD was modelled, and small fillets in the archwire slot were included to reduce the stress concentrations at the corners of the slot when performing the FE analysis.

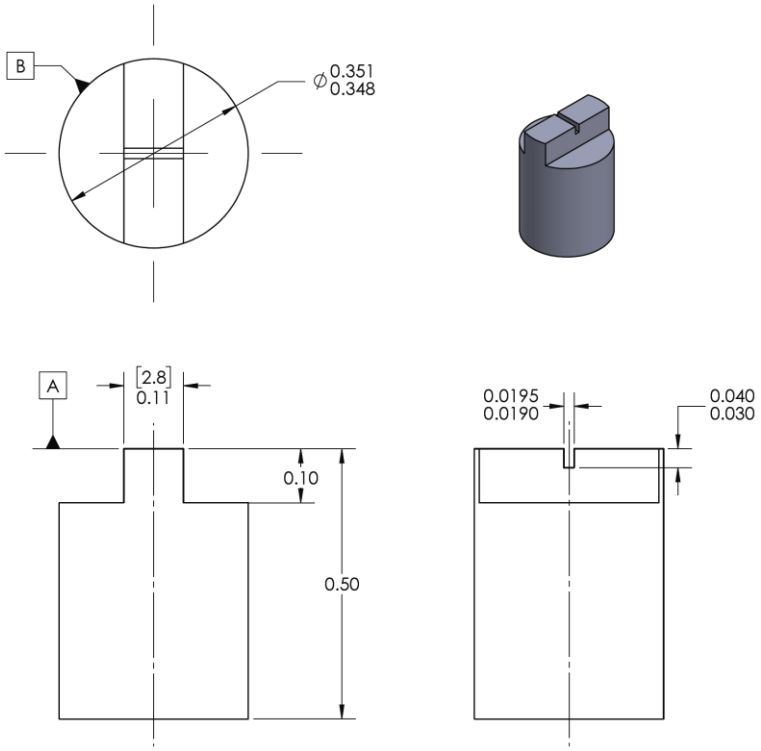

Figure D.3. Manufacturing drawing of rigid dowel, dimensioned in inches (bracketed values are in millimetres).

In the case of dimensions with tolerances, the slot width was modelled with a dimension of 0.0195" to include a small gap on either side of the archwire when it is inserted into the slot. The slot depth was modelled as 0.035" to be taken as the midpoint between the allowable tolerances.

D.1.3 Archwire Geometry

In practise, an archwire is not a perfect rectangular prism, as the corners are rounded during the manufacturing process. The archwire was modelled to include rounded corners to better match archwire geometry seen in commercial archwires. The dimensions of the rounded corners were determined by superimposing the cross-section of the solid model with an actual image of an 0.019”x0.025” archwire cross-section from literature [58]. It was assumed that the four bevels would be circular and have the same dimensions, though in manufacturing archwires, bevel dimensions may deviate from a circle as well as from each other [58]. The comparison between the modelled archwire with the commercial archwire can be seen in Figure D.4. The length of the archwire was modelled such that it spanned from the centre of the RD up to the clamp tips, thus including the inter-bracket distance (IBD) between the edge of the RD and clamps. Therefore, in the symmetric model, the length of the archwire totalled 6.4 mm from the plane of symmetry up to the end of one IBD. The archwire was positioned inside the RD slot such that it was both vertically and horizontally centred within the slot, which is shown in Figure D.5.

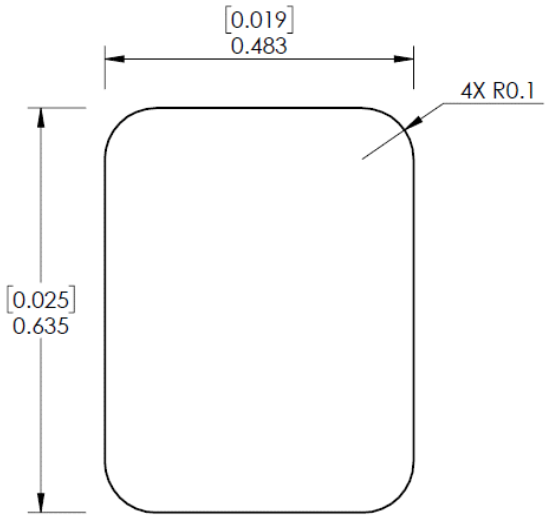

Figure D.4. 0.019”x0.025” rectangular archwire cross-sections as modelled for finite element analysis.

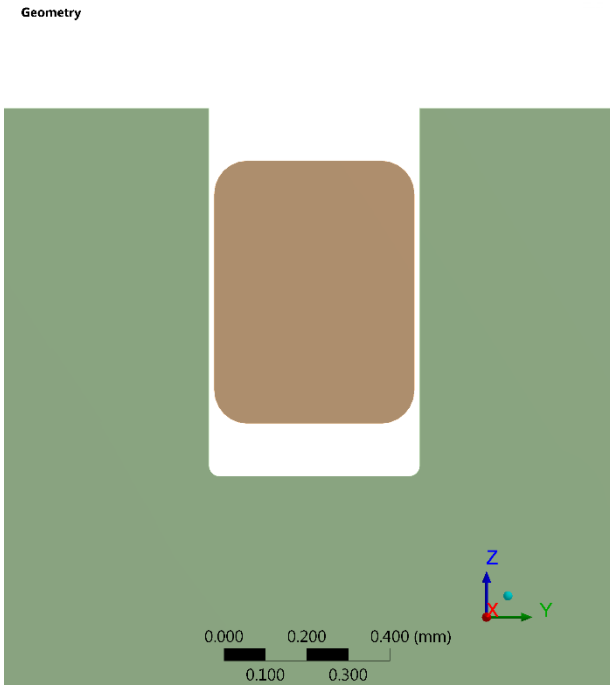

Figure D.5. Archwire placement inside rigid dowel slot.

D.2 Material Properties

In the model, program-default stainless steel was applied to both the RD and archwire [85]. Using these properties with the initial analysis would indicate whether non-linearities in material properties would have to be considered for the final model. The material properties of the steel are shown in Table D.1. The material properties were cross-referenced with online material databases and it was found that the values closely matched conventional 304 stainless steel [97].

Table D.1. Stainless steel material properties used in the simplified finite element analysis of third-order torque of a 0.019"x0.025" archwire in a rigid dowel [85]**.**

Property	Value [Unit]
Density	7750 kg/m^3
Young's Modulus	193 GPa
Poisson's Ratio	0.31
Yield Strength	207 MPa
Ultimate Strength	586 MPa

The element mesh for both components were quadratic order, with the archwire using hexahedral elements and the RD using a hexahedral-dominant mesh with quadrilateral and triangular face meshing. Archwire elements were sized to 0.1 mm, and RD elements were left at program defaults; however, the contact region included a mesh refinement on all RD slot surfaces. The refinement was applied to approximately match the element sizing seen on the archwire. The resultant mesh is shown in Figure D.6.

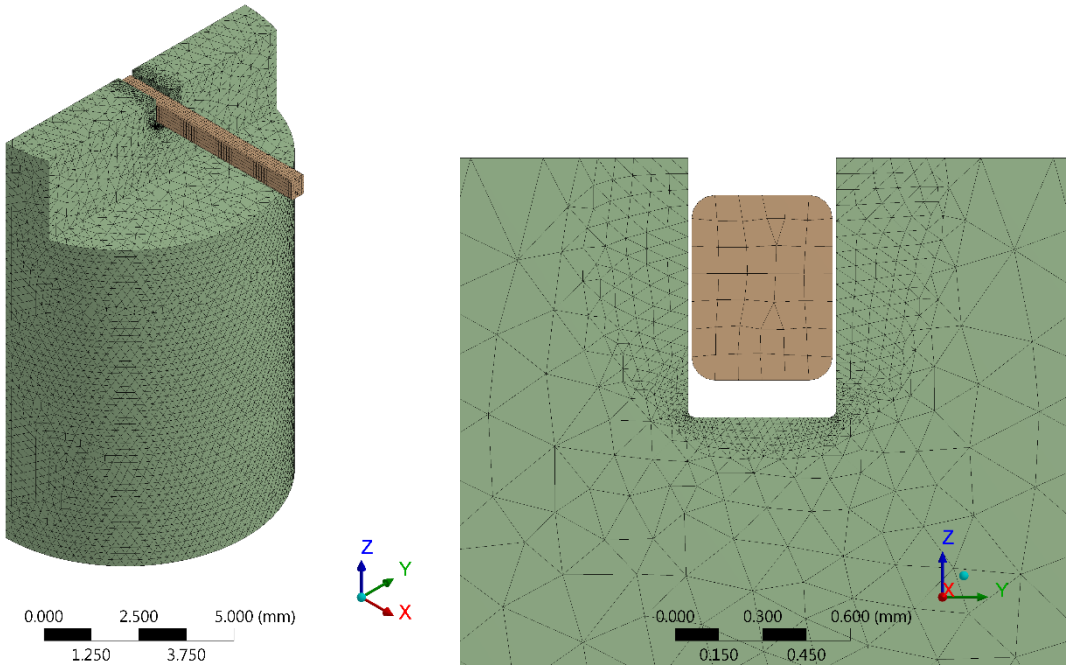

(a) (b)

Figure D.6. Finite element mesh shown with an (a) isometric view and (b) zoomed view of refined elements in the contact region.

D.3 Boundary Conditions

The boundary conditions, in addition to the symmetry for both components, included the behaviour of the RD and the archwire independent of one another, and the behaviour of the resultant contact during torsion. For the RD, the constraints were applied to fix the RD in space. This was done by fixing surfaces in the bottom half of the RD. The length of the fixed cylindrical face was 6.0 mm to match the depth of the dowel holder of the OTS and the entire bottom face was also fixed. For the archwire, the exposed face at the end of the archwire (5 mm away from the RD edge) was rotated 30° about the x-axis. This effectively matches the rotation applied by the OTS clamps, assuming a perfect fit between the archwire and clamp, and also assuming the clamp's rotation exactly about the centre of the archwire. The overall boundary conditions applied to the RD and

archwire can be seen in Figure D.7. Lastly, the contact between the two components was applied as frictional contacts with a coefficient of friction set at 0.7 to match stainless steel. The contact surface properties were applied to the RD slot walls and the corresponding archwire surfaces that were expected to contact the walls during simulated rotation. The interface treatment was set as adjust to touch, which closes initial gaps between the RD and archwire such that contact pairs make contact in an initial stress-free state [98]. This setting was included to close the initial gaps between the RD and archwire as a means to maintain contact between the two bodies instead of having the solution not converge due to an unsolvable contact state [98].

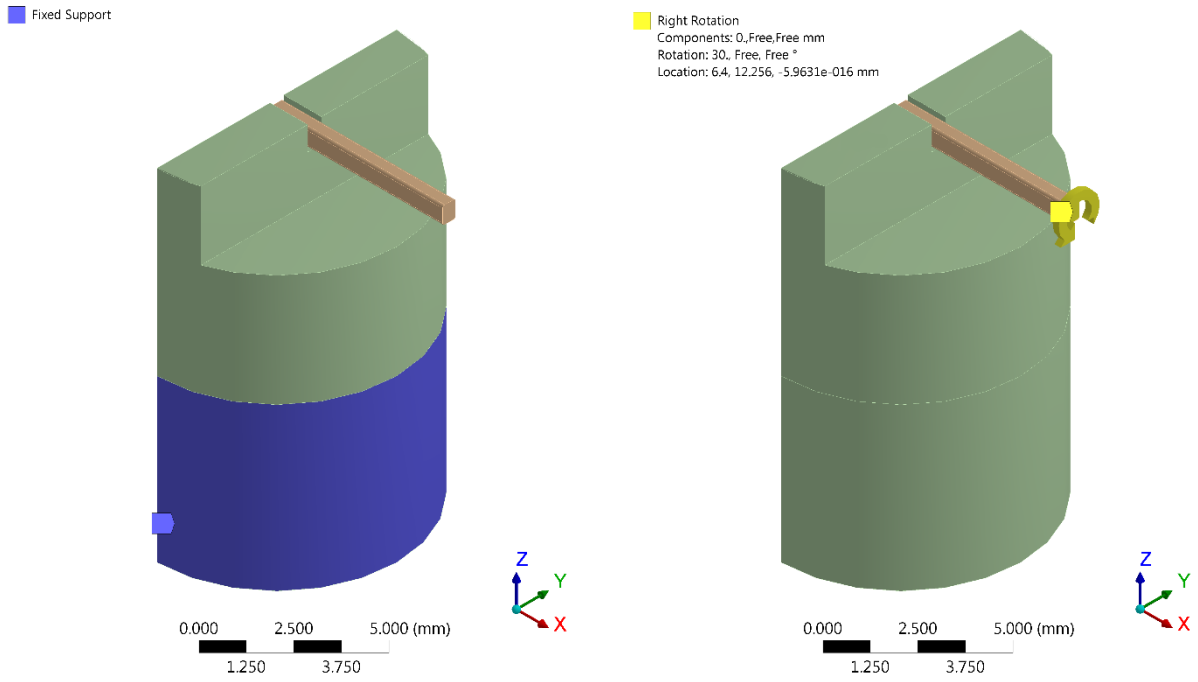

(a) **(b)**

Figure D.7. Boundary conditions for the (a) rigid dowel showing fixed surfaces and (b) archwire showing the surface with 30° of angular displacement about the *x*-axis.

D.4 Model Refinement

Using the initial results from the analysis, the model may be refined with additional parameters and settings to better reflect the archwire and bracket behaviour under OTS third-order torque loading conditions. The resultant von Mises stresses determined through the preliminary model can be seen in Figure D.8.

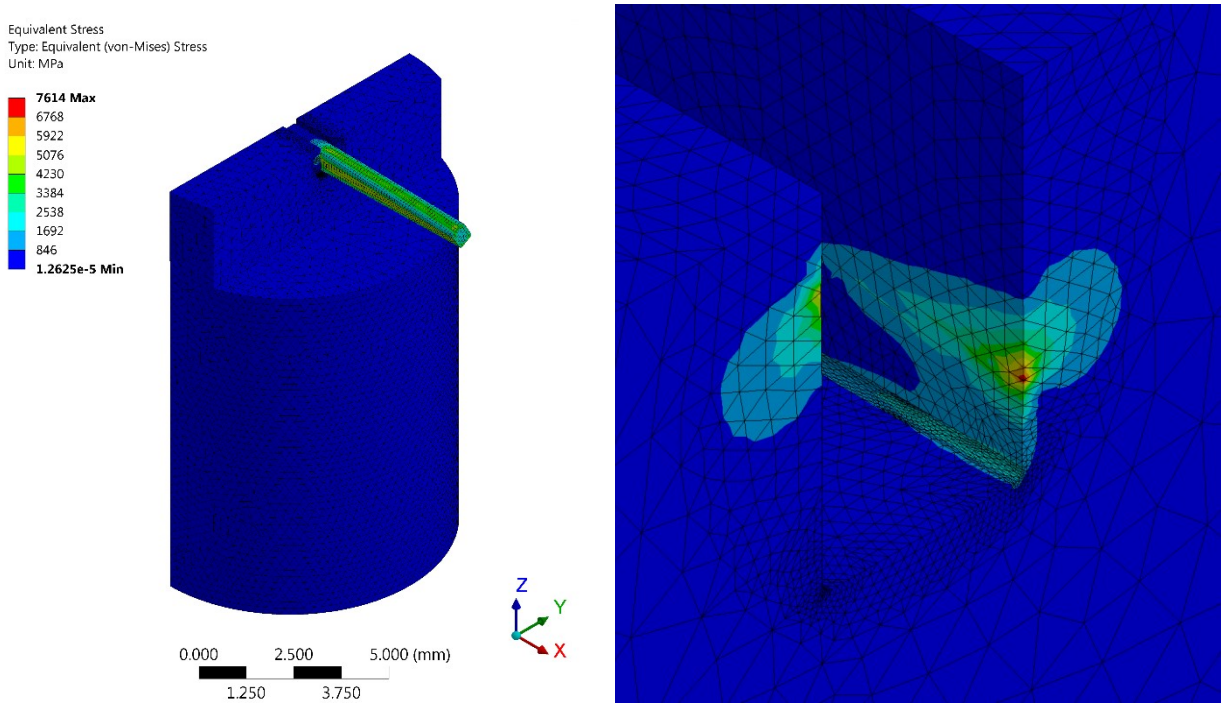

(a) (b)

Figure D.8. Resultant von Mises stresses in MPa on the (a) rigid dowel and archwire from 30° of archwire rotation and (b) zoomed into the rigid dowel slot.

The magnitudes of the stresses showed that the material yielded as per the von Mises yield criteria, therefore non-linear stainless steel should be implemented for the material properties of both components. Much of the archwire body displays stresses much larger than the yield stress, and similarly the contact region does as well. The inclusion of plastic deformation would be more representative of the actual stresses and strains experienced by the archwire and RD under the

torsion regime. Further, the stress distribution around the RD slot indicated discontinuities in the material, which questioned the use of the adjust to touch contact. In experimenting with various contact regimes, it was found that the adjust to touch interface treatment was not suitable for the model, as the initial zero-stress state with surfaces in contact resulted in poor stress propagation throughout the material. Instead, weak springs were used in the updated model to keep the bodies in contact without affecting the evolution of stresses over the applied load.

APPENDIX E R CODE FOR PLOTS AND STATISTICAL ANALYSIS

R (R Core Team, 2017) [88] was used throughout this thesis for plotting data and statistical analysis. This appendix includes all R code used throughout main chapters of the thesis. Scripts for figure generation and statistical analysis are included, and all R packages used are also included.

E.1 Figure Generation

Figures created using R were done so using the "ggplot2" package as a part of the "tidyverse" package collection [89], [90]. Figures were exported as portable document formats for post-generation formatting of size and visual elements. All plots are created following the general "ggplot2" syntax. Plot codes are presented in chronological order.

E.1.1 Third-Order Torque Plots

The process of plotting third-order torque using R highlighted. Third-order torque plotting methods are consistent throughout the thesis. Prior to importing the data into R, the data frame was organised into the following columns:

Trial: Indicates trial number as a numeric variable

Angle: Indicates measured rotation angle as a numeric variable

Condition: Indicates whether the Orthodontic Torque Simulator (OTS) is “Loading” or “Unloading” as a character variable

Torque: Indicates measured third-order torque as a numeric variable

Each row contains a unique combination of the four variables. For example, a row containing [3, 15, Loading, -46.2] indicates that during Trial 3, at 15° loading, -46.2 N·mm of torque was measured. The code for generating the plot is included below:

```
# Load libraries
library(tidyverse)

# Create variable containing string of where data is saved
filepath <- file.path(
  "[personal filepath redacted]"
)
# Set working directory
setwd(filepath)

# Import data
data <- read_csv("Tx.csv")
# Reformat data to prepare for plotting, calculate the mean and standard
deviation for each unique angular instance
data <- group_by(data, Angle, Condition) %>%
  summarise(
    count = n(),
    mean = mean(Torque, na.rm = TRUE),
    sd = sd(Torque, na.rm = TRUE)
  )

# Generate plot
p1 <- ggplot(data = data, mapping = aes(
  x = data$Angle,
  y = data$mean,
  shape = factor(data$Condition)
)) +
  geom_point(size = 1.5) +
  geom_errorbar(aes(
    ymin = mean - sd,
    ymax = mean + sd
  ),
  width = 0.5,
  size = 0.25
  ) +
  labs(x = "Angle [deg]", y = "Third-Order Torque [Nmm]") +
  scale_shape_manual(values = c(25, 24)) +
```

```
  theme_light() +
  theme(
    text = element_text(size = 12, family = "serif")
  )

# Show plot in plot pane
p1

# Export plot to pdf, can be in other image formats such as png
ggsave("Torque.pdf", width = 6, height = 4, units = "in", dpi = 320)
```

The graphical output of third-order torque from R is shown in Figure E.1.

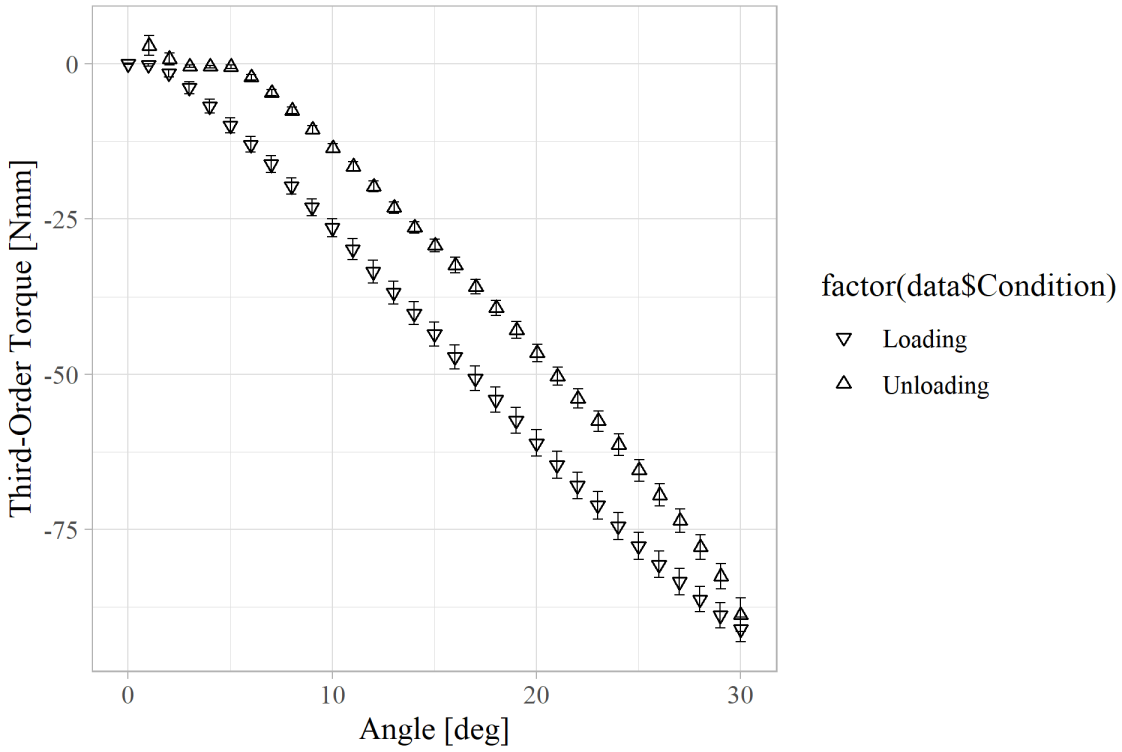

Figure E.1. R output of third-order torque plot.

E.1.2 Bilateral Archwire Surface Strain Plots

Similar to third-order torque, strain was plotted as a function of angle. The bilateral strain plots included data for both the left and right sides of the imaged archwire and the code highlights how

the data was handled. Strain data was collected from digital image correlation (DIC) results and organised into a data frame with the following columns:

Trial: Indicates trial number as a number variable

Angle: Indicates measured rotation angle as a numeric variable

Condition: Indicates whether the OTS is “Loading” or “Unloading” as a character variable

Side: Indicates whether the archwire strain is calculated on the left “L” or right “R” surfaces relative to the rigid dowel as a character variable

Exx: Indicates measured surface strain in the principal x-direction as a numeric variable

Eyy: Indicates measured surface strain in the principal y-direction as a numeric variable

Exy: Indicates measured surface shear strain on the xy-plane as a numeric variable

The code for generating strain plots is shown below:

```
# Load libraries
library(tidyverse)

# Create variable containing string of where data is saved
filepath <- file.path(
  "[personal filepath redacted]"
)
# Set working directory
setwd(filepath)
```

```
# Import data
data <- read_csv("Strain.csv")

# Group data into three data frames, one for each strain measured
data_xx <- group_by(data, Angle, Condition, Side) %>%
  summarise(
    count = n(),
    mean = mean(Exx, na.rm = TRUE),
    sd = sd(Exx, na.rm = TRUE)
  )

data_yy <- group_by(data, Angle, Condition, Side) %>%
  summarise(
    count = n(),
    mean = mean(Eyy, na.rm = TRUE),
    sd = sd(Eyy, na.rm = TRUE)
  )

data_xy <- group_by(data, Angle, Condition, Side) %>%
  summarise(
    count = n(),
    mean = mean(Exy, na.rm = TRUE),
    sd = sd(Exy, na.rm = TRUE)
  )

# Filter the data to only include strains measured during loading
data_xx <- filter(data_xx, Condition == "Loading")
data_yy <- filter(data_yy, Condition == "Loading")
data_xy <- filter(data_xy, Condition == "Loading")

# Generate and export the plots
p1 <- ggplot(data = data_xx, mapping = aes(
  x = data_xx$Angle,
  y = data_xx$mean,
  colour = factor(data_xx$Side),
  shape = factor(data_xx$Side)
)) +
  geom_point(size = 1.5) +
  geom_errorbar(aes(
    ymin = mean - sd,
    ymax = mean + sd
  ),
  width = 0.5,
  size = 0.25
  ) +
  ylim(-0.02, 0.02) +
  labs(x = "Angle [deg]", y = "Strain [mm/mm]") +
  scale_shape_manual(values = c(1, 4)) +
  theme_light() +
  theme(
    text = element_text(size = 12, family = "serif")
  )
p1
ggsave("Exx.pdf", width = 6, height = 4, units = "in", dpi = 320)
```

```
p2 <- ggplot(data = data_yy, mapping = aes(
  x = data_yy$Angle,
  y = data_yy$mean,
  colour = factor(data_yy$Side),
  shape = factor(data_yy$Side)
)) +
  geom_point(size = 1.5) +
  geom_errorbar(aes(
    ymin = mean - sd,
    ymax = mean + sd
  ),
  width = 0.5,
  size = 0.25
  ) +
  ylim(-0.02, 0.02) +
  labs(x = "Angle [deg]", y = "Strain [mm/mm]") +
  scale_shape_manual(values = c(1, 4)) +
  theme_light() +
  theme(
    text = element_text(size = 12, family = "serif")
  )
p2
ggsave("Eyy.pdf", width = 6, height = 4, units = "in", dpi = 320)

p3 <- ggplot(data = data_xy, mapping = aes(
  x = data_xy$Angle,
  y = data_xy$mean,
  colour = factor(data_xy$Side),
  shape = factor(data_xy$Side)
)) +
  geom_point(size = 1.5) +
  geom_errorbar(aes(
    ymin = mean - sd,
    ymax = mean + sd
  ),
  width = 0.5,
  size = 0.25
  ) +
  ylim(-0.02, 0.02) +
  labs(x = "Angle [deg]", y = "Strain [mm/mm]") +
  scale_shape_manual(values = c(1, 4)) +
  theme_light() +
  theme(
    text = element_text(size = 12, family = "serif")
  )
p3
ggsave("Exy.pdf", width = 6, height = 4, units = "in", dpi = 320)
```

The graphical output of surface shear strain from R is shown in Figure E.2. Principal strain plots have similar R outputs and are not shown.

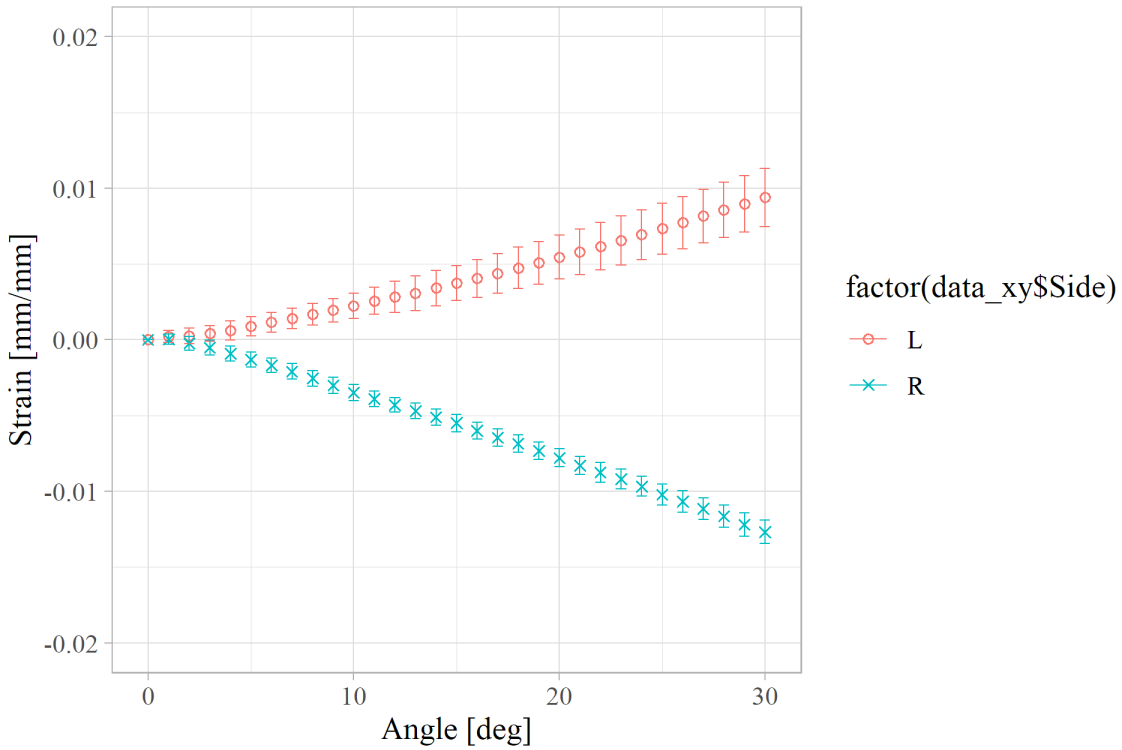

Figure E.2. R output of surface shear strain plot.

E.1.3 Mesh Convergence Plot

The data for the mesh convergence plot was collected during the finite element (FE) analysis. The data frame for the mesh convergence plot was organised as follows:

Nodes: Indicates the total number of nodes used to mesh the archwire body for each simulation during the mesh convergence test a numeric variable

Shear: Indicates the maximum surface shear strain measured along the selected path as a numeric variable

The code for generating the plot is shown below:

```
# Load libraries
library(tidyverse)

# Create variable containing string of where data is saved
filepath <- file.path(
  "[personal filepath redacted]"
)
# Set working directory
setwd(filepath)

# Import data
data <- read_csv("MeshConvergence.csv")

# Generate and export the plot
p1 <- ggplot(data = data, mapping = aes(
  x = data$Nodes,
  y = data$Shear
)) +
  geom_point() +
  geom_line() +
  xlim(0, 55000) +
  ylim(0, 1200) +
  labs(x = "Number of Archwire Nodes",
       y = "Maximum Shear Stress Along Path [MPa]") +
  theme_light() +
  theme(
    text = element_text(size = 12, family = "serif")
  )
p1
ggsave("MeshConvergence.pdf", width = 6, height = 4, units = "in", dpi =
320)
```

The graphical output of the FE mesh convergence from R is shown in Figure E.3.

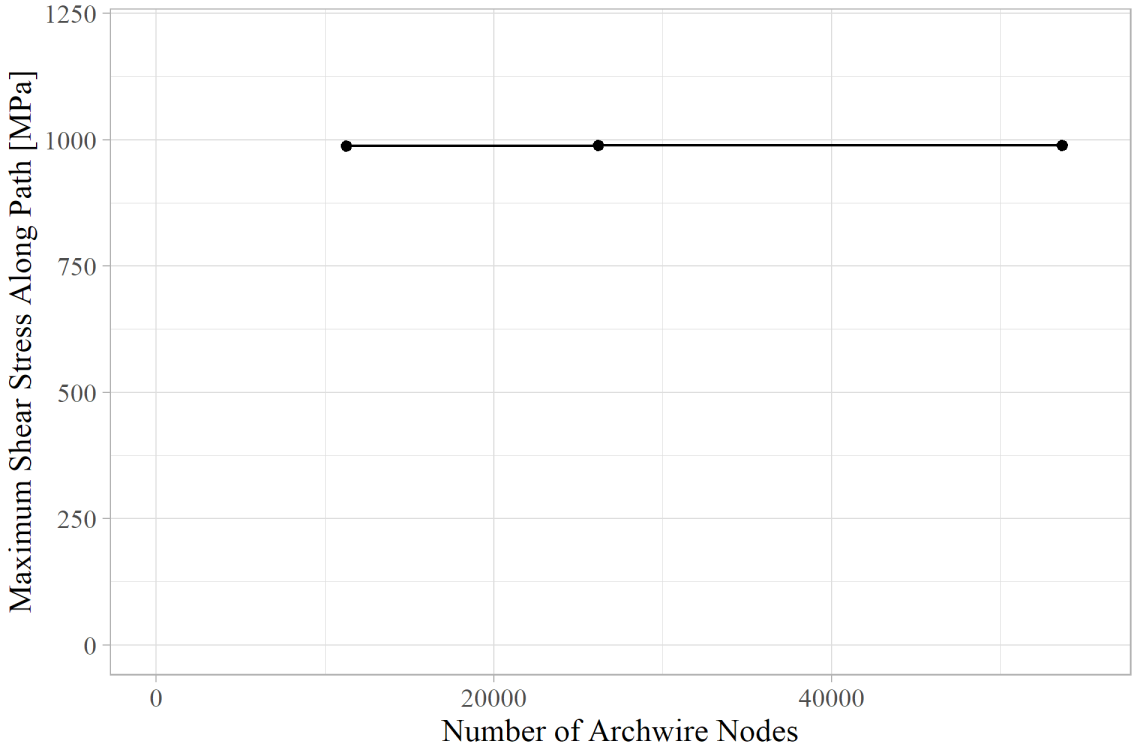

Figure E.3. R output of mesh convergence plot.

E.1.4 DIC versus FE Analysis Archwire Shear Strain Comparison Plot

The plots for shear strains measured using DIC versus FE analysis utilised the technique of plotting data from multiple data frames onto the same plot. The DIC strain data frame is identical to the one used in E.1.2 in both structure and enclosed data. Two separate FE data frames are used with different data, but both data frames were organised as follows:

FE_Angle: Indicates the simulated rotation angle as a numeric variable

FE_Exy: Indicates the simulated surface shear strain as a numeric variable

The code to generate the plot is shown below:

```r
# Load libraries
library(tidyverse)

# Create variable containing string of where data is saved
filepath <- file.path(
  "[personal filepath redacted]"
)
# Set working directory
setwd(filepath)

# Import data
data <- read_csv("Strain.csv")
FEdata <- read_csv("FEStrain.csv")
FEdata2 <- read_csv("FEStrain2.csv")

data_xy <- group_by(data, Angle, Condition, Side) %>%
  summarise(
    count = n(),
    mean = mean(Exy, na.rm = TRUE),
    sd = sd(Exy, na.rm = TRUE)
  )

data_xy <- filter(data_xy, Condition == "Loading")
data_xy <- filter(data_xy, Side == "R")

p1 <- ggplot() +
  geom_point(
    data = data_xy, mapping = aes(
      x = data_xy$Angle,
      y = data_xy$mean
    ),
    colour = "#00BFC4",
    shape = 4
  ) +

  geom_errorbar(
    data = data_xy, mapping = aes(
      x = data_xy$Angle,
      ymin = data_xy$mean - data_xy$sd,
      ymax = data_xy$mean + data_xy$sd
    ),
    colour = "#00BFC4",
    width = 0.5,
    size = 0.25
  ) +

  geom_point(
    data = FEdata, mapping = aes(
      x = FEdata$FE_Angle,
      y = FEdata$FE_Exy
    ),
    colour = "#7CAE00",
    shape = 3
  ) +
```

```
  ylim(-0.02, 0.02) +
  labs(x = "Angle [deg]", y = "Strain [mm/mm]") +
  scale_shape_manual(values = 4) +
  theme_light() +
  theme(
    text = element_text(size = 12, family = "serif")
  )
p1
ggsave("ExyFE.pdf", width = 4, height = 4, units = "in", dpi = 320)

p2 <- ggplot() +
  geom_point(
    data = data_xy, mapping = aes(
      x = data_xy$Angle,
      y = data_xy$mean
    ),
    colour = "#00BFC4",
    shape = 4
  ) +

  geom_errorbar(
    data = data_xy, mapping = aes(
      x = data_xy$Angle,
      ymin = data_xy$mean - data_xy$sd,
      ymax = data_xy$mean + data_xy$sd
    ),
    colour = "#00BFC4",
    width = 0.5,
    size = 0.25
  ) +

  geom_point(
    data = FEdata, mapping = aes(
      x = FEdata$FE_Angle,
      y = FEdata$FE_Exy
    ),
    colour = "#7CAE00",
    shape = 3
  ) +

  geom_point(
    data = FEdata2, mapping = aes(
      x = FEdata2$FE_Angle,
      y = FEdata2$FE_Exy
    ),
    colour = "#F8766D",
    shape = 3
  ) +

  ylim(-0.02, 0.02) +
  labs(x = "Angle [deg]", y = "Strain [mm/mm]") +
  scale_shape_manual(values = 4) +
```

```
  theme_light() +
  theme( # panel.grid.major = element_blank(),
    #       panel.grid.minor = element_blank(),
    text = element_text(size = 12, family = "serif")
  )
p2
ggsave("ExyFE2.pdf", width = 4, height = 4, units = "in", dpi = 320)
```

The graphical output for the DIC and FE strain comparisons from R is shown in Figure E.4. The second plot is shown with the two FE results rather than the first plot with a single FE result.

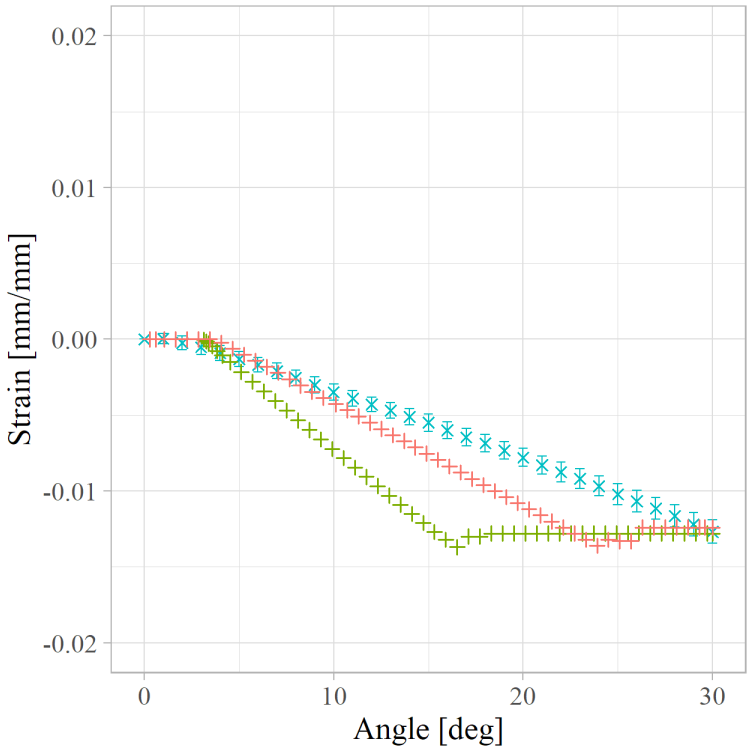

Figure E.4. R output of shear strain comparison between DIC and FE techniques.

E.1.5 Maximum Third-Order Torque Plots

Maximum third-order torques at 30° rotation are plotted for each group in the factorial design. The data frame for maximum torque was organised as follows:

Material: Indicates the archwire material as “Stainless Steel” or “Titanium Molybdenum Alloy” as a character variable

Bracket: Indicates the bracket type as “Rigid Dowel” or “Damon Q” as a character variable

Torque: Indicates the measured torque as a numeric variable

The code used the generate the plot is shown below:

```
# Load libraries
library(tidyverse)

# Create variable containing string of where data is saved
filepath <- file.path(
  "[personal filepath redacted]"
)
# Set working directory
setwd(filepath)

# Import data
data <- read_csv("TorqueResults.csv")
# Convert negative torque values to positive
data$Torque <- -1*data$Torque

# Generate and export the plot
p1 <- ggplot(data = data, mapping = aes(
  x = factor(data$Material),
  y = data$Torque,
  colour = factor(data$Bracket),
  stroke = 0
)) +
  geom_jitter(width = 0.07) +
  ylim(0, 100) +
  labs(x = "Archwire Material", y = "Third Order Torque", colour = "Bracket
Type") +
  scale_colour_discrete(limits = c("Rigid Dowel", "Damon Q")) +
  theme_light() +
  theme(panel.grid.major = element_blank(),
        panel.grid.minor = element_blank(),
        text = element_text(size = 12, family = "serif"))
p1
ggsave("MaxTorqueGroups.pdf", width = 6, height = 4, units = "in", dpi =
320)
```

The graphical output of maximum third-order torque from R is shown in Figure E.5.

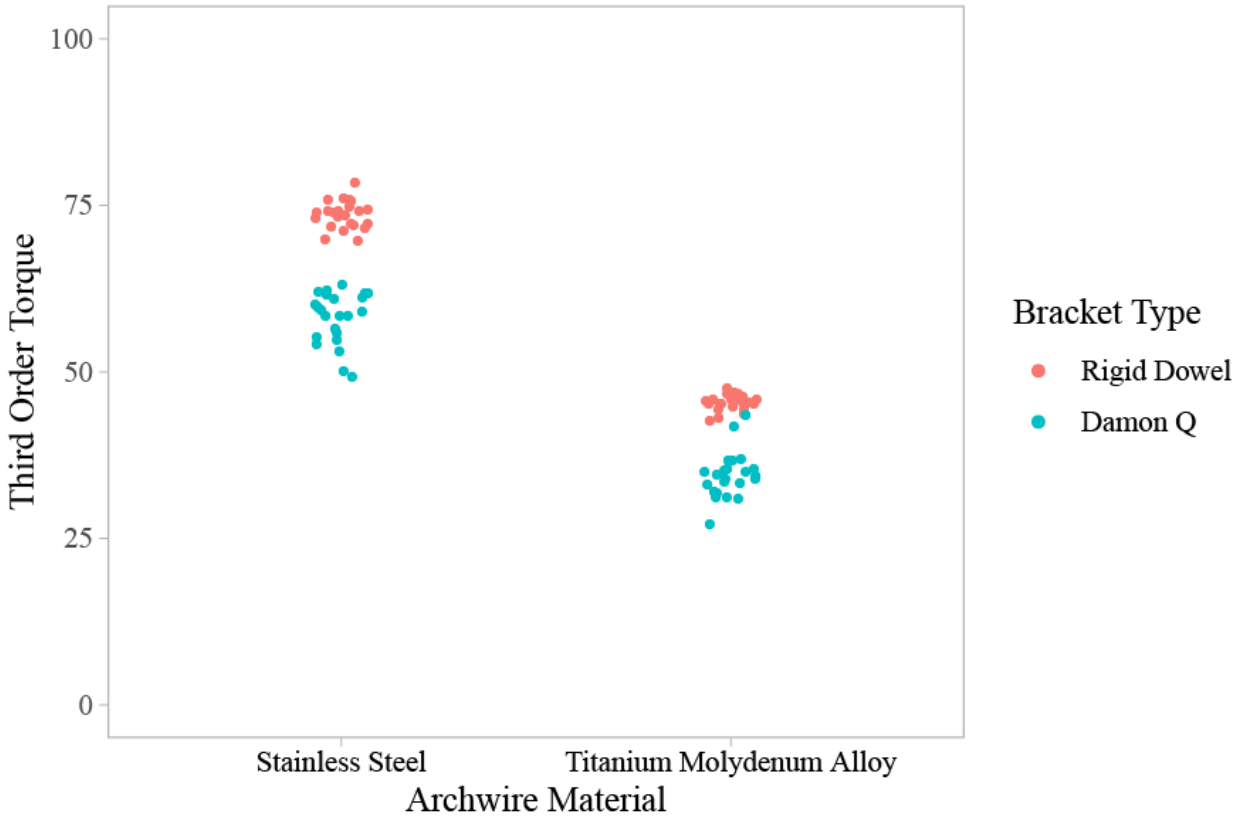

Figure E.5. R output of maximum third-order torque plot.

E.1.6 Archwire Surface Shear Strain Versus Total Number of Vectors in Probed Area Plots

Average surface shear strain values were compared based on the number of total vectors included in the area used for averaging. The data frame was organised as follows:

Vectors: Indicates the number of vectors used to average the shear strain material as a numeric variable

Angle: Indicates the measured rotation angle as a numeric variable

Condition: Indicates whether the OTS is “Loading” or “Unloading” as a character variable

Strain: Indicates average surface shear strain on the xy-plane as a numeric variable

The code used to generate the plot is shown below:

```
# Load libraries
library(tidyverse)

# Create variable containing string of where data is saved
filepath <- file.path(
  "[personal filepath redacted]"
)
# Set working directory
setwd(filepath)

# Import data
data <- read_csv("ExyVsAreaRD.csv")

loading <- filter(data, Condition == "Loading")
unloading <- filter(data, Condition == "Unloading")

# Generate and export the plots
p1 <- ggplot(data = loading, mapping = aes(
  x = loading$Vectors,
  y = loading$Strain,
  colour = factor(loading$Angle)
)) +
  geom_point(size = 1.5) +
  geom_line() +
  xlim(0, 4000) +
  ylim(-0.003, 0.007) +
  labs(
    x = "Vectors in Rectangular Area", y = "Shear Strain on XY-Plane
[mm/mm]",
    colour = "Angle"
  ) +
  scale_colour_viridis_d(begin = 0, end = 0.75) +
  theme_light() +
  theme(
    legend.position = "none",
    text = element_text(size = 12, family = "serif")
  )
p1
ggsave("ExyVsProbeArea_loading.png", width = 6, height = 4, units = "in",
dpi = 320)

p2 <- ggplot(data = unloading, mapping = aes(
```

```
  x = unloading$Vectors,
  y = unloading$Strain,
  colour = factor(unloading$Angle)
)) +
  geom_point(size = 1.5) +
  geom_line() +
  xlim(0, 4000) +
  ylim(-0.003, 0.007) +
  labs(
    x = "Vectors in Rectangular Area", y = "Shear Strain on XY-Plane
[mm/mm]",
    colour = "Angle"
  ) +
  scale_colour_viridis_d(begin = 0, end = 0.75) +
  theme_light() +
  theme(
    legend.position = "none",
    text = element_text(size = 12, family = "serif")
  )
p2
ggsave("ExyVsProbeArea_unloading.pdf", width = 6, height = 4, units = "in",
dpi = 320)
```

The graphical output of surface shear strain as a function of total vectors from R is shown in Figure E.6. The plot shown is for loading; the output for unloading is similar and is not shown.

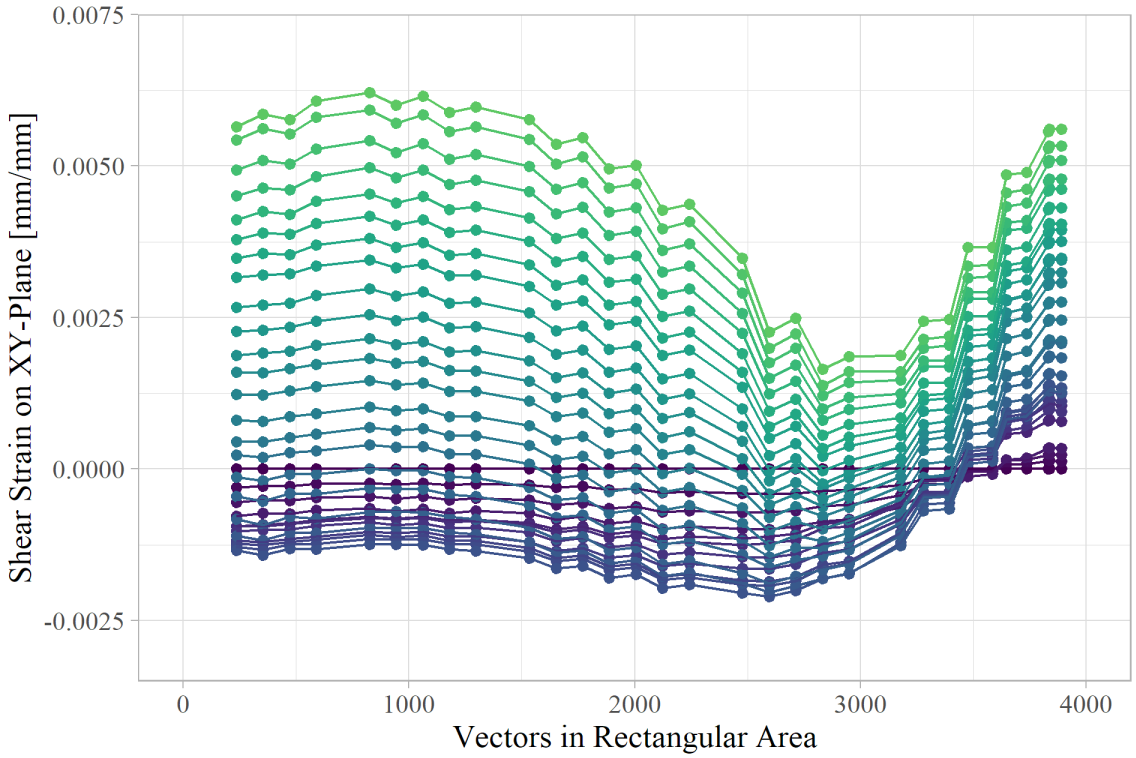

Figure E.6. R output of surface shear strain as a function of total vectors.

E.1.7 Archwire Surface Shear Strain versus Probe Rectangle Height Plot

The surface strains were plotted for each group based on the height of the rectangle used to average the strain values. The data frame was organised as follows:

Bracket: Indicates the bracket type as “Rigid Dowel” or “Damon Q” as a character variable

Material: Indicates the archwire material as “Stainless Steel” or “Titanium Molybdenum Alloy” as a character variable

Height: Indicates the height of the rectangle as a numeric variable

Mean: Indicates the measured average surface strain as a numeric variable

SD: Indicates the standard deviation of average surface strain as a numeric variable

The code to generate the plot is shown below:

```
# Load libraries
library(tidyverse)

# Create variable containing string of where data is saved
filepath <- file.path(
  "[personal filepath redacted]"
)
# Set working directory
setwd(filepath)
# Import data
data <- read_csv("ExyVsArea.csv")

# Generate and export the plot
p1 <- ggplot(data = data, mapping = aes(
  x = data$Area,
  y = data$Mean,
  colour = factor(data$Material):factor(data$Bracket),
  shape = factor(data$Material):factor(data$Bracket)
)) +
  geom_point(size = 1.5) +
  geom_errorbar(aes(
    ymin = data$Mean - data$`Standard Deviation`,
    ymax = data$Mean + data$`Standard Deviation`
  ),
  width = 0.01,
  size = 0.25
  ) +
  xlim(-0.01,0.31) +
  ylim(0,0.015) +
  labs(x = "Rectangle Height [mm]", y = "Surface Strain",
       colour = "Bracket Type", shape = "Bracket Type") +
  scale_shape_manual(values = c(15, 16, 17, 18)) +
  theme_light() +
  theme(
    text = element_text(size = 12, family = "serif")
  )
p1
ggsave("ExyVsArea.pdf", width = 6, height = 4, units = "in", dpi = 320)
```

The graphical output of surface shears strain as a function of rectangle height from R is shown in Figure E.7.

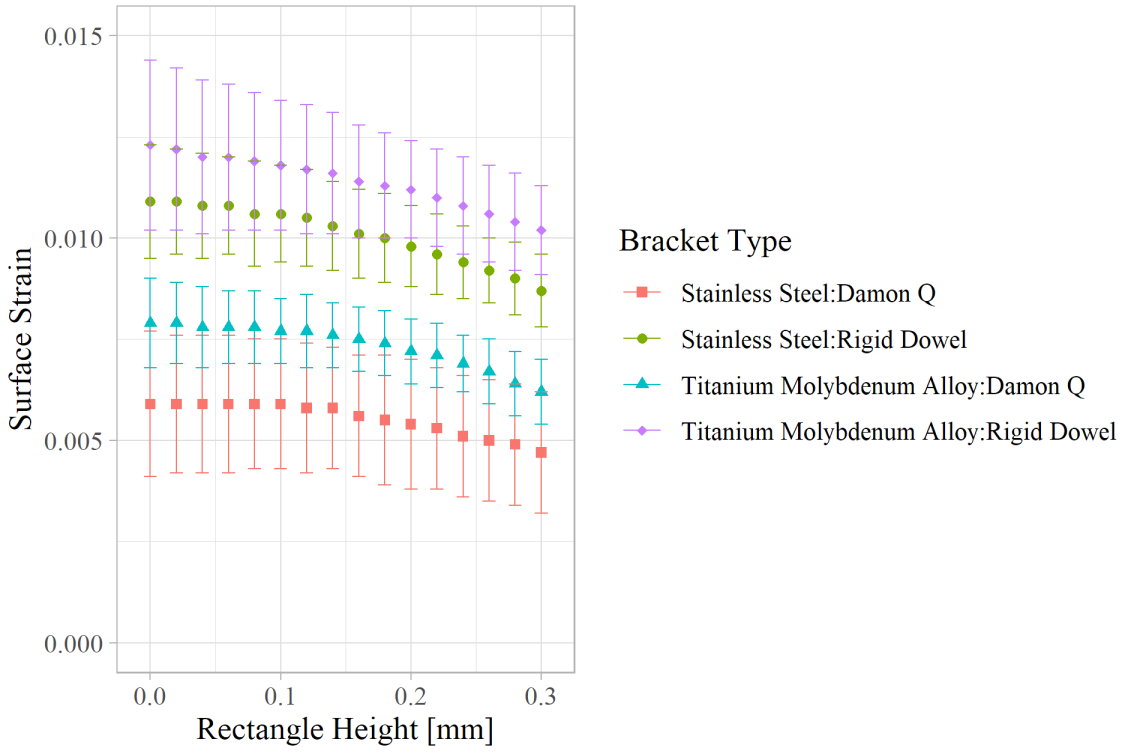

Figure E.7. R output of surface shear strain as a function of rectangle height.

E.1.8 Archwire Surface Shear Strain Plots

The archwire surface shear strain plots for each group are plotted for comparison. The data frame was organised as follows:

Material: Indicates the archwire material as “Stainless Steel” or “Titanium Molybdenum Alloy” as a character variable

Bracket: Indicates the bracket type as “Rigid Dowel” or “Damon Q” as a character variable

Angle: Indicates the measured rotation angle as a numeric variable

Strain: Indicates the measured average surface strain as a numeric variable

The code to generate the plots is shown below:

```
# Load libraries
library(tidyverse)

# Create variable containing string of where data is saved
filepath <- file.path(
  "[personal filepath redacted]"
)
# Set working directory
setwd(filepath)

# Import data
data <- read_csv("ShearStrain.csv")
data <- group_by(data, Material, Bracket, Angle) %>%
  summarise(
    count = n(),
    mean = mean(Strain, na.rm = TRUE),
    sd = sd(Strain, na.rm = TRUE)
  )

Exys_loading <- filter(data, Angle %% 1 == 0)
Exys_unloading <- filter(data, Angle %% 1 != 0)

# Generate and export the plots
p1 <- ggplot(data = Exys_loading, mapping = aes(
  x = Exys_loading$Angle,
  y = Exys_loading$mean,
  colour = factor(Exys_loading$Bracket):factor(Exys_loading$Material),
  shape =  factor(Exys_loading$Bracket):factor(Exys_loading$Material),
  stroke = 0
)) +
  geom_point(size = 1.5) +
  geom_errorbar(aes(
    ymin = mean - sd,
    ymax = mean + sd
  ),
  width = 0.5,
  size = 0.25
  ) +
  labs(
    x = "Angle", y = "Surface Strain",
    colour = "Bracket Type", shape = "Material"
  ) +
  xlim(0,30.5) +
  ylim(-0.003, 0.017) +
```

```
  scale_shape_manual(values = c(15, 16, 17, 18)) +
  theme_light() +
  theme(text=element_text(size = 12, family = "serif"))
p1
ggsave("ExyLoading.pdf", width = 6, height = 4, units = "in", dpi = 320)

p2 <- ggplot(data = Exys_unloading, mapping = aes(
  x = Exys_unloading$Angle,
  y = Exys_unloading$mean,
  colour = factor(Exys_loading$Bracket):factor(Exys_loading$Material),
  shape =  factor(Exys_loading$Bracket):factor(Exys_loading$Material),
  stroke = 0
)) +
  geom_point(size = 1.5) +
  geom_errorbar(aes(
    ymin = mean - sd,
    ymax = mean + sd
  ),
  width = 0.5,
  size = 0.25
  ) +
  labs(
    x = "Angle", y = "Surface Strain",
    colour = "Bracket Type", shape = "Material"
  ) +
  xlim(0,30.5) +
  ylim(-0.003, 0.017) +
  scale_shape_manual(values = c(15, 16, 17, 18)) +
  theme_light() +
  theme(text=element_text(size = 12, family = "serif"))
p2
ggsave("ExyUnloading.pdf", width = 6, height = 4, units = "in", dpi = 320)
```

The graphical output for surface shear as a function of rotation angle from R is shown in Figure E.8. The plot shows strains measured when loading; the output for strains measured when unloading is not shown.

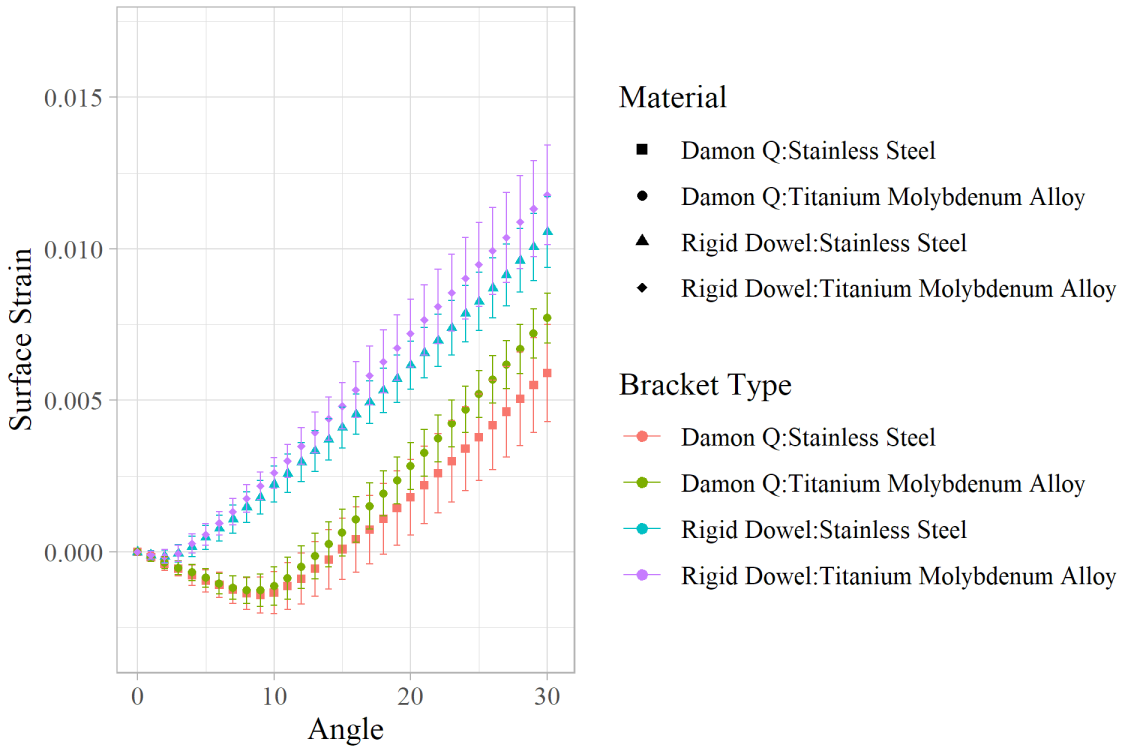

Figure E.8. R output of surface shear strain as a function of rotation angle.

E.1.9 Bracket Tie-Wing Displacement Plots

Damon Q bracket displacements were measured by comparing the distances between the top and bottom tie-wings on the left side of the bracket. The displacements were measured in the y- and z-directions. The data frame was organised as follows:

Material: Indicates the archwire material as "Stainless Steel" or "Titanium Molybdenum Alloy" as a character variable

Angle: Indicates the measured rotation angle as a numeric variable

TopY: Indicates the measured y-position of the top tie-wing as a numeric variable

BotY: Indicates the measured y-position of the bottom tie-wing as a numeric variable

TopZ: Indicates the measured z-position of the top tie-wing as a numeric variable

BotZ: Indicates the measured z-position of the bottom tie-wing as a numeric variable

The code to generate the plots is shown below:

```
# Load libraries
library(tidyverse)

# Create variable containing string of where data is saved
filepath <- file.path(
  "[personal filepath redacted]"
)
# Set working directory
setwd(filepath)

# Import data
Disp <- read_csv("RawDisp.csv")
# Calculate differences in tie-wing distance
Disps <- group_by(Disp, Material, Bracket, Angle) %>%
  summarise(
    count = n(),
    mean_y = mean(TopY - BotY, na.rm = TRUE),
    sd_y = sd(TopY - BotY, na.rm = TRUE),
    mean_z = mean(TopZ - BotZ, na.rm = TRUE),
    sd_z = sd(TopZ - BotZ, na.rm = TRUE)
  )

Disps_loading <- filter(Disps, Angle %% 1 == 0)
Disps_unloading <- filter(Disps, Angle %% 1 != 0)
# Generate and export the plots
p1 <- ggplot(data = Disps_loading, mapping = aes(
  x = Disps_loading$Angle,
  y = Disps_loading$mean_y,
  colour = factor(Disps_loading$Material),
  shape =  factor(Disps_loading$Material),
  stroke = 0
)) +
  geom_point(size = 1.5) +
  geom_errorbar(aes(
    ymin = mean_y - sd_y,
    ymax = mean_y + sd_y
```

```
  ),
  width = 0.5,
  size = 0.25
  ) +
  labs(
    x = "Angle", y = "Y-Displacements (mm)",
    colour = "Material", shape = "Material"
  ) +
  xlim(0,30.5) +
  ylim(-0.002,0.020) +
  scale_shape_manual(values = c(15, 16)) +
  theme_light() +
  theme(text=element_text(size = 12, family = "serif"))
p1
ggsave("DispYLoading.pdf", width = 6, height = 4, units = "in", dpi = 320)

p2 <- ggplot(data = Disps_unloading, mapping = aes(
  x = Disps_unloading$Angle,
  y = Disps_unloading$mean_y,
  colour = factor(Disps_unloading$Material),
  shape =  factor(Disps_unloading$Material),
  stroke = 0
)) +
  geom_point(size = 1.5) +
  geom_errorbar(aes(
    ymin = mean_y - sd_y,
    ymax = mean_y + sd_y
  ),
  width = 0.5,
  size = 0.25
  ) +
  labs(
    x = "Angle", y = "Y-Displacements (mm)",
    colour = "Material", shape = "Material"
  ) +
  xlim(0,30.5) +
  ylim(-0.002,0.020) +
  scale_shape_manual(values = c(15, 16)) +
  theme_light() +
  theme(text=element_text(size = 12, family = "serif"))
p2
ggsave("DispYUnloading.pdf", width = 6, height = 4, units = "in", dpi = 320)

p3 <- ggplot(data = Disps_loading, mapping = aes(
  x = Disps_loading$Angle,
  y = Disps_loading$mean_z,
  colour = factor(Disps_loading$Material),
  shape =  factor(Disps_loading$Material),
  stroke = 0
)) +
  geom_point(size = 1.5) +
  geom_errorbar(aes(
    ymin = mean_z - sd_z,
    ymax = mean_z + sd_z
  ),
```

```
  width = 0.5,
  size = 0.25
  ) +
  labs(
    x = "Angle", y = "Z-Displacements (mm)",
    colour = "Material", shape = "Material"
  ) +
  xlim(0,30.5) +
  ylim(-0.002,0.020) +
  scale_shape_manual(values = c(15, 16)) +
  theme_light() +
  theme(text=element_text(size = 12, family = "serif"))
p3
ggsave("DispZLoading.pdf", width = 6, height = 4, units = "in", dpi = 320)

p4 <- ggplot(data = Disps_unloading, mapping = aes(
  x = Disps_unloading$Angle,
  y = Disps_unloading$mean_z,
  colour = factor(Disps_unloading$Material),
  shape =  factor(Disps_unloading$Material),
  stroke = 0
)) +
  geom_point(size = 1.5) +
  geom_errorbar(aes(
    ymin = mean_z - sd_z,
    ymax = mean_z + sd_z
  ),
  width = 0.5,
  size = 0.25
  ) +
  labs(
    x = "Angle", y = "Z-Displacements (mm)",
    colour = "Material", shape = "Material"
  ) +
  xlim(0,30.5) +
  ylim(-0.002,0.020) +
  scale_shape_manual(values = c(15, 16)) +
  theme_light() +
  theme(text=element_text(size = 12, family = "serif"))
p4
ggsave("DispZUnloading.pdf", width = 6, height = 4, units = "in", dpi = 320)
```

The graphical output for tie-wing displacement differences in the *y*-direction while loading from R is shown in Figure E.9. The outputs for unloading, as well as for the *z*-direction are similar and are not shown.

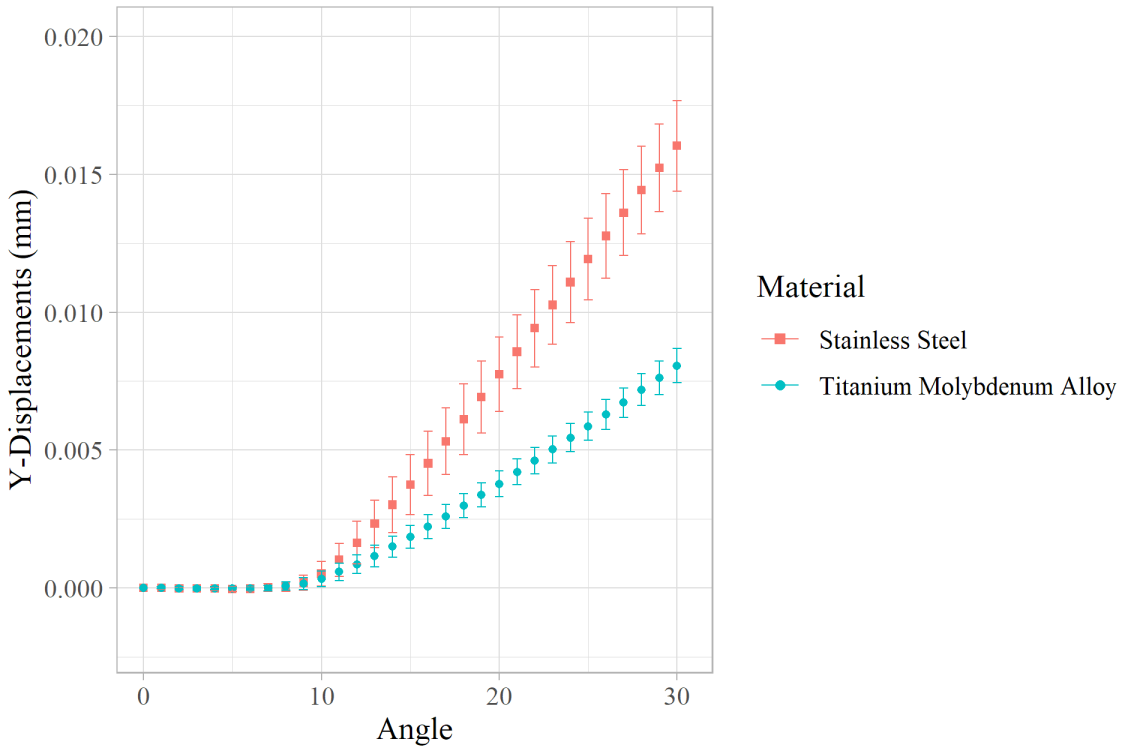

Figure E.9. R output of as a function of rotation angle.

E.2 Statistical Methods

Statistical analysis was performed using R. Some functions used were available in base R, but the "tidyverse" package was used to import data.

E.2.1 Factorial Design Randomisation

The randomisation for testing order was determined for the RD and the brackets separately, as the RD trials were completed prior to the Damon Q bracket trials. The randomisation determined the archwire material as either SS or TMA. Seeds were used to generate pseudo-random sequences. By setting seeds, the same randomised sequence is reproducible. Seeds were arbitrarily chosen. The code used to generate the randomised sequences is shown below:

```r
# Initialise levels for randomization for full study
material <- rep(c("SS", "TA"), 23)

# Randomisation for Rigid Dowel
set.seed(2017)
rdsequence <- sample(material, 46)

# Randomisation for Damon Q Brackets
set.seed(2019)
dqsequence <- sample(material, 46)
```

The output from the randomisation for the RD sequence is:

```
"TA" "SS" "TA" "TA" "SS" "SS" "TA" "TA" "TA" "TA" "SS" "SS" "SS" "SS" "SS" "TA"

"SS" "TA" "TA" "SS" "TA" "TA" "SS" "TA" "SS" "SS" "SS" "SS" "TA" "SS" "SS" "TA"

"TA" "SS" "SS" "TA" "TA" "SS" "TA" "SS" "SS" "TA" "TA" "SS" "TA" "TA"
```

The output from the randomisation for the Damon Q bracket sequence is:

```
"SS" "TA" "SS" "SS" "TA" "SS" "TA" "SS" "TA" "TA" "SS" "TA" "SS" "SS" "TA" "SS"

"TA" "SS" "TA" "SS" "TA" "TA" "SS" "TA" "SS" "TA" "SS" "SS" "TA" "TA" "SS" "SS"

"TA" "SS" "SS" "TA" "TA" "SS" "SS" "TA" "TA" "TA" "TA" "TA" "SS" "SS"
```

These sequences determined the testing order performed for the factorial design.

E.2.2 Two-Way ANOVA

The code used to perform the two-way ANOVA is shown below:

```r
# Load libraries
library(tidyverse)

# Create variable containing string of where data is saved
filepath <- file.path(
  "[personal filepath redacted]"
)
# Set working directory
setwd(filepath)

# Import data
```

```r
data <- read_csv("TorqueResults.csv")
# Convert negative torque values to positive
data$Torque <- -1*data$Torque

# Prepare group vectors for ANOVA
material <- rep(c(1, 2), each = 46)
bracket <- rep(c(1, 2), each = 23, times = 2)

# Perform ANOVA and get ANOVA table
anova1 <- aov(data$Torque ~ material + bracket)
summary(anova1)
```

The R output of the ANOVA is shown below:

```
            Df Sum Sq Mean Sq F value Pr(>F)
material     1  15458   15458  1637.6 <2e-16 ***
bracket      1   3978    3978   421.5 <2e-16 ***
Residuals   89    840       9
---
Signif. codes:  0 ‘***’ 0.001 ‘**’ 0.01 ‘*’ 0.05 ‘.’ 0.1 ‘ ’ 1
```

APPENDIX F MATLAB CODE FOR DIC POST-PROCESSING AND PLOTTING

MATLAB (MATLAB 2019a, The MathWorks, Inc., Massachusetts, USA) was used for image post-processing. Digital image correlation (DIC) outputs were exported as vector fields as ".im7" and ".vc7" files and were analysed using a post-processing toolbox (PIVMat 4.10, F. Moisy, Île-de-France, France) [91]. The colour maps used were imported from the MATLAB package "Perceptually uniform colormaps" [92]. The script was used to extract displacement and strain data for all DIC outputs. It requires manual folder navigation to get data for all trials. Plots are manually exported as ".pdf" files. The MATLAB code is shown below:

```
%% OTS Archwire Torsion DIC Results Processing

% Results of interest: Exy, Displacements
% Must navigate to corresponding folder
% One trial contains 62 images: 1-31 loading, 32-62 unloading


%% Exy -- need to be in Exy exported folder
% Goes through the shear strains
Exy = loadvec('*.im7');
showf(Exy, 'Loop', 'CMap', 'viridis')


%% Exy Individual
% Plots each shear strain and individual angles
close all
% Prepares figures positions relative to monitor
screen = get(0,'screensize');
width = screen(3)/4; height = screen(4)/4;
figure(1); figure(2);
set(1,'Position', [screen(3)/2-width-10,screen(4)/2, width, height]);
set(2,'Position', [screen(3)/2+10,screen(4)/2, width, height]);

% Input which image # to plot
imgnum = '31'; % 01 will show very small values due to no movement

% Plot images
% Be in the folder containing .im7 files for Exy
exy = loadvec(strcat('B000',imgnum,'.im7'));
```

```
statf(exy)
% exy = maskrectf(exy, [-1.55 -0.22 -1.47 -0.14], 'phys');
figure(1);
showf(exy, 'CMap', 'viridis')
set(gca,'fontname','Times New Roman', 'fontsize', 12)
caxis([-0.05 0.05])

% Initialise coordinates for rectangular box for probing
x1 = -2.5;
x2 = x1 + 2;
y = -0.04;
line = [x1 y-0.05 x2 y+0.05];
% plot rectangle for visual confirmation
rectangle('Position', [x1 y-0.05 2 0.1])
exy_line = extractf(exy,line); % delta_y of 0 = two rows
statf(exy_line)
figure(2)
showf(exy_line, 'CMap', 'viridis')
caxis([-0.05 0.05])


%% Exy -- cycle through all angles
% Automatically get strain data for all images in data set
% Be in the folder containing .im7 files for Exy

vector = ["01" "02" "03" "04" "05" "06" "07" "08" "09" "10" ...
          "11" "12" "13" "14" "15" "16" "17" "18" "19" "20" ...
          "21" "22" "23" "24" "25" "26" "27" "28" "29" "30" ...
          "31" "32" "33" "34" "35" "36" "37" "38" "39" "40" ...
          "41" "42" "43" "44" "45" "46" "47" "48" "49" "50" ...
          "51" "52" "53" "54" "55" "56" "57" "58" "59" "60" ...
          "61" "62"];


output = zeros(62,1);

for i = 1:numel(vector)
    exy = loadvec(strcat('B000',vector(i),'.im7'));
    exy = extractf(exy,[x1 y x2 y]);
%     Mask to remove high noise regions that may affect averages
%     exy = maskrectf(exy, [-1.55 -0.22 -1.47 -0.14], 'phys');
    strains = statf(exy);
    output(i) = strains.mean;
end

% Code to check effects of changing probed area
% Outputs strain values at all rectangle heights from 0 to 0.30
% "y1" goes from 0 to 0.15 since it goes in both +ve and -ve directions
%
% output = zeros(62,16);
% y1 = 0:0.01:0.15;
% for j = 1:numel(y1)
%     for i = 1:numel(vector)
%         exy = loadvec(strcat('B000',vector(i),'.im7'));
```

```
%          exy = extractf(exy,[x1 y-y1(j) x2 y+y1(j)]);
% %          exy = maskrectf(exy, [-1.55 -0.22 -1.47 -0.14], 'phys');
%          strains = statf(exy);
%          output(i,j) = strains.mean;
%      end
% end

statf(exy)
showf(exy, 'CMap', 'viridis')
disp("DONE")


%% VC7
% Be in the folder containing .vc7 files

V = loadvec('*.vc7');
showf(vec2scal(V, 'norm3d'), 'Loop', 'CMap', 'viridis', 'mesh')
daspect([1 1 1])


%% VC7 Individual
% Be in the folder containing .vc7 files

close all
screen = get(0,'screensize');
width = screen(3)/4; height = screen(4)/4;
figure(1); figure(2);

set(1,'Position', [screen(3)/2-width-10,screen(4)/2, width, height]);
set(2,'Position', [screen(3)/2+10,screen(4)/2, width, height]);

imgnum = '31'; % 01 will show very small values due to no movement

v = loadvec(strcat('B000',imgnum,'.vc7'));
figure(1)
% can change "ux" below to any of: norm3d, ux, uy, uz
showf(vec2scal(v,'ux'), 'CMap', 'viridis')
daspect([1 1 1])
set(gca,'fontname','Times New Roman', 'fontsize', 12)
caxis([-0.15 0.15])
% can change "ux" below to any of: norm3d, ux, uy, uz
statf(vec2scal(v,'ux'))
% Initialise box for probing values
left = -0.3;
bottom = 0.1;
box = [left bottom (left + 0.5) (bottom + 0.7)];
% rectangle('Position',[left bottom 0.5 0.7])
v_box = extractf(v,box);
% v_box = maskrectf(v_box, [0.18 -1.35 0.31 -1.22],'phys');

statf(vec2scal(v_box,'norm3d'))
figure(2)
showf(vec2scal(v_box,'norm3d'), 'CMap', 'viridis')
```

```
%% VC7 -- cycle through all angles
% Automatically get displacement data for all images in data set
% Be in the folder containing .vc7 files

vector = ["01" "02" "03" "04" "05" "06" "07" "08" "09" "10" ...
          "11" "12" "13" "14" "15" "16" "17" "18" "19" "20" ...
          "21" "22" "23" "24" "25" "26" "27" "28" "29" "30" ...
          "31" "32" "33" "34" "35" "36" "37" "38" "39" "40" ...
          "41" "42" "43" "44" "45" "46" "47" "48" "49" "50" ...
          "51" "52" "53" "54" "55" "56" "57" "58" "59" "60" ...
          "61" "62"];
 output = zeros(62,2);

for i = 1:numel(vector)
     v = loadvec(strcat('B000',vector(i),'.vc7'));
     v = extractf(v,box);
%      v = maskrectf(v, [0.18 -1.35 0.31 -1.22],'phys');
     disp_y = statf(vec2scal(v,'uy'));
     disp_z = statf(vec2scal(v,'uz'));
     output(i,1) = disp_y.mean;
     output(i,2) = disp_z.mean;
end

disp("DONE")
```

An example of a MATLAB generated plot is shown in Figure F.1, where displacements in the *z*-direction at 30° loading are projected onto the undeformed image of an stainless steel archwire and Damon Q bracket.

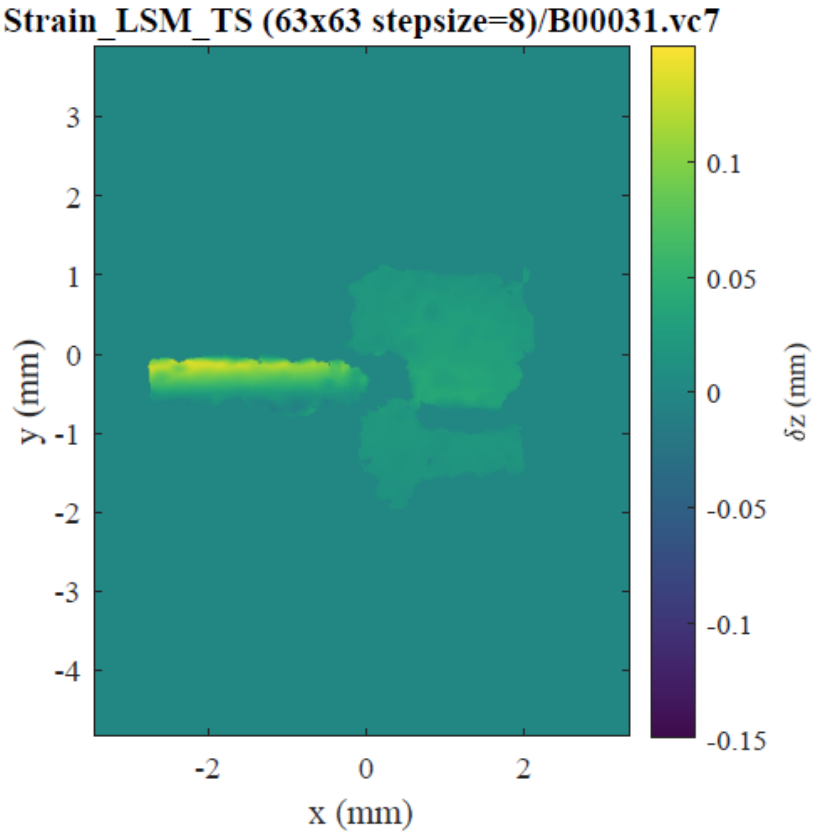

Figure F.1. MATLAB output of *z*-displacements of an archwire and bracket at 30° loading as measured from DIC.

APPENDIX G PILOT STUDY FOR FACTORIAL DESIGN

A pilot two-by-two factorial was first performed to determine the appropriate sample size necessary for the full study. Due to the large difference in archwire material properties and the resultant interaction with the rigid dowel (RD) versus orthodontic brackets, third-order torque responses was expected to differ, and a two-way analysis of variance (ANOVA) could be performed on the torque data to determine sample size. With third-order torque being the only parameter of interest for sample size calculation, DIC was omitted for the pilot study and was only utilised for the full study.

The pilot study consisted of five trials per group for a total of 20 trials, making it a balanced design. Instead of a full randomisation between all 20 trials, archwire material was randomised, while all testing with the rigid dowel was completed prior to testing with the Damon Q brackets. Statistical analysis including randomisation sequencing and ANOVA was conducted with R (R Core Team, 2017) [88].

G.1 Third-Order Torque

Third-order torque was measured following the same methodology as previous testing, where a 30° rotation was applied in 1° increments. The torque value at 30° loading was used to perform the two-way ANOVA. During pilot testing, a procedural error occurred whereby the angular position of the Orthodontic Torque Simulator (OTS) was not at the passive position to begin a trial. This resulted in outlier trials which had significantly lower torque values due to the archwire being rotated at smaller actual angles compared to the recorded angles. Consequently, additional

trials were performed to ensure that each group had five trials to maintain a balanced design for the pilot study, and the outlier trials were removed when performing the ANOVA and sample size calculation. The absolute values of resultant torque at 30° are individually shown in Figure G.1, including torque from the outlier trials.

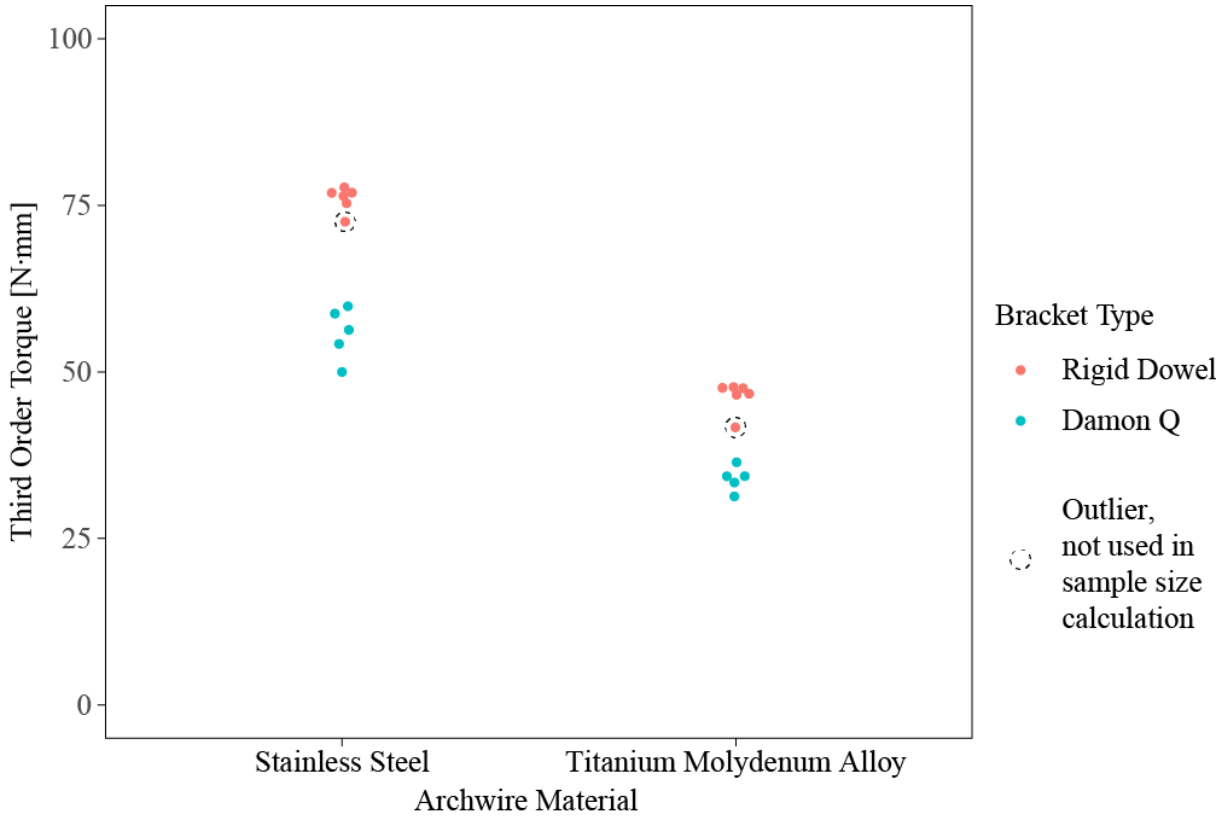

Figure G.1. Individual maximum torques of 0.019”x0.025 archwires at 30° loading among all trials in the pilot study.

The full torque curves from 0° to 30° with loading and unloading are shown for each group in Figure G.2. Evidently, both archwire material and bracket type had a significant effect on the maximum torque obtained. Stainless steel (SS) archwires led to higher torque values compared to titanium molybdenum alloy (TMA) archwires, as did using the RD compared to Damon Q brackets.

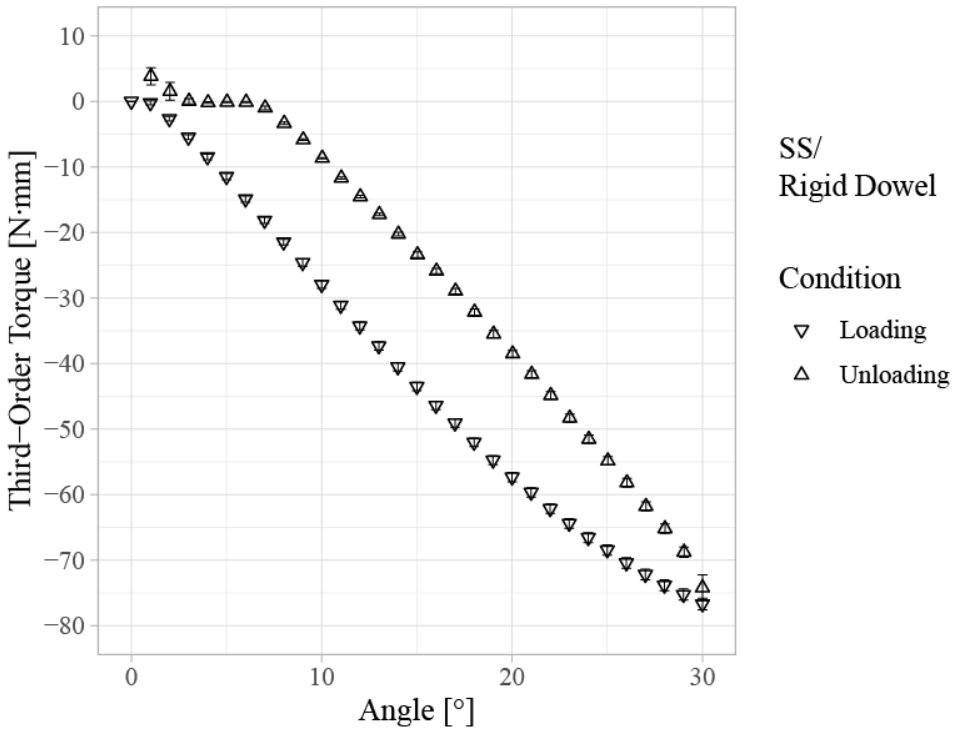
Third−Order Torque [N·mm]
10
0
−10
−20
−30
−40
−50
−60
−70
−80
0
10
20
30
Angle [°]
SS/
Rigid Dowel
Condition
Loading
Unloading

(a)

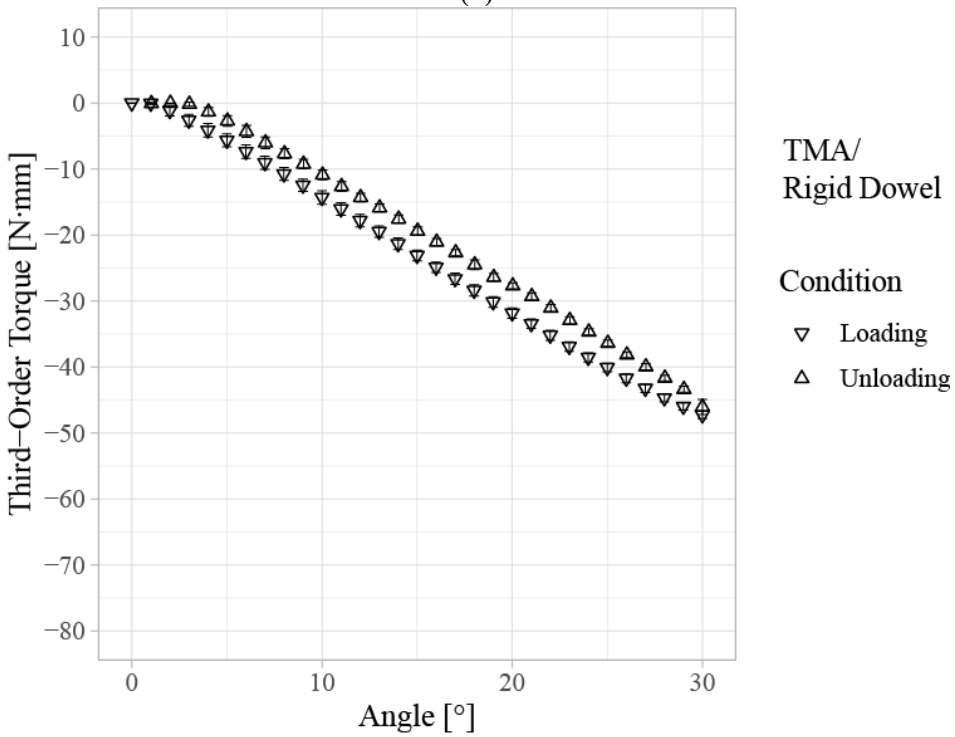
Third−Order Torque [N·mm]
10
0
−10
−20
−30
−40
−50
−60
−70
−80
0
10
20
30
Angle [°]
TMA/
Rigid Dowel
Condition
Loading
Unloading

(b)

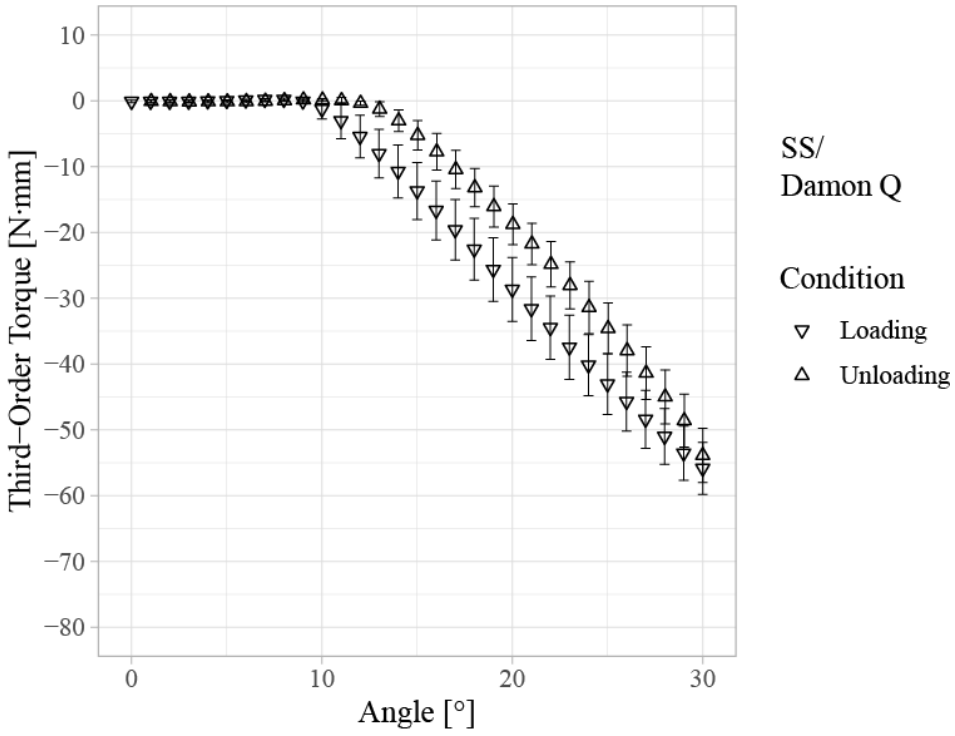

(c)

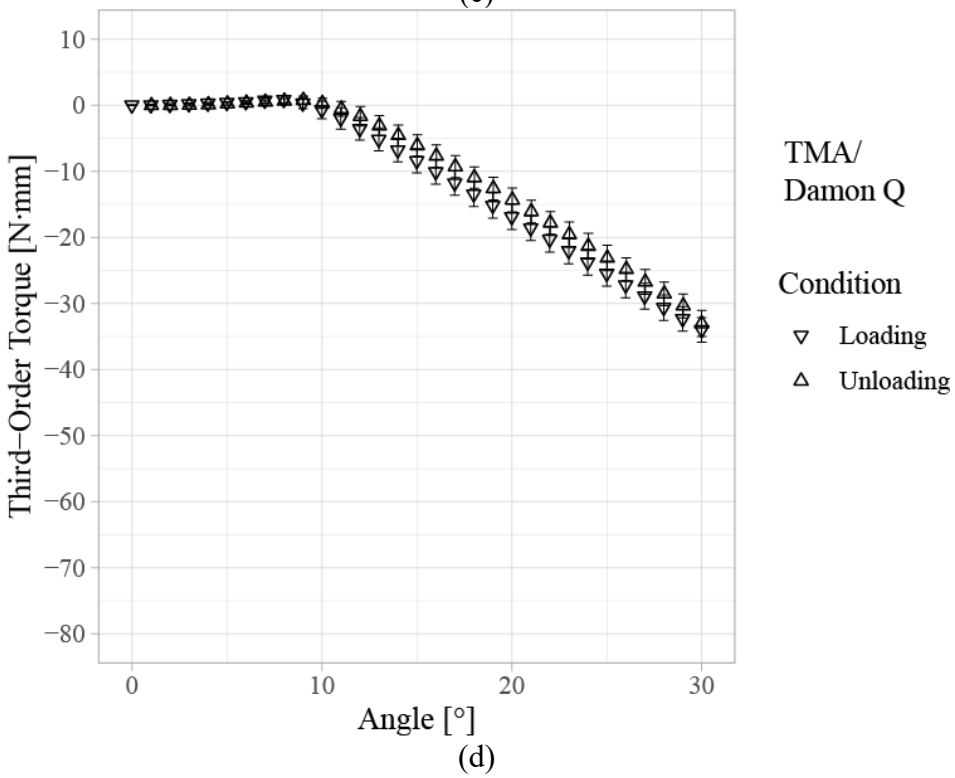

(d)

Figure G.2. Third-order torque responses of 0.019”x0.025” archwires rotated to 30° with the configurations of (a) stainless steel archwire with rigid dowel, (b) titanium molybdenum alloy archwire with rigid dowel, (c) stainless steel archwire with Damon Q bracket, and (d) titanium molybdenum alloy archwire with Damon Q bracket, n = 5.

To compare the four groups, a two-way ANOVA was performed on the maximum torque values, and the ANOVA table is shown in Table G.1. The p-values for archwire material and bracket type are both much less than 0.1, indicating that there is strong evidence against the null hypothesis of there being no difference between archwire materials or bracket type. This result was intuitive, and further analysis using the maximum torque values can be performed to obtain the sample size for the full study.

Table G.1. Two-way ANOVA table of the two-by-two factorial design used in the pilot study.

	Df	Sum Sq	Mean Sq	F-value	p-value	
Material	1	1453	1453	163.3	**<0.001**	***
Bracket	1	3287	3287	369.4	**<0.001**	***
Residuals	17	151	9			

Signif. codes: 0 '***' 0.001 '**' 0.01 '*' 0.05 '.' 0.1 ' ' 1						

G.2 Sample Size Calculation

To calculate the sample size, effect sizes (η^2 values) for each factor were calculated using the R package "DescTools" [95]. Then, the sample size was calculated using the R package "pwr2" [99]. The effect sizes were found to be $\eta^2_{material}$ = 0.2970 and $\eta^2_{bracket}$ = 0.6720. Using these effect sizes, the sample size was determined by setting α = 0.05 (probability of Type I error) and β = 0.20 (probability of Type II error). The sample size required for the full study was found to be 23 trials per group for a total of 92 trials.

G.3 R Code

The R code used for the pilot study includes all code required for sample size calculation. Code for figure generation is omitted here as all figure generation code is found in Appendix E. The data frame used in the pilot study was organised as follows:

Trial: Indicates trial number as a numeric variable

Angle: Indicates measured rotation angle as a numeric variable

Condition: Indicates whether the OTS is “Loading” or “Unloading” as a character variable

Torque: Indicates measured third-order torque as a numeric variable

```
# Load libraries
library(tidyverse)
library(DescTools)
library(pwr2)

# Initialise levels for randomization for pilot test
materials <- rep(c("SS", "TA"), 5)

# Randomisation for Rigid Dowel
set.seed(01110010)
rdsequence <- sample(materials, 10)

# Randomisation for Damon Q Brackets
set.seed(01100100)
dqsequence <- sample(materials, 10)

# Create variable containing string of where data is saved
filepath <- file.path(
  "[personal filepath redacted]")

# Set working directory
setwd(filepath)

# Import data
data <- read_csv("PilotTorque.csv")
# Convert negative torque values to positive
```

```r
data$Torque <- -1*data$Torque

# Prepare group vectors for ANOVA
material <- rep(c(1, 2), each = 10)
bracket <- rep(c(1, 2), each = 5, times = 2)

# Perform ANOVA and get ANOVA table
anova1 <- aov(data$Torque ~ material + bracket)
summary(anova1)

# Calculate effect size using "EtaSq" function from "DescTools" package
eta <- EtaSq(anova1)

# Calculate sample size using "ss.2way" function from "pwr2" package
ss.2way(a = 2, b = 2, alpha = 0.05, beta = 0.2, f.A = eta[1], f.B = eta[2],
B = 100)

# alpha Significant level (Type I error probability)
# beta Type II error probability (Power=1-beta)
```

G.3.1 Factorial Design Randomisation

The output from the randomisation for the RD sequence is:

```
"SS" "TA" "TA" "TA" "SS" "SS" "TA" "SS" "TA" "SS"
```

The output from the randomisation for the Damon Q bracket sequence is:

```
"TA" "SS" "TA" "TA" "TA" "SS" "SS" "SS" "TA" "SS"
```

These sequences determined the testing order performed for the pilot study.

G.3.2 Two-Way ANOVA

The R output of the ANOVA table is shown below:

```
            Df Sum Sq Mean Sq F value   Pr(>F)
material     1   1453    1453   163.3 3.83e-10 ***
bracket      1   3287    3287   369.4 5.73e-13 ***
Residuals   17    151       9
---
Signif. codes:  0 ‘***’ 0.001 ‘**’ 0.01 ‘*’ 0.05 ‘.’ 0.1 ‘ ’ 1
```

G.3.3 Effect Size and Sample Calculation

The R output for the effect sizes is:

```
             eta.sq eta.sq.part
material 0.2970490   0.9057050
bracket  0.6720246   0.9560048
```

The R output for the sample size is:

```
     Balanced two-way analysis of variance sample size adjustment

              a = 2
              b = 2
      sig.level = 0.05
          power = 0.8
              n = 23

NOTE: n is number in each group, total sample = 92
```